

UNIVERSITY OF CALIFORNIA,  
IRVINE

Hydrogen Gas Separation from Hydrogen/Natural Gas Mixtures by High Temperature Proton  
Exchange Membrane Electrochemical Hydrogen Pump

DISSERTATION

Submitted in partial satisfaction of the requirements  
for the degree of

DOCTOR OF PHILOSOPHY

in Mechanical and Aerospace Engineering

by

John Michael Stansberry

Dissertation Committee:  
Professor Jack Brouwer, Chair  
Professor Iryna Zenyuk  
Professor Yun Wang

2024



## **DEDICATION**

To Amber, my best friend and partner in life, thank you for taking this journey with me.

To all my friends and my family who believed in me.

To Eric, a beautiful soul.

# TABLE OF CONTENTS

LIST OF FIGURES .....	vi
LIST OF TABLES .....	xii
ACKNOWLEDGEMENTS .....	xiii
VITA .....	xiv
ABSTRACT OF THE DISSERTATION .....	xvi
Chapter 1 Introduction.....	1
Chapter 2 Literature Review.....	6
2.1 Hydrogen Gas Separation .....	6
2.1.1 Separation by Adsorption Processes .....	9
2.1.2 Separation by Cryogenic Distillation.....	10
2.1.3 Separation by Porous Membranes .....	10
2.1.4 Separation by Dense Membranes.....	12
2.1.5 Separation by Hybrid Separation Designs .....	13
2.2 Electrochemical Hydrogen Pump .....	15
2.2.1 Low Temperature Proton Exchange Membrane EHP .....	21
2.2.2 High Temperature Proton Exchange Membrane EHP based on PBI-PA.....	25
2.2.3 Recent developments in High-Temperature Proton Exchange Membranes and Ionomers .....	32
Chapter 3 Goal & Objectives.....	35
Chapter 4 Approach.....	36
Chapter 5 Experimental Characterization of PA-PBI based HT-PEM EHP for the separation of low H <sub>2</sub> content Methane/H <sub>2</sub> gas mixtures.....	39
5.1 Introduction.....	39
5.2 Experimental Materials.....	39
5.2.1 HT-PEM EHP test stand for gas separation .....	39
5.2.2 Phosphoric Acid Doped Polybenzimidazole (PA-PBI) Membranes.....	41
5.2.3 Gas Diffusion Electrodes & MEA Assembly.....	42
5.3 Experimental Methods .....	44
5.3.1 Cell Start-Up & Conditioning.....	44
5.3.2 H <sub>2</sub> /CH <sub>4</sub> Gas Separation .....	45
5.4 Results & Discussion .....	45



5.5 Summary & Conclusions .....	59
Chapter 6 Operando X-Ray CT of PA-PBI based HT-PEM EHPs.....	61
6.1 Experimental Materials.....	63
6.2 Experimental Methods.....	65
6.3 Results & Discussion.....	66
6.4 Summary & Conclusions.....	68
Chapter 7 Two-Dimensional Model of PA-PBI based HT-PEM EHP for gas separation .....	69
7.1 Introduction.....	69
7.2 Modelling Methodology and Description.....	70
7.2.1 Gaseous Species Transport .....	72
7.2.2 Conservation of Electronic Charge.....	79
7.2.3 Conservation of Protons.....	81
7.2.4 Aqueous Phosphoric Acid Phase.....	83
7.2.5 Electrode Kinetics.....	87
7.2.6 Conservation of Energy .....	92
7.2.7 Voltage Breakdown by Spatially Normalized Power-Losses.....	95
7.3 Results & Discussion.....	99
7.3.1 Model Validation with Varying Operating Conditions .....	99
7.3.2 Influence of humidification and operating pressure on H <sub>2</sub> product purity .....	101
7.3.3 Voltage loss breakdown analysis.....	103
7.3.4 Influence of increasing compression ratios on HT-PEM EHP .....	107
7.3.5 Influence of electrode acid content on HT-PEM EHP .....	110
7.4 Summary & Conclusions.....	113
Chapter 8 Stability and performance of Ion-Pair HT-PEM for EHP application .....	115
8.1 Introduction.....	115
8.2 Experimental Materials.....	116
8.2.1 Membrane .....	116
8.2.2 MEA Assembly .....	117
8.2.3 Ion-Pair HT-PEM EHP Test Stand.....	119
8.3 Experimental Methods.....	119
8.3.1 Cyclic Voltammetry .....	119
8.3.2 Electrochemical Impedance Spectroscopy .....	124

8.3.3 Distribution of Relaxation Times.....	127
8.3.4 Cell Start-Up and Conditioning .....	128
8.3.5 Stability Characterization of Ion-Pair HT-PEM EHP .....	129
8.4 Results & Discussion .....	132
8.4.1 Non-Ionomeric Gas Diffusion Electrodes .....	132
8.4.2 Ionomeric Gas Diffusion Electrodes.....	144
8.4.3 Distribution of Relaxation Times & Non-ionomeric vs. Ionomeric GDEs in Ion-pair EHP .....	152
8.4.4 Performance of Ion-pair HT-PEM EHPs with bimetallic PGM catalyst for HOR and HER.....	158
8.4.5 Natural Gas Separation with Ion-Pair HT-PEM EHP .....	171
8.5 Conclusions.....	180
Chapter 9 Characterization of highly sulfonated ionomers in Ion-Pair based HT-PEM EHP electrodes for H <sub>2</sub> gas separation from low H <sub>2</sub> content H <sub>2</sub> /Natural Gas Blends .....	182
9.1 Introduction.....	182
9.2 Experimental Materials.....	185
9.2.1 Membrane .....	185
9.2.2 Catalyst Inks & Gas Diffusion Electrodes .....	185
9.2.3 MEA Assembly .....	187
9.3 Experimental Methods.....	187
9.3.1 Ion-pair HT-PEM EHP Start-up & Conditioning.....	187
9.3.2 Sol-Gel PBI HT-PEM EHP Start-up & Conditioning.....	188
9.4 Results & Discussion .....	188
9.4.1 Comparison of ionomeric binders in 100% H <sub>2</sub> pump.....	188
9.4.2 Gas Separation & Compression with Ion-pair HT-PEM EHP.....	193
9.5 Conclusions.....	208
Chapter 10 Summary & Conclusions .....	210
10.1 Summary.....	210
10.2 Conclusions.....	211
10.3 Future Work .....	215
References.....	217

## LIST OF FIGURES

Figure 1.1 CAISO curtailments of solar and wind generation assets[16].....	2
Figure 1.2 Power-to-gas (P2G) technology pathways. Reproduced from [25] .....	4
Figure 2.1 SAE J2719/ ISO14687-2 fuel cell road vehicle fuel quality standards. Reproduced from [56]. .....	8
Figure 2.2 Robeson plot for H <sub>2</sub> /CH <sub>4</sub> selectivity of polymeric and CSMS membranes. Reproduced from [71] .....	11
Figure 2.3 Mechanism of hydrogen transport in palladium membranes. Reproduced from [73].	13
Figure 2.4 HylyPure hydrogen gas separation process concept. Reproduced from [79].....	14
Figure 2.5 Hybrid gas separation process proposed from HyGrid process optimization study. Reproduced from [78]. .....	15
Figure 2.6 Original US patent for EHP[82] .....	16
Figure 2.7 Electrochemical hydrogen pump for gas separation and compression of hydrogen. ..	16
Figure 2.8 Ideal compression work in kWh/kg (top) and as a fraction of % LHV (bottom) as a function of pressure ratio. ....	20
Figure 2.9 a) Chemical structure of Nafion® b) Proton transport mechanisms of Nafion®. Reproduced from [89]. .....	22
Figure 2.10 HyET EHP compression stack. Reproduced from [95]. .....	23
Figure 2.11 Impact of CO <sub>2</sub> introduction to LT-PEM EHP in non-polarized condition. Reproduced from [104]. .....	24
Figure 2.12 Proton conduction mechanisms for PA-PBI. Reproduced from [112]. .....	26
Figure 2.13 H <sub>2</sub> S and CO tolerance over 3500 hours of sol-gel PA-PBI in fuel cell operation. Reproduced from [122]. .....	28
Figure 2.14 Sol-gel cast m/p PA-PBI membranes in EHP operation at 30 psi differential pressure, 160 °C, 0.2 A cm <sup>-2</sup> . Reproduced from [127]. .....	29
Figure 2.15 Schematic of HT-PEM in EHP operation at MEA level. Modified from [128]. .....	30
Figure 2.16 Comparison of effective operation window and of fuel cells based on PA-PBI and QAPOH-PA HT-PEM (left). Interaction energy between base moiety and phosphoric acid dopant (right). .....	33
Figure 2.17 Rated power density of Ion-pair HT-PEMFC ('This work') compared to other existing polymer electrolyte fuel cell technologies. Reproduced from [157]. .....	34
Figure 5.1 Test stand for PA-PBI HT-PEM EHP testing .....	40
Figure 5.2 X-Ray CT of De Nora gas diffusion electrodes with loading of 1 mg Pt cm <sup>2</sup> . .....	43
Figure 5.3 5 cm <sup>2</sup> cell assembly. ....	44
Figure 5.4 Temperature vs. vapor pressure of water for equilibration of 99 and 100% wt H <sub>3</sub> PO <sub>4</sub> phosphoric acid and observed reversal of dimerization of phosphoric acid species at anhydrous conditions from Daletou et al [163]. .....	46
Figure 5.5 Polarization curve (left), EIS with impedance values (middle), and iR-corrected polarization curves (right) for varying amounts of phosphoric acid added to Freudenberg type gas diffusion electrodes for PBI-PA HT-PEM EHP .....	48
Figure 5.6 Polarization curve (left), EIS with impedance values (middle), and iR-corrected polarization curves (right) for varying amounts of phosphoric acid added to De Nora type gas diffusion electrodes for PBI-PA HT-PEM EHP .....	49
Figure 5.7 HT-PEM EHP polarization curves for Freudenberg and De Nora GDEs for H <sub>2</sub> /CH <sub>4</sub> gas separations. ....	50

Figure 5.8 Nernst potential prediction versus observed open-circuit voltage in H <sub>2</sub> /CH <sub>4</sub> separation and corresponding minimum theoretical separation efficiency. ....	51
Figure 5.9 Polarization curve, Nyquist plot of EIS at 0.02 A cm <sup>-2</sup> , and iR + OCV corrected polarization behavior of the HT-PEM EHP with De Nora GDE for H <sub>2</sub> /CH <sub>4</sub> gaseous mixtures at equal pressure operation and co-compression operation. ....	52
Figure 5.10 Specific energy consumption of H <sub>2</sub> separation for equal compression and co-compression of H <sub>2</sub> /CH <sub>4</sub> blends in PA-PBI based HT-PEM EHP .....	53
Figure 5.11 Cathode effluent H <sub>2</sub> purity for HT-PEM EHP operation in H <sub>2</sub> /CH <sub>4</sub> blends for equal pressure and co-compression gas separation modes. ....	54
Figure 5.12 Permeation rates of H <sub>2</sub> (top left) and CH <sub>4</sub> (top right) as a function of anode pressure for net pressure differential permeation and partial pressure differential only. Fitted diffusive and convective permeation coefficients (bottom). ....	56
Figure 5.13 Comparison of EHP performance with published EHP performance for low % H <sub>2</sub> in CH <sub>4</sub> blends. Data reproduced from Nordio et al., 2019[169], Mrusek et al., 2024[102], and Vermaak et al., 2021 [148]. ....	57
Figure 5.14 Specific energy of separation comparison of PBI-PA HT-PEM EHP against HyLyPure hybrid separation system for ultra-low H <sub>2</sub> concentration separations from H <sub>2</sub> /CH <sub>4</sub> blends. ....	58
Figure 6.1 Re-distribution of phosphoric acid to the anode GDL/flow field in HT-PEMFC with increasing current density. Reproduced from [183]. ....	62
Figure 6.2 HT-PEM EHP Operando cell hardware .....	64
Figure 6.3 Operando HT-PEM EHP cell mounted on X-ray CT stage at ALS beamline 8.3.2 ...	65
Figure 6.4 Polarization curves of operando HT-PEM EHP compared to 5 cm <sup>2</sup> MEA bench tests. ....	66
Figure 6.5 Representative slice of X-Ray CT reconstruction of HT-PEM EHP cell. ....	67
Figure 7.1 HT-PEM EHP model geometry and domains .....	71
Figure 7.2 Conductivity of aqueous phosphoric acid as function of temperature and % wt H <sub>3</sub> PO <sub>4</sub> . Reproduced from [212]. ....	82
Figure 7.3 Experimental measurements of binary diffusion coefficients of pure H <sub>2</sub> O-Phosphoric Acid. Reproduced from [217] .....	85
Figure 7.4 Water vapor pressure of aqueous phosphoric acid solutions. ....	86
Figure 7.5 Influence of transfer coefficient and pressure coefficient on predicted electrode overpotential of HOR/HER by Butler-Volmer equation. ....	90
Figure 7.6 HT-PEM EHP structure: GDE structure from x-ray CT (left), MEA structure from operando x-ray CT (middle), illustration of catalyst layer structure with increasing volume fractions of phosphoric acid (right). ....	91
Figure 7.7 Correlation between activity coefficient $\theta_{active}$ and phosphoric acid volume fraction in the catalyst layer. Reproduced from [134]. ....	91
Figure 7.8 HT-PEM EHP model agreement with polarization curves from experiments. ....	100
Figure 7.9 HT-PEM EHP model agreement with cathode outlet purity measurements. ....	100
Figure 7.10 Water vapor pressure in along the length of the cathode channel, inlet at channel length = 0 (Top). H <sub>2</sub> volumetric content at the cathode outlet before drying as a function of current density. ....	102
Figure 7.11 Methane concentration in cathode outlet on dry basis as function of current density for compression ratio of 1 and 1.3. ....	103
Figure 7.12 Voltage loss breakdown analysis for 2% and 100% H <sub>2</sub> anode feeds. ....	104

Figure 7.13 Current density distribution in membrane and catalyst layers in HT-PEM EHP model at 2% H <sub>2</sub> .	105
Figure 7.14 Voltage loss breakdowns at 0.1 and 0.2 V cell potentials for tested compression ratio and varying H <sub>2</sub> concentrations.	106
Figure 7.15 Varying compression ratio for 10% H <sub>2</sub> feed in HT-PEM EHP.	108
Figure 7.16 Varying compression ratio for 2% H <sub>2</sub> feed in HT-PEM EHP	109
Figure 7.17 Voltage loss breakdown of increasing compression ratio for 2 and 10% H <sub>2</sub> at 0.1 and 0.2 V cell voltage.	110
Figure 7.18 Validation of varying electrode acid content with experimental polarization curves.	111
Figure 7.19 Voltage loss breakdown of varying acid electrode content.	112
Figure 7.20 Acid distribution of HT-PEM EHP and HT-PEMFC[134].	113
Figure 8.1 Ion-pair HT-PEM MEA with protonated phosphonic acid electrodes. Reproduced from [158].	116
Figure 8.2 Ion exchange process for QAPOH membrane from OH <sup>-</sup> to biphosphate anion form[230].	117
Figure 8.3 Ionomeric GDE fabrication process	118
Figure 8.4 Test stand for HT-PEM EHP testing modified for Ion-pair HT-PEM.	119
Figure 8.5 A cyclic-voltammetry profile for Pt(poly) obtained in 0.05 M	120
Figure 8.6 Cyclic voltammograms of (a) Pt(100), (b) Pt(110), (c) Pt(111) and (d) PtSn(111) electrodes in 0.1 M HClO <sub>4</sub> with the addition of various amounts of H <sub>3</sub> PO <sub>4</sub> (shown as figure legends). Potential scan rate 50 mV s <sup>-1</sup> . Reproduced from [234].	121
Figure 8.7 Cyclic Voltammogram of PBI based HT-PEM EHP after operation in dry condition at 160 °C for 72 hours. Reproduced from [243]	124
Figure 8.8 Representative Nyquist Plot of PEM Fuel Cell EIS	125
Figure 8.9 Simplified Randles circuit for interpretation of EHP EIS Data	126
Figure 8.10 Stability testing procedure for Ion-pair HT-PEM EHP testing.	130
Figure 8.11 Gas and electrode configuration for Ion-pair HT-PEM EHP operation and cyclic voltammetry measurements.	131
Figure 8.12 Simplified Randles equivalent circuit model with additional inductor element for EIS data interpretation.	132
Figure 8.13 EIS of non-ionic Ion-Pair HT-PEM in potentiostatic stability testing.	133
Figure 8.14 Effect of cyclic voltammetry on non-ionic HT-PEM EHP at anode feed T <sub>sat</sub> = 80 deg C. a) Cathodic CV and b) anodic CV, c) shows the amperometric response before and following anodic and cathodic CV d) EIS spectrum before and following cathodic and anodic CV.	134
Figure 8.15 Amperometric response of non-ionic HT-PEM EHP at 0.1 V over time with HFR and R <sub>CT</sub> measured hourly.	135
Figure 8.16 Cathodic & anodic CVs and EIS response preceding and following CV measurements for non-ionic ion-pair HT-PEM EHP	136
Figure 8.17 Characterization of dry operation of non-ionic ion-pair HT-PEM EHP	138
Figure 8.18 Bar chart summary of HFR and R <sub>CT</sub> change due to cyclic voltammetry for non-ionic ion-pair HT-PEM EHP	139
Figure 8.19 Cyclic voltammetry vertex variation on non-ionic ion-pair HT-PEM EHP. a) 0.1V potentiostatic hold and HFR/R <sub>CT</sub> change with respect to time b-d) EIS spectra for potentiostatic hold.	140

Figure 8.20 Varying vertex CVs for non-ionomeric ion-pair HT-PEM EHP, transparency of CVs corresponding to cycle number a) 0.5 V vs. RHE peak vertex b) 0.7 V vs. RHE vertex c) 0.9 V vs. RHE vertex .....	141
Figure 8.21 a) Anodic and b) cathodic recovery CV vertex variation in non-ionomeric GDE ion-pair HT-PEM EHP. c) EIS spectra preceding and following cathodic and anodic CV d-e) HFR and $R_{CT}$ values fitted EIS data .....	142
Figure 8.22 High temperature RDE in pure phosphoric acid on platinum electrode. Reproduced from[235]. .....	143
Figure 8.23 Potentiostatic stability and EIS of non-ionomeric GDE ion-pair HT-PEM EHP at 120 and 160 °C at anodic humidification of $T_{sat} = 40$ °C.....	144
Figure 8.24. EIS of Nafion®/PWN ionomeric GDE Ion-Pair HT-PEM in potentiostatic stability testing.....	145
Figure 8.25 Amperometric response of Nafion®/PWN ionomeric GDE HT-PEM EHP at 0.1 V over time with HFR and $R_{CT}$ measured hourly.....	146
Figure 8.26 Cathodic & anodic CVs and EIS response preceding and following CV measurements for Nafion®/PWN ionomeric ion-pair HT-PEM EHP. ....	147
Figure 8.27 Bar chart summary of HFR and $R_{CT}$ change due to cyclic voltammetry for Nafion®/PWN ionomeric ion-pair HT-PEM EHP.....	148
Figure 8.28 EIS stability data of Nafion®/PWN ionomeric GDE ion-pair HT-PEM operating at high temperatures 160/180/200 °C.....	149
Figure 8.29 16-hour potentiostatic stability of Nafion®/PWN ionomeric GDE Ion-pair HT-PEM EHP at elevated temperatures 160/180/200 °C with HFR and $R_{CT}$ trends. ....	150
Figure 8.30 Polarization curves and Ir-Corrected polarization curves of Nafion®/PWN ionomeric GDE Ion-pair HT-PEM EHP with respect to humidity at 160 °C and respect to temperature at anode $T_{sat} = 80$ °C. Comparisons to conventional and sol-gel PBI HT-PEM EHP. ....	151
Figure 8.31 Selection of regularization parameter for DRT analysis based on sum of squared residuals analysis. ....	153
Figure 8.32 Example DRT spectrum of Nafion®/PWN ionomeric GDE ion-pair HT-PEM with peaks identified. ....	154
Figure 8.33 DRT function time-series for 0.1 V potentiostatic hold with EIS taken hourly, comparing non-ionomeric vs ionomeric GDE ion-pair HT-PEM stability .....	155
Figure 8.34 Non-ionomeric ion-pair HT-PEM EHP 0.1 V a) Before CV b) following cathodic CV c) following anodic CV DRT function with respect to frequency and DRT-Nyquist fit. d) Total impedance contribution by mechanism from DRT. ....	157
Figure 8.35 Nafion®/PWN ionomeric ion-pair HT-PEM EHP 0.1 V a) Before CV b) following cathodic CV c) following anodic CV DRT function with respect to frequency and DRT-Nyquist fit. d) Total impedance contribution by mechanism from DRT. ....	158
Figure 8.36 a) HOR mass activity of PtRu/C in RDE with phosphoric acid(PA) and pentafluorophenyl phosphonic acid (PPA) and in ion-pair HT-PEMFC MEA with PWN ionomeric binder (‘non-protonated anode’) and Nafion®/PWN ionomeric binder (‘protonated anode’) with equivalent acid concentration. B) HOR mass activity in RDE of PtC vs. PtRu/C as a function of perfluoro-1,4-phenylene) bis(phosphonic acid) concentration. Reproduced from[157]. ....	160
Figure 8.37 Polarization and iR-corrected polarization curves of ion-pair HT-PEM EHP with Pt/C and PtRu/C electrodes at 160 °C from anode $T_{sat} = 60$ °C to $T_{sat} = 80$ °C .....	161
Figure 8.38 Anodic and Cathodic cyclic voltammograms of Pt/C vs. PtRu/C electrodes at 160 °C for anodic humidification of $T_{sat} = 60$ °C and $T_{sat} = 80$ °C .....	162

Figure 8.39 EIS and DRT and associated DRT function at 50 mV of Ion-pair HT-PEM EHP with Pt/C and PtRu/C electrodes at 160 °C with varying anodic humidification. ....	164
Figure 8.40 a) DRT with frequency domains highlighted for 100% H <sub>2</sub> operation b)-d) Impedance contributions calculated from DRT analysis at 50 mV for Pt/C and PtRu/C electrodes at 160 °C with varying anodic humidification. ....	165
Figure 8.41 Polarization curves of ion-pair HT-PEM EHP with PtRu/C vs. Pt/C electrodes for 120, 140, 160 °C. ....	167
Figure 8.42 OCV and ohmic loss corrected polarization curves of ion-pair HT-PEM EHP with PtRu/C vs. Pt/C electrodes for 120, 140, 160 °C ....	168
Figure 8.43 Cyclic voltammetry taken at 50 mV/sec of PtRu/C and Pt/C electrodes in MEA for 120, 140, and 160 °C. ....	169
Figure 8.44 DRT at 50 mV for PtRu/C vs. Pt/C electrodes in ion-pair HT-PEM EHP for varying temperature and relative humidity. ....	170
Figure 8.45 Net impedance contribution at 50 mV calculated from DRT for PtRu/C vs. Pt/C electrode ion-pair HT-PEM EHP. ....	171
Figure 8.46 Gas chromatography of natural gas, H <sub>2</sub> , and humidified (T <sub>sat</sub> = 60 °C) then dried (~T <sub>sat</sub> = 20 °C) 10% H <sub>2</sub> in natural gas anodic feed to HT-PEM EHP for nat. gas separation testing. ....	172
Figure 8.47 Dilution of hydrogen content in blended gas feed with increasing pressure and relative humidity. ....	174
Figure 8.48 Open-circuit voltage variation due to varying partial pressures of hydrogen in EHP at 160 °C and 40 kPaG anode pressure with respect to varying cathodic pressure and humidification. ....	176
Figure 8.49 10% H <sub>2</sub> /Natural Gas blend separation in ion-pair HT-PEM EHP at 1.0 SLPM anode flow rate and pressure ratio of 1.5 a) Polarization curve b-d) 16 hour 0.15 V potentiostatic stability and separation test. ....	177
Figure 8.50 DRT and EIS data from 16-hour stability of 10% H <sub>2</sub> /Natural Gas separation testing. ....	178
Figure 8.51 300 mV 100 hour stability test of 10% H <sub>2</sub> / Natural Gas blend separation with HFR change. ....	180
Figure 9.1 H <sup>+</sup> conductivity of PWN2010 compared to Nafion®, PVPA, and PmPRA in P <sub>v</sub> = 10 <sup>5</sup> Pa at 100 to 160 °C. Reproduced from [154]. ....	183
Figure 9.2 a) Protonation of phosphonic acid sites on PWN binder and enhanced acidity of the resulting ‘protonated’ ionomer b) DFT calculations on propensity of protonation between phosphonic acid and sulfonic acid site of the PFSA. Reproduced from [157]. ....	184
Figure 9.3 From left to right: Chemical structure and ion exchange capacity of PWN, SPPsf-55/SPPsf-80, and Nafion ® 211 ionomeric binders. ....	186
Figure 9.4 Initial characterization cyclic voltammetry at 40 °C of 1:1 wt ratio PWN/PFSA ionomer blends and PWN only ionomer in ion-pair HT-PEM EHP. ....	189
Figure 9.5 a) 100% H <sub>2</sub> polarization curves at 160 °C, T <sub>sat</sub> 80 °C for 1:1 wt ratio PWN/PFSA ionomer ion-pair HT-PEM EHP b) iR-corrected polarization curve c) 5 and 25mV EIS spectra. ....	190
Figure 9.6 a) 100% H <sub>2</sub> polarization curve at 160 °C with varying anodic humidity for ion-pair HT-PEM EHP with Nafion®/PWN ionomeric binder blend vs. SPPsf55/PWN ionomeric binder blend at 1:1 wt ratios b) iR and OCV corrected polarization curve c) 5 and 25 mV EIS spectra d) ECM fitted HFR and R <sub>CT</sub> values from EIS spectra at 25 mV. ....	191

Figure 9.7 Humidity dependence of ion-pair HT-PEM EHP with Nafion®/PWN ionomer vs. SPPsf-55/PWN ionomer at P/S ratio 0.75 and 2.0 a) polarization curve b) iR+OCV corr. polarization curve c) initial cyclic voltammetry at 40 °C d) ECM fitted HFR and R <sub>CT</sub> e) EIS at 5 and 25 mV.....	193
Figure 9.8 Polarization dependence of HT-PEM EHP with stepping of compression ratio from P <sub>r</sub> = 1.0 to P <sub>r</sub> = 1.5 a) polarization curve b) EIS spectra at 25 mV c) overpotential increase versus current density at P <sub>r</sub> = 1.5 versus P <sub>r</sub> = 1.0.....	195
Figure 9.9 a-d) DRT analysis of 100% H <sub>2</sub> EHP operation at P <sub>r</sub> = 1.0 and P <sub>r</sub> = 1.5 for the four different HT-PEM EHP MEAs e-g) Net impedance change due to pressure ratio calculated from DRT analysis.....	196
Figure 9.10 Polarization curves of HT-PEM EHP with blends of H <sub>2</sub> and CH <sub>4</sub> gas for 10/5/2% volumetric concentrations of H <sub>2</sub> gas in the blend. ....	198
Figure 9.11 a-c) EIS spectra at 5, 25, and 50 mV from OCV and d-f) iR-corrected polarization curves of HT-PEM EHP in CH <sub>4</sub> .....	200
Figure 9.12 DRT analysis from EIS analysis of 10/5/2 % vol. H <sub>2</sub> blended with CH <sub>4</sub> in HT-PEM EHPs at 25 and 50 mV applied voltage over OCV.....	201
Figure 9.13 Impedance contributions calculated from DRT analysis at 25 and 50 mV overpotential from OCV for HT-PEM EHP with H <sub>2</sub> /CH <sub>4</sub> gas blend anodic feed. ....	202
Figure 9.14 12-hour equilibration at 0.3 V for CH <sub>4</sub> and natural gas H <sub>2</sub> gas blends containing 5 % vol H <sub>2</sub> . Failure of Sol-gel PBI in H <sub>2</sub> /Nat. Gas. ....	203
Figure 9.15 Polarization curves of HT-PEM EHP with blends of H <sub>2</sub> in natural gas and pure methane gas for 10/5/2% volumetric concentrations of H <sub>2</sub> gas in the blend. ....	204
Figure 9.16 a-c) EIS taken at 25 mV overpotential and d-f) EIS at 50 mV overpotential for both methane and natural gas H <sub>2</sub> blends g-i) iR-corrected polarization curves of HT-PEM EHP in natural gas and pure methane gas H <sub>2</sub> blends.....	204
Figure 9.17 DRT functions for methane and natural gas blends in 10/5/2 % vol. hydrogen at 25 and 50 mV overpotentials. ....	205
Figure 9.18 Impedance analysis from DRT functions for methane and natural gas blends in 10/5/2 % vol. hydrogen at 25 and 50 mV overpotentials. ....	206
Figure 9.19 Methane and natural gas H <sub>2</sub> blend HT-PEM EHP separations for 10, 5 and 2 %, cathode effluent composition at 0.3 V 1-hour holds.....	207
Figure 9.20 Specific energy of separated H <sub>2</sub> gas versus outlet mass flux per active cell area (top) and hydrogen recovery factor (bottom). ....	208



## LIST OF TABLES

Table 2-1 Natural gas composition taken at Engineering Lab Facility, University of California Irvine .....	7
Table 2-2 Separation technologies by minimum H <sub>2</sub> feed and outlet purity compared to targets ...	8
Table 2-3 PA-doped PBI polymer properties based on preparation method. ....	27
Table 5-1 Physical characteristics of Freudenberg and De Nora based GDEs for HT-PEM EHP	43
Table 6-1 MEA composition for operando HT-PEM EHP cells .....	64
Table 6-2 Membrane thickness of operando cell for varying operating conditions .....	67
Table 7-1 Governing equations of HT-PEM EHP model by domain .....	72
Table 7-2. Dynamic viscosities of gaseous components .....	73
Table 7-3 Carmen-Kozeny parameter values for permeability coefficient calculation in Darcy's Law .....	74
Table 7-4 Binary diffusion coefficient of gaseous species correlation implemented in HT-PEM EHP model .....	76
Table 7-5 Gaseous Species Transport Boundary and Initial Conditions .....	76
Table 7-6 Source terms for gaseous species transport equations in the catalyst layer .....	78
Table 7-7 Permeability coefficients for gaseous species cross-over .....	79
Table 7-8 Potentiostatic boundary and initial conditions for conservation of electrons.....	80
Table 7-9 Source terms for conservation of electrons .....	80
Table 7-10 Boundary and Initial conditions for conservation of ionic current.....	83
Table 7-11 Source and sink terms for conservation of ionic current.....	83
Table 7-12 Boundary and initial conditions for aqueous phosphoric acid phase conservation of species .....	86
Table 7-13 Source terms for aqueous phosphoric acid phase conservation of species .....	87
Table 7-14 Properties for Butler-Volmer kinetics of HOR and HER.....	92
Table 7-15 Material thermal properties .....	94
Table 7-16 Source terms for conservation of energy .....	95
Table 7-17 Boundary and initial conditions for conservation of energy .....	95
Table 7-18 Power-loss voltage breakdown equations in model .....	98
Table 7-19 Simulation parameters for HT-PEM EHP model .....	99
Table 8-1 Literature Survey of DRT frequency domains in HT-PEM fuel cells & H <sub>2</sub> Pump....	128
Table 8-2. DRT frequency domains for Ion-pair HT-PEM EHP.....	153
Table 8-3. MEA composition for PtRu/C vs. Pt/C study in Ion-pair HT-PEM EHP .....	160
Table 8-4 DRT analysis of HOR + HER impedance contributions combined. ....	166
Table 8-5 Composition of de-sulfurized natural gas from 40 psig distribution line and composition of natural gas blended with 10% volumetric H <sub>2</sub> and fed through anode of HT-PEM EHP at humidification of T <sub>sat</sub> = 60 °C followed by drying at 20 °C. ....	173
Table 9-1 Catalyst ink composition and GDE loading targets. ....	187
Table 9-2 HT-PEM EHP MEAs for gas separation performance comparisons .....	194
Table 9-3 Hydrogen recovery factor of HT-PEM EHPs based on theoretical limiting current for H <sub>2</sub> /CH <sub>4</sub> gas separation.....	199

## ACKNOWLEDGEMENTS

I owe an endless amount of thanks to Professor Jack Brouwer for his support throughout a large portion of my career. His drive and passion to make the world a better place has inspired me immensely in my own work.

Many thanks to Professor Iryna Zenyuk, who contributed so much of her time to advise this dissertation. She is a truly one-of-a-kind individual with an immense talent for research and instruction and I am incredibly blessed to have had the opportunity to work with her.

I owe a lot to the guidance of many over the years. Richard Hack took me under his wing early on and shared with me countless lessons that I employ regularly and am proud to share with future generations, we miss him dearly. Max Venaas thank you for all of your support in complicated experimental set ups and facilities related issues, you took every new headache with a smile, and I learned a lot from that.

Dr. Li Zhao, Dr. Luca Mastropasqua, Dr. Robert Flores, and Dr. Andrea Perego all at varying intervals kindly shared their mentorship with me and all ultimately contributed to the professional I am today. Their wisdom and time were truly invaluable.

To all my colleagues at the Clean Energy Institute, thank you all for the wonderful experiences and immensely valuable perspectives and opportunities. Yan Zhao, Ryan Ehlig, Hung-Ming Chang and Magnolia Pak, thank you all for your contributions and time either directly to my work or through enlightening conversations. To the countless others who contributed, thank you.

# VITA

## John Michael Stansberry

- 2014-2016 Undergraduate Researcher  
National Fuel Cell Research Center, University of California, Irvine
- 2016 Environmental Engineering, B.S.  
University of California, Irvine
- 2019 Teaching Assistant, Mechanical and Aerospace Engineering  
University of California, Irvine
- 2019 Mechanical Engineering, M.S.  
Advisor: Jack Brouwer  
University of California, Irvine  
Thesis: Dynamic analysis of a proton exchange membrane electrolyzer integrated with a natural gas combined cycle power plant for power-to-gas applications
- 2021-2022 Fuel Cell Systems Engineering Consultant  
Hydroplane Ltd., Thousand Oaks, CA
- 2022-2023 Senior Program Manager  
KRE Consulting, Los Angeles, CA
- 2016-2024 Graduate Research Assistant  
National Fuel Cell Research Center, University of California, Irvine
- 2024 Ph.D. Mechanical and Aerospace Engineering  
Advisor: Jack Brouwer  
University of California, Irvine

## PUBLICATIONS

**Stansberry, John**, Devashish Kulkarni, Dula Parkinson, Iryna Zenyuk, and Jack Brouwer. "Two-Dimensional Model of a High-Temperature Proton Exchange Membrane Hydrogen Pump for Efficient, Single-Stage Separation of Fuel Cell Quality Hydrogen Gas from Hydrogen-Enriched Natural Gas". Electrochemical Society Meeting Abstracts 242 (2022), 1033-1033.

Siddharth Komini Babu, Rangachary Mukundan, Jacob Michael LaManna, Abdurrahman Yilmaz, Jacob S Spendelow, Federico Suarez, Sanghun Lee, Tobias Schuler, Devashish Kulkarni, **John Stansberry**, David Jacobson, Daniel Hussey, Scott A Mauger, Guido Bender, Iryna V Zenyuk, Boris Khaykovich. "Characterizing Effect of Porous Transport Layers on Electrolyzer Performance Using Neutron Imaging". Electrochemical Society Meeting Abstracts 242 (2022), 1654-1654.

**Stansberry, John**, Andrea Perego, Iryna Zenyuk, and Jack Brouwer. "Measurement and Dynamic Modeling of Hydrogen Separation from Hydrogen Enriched Natural Gas Using Phosphoric Acid Doped Polybenzimidazole Hydrogen Pump". Electrochemical Society Meeting Abstracts 240 (2021), 755-755.

**Stansberry, John**, and Jack Brouwer. "Experimental Dynamic Dispatch of a 60 kW Proton Exchange Membrane Electrolyzer in Power-to-Gas Application." International Journal of Hydrogen Energy 45, no. 16 (2020): 9305-9316.

**Stansberry, John**, Alejandra Hormaza Mejia, Li Zhao, and Jack Brouwer. "Experimental Analysis of Photovoltaic Integration with a Proton Exchange Membrane Electrolysis System for Power-to-Gas." International Journal of Hydrogen Energy 42, no. 52 (2017): 30569-30583.

# **ABSTRACT OF THE DISSERTATION**

Hydrogen Gas Separation from Hydrogen/Natural Gas Mixtures by High Temperature Proton Exchange Membrane Electrochemical Hydrogen Pump

By

John Michael Stansberry

Doctor of Philosophy in Mechanical and Aerospace Engineering

University of California, Irvine, 2024

Professor Jack Brouwer, Chair

The proliferation of variable renewable energy resources that generate electrical power from solar and wind is a critical step in achieving a climate neutral and sustainable energy system. The successful implementation of these electrical power generators is limited due to the uncontrollable nature of their availability to produce electrical power. One method by which to shift this energy production temporally and spatially to the time and place of its demand is the production of hydrogen as a chemical energy carrier. However, this approach would require large-scale infrastructure investments to produce, store, and transport hydrogen gas.

One proposed strategy for the storage and transport of hydrogen is to blend with natural gas and inject it into pre-existing natural gas infrastructure. Hydrogen gas blended into natural gas in this way can contribute to the decarbonization of the natural gas system, however it is not as valuable in terms of its economic and carbon reduction potential. This value could be recovered if the separation of high-purity hydrogen gas from a blended gas system is done in an efficient manner.

Electrochemical hydrogen separation is a well-established technology for efficient hydrogen separation, which can be accomplished by electrochemical hydrogen pump (EHP) based on a proton conducting membrane (PEM). The EHP works to separate hydrogen by facilitating the electrochemical process of oxidation of hydrogen at an anode and subsequent evolution of hydrogen gas at a cathode, while other gaseous impurities are ideally unable to permeate through the membrane. The goal of this work is to investigate the potential of

electrochemical separation as a highly efficient means of separating trace volumetric quantities of hydrogen gas from natural gas by using high-temperature proton exchange membrane (HT-PEM).

To investigate the efficacy of this approach, a high temperature proton exchange membrane electrochemical hydrogen pump (HT-PEM EHP) based on phosphoric acid doped polybenzimidazole (PA-PBI) PEM is tested in hydrogen/methane gaseous blends while also testing the impacts of varying phosphoric acid contents in the membrane electrode assembly. Operando X-ray CT testing of the PA-PBI HT-PEM EHP is implemented to investigate the structure of the cell during pump operation under varying acid content and humidification. A two-dimensional cell model of the PBI-PA based HT-PEM EHP is developed and validated with cell testing data as well as with data from X-ray CT measurements. The emphasis of the model is on the electrochemical performance of the cell under mass transport limiting conditions and the influence of varying acid contents in the MEA.

HT-PEM EHP based on a quaternary ammonium biphosphate anion ion-pair coordinated with polyphenylene (PA-QAPOH) membrane were investigated experimentally to determine their stability and performance in EHP configuration. The presence of phosphanated poly(pentafluorostyrene) (PWN) and Nafion® ionomeric binders in the electrodes of the ion-pair EHP was found to be critical to the stability of the ion-pair EHP. Ion-pair EHP performance was characterized with respect to cell temperature and relative humidity, and the separation of high purity H<sub>2</sub> gas from pipeline natural gas and H<sub>2</sub> blends was demonstrated. The suitability of alternative sulfonic acid ionomers in the ion-pair HT-PEM EHP was measured and compared to state of the art HT-PEM EHP based on sol-gel PBI-PA membrane for low concentration hydrogen gas concentration blends in methane and in natural gas.

## Chapter 1 Introduction

The decarbonization of the global energy system has been identified as essential to reaching goals set out by the 195 nation states in the Paris Climate Agreement of 2015 to limit the rise in mean global temperatures to 1.5 °C above pre-industrial levels. As of the writing of this dissertation, the IPCC has most recently determined that global greenhouse gas emissions trends suggest a greater than 50% chance that global temperatures will exceed the 1.5 °C above pre-industrial level target by 2040 even with a 70% cut in greenhouse gas emissions from a 2019 level of 59.1 Gt CO<sub>2</sub>e/yr[1]. In response to this crisis a growing number of countries have developed net-zero carbon emission plans with timescales spanning from 2035 to 2070. As the energy sector currently drives more than three quarters of global greenhouse gas emissions, these plans ultimately require a complete overhaul in how we approach the consumption, movement, and production of energy[2].

Significant investment and policy support has successfully driven the cost of renewable energy production, particularly solar photovoltaic and land based wind turbines, to a point of cost competitiveness with many forms of conventional power generation today and forecasts of electrical power generation mixes dominated by wind and solar based generation capacity[3][4]. To achieve a carbon-free energy system, much emphasis has been placed on the combination of large deployments of solar and wind based electrical power generation with energy-storage such as long-term battery storage, in combination with electrification of carbon intensive end-uses such as transportation, heating, and industrial to achieve totally carbon-free energy systems[5][6][7][8].

In some cases the approach of electrification is highly effective, particularly in the case of residential and commercial heating and cooling[9]. In transportation, deep electrification of light-duty vehicle fleets is challenging as it will significantly increase peak electrical grid demand and thus require specific charging strategies to maintain grid reliability[10]. For heavy-duty vehicles[11], aviation[12], maritime[13], and other transportation applications, payload and range are major limiting factors in their potential electrification. Electrification of the industrial sector is a less straightforward question due to the complexity and unique nature of the various sub sectors and thus is not easily addressed in a broad sense [14][15]. When considering the

complete electrification of all energy sectors, there are significant challenges that suggest that the implementation of a renewable fuel along with the implementation of a renewable electrical grid could provide the best solution for zero emissions energy.

The implementation of a renewable fuel or chemical energy carrier to complement a renewable electrical grid becomes more attractive when considering the magnitude of energy storage required by increasing penetrations of wind and solar. Figure 1.1 displays the monthly curtailments of solar and wind energy resources in the California electrical grid and highlights the disparity between the month-to-month curtailment totals and the peak curtailments that occur due to the high production of solar PV coinciding with low electricity demand in the spring[16]. This seasonal variation in energy production requires energy storage that can scale to peak demands of 100s of gigawatt-hours (GWh) and shift energy over time scales of months. Furthermore, these curtailments are the result of an electrical grid that as of 2022 was served by 45.7 % fossil fuel generation, with 28% solar and wind power[17]. Similar challenges have been experienced in other electric grids seeking to transition from fossil fuel based electricity to solar and wind[18].

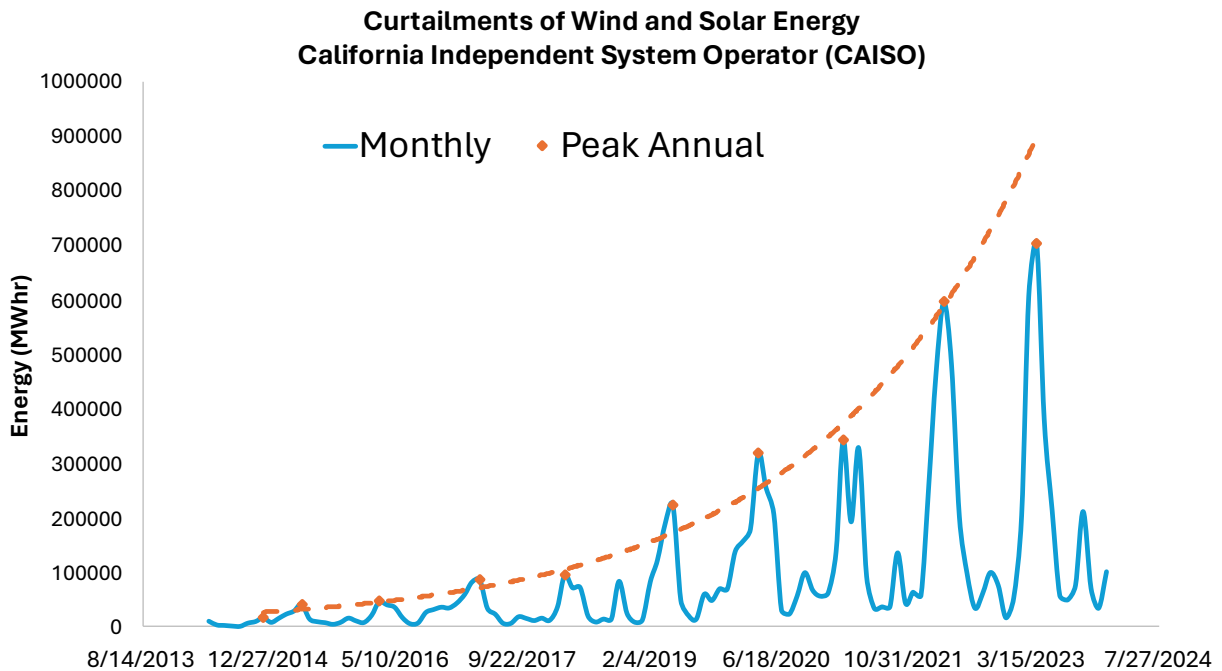


Figure 1.1 CAISO curtailments of solar and wind generation assets[16].



Since 2019, California has also added 6 GW of battery capacity, or an increase of roughly 760%, to support the further deployment of solar and wind assets currently limited by poor capacity factors and curtailments[19]. Battery based energy storage is practical for small magnitudes of energy storage and short durations making it a crucial resource for supporting variable renewable energy assets through frequency and voltage regulation (seconds to minutes time scales) up to hour-to-hour time scale energy shifting that could be required daytime in the case of solar power shifting to the evening peak demand and for short periods of inclement weather effects[20]. Ultimately, to provide the majority of electrical demand from intermittent renewable resources, geophysical constraints require energy storage on the order of several weeks to offset the seasonality of wind and solar[21] and to reduce costs relative to battery energy storage only scenarios[22].

The production of electrolytic hydrogen to serve as a chemical energy carrier, known as power-to-gas (P2G) (Figure 1.2) has been identified as a key enabler of decarbonization in part through its ability to provide the long-duration, large magnitude energy storage required for enabling renewable assets in the electrical power sector[23][24][25][26]. Furthermore, hydrogen gas produced from renewable electricity can be used as a carbon-free fuel source or commodity in difficult to decarbonize sectors, shifting overproduction of energy in the electrical sector into other energy sectors such as transportation and industrial. In transportation, hydrogen is a promising carbon-free option for heavy-duty vehicles, aviation, and maritime applications[11]. Hydrogen is a primary feedstock in the production of ammonia, oil refining, and can also be used to decarbonize steel production through direct iron reduction processes. Global policy support and investment into hydrogen energy technologies as a sustainable energy solution has increased appreciably in recent years as well as projections in future demand for clean and green hydrogen[27][28]. Currently 45 countries have produced hydrogen energy focused roadmaps outlining a future global network of importers and exporters of zero carbon ('clean') or green hydrogen [29][30].

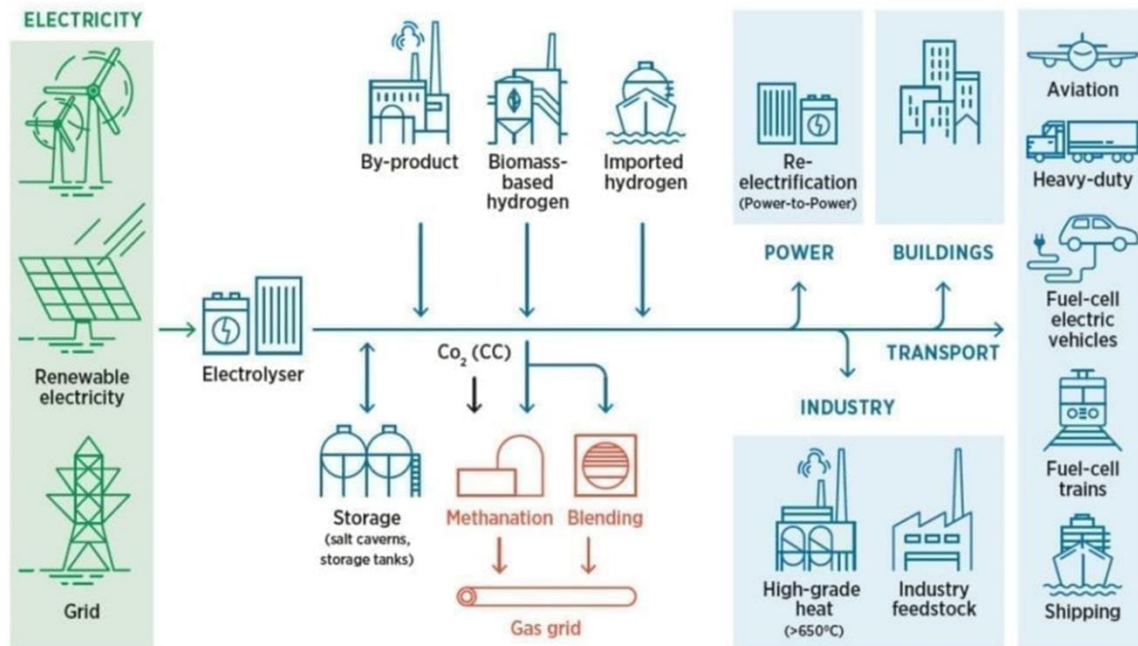


Figure 1.2 Power-to-gas (P2G) technology pathways. Reproduced from [25]

A major barrier to the introduction of a hydrogen economy on a broader scale is the lack of effective hydrogen infrastructure to store and distribute hydrogen. Hydrogen can be produced ‘on-site’ at smaller scales based on the local demands of the site, alternatively, it can be produced centrally enabling economies of scale but requiring reliable storage and distribution systems[31]. Hydrogen can be stored as a gas in above ground tanks, geological formations such as salt caverns, compressed gas trailers, or in dedicated gas pipelines which can also distribute hydrogen, or can be moved by truck and freight in the aforementioned gas trailers[32][33][34].

The utilization of pipeline transport scales best with cost and carbon intensity compared to other forms of gaseous hydrogen distribution making it the most preferred option for the large-scale deployment of power-to-gas[35]. The blending of hydrogen gas into pre-existing natural gas infrastructure has been considered due to the potential to store massive quantities of hydrogen gas in a low cost manner[36][37][38][39]. Hydrogen produced from low or zero carbon sources can then serve to decarbonize existing critical energy infrastructure while maintaining the benefits of the natural gas network due to its high reliability, the relatively low cost of energy transmission when in gaseous fuel form, and large energy storage capabilities in the form of line pack and geological storage facilities. The natural gas network also contains many otherwise

difficult to decarbonize end-uses in the chemical and industrial space such as production of fertilizer, metals, and oil refining[40].

Consensus is somewhat mixed on the maximum allowable volumetric hydrogen content in current natural gas infrastructure. This is due to the impact of hydrogen on combustion properties of the gas mixture[41][42][43][44], compressibility[45][46], the tendency of hydrogen to stress pressurized steel pipelines and reduce their ductility over time known as ‘hydrogen embrittlement’[47][48][49], and hydrogen containing gas blend leakage which has a higher risk of auto-ignition than pure natural gas and potentially more severe explosion risk with increasing hydrogen concentration[50][51]. Volumetric concentrations of hydrogen gas on the order of 1-5% by volume have been found to have negligible impact on operation and end-users while concentrations up to 10-20% by volume for most end-uses with little to no modification although ultimately the allowable concentration remains case dependent[45][52].

Global demand for hydrogen was 94 Mt in 2021, accounting for nearly 2.5% of global energy consumption - nearly half of this demand went towards the refining of hydrocarbons (40 Mt), and the rest was directed to the production of Ammonia (34 Mt), methanol (15 Mt), and steel (5 Mt) by direct reduction of iron (DRI)[53]. To meet net-zero carbon objectives, the IEA projects upwards of 660 Mt in global hydrogen demand by 2050, with much of the growth coming from the transportation sector at a predicted 285 Mt demand[28]. To distribute hydrogen as a blended gas in pre-existing natural gas infrastructure, while still meeting the growing demand for clean hydrogen in difficult to decarbonize sectors such as transportation fuel or chemical feed stocks, an efficient method to separate fuel cell quality hydrogen from gaseous blends is of critical interest.

## **Chapter 2      Literature Review**

The literature review for this work encompasses the topic of hydrogen gas separation from hydrogen blended into natural gas infrastructure and an overview of hydrogen gas separation technologies and their applicability to this use case. This is followed by a more thorough review of hydrogen gas separation by electrochemical hydrogen pumps (EHP). Literature is surveyed on high temperature proton exchange membrane (HT-PEM) electrochemical cells based on polybenzimidazole doped with phosphoric acid (PA-PBI) with an emphasis on electrochemical hydrogen pump studies, MEA composition and design, and physical modelling. Finally, recent developments in alternative HT-PEM materials are examined with respect to any promising characteristics for hydrogen natural gas separations in EHP that may exist.

### **2.1 Hydrogen Gas Separation**

Natural gas refers to a gaseous fossil fuel that is obtained either in the process of crude oil drilling, directly from natural gas fields, or from coal bed processing[54]. Depending on the source, the composition of this gas can vary appreciably but generally it is primarily comprised of methane gas along with higher hydrocarbons at lower concentrations, as well as trace constituents primarily in the form of carbon dioxide (CO<sub>2</sub>), helium, hydrogen sulfide and nitrogen. To be suitable for pipeline usage natural gas must be processed to meet environmental standards[55]. Pipeline natural gas remains a blend of gaseous hydrocarbons, primarily consisting of methane, but with lower concentrations of higher hydrocarbons such as propane that could be recovered as more valuable liquid hydrocarbon products, and with lower concentrations of inerts such as CO<sub>2</sub> and N<sub>2</sub>. Trace amounts of sulfur compounds (~1 ppm) and siloxanes can remain post-processing, with the former often added as an odorant at the distribution level (<80 psig) for detection and safety purposes. Table 2-1 shows measurements for pipeline natural gas in the SoCalGas utility territory taken at the University of California Irvine. Notably, there is an appreciable concentration of CO<sub>2</sub> and detectable levels of non-methane hydrocarbons (NMHC) up to C<sub>7</sub> species (Hexane).

*Table 2-1 Natural gas composition taken at Engineering Lab Facility, University of California Irvine*

<b>Pipeline Natural Gas Composition - % mol fraction</b>			
<b>Methane</b>	95.800	<b>Hexane</b>	0.017
<b>Ethane</b>	1.400	<b>Heptane</b>	0.017
<b>Propane</b>	0.400	<b>Octane</b>	0.016
<b>Iso-Butane</b>	0.050	<b>Carbon Dioxide</b>	1.900
<b>n-Butane</b>	0.050	<b>Oxygen</b>	0.000
<b>Iso-Pentane</b>	0.025	<b>Nitrogen</b>	0.300

There are a few approaches to hydrogen gas separation that vary widely in their application. Most notable among these are adsorption-based processes such as pressure swing adsorption (PSA) and temperature swing adsorption (TSA), membrane based separation either through conventional porous membranes or dense membranes, cryogenic distillation, and electrochemical separation. For hydrogen gas to be used as a fuel for power generation or transportation in fuel cells, or as a chemical feedstock, a high purity product is required. SAE J2719/ ISO14687-2 provides the hydrogen fuel quality requirements for fuel cell usage (Figure 2.1), with an absolute minimum hydrogen volumetric concentration of 99.97% required. More stringent requirements are in place for diluents such as N<sub>2</sub>, Ar, and methane which are all potentially present in natural gas. Furthermore, there are very stringent requirements for CO<sub>2</sub> and H<sub>2</sub>S which can also be present in trace amounts in natural gas.

Characteristics (assay)	Type I, Type II
	Grade D
Hydrogen fuel index (minimum mole fraction) <sup>a</sup>	99,97%
Total non-hydrogen gases	300 μmol/mol
<b>Maximum concentration of individual contaminants</b>	
Water (H <sub>2</sub> O)	5 μmol/mol
Total hydrocarbons <sup>b</sup> (Methane basis)	2 μmol/mol
Oxygen (O <sub>2</sub> )	5 μmol/mol
Helium (He)	300 μmol/mol
Total Nitrogen (N <sub>2</sub> ) and Argon (Ar) <sup>b</sup>	100 μmol/mol
Carbon dioxide (CO <sub>2</sub> )	2 μmol/mol
Carbon monoxide (CO)	0,2 μmol/mol
Total sulfur compounds <sup>c</sup> (H <sub>2</sub> S basis)	0,004 μmol/mol
Formaldehyde (HCHO)	0,01 μmol/mol
Formic acid (HCOOH)	0,2 μmol/mol
Ammonia (NH <sub>3</sub> )	0,1 μmol/mol
Total halogenated compounds <sup>d</sup> (Halogenate ion basis)	0,05 μmol/mol
Maximum particulates concentration	1 mg/kg

Figure 2.1 SAE J2719/ ISO14687-2 fuel cell road vehicle fuel quality standards. Reproduced from [56].

Table 2-2 outlines the general suitability of the various separation technologies to meet the baseline hydrogen concentration purity requirements with limited inlet hydrogen concentrations in accordance with allowable H<sub>2</sub> gas concentrations in natural gas infrastructure currently.

Table 2-2 Separation technologies by minimum H<sub>2</sub> feed and outlet purity compared to targets

Separation Technologies by minimum H <sub>2</sub> inlet and maximum H <sub>2</sub> purity at outlet		
Type	Min. Feed Purity (% H <sub>2</sub> vol.)	Product Purity (% H <sub>2</sub> vol.)
Target*	1 – 20	> 99.97
PSA	> 40	98 – 99.9995
Membrane – Conventional	> 10	< 98
Membrane - Dense	> 10	
Cryogenic	15 – 80	95 – 99.8
Hybrid	> 1	99.97
EHP	≥ 1	> 99.99 (demo. @ 20% H <sub>2</sub> )

\* target based on current expected allowable H<sub>2</sub> concentrations in NG infrastructure and ISO14687-2 fuel standards

### 2.1.1 Separation by Adsorption Processes

Pressure swing adsorption (PSA) and temperature swing adsorption (TSA) are two well known methods to separate hydrogen gas, with the former playing a role in 85% of global hydrogen production due to its integration with petrochemical based hydrogen production processes such as steam methane reforming (SMR)[57]s. Adsorption processes separate hydrogen gas from other impurities through the adsorption of the impurities as it passes through a bed of adsorbents. The adsorbents involved depend on the targeted impurities and as such multiple adsorbents are typically present when dealing multi-component gaseous blends. Once the adsorbents are sufficiently saturated with adsorbed gas impurities, they must be regenerated (desorbed) from the bed, which is accomplished either through a reduction in pressure (pressure swing adsorption/PSA) or through an increase in temperature (temperature swing adsorption/TSA) although TSA is not typically employed due to lower cycling times[58]. Typically, in series to arrive at the desired purity and multiple beds are run in parallel to provide a continuous process gas stream through the purification system and allowing for only slight pressure loss in the hydrogen product.

PSA based gas separation is commonly employed to obtain high purity hydrogen from steam methane reforming (SMR) processes where natural gas and steam are the feedstock to produce a high hydrogen content gas blend (~75% vol H<sub>2</sub>) also composed largely of water vapor, CO<sub>2</sub>, CH<sub>4</sub>, and CO[59][60]. This process is already commercially viable but unfortunately does not translate well to lower hydrogen concentration blends; the amount of adsorbent in the bed scales with the concentration impurities present, thus the size of the bed increases appreciably with lower hydrogen concentrations and the retentate, natural gas, will need to be recovered in large quantities at low pressures[61]. In one study, the National Renewable Energy Laboratory (NREL) proposed the implementation of PSA separation at natural gas pressure reduction facilities, avoiding recompression costs associated with recovery of natural gas retentate, reducing the cost of the separation process immensely for a feed-in concentration case of 10% H<sub>2</sub>[38]. Due to limitations of process design, PSA is not considered as a viable candidate for hydrogen concentrations below 40% in the inlet feed[62].

### 2.1.2 Separation by Cryogenic Distillation

Cryogenic distillation involves the separation of gas species by making use of their different boiling points in a relatively energy intensive process due to the need to cool gaseous species to the point of condensation[63]. Cryogenic distillation is typically employed at large economies of scale and in scenarios where other pure products of interest are present that can be extracted contemporaneously[64]. Furthermore, it is not able to produce fuel cell quality hydrogen requiring further purification downstream[65]. When considering separation processes for hybrid systems, membrane separation can fulfill a similar role with much more flexibility with respect to scale and feed gas composition[66].

### 2.1.3 Separation by Porous Membranes

Porous type membranes work to separate gas by the difference in the permeation rates of various gas species through the membrane phase. The efficacy of a porous membrane in its ability to transport certain gases over others depends on the interaction between membrane and gaseous species due to size, shape and material affinities[67].

There are multiple mass transport mechanisms by which gaseous species move through porous membranes. With respect to the separation of hydrogen gas, which has a small kinetic diameter and is typically mixed with low molecular weight gaseous species (and thus low solubility in membrane phases), molecular sieving tends to dominate the preferential transport of hydrogen gas through the membrane phase along with the high molecular diffusivity of hydrogen gas [68].

Two important parameters that serve to identify whether a membrane is effective for the separation of a certain gaseous species are the selectivity and permeability[69]. A permeability coefficient  $P_i$  of a gaseous species  $i$ , defines the permeation rate  $Q_i$ , or flux of gaseous species, through a unit area of membrane at a given pressure gradient normalized to the membrane thickness  $t$ ,

$$Q_i[\text{mol m}^{-2} \text{s}^{-2}] = \frac{P_i \nabla p}{t} \quad (\text{Eq. 2-1})$$



The selectivity of a membrane between two gas species  $i$  and  $j$ , is the ratio of their permeability coefficients,

$$\alpha_{i,j} = \frac{P_i}{P_j} \quad (\text{Eq. 2-2})$$

Porous membrane gas separation is a mature and widely implemented technology and in industry are typically polymeric in nature[62]. Polymeric membranes tend to be low cost and highly scalable, capable of handling the large pressure drops required to facilitate high permeation rates. These polymeric membranes are limited by a trade-off in permeability and selectivity between hydrogen and methane known as Robeson Upper Limit for polymeric membranes in gas separation [70].

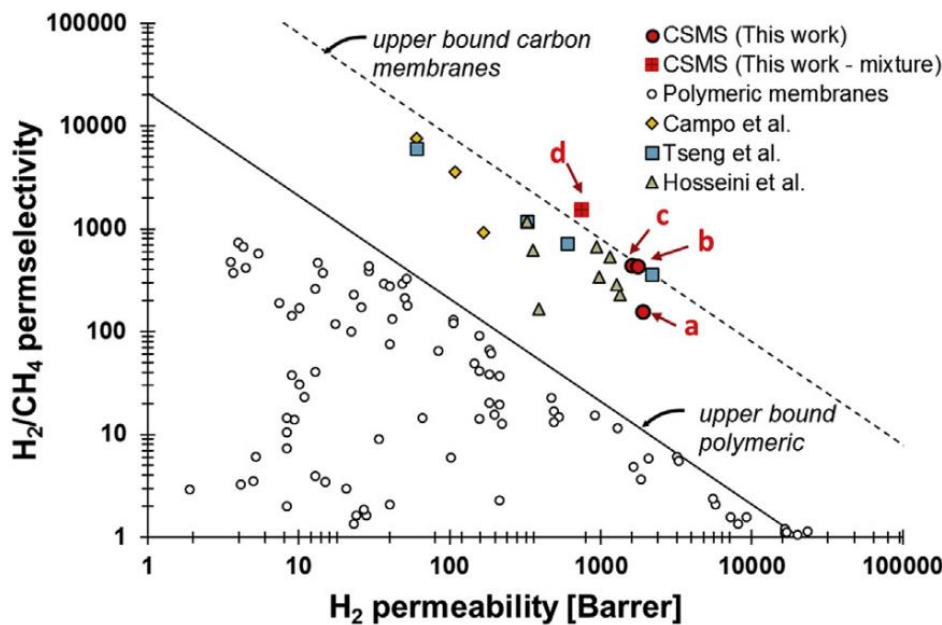


Figure 2.2 Robeson plot for  $H_2/CH_4$  selectivity of polymeric and CSMS membranes. Reproduced from [71]

Figure 2.2 displays the upper Robeson limit for polymeric membrane, and also highlights recent advancements in carbon molecular sieve membranes (CMSM) that exhibit superior selectivity and permeability of  $H_2$  over methane to polymeric membranes that have historically been deployed, making these an attractive approach for hydrogen separation from natural gas blends. Due to their high selectivity, CSMS have demonstrated operation in hydrogen concentrations as low as 10% in methane with a hydrogen product purity of 99.4% in single-stage separations at a

driving pressure differential of 7.5 bar[71]. Compared to other membrane type separations with high hydrogen purity potential such as ceramic and dense membranes, CSMS have significantly lower production cost[72].

Porous membrane separation is a strong candidate for low concentration hydrogen gaseous feeds in natural gas blends due to its flexibility with respect to gaseous impurities and scalability. Membrane separation does produce hydrogen product at low pressure, requiring recompression if needed for any hydrogen separated potentially adding significant capital cost to the process. To reach fuel cell quality hydrogen, porous type membranes are unable to produce sufficiently pure hydrogen in a single-stage of separation. Multiple stages of separation would require recompression to drive further stages of permeation, significantly impacting the cost and efficiency of such an approach.

#### 2.1.4 Separation by Dense Membranes

At very low pore sizes, solid-state diffusion of gaseous species can be utilized to separate gaseous species. In this case, there is significant interaction between molecule and gaseous species of interest and the permeability is a function of the solubility of the gas in the membrane phase as well as the diffusivity[73][74]. For hydrogen separations, dense metallic membranes based on palladium and palladium alloys are of great interest due to their ability to achieve ultra-high purity hydrogen in single-stage separations of > 99.999% by volume[61][75].

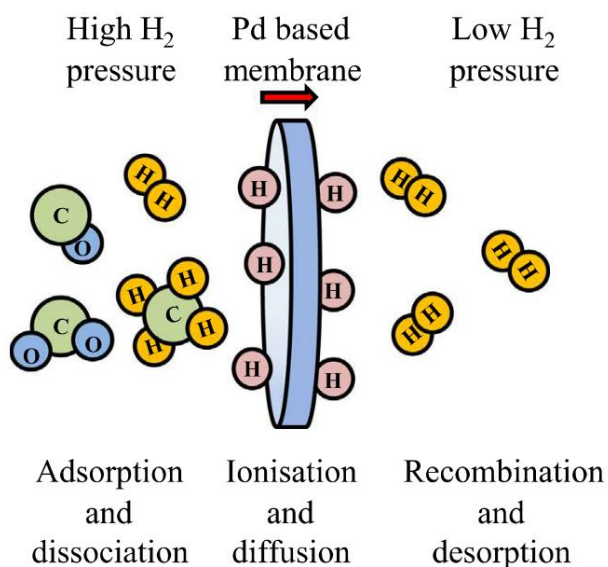


Figure 2.3 Mechanism of hydrogen transport in palladium membranes. Reproduced from [73].

At sufficiently high temperatures around 400 °C, hydrogen dissociates upon contact with palladium into protons, which can then diffuse to a lower hydrogen pressure environment and recombine into hydrogen gas (Figure 2.3). Pd membranes are also highly sensitive to various contaminants such as sulfur compounds (H<sub>2</sub>S, thiophene) as well as chlorides, and carbon monoxide[76]. There are also concerns with the durability of Pd alloys due to hydrogen embrittlement combined with high temperatures and increasingly high pressure differentials necessitated by lower hydrogen concentration in the feed[39][77].

Nordio et al. compared Pd-Ag alloy membranes to CMSM porous membranes in 10% H<sub>2</sub>/90% CH<sub>4</sub> gaseous mixtures and found that Pd-Ag alloy membranes obtained higher product purities at low feed pressures (8 barg) but were outperformed economically and in terms of purity at high feed pressures (> 20 barg) reaching hydrogen purities of ~99.5% by vol on the permeate side [72]. As a first stage separation, porous membranes seem to be the preferred approach from an economic perspective. For a final stage separation for high purity product, dense metal membranes are not as efficient as PSA processes and more difficult to integrate[78].

### 2.1.5 Separation by Hybrid Separation Designs

To achieve high purity, fuel cell quality hydrogen gas from low hydrogen concentration natural gas blends, it is apparent that no singular conventional separation technology can effectively

meet these requirements. Instead, several hybrid approaches combining different separation technologies have been proposed as a way to enable these separations.

A combination of polymeric membranes, compressors, and pressure swing adsorption was proposed by Liemberger et al. for hydrogen gas separation from natural gas infrastructure[66]. The process, termed HylyPure® (see Figure 2.4), is proposed to be capable of delivering fuel cell quality hydrogen from hydrogen blends in methane down to 1% by volume H<sub>2</sub> for 51 bar inlet pressure and 25 bar hydrogen product [79]. For hydrogen recovery factor of 50% (fraction of hydrogen in the feed extracted as a pure product), the specific energy cost of this separation was highly sensitive to H<sub>2</sub> concentration in the feed spanning 3.93 – 20.08 kWh/kg H<sub>2</sub> for 1 to 10% H<sub>2</sub> concentrations, corresponding to 11.8 to 60.3% of the lower heating value of the hydrogen separated.

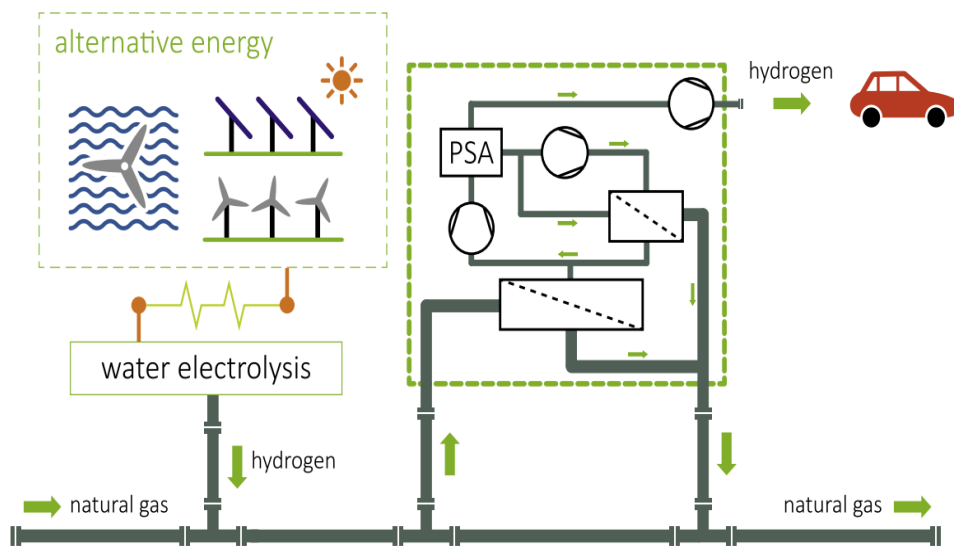


Figure 2.4 HylyPure hydrogen gas separation process concept. Reproduced from [79].

Under the HyGrid consortium tasked by the EU to investigate hydrogen gas separation from natural gas blends, a hybrid separation study was conducted targeting the separation of 99.99% purity hydrogen from 10 % volume hydrogen concentrations in natural gas. Across a wide range of process designs with a wide range of separation technologies considered, the most effective process was found to consist of carbon molecular sieve membranes, Pd-Ag membranes, an electrochemical separation module and supporting heat exchangers and vacuum pumps [78]. The

most effective process for a 40 barg gas feed with 2 barg hydrogen product at 99.99% purity is displayed in Figure 2.5 and separated hydrogen at 5.62 kWh/kg H<sub>2</sub>.

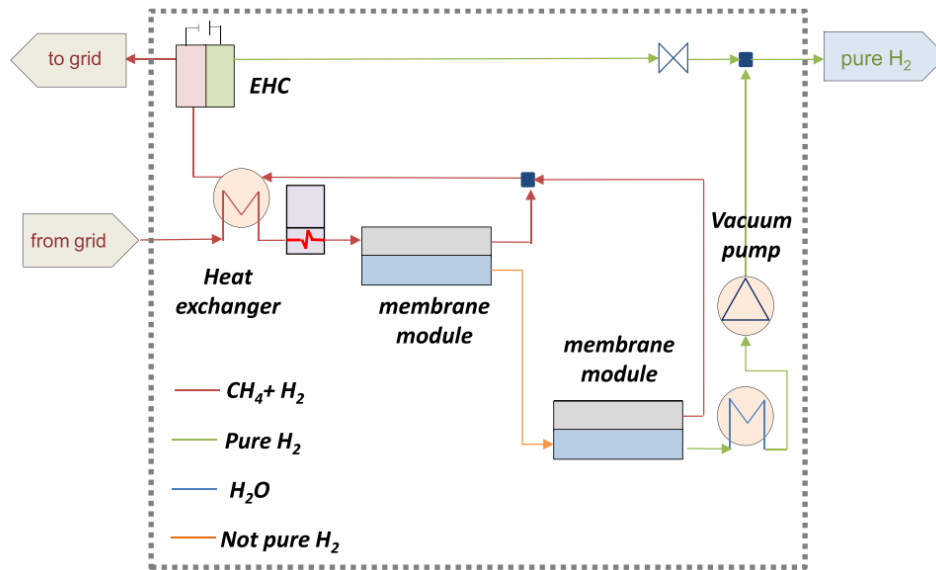


Figure 2.5 Hybrid gas separation process proposed from HyGrid process optimization study. Reproduced from [78].

The HyGrid consortium further deployed a prototype scale demonstration of the separation of hydrogen from natural gas by a hybrid process like what was proposed in Figure 2.5 at a scale of 12-13 kg H<sub>2</sub>/day. Purportedly the electrochemical separation module as well as the membrane separators were contaminated by real natural gas operation[80], although no peer reviewed publications or data concerning the demonstration operation were published.

## 2.2 Electrochemical Hydrogen Pump

Electrochemical hydrogen pumps (EHP) came about followed the development of proton exchange membrane based fuel cell technology in the 1960s[81], with the first instance of an EHP appearing shortly thereafter [82].

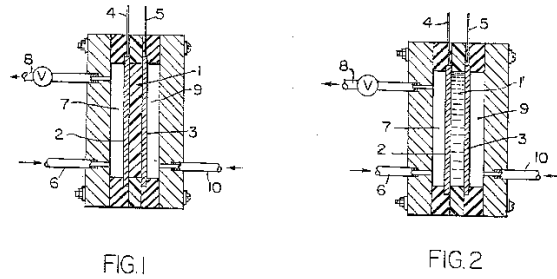


Figure 2.6 Original US patent for EHP[82]

The basic working principle of the electrochemical hydrogen pump is the combination of an anode that undergoes hydrogen oxidation reaction (HOR), and a cathode that facilitates a complementary hydrogen evolution reaction (HER) with both electrodes separated electronically and physically by a proton conducting medium.

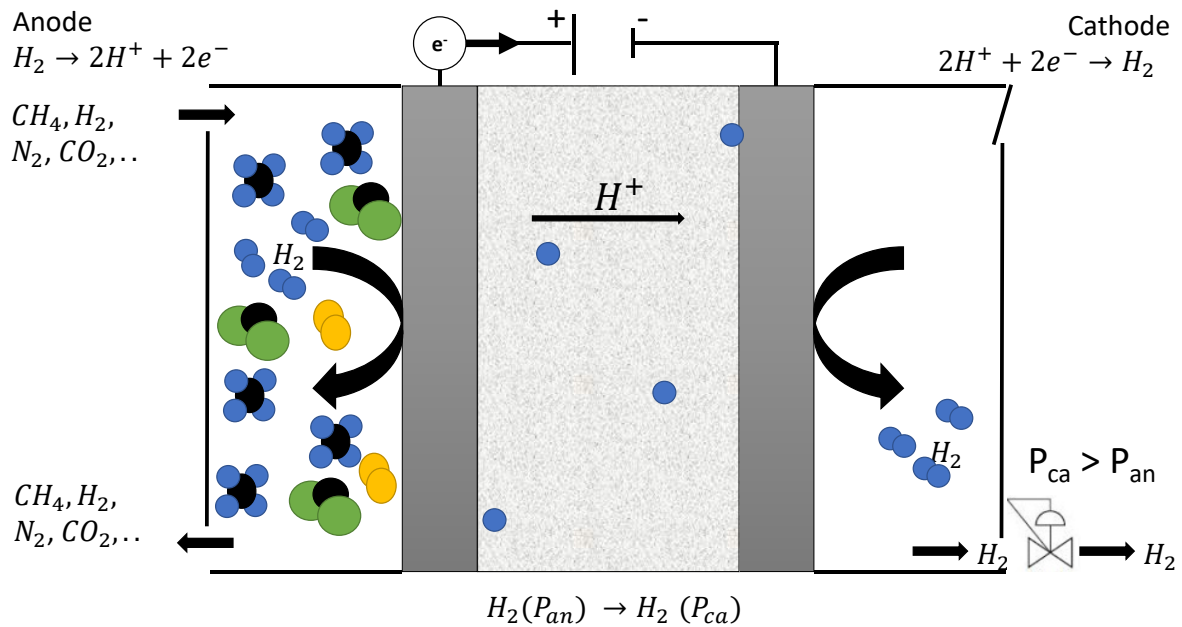


Figure 2.7 Electrochemical hydrogen pump for gas separation and compression of hydrogen.

For EHP for gas separation applications, gas containing some quantity of hydrogen is fed to the anodic side, where it is transported to the electrode surface and oxidized into protons and electrons under an applied potential according to,



Electrons are conducted from the catalyst layer and then carried by an external power supply from the anode to the cathode, while protons are transported across the proton conducting phase separating the anode and cathode. At the cathode protons and electrons recombine forming hydrogen gas,



The potential required between anode and cathode to drive the electrochemical reactions is,

$$E_{cell} = E_{Nernst} + E_{pol} + E_{iR} \quad (Eq. 2-5)$$

Where  $E_{Nernst}$  is the thermodynamic potential at net zero current, described by the Nernst equation for a hydrogen concentration cell,

$$E_{cell} = E^0 + \frac{RT}{2F} \ln \left( \frac{P_{H_2,cat}}{P_{H_2,an}} \right) \quad (Eq. 2-6)$$

Where the standard potential  $E^0$ , for hydrogen oxidation versus a hydrogen electrode is zero, and the cell open-circuit potential at nonstandard conditions is accounted for by the shift in temperature and the partial pressures of hydrogen at the cathode and anode, where  $R$  is the ideal gas constant,  $F$  is Faradays constant and is multiplied by 2 to account for the stoichiometry of 2 electrons for every mol of hydrogen gas reacted and  $P_{H_2}$  is the partial pressure of hydrogen at each electrode.

$E_{pol}$  describes the electrode overpotential of both anode and cathode due to kinetic losses of HOR and HER respectively. The overpotential for these reactions can be described by Butler-Volmer equation, presented in simplified form as,

$$E_{pol} = \frac{RT}{\alpha F} \ln \left( \frac{i}{i_0} \right) \quad (Eq. 2-7)$$

Where  $i$  is the current density,  $i_0$  is the exchange current density of the given reaction, and  $\alpha$  is the sum of the electrode symmetry coefficients.  $\alpha$  is often taken as equal to 1 for high overpotentials, although in some cases values between 1 and 2, suggesting varying rate determining steps in the reaction, are applied[83].

In the case of HOR and HER reactions, where electrode overpotentials are relatively low due to the fast kinetics of the reactions and thus high exchange current density values, ohmic losses tend to be the dominant loss in real EHP operation. These resistive losses are largely related to the movement of protons through the membrane phase with contributions for electronic conduction and interfacial contact resistances, quantified together as a net resistance  $R$  of the cell,

$$E_{iR} = iR \quad (Eq. 2-8)$$

From the Nernst equation, it can be observed that ideal electrochemical hydrogen compression is equivalent to ideal isothermal hydrogen compression, where ideal refers to the thermodynamic condition of a process approaching occurring an infinitesimally slow time scale. For isothermal compression work of hydrogen gas, the amount of work per molar unit of hydrogen compressed is,

$$W_{comp, isothermal} = RT \ln \left( \frac{P_2}{P_1} \right) \quad (Eq. 2-9)$$

And defining work as the movement of charge through a electric field,

$$W = \Delta V \times Q \quad (Eq. 2-10)$$

Then, with respect to the charge moved during EHP operation  $Q = 2F$ ,

$$W = \Delta V \times 2F \quad (Eq. 2-11)$$

The compression work becomes,



$$V = \frac{RT}{2F} \ln\left(\frac{P_2}{P_1}\right) \quad (\text{Eq. 2-12})$$

Which is equivalent to an EHP operating on pure hydrogen anode feed,  $P_1$  and producing hydrogen at the cathode at a pressure  $P_2$  according to the Nernst Equation.

Much of gaseous compression, particularly in natural gas infrastructure, is accomplished by mechanical compression devices such as reciprocating, centrifugal, and in some cases rotary base compressors [84]. For hydrogen compression, reciprocating compressors currently offer the best efficiency but can suffer from gas sealing issues and leakage. In centrifugal compressors there are appreciable design challenges with regard to increased tip speed of fan blades due to the relatively light hydrogen molecules [85].

Ideal mechanical compression from a thermodynamic perspective can be modelled as an adiabatic compression process, which for an ideal gas takes the form,

$$W_{comp,adiabatic} = \frac{kRT_1}{k-1} \left[ \left(\frac{P_2}{P_1}\right)^{\frac{k-1}{k}} - 1 \right] \quad ()$$

The compression of hydrogen gas is more energy intensive than methane gas on a mass basis, in part due to the lower volumetric density of hydrogen (Figure 2.8). When examining adiabatic compression work for methane and hydrogen as a fraction of the lower heating value (LHV) of the fuel gas, hydrogen still incurs a far more significant energy loss than methane. The unique ability to utilize an EHP to compress hydrogen in a more isothermal manner becomes increasingly attractive when considering this limitation of hydrogen in mechanical compressor. Comparing ideal electrochemical compression and ideal mechanical compression for hydrogen, the theoretical limit of the latter approach is far more efficient particularly at achieving high product pressures, although hydrogen remains a more energetically intensive gas to compress than methane.

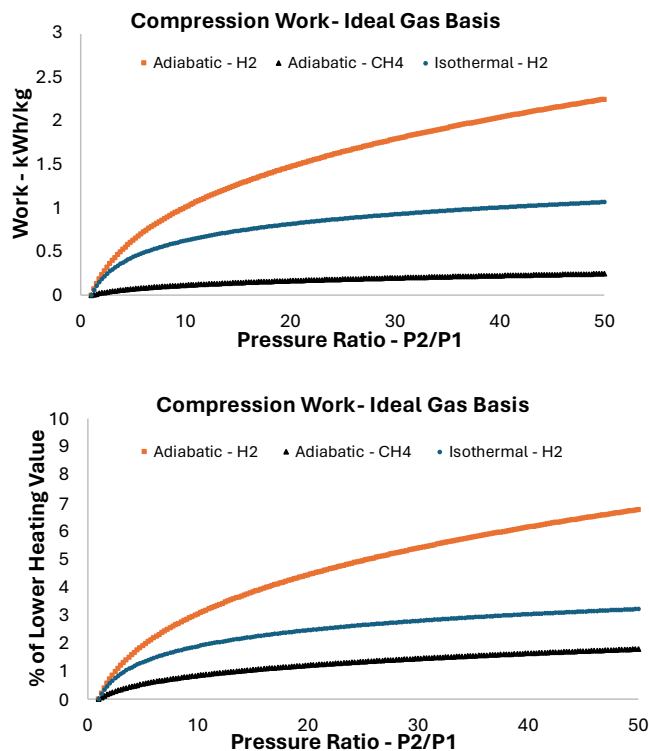


Figure 2.8 Ideal compression work in kWh/kg (top) and as a fraction of % LHV (bottom) as a function of pressure ratio.

In either case, actual gas compression work deviates appreciably theoretical limits. For mechanical compressors, adiabatic limits can only be approached through dividing compression steps infinitesimally small with intercooling stages bringing the gas temperature back down. Each intercooling stage adds complexity and cost with significant trade-off in any potential efficiency gains. In an EHP, drawing increasing amounts of current to increase the hydrogen flux leads to higher overpotentials due to ohmic and electrode overpotentials and thus increasing the compression work. Furthermore, high cathodic pressures can lead to parasitic back-diffusion of hydrogen gas to the anode. Isothermal compression via EHP scales with surface area making it easily scalable and allowing for more efficient operation by operating in a low flux regime and instead scaling up membrane size, while mechanical compressor scalability is limited by surface to volume ratios due to heat loss.

When purifying hydrogen from a gas stream, EHP has the unique capability to compress and separate hydrogen contemporaneously with one device. In addition, the flux of product hydrogen

across the membrane phase is a function of current applied to the EHP, according to Faraday's law of electrolysis,

$$n_{H_2} = \frac{iA}{nF} \quad ()$$

Where  $n_{H_2}$  is the molar rate of hydrogen consumption and production at the anode and cathode respectively,  $i$  is the current density, and  $A$  is the cross sectional area of the EHP membrane electrode assembly (MEA). Unlike membrane separation through conventional membranes, which is driven by pressure and concentration gradients, hydrogen can be pumped against such gradients in an EHP. Consequently, it is possible to decouple the  $H_2$  selectivity from the permeation rate that limits conventional membranes, and tune permeation rate and product purity by varying current density and pressure differentials independently.

EHP are broadly separable into two categories based on the proton conducting phase employed; low-temperature ( $< 100\text{ }^\circ\text{C}$ ) LT-PEM EHP largely based on perfluorosulfonic acid (PFSA) membranes, and high temperature ( $< 200\text{ }^\circ\text{C}$ ) HT-PEM EHP that predominantly employ a phosphoric acid doped polybenzimidazole (PA-PBI) proton conducting membrane.

### 2.2.1 Low Temperature Proton Exchange Membrane EHP

Generally LT-PEM EHP membranes are based on ionomeric materials that contain sulfonic acid groups to provide proton conductivity [86]. Nafion® membranes exhibit high proton conductivities, high mechanical strength, and low gas permeability and are ubiquitously found throughout research and commercial efforts in PEM fuel cell, electrolyzers, and EHP [87]. In the electrodes, platinum nanoparticles supported on carbon, Pt/C, are most commonly employed due to the high suitability of Pt for HOR and HER reactions. To provide an effective proton conductive pathway from the catalytic site to the membrane phase, Nafion® or another sulfonic acid containing ionomer is also present in the electrodes. Gas diffusion layers (GDL) based on carbon paper or carbon cloth provide mechanical strength, porosity for gas distribution, and electrical conductivity.

To maintain sufficient proton conductivity in the LT-PEM, liquid water is required to facilitate these proton conduction pathways and thus the effective temperature range of the LT-PEM EHP lies below boiling point of water ( $<100\text{ }^\circ\text{C}$ ). In hydrogen compression, operating at a low cell temperature is favorable from a thermodynamic perspective, however higher temperatures

facilitate better proton transport through the PEM and thus lower ohmic losses in the EHP which are the dominant source of loss ultimately leading to better electrochemical performance overall at higher operating temperatures[88].

In LT-PEM fuel cells and electrolyzers, water is a by-product and reactant respectively, and is thus inherently present during operation. In EHP, water must be introduced solely to maintain proton conductivity in the membrane (Figure 2.9).

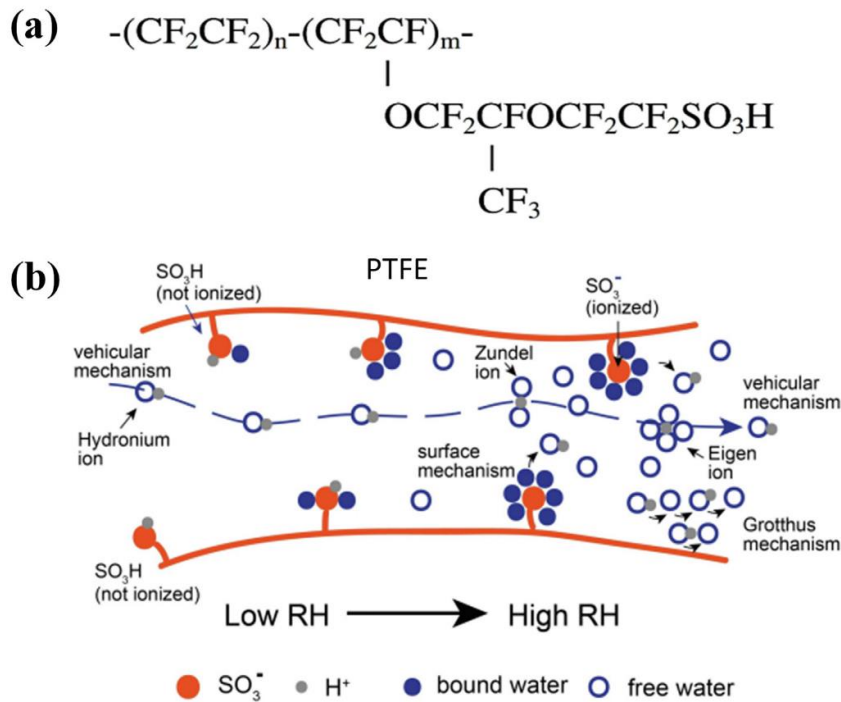


Figure 2.9 a) Chemical structure of Nafion® b) Proton transport mechanisms of Nafion®. Reproduced from [89].

The water management of LT-PEM EHP is a critical subsystem due to the complex nature of water transport in the LT-PEM. At the cell level, water is typically introduced at the anode as a vapor from a humidification system close to saturation i.e; humidifier temperature set close to the cell temperature[90] to produce the best cell performance. During operation of LT-PEM EHP in compressing hydrogen, water tends to cross the membrane from cathode to anode due to the presence of elevated pressure at the cathode[91][92]. In the opposite direction, electro-osmotic drag caused by the movement of protons from anode to cathode as a function of the electrical

field applied carries water molecules in the same direction, with the electro-osmotic drag coefficient ( $\text{mol H}_2\text{O/mol H}^+$ ) depending on the water content of the membrane[93].

At the system level the water transport across the cell affects thermal management as well due to evaporative cooling at the cathode side[86]. Thus, water and thermal management subsystems must be designed to provide ideal humidification to the cell for a set hydrogen flow rate, cell temperature, and pressure, presenting a significant engineering challenge[87][94].

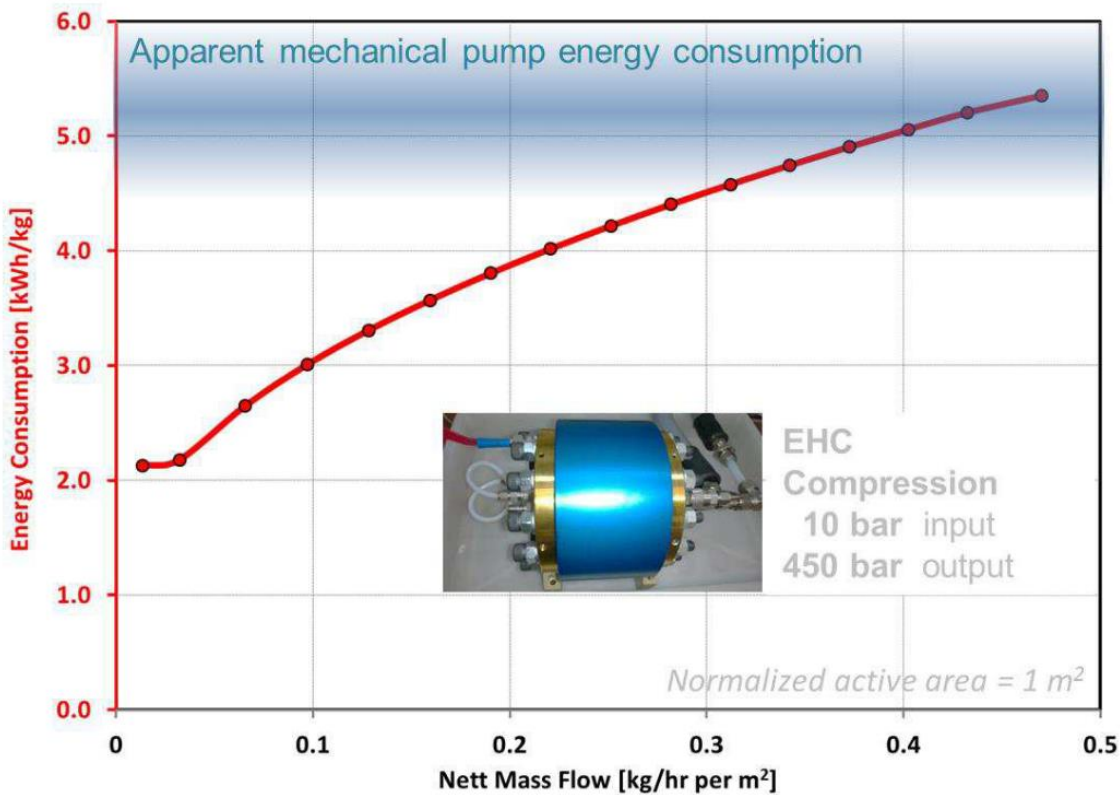


Figure 2.10 HyET EHP compression stack. Reproduced from [95].

As a hydrogen compressor, LT-PEM EHP are still early in their development. Hydrogen pressures above 700 bar have been achieved in single-stage compressions [96][97] and one commercial producer of LT-PEM EHP, HyET Hydrogen, previously demonstrated compression up to 1000 bar hydrogen at the single cell level and 450 bar at the stack level (FIGURE)[98]. In hydrogen gas separation/purification, LT-PEM EHP has had some limited applications explored such as anode exhaust recovery [99], methane/H<sub>2</sub> blends to simulate natural gas/H<sub>2</sub> separations [100][101], natural gas/H<sub>2</sub> blends[102], and syngas purification[95] although for the latter case no actual cell performance was reported.

For methane/H<sub>2</sub> blends, the LT-PEM EHP is able to separate hydrogen gas from mixture concentrations as low as 20% volume at fuel cell quality product with no loss in pressure in the hydrogen product and at a specific energy consumption 1/3 the amount required by PSA for the same application [101]. H<sub>2</sub> concentrations as low as 8% have been demonstrated in methane with stable LT-PEM EHP performance and high product purity of > 99.9% H<sub>2</sub> [102][103]. Low operating temperature limitations of the LT-PEM EHP make it susceptible to gaseous impurities that can impede electrode performance such as CO, CO<sub>2</sub>, and H<sub>2</sub>S.

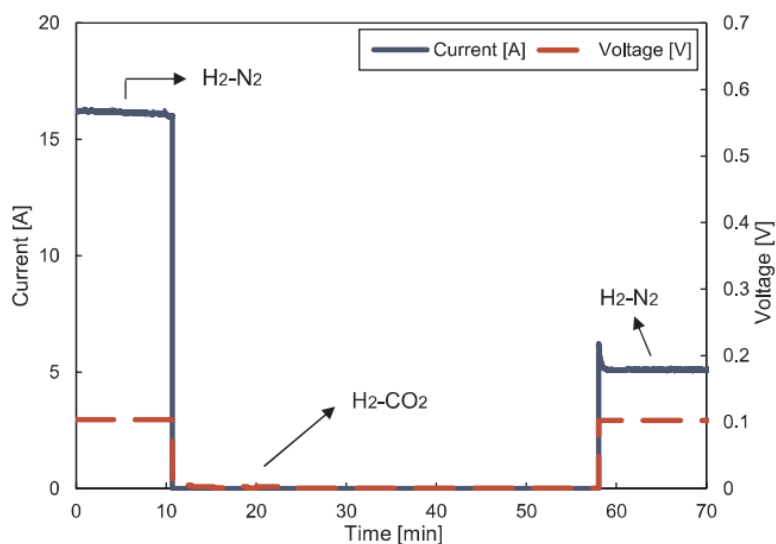


Figure 2.11 Impact of CO<sub>2</sub> introduction to LT-PEM EHP in non-polarized condition. Reproduced from [104].

Nordio et al. introduced CO<sub>2</sub> at 50 % volumetric concentration to an LT-PEM EHP with the cell under no applied potential and then introduced a 50% N<sub>2</sub> blend and observed significant catalyst poisoning, suggesting some contribution of CO poisoning which can for chemically through reverse water gas shift (RWGS) rather than electrochemically through CO<sub>2</sub> reduction (Figure 2.11)[104]. In another study, the introduction of natural gas/H<sub>2</sub> blends was found to significantly impact LT-PEM EHP performance, but stable operation was achieved by introduction of carbon filtration upstream of the EHP to remove sulfur compounds although no composition of the natural gas feed was provided[102].

As a hydrogen compressor LT-PEM EHP can be a more efficient technology to compress hydrogen gas than the mechanical counterparts[95][87]. The inherent presence of water at the cathode in LT-PEM EHP makes its direct integration with hydrogen fueling infrastructure such as FCEV fueling slightly more complicated due to the need to remove water from product

hydrogen stream, although it could engender the integration of LT-PEM EHP for downstream compression from water saturated hydrogen that is produced from water electrolyzers. In gas purification, LT-PEM EHP can produce a very high purity hydrogen product from dilute gaseous blends at relatively high efficiency in a single-stage of separation (after removal of water). Operation of the LT-PEM EHP is complicated by the critical need for sufficient membrane hydration and by the sensitivity of the electrode materials to gaseous impurities that could be overcome by higher operating temperatures.

### 2.2.2 High Temperature Proton Exchange Membrane EHP based on PBI-PA

Electrochemical purification at elevated temperatures became of interest to deal with common reformate gas impurities in hydrogen purification processes that LT-PEM EHP could not handle effectively. To increase the operating temperature of PEM based cells, greater degrees of humidification are required or a different proton conducting medium that is less sensitive to evaporation is needed. Of these alternative proton conductors, concentrated phosphoric acid (> 85 % wt  $\text{H}_3\text{PO}_4$ ) has seen the most success due to its high proton conductivity and thermal stability, with phosphoric acid fuel cells operating at temperatures up to 210 °C [105].

The earliest high temperature (> 100 °C) EHP was based on phosphoric acid fuel cell (PAFC) cell construction and operated in methanol reformate gas, producing a hydrogen product at 99.81% and operating at 190 °C [106]. A few years later, in 1995, Wainright et al. introduced the application of phosphoric acid imbibed polybenzimidazole as a proton conducting membrane for methanol fuel cells operating at 200 °C [107]. Since then, phosphoric acid doped polybenzimidazole has been the material of choice for HT-PEM fuel cells and EHP.

Polybenzimidazole (PBI) are a class of polymers comprised of benzimidazole as part of the repeat unit. PBI membranes have a high degree of thermal stability with glass transition temperatures of around 430 °C, along with a high degree of mechanical strength and chemical stability [108][109]. PBI based membranes exhibit a high degree of gas selectivity for  $\text{H}_2$  permeation, making them a strong candidate for conventional membrane gas separations of  $\text{H}_2$  [110].

PBI membranes are doped with phosphoric acid to introduce a proton conducting phase. In the PBI, a proton from the phosphoric acid molecule associates with the basic benzimidazole site in weak acid-base interaction, with an interaction energy slightly higher than between phosphoric acid and water[111]. Figure 2.12 shows the structure of meta-PBI (*m*PBI) doped with phosphoric acid and the various proposed proton conduction pathways, where up to 2 mol H<sub>3</sub>PO<sub>4</sub> can coordinate with 1 mol polymer repeat unit (RPU) and additional phosphoric acid beyond that ratio is present as a free phosphoric acid aqueous phase. The mechanism of proton conduction in the PBI-PA phase depends on the degree of acid doping level (ADL), the water content as a function of local humidities, and the temperature[112].

Mechanisms of proton conduction in PA doped PBI

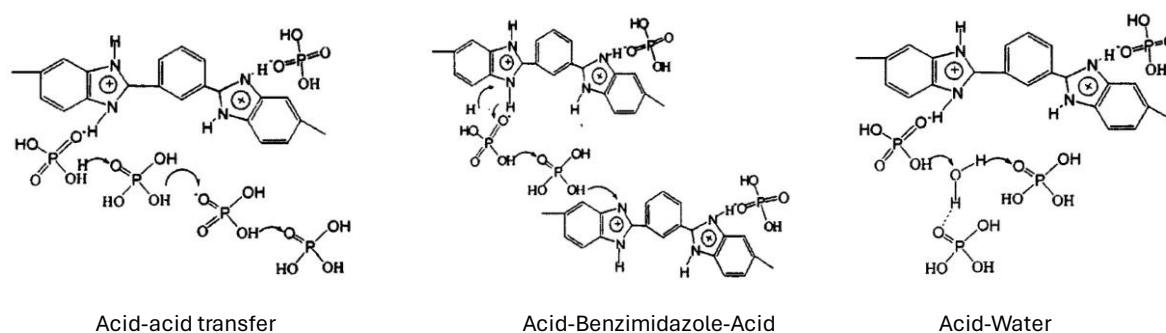


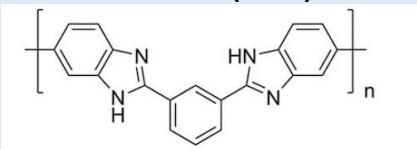
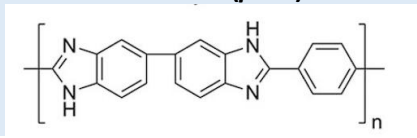
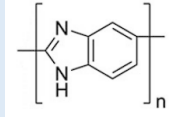
Figure 2.12 Proton conduction mechanisms for PA-PBI. Reproduced from [112].

Phosphoric acid doped PBI membranes can be split into two distinct categories depending on the method of introduction of phosphoric to PBI; a conventional process where PBI polymers are placed in a phosphoric acid bath, and a sol-gel process where the PBI polymer is cast in phosphoric acid solution. PBI polymers are most often produced by a polycondensation process utilizing an organic solvent such as DMAc[113]. These ‘conventional’ PBI polymers are then immersed in a concentrated phosphoric acid bath to achieve acid doping levels on the order of 2 – 10, with the amount dependent on the polymer structure, doping temperature, and duration of doping[114][115]. Sol-gel casting of PBI polymers was introduced in 2005 by Benicewicz group to produce PBI films with very high acid doping levels (>14) [116]. In this process, polyphosphoric acid (PPA) was used as the polymerization medium and the solvent. The term sol-gel refers to the solution to gel transition that occurs as PPA readily uptakes local humidity to transition to phosphoric acid creating a gel phase as the solubility of the PBI is lower in



phosphoric acid than PPA. Table 2-3 reports the most prevalent PBI polymer configurations employed in phosphoric acid doped PBI and their respective ADL and proton conductivities for the conventional and sol-gel imbibing processes.

Table 2-3 PA-doped PBI polymer properties based on preparation method.

PA-PBI polymer ADL and Conductivities based on preparation method				
Type	ADL [mol PA/mol RPU]		Proton Conductivity 160 °C, Anhydrous [S/cm]	
	Conv.	Sol-gel (PPA)	Conv.	Sol-gel (PPA)
<b>Meta-PBI (mPBI)</b> 	6-10 [117][118]	14-26 [117][118]	0.01-0.08 [117][118]	0.13 [117][118]
<b>Para-PBI (pPBI)</b> 	N/A*	30-40 [119]	N/A*	0.2 [119]
<b>AB-PBI/i-AB-PBI</b> 	2-10 [118]	22-35 [118]	0.04 (AB-PBI) [120]	0.2 (i-AB-PBI) [121]

PA-PBI membranes prepared from sol-gel processes exhibit much higher proton conductivities than their conventional counterparts while also maintaining comparable mechanical and chemical stability to conventional doped counterparts. Para-PBI membranes (Celtec-P) demonstrated 3500 hour lifetime stability in fuel cell operation at 160 °C in 2% CO and 5 ppm H<sub>2</sub>S with a voltage decay rate of 17 μV hr<sup>-1</sup> (Figure 2.13) [122]. At current densities of 0.2 A cm<sup>-2</sup> conventional and sol-gel PA-PBI have exhibited comparable voltage decay rates in fuel operation of 6 μV hr<sup>-1</sup>, while at higher current densities (0.6 A cm<sup>-2</sup>) conventional PBI were severely impacted (308 μV hr<sup>-1</sup>) compared to sol-gel PBI (16 μV hr<sup>-1</sup>)[123][124]. This improved durability can be attributed to the much higher ADL that also enabled higher performance due to the higher acid retention capabilities of the sol-gel membranes.

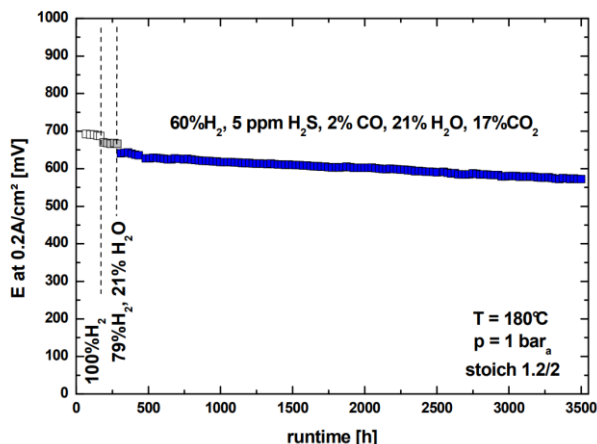


Figure 2.13 H<sub>2</sub>S and CO tolerance over 3500 hours of sol-gel PA-PBI in fuel cell operation. Reproduced from [122].

While sol-gel PA-PBI were found to exhibit better mechanical stability at comparable ADL to conventional PBI, the overall lower solids content of the typical sol-gel PBI does lead to a higher degree of mechanical creep compression of the membrane, limiting the longer lifetime operation (>40,000 hours) potential of the sol-gel PA-PBI for fuel cell operation [123][117][125]. This creep intolerance has significant implications for HT-PEM EHP application, which involves differential pressure operation and high net feed gas flow rates at the anode due to low hydrogen concentrations. Pingitore et al. attempted to address this issue by demonstrating that tuning the ADL of the PBI-PA cast from sol-gel process could be accomplished by mixing meta- and para-PBI polymers to a ‘m/p’ PA-PBI with an ADL closer to conventional imbibing levels of ~8-9 PA with improved mechanical properties at the cost of conductivity compared to para-PBI cast in the same way[126]. In HT-PEM EHP operation the m/p PBI demonstrated sustained operation up to 30 psi differential pressure for 3000 hours in varying gas feed compositions while para-PBI failed at ~12 hours of operation (Figure 2.14)[127].

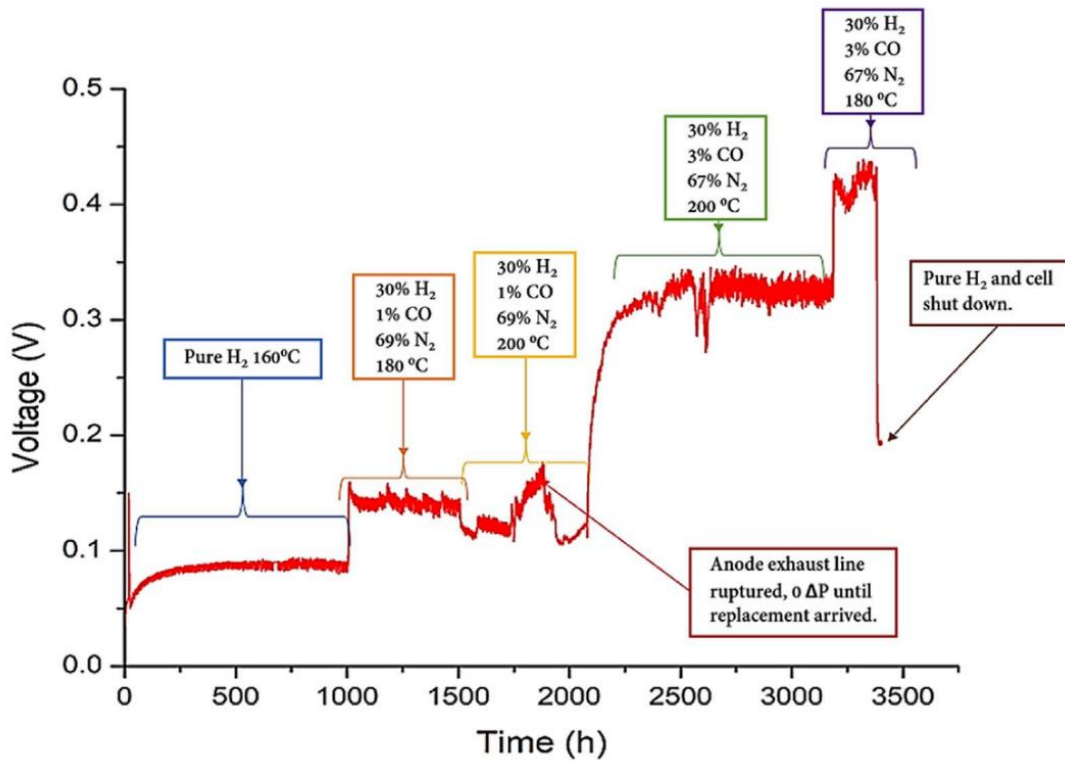


Figure 2.14 Sol-gel cast m/p PA-PBI membranes in EHP operation at 30 psi differential pressure, 160 °C, 0.2 A cm<sup>-2</sup>. Reproduced from [127].

The structure of a HT-PEM EHP based on PA-PBI membranes is shown below in . During operation, a gaseous mixture containing hydrogen is fed to the anode and hydrogen gas then must transport to a platinum interface in contact with the proton conducting aqueous phase to facilitate the HOR reaction. Protons are carried by the phosphoric acid phase in the electrodes to the PA-PBI proton conduct membrane. At the cathode, protons recombine with electrons from the external circuit to form hydrogen gas. Often, the anode gas feed is humidified as well to a slight extent, and thus water vapor also enters the hygroscopic aqueous phosphoric acid and transports across the membrane by diffusion to the drier cathode side.

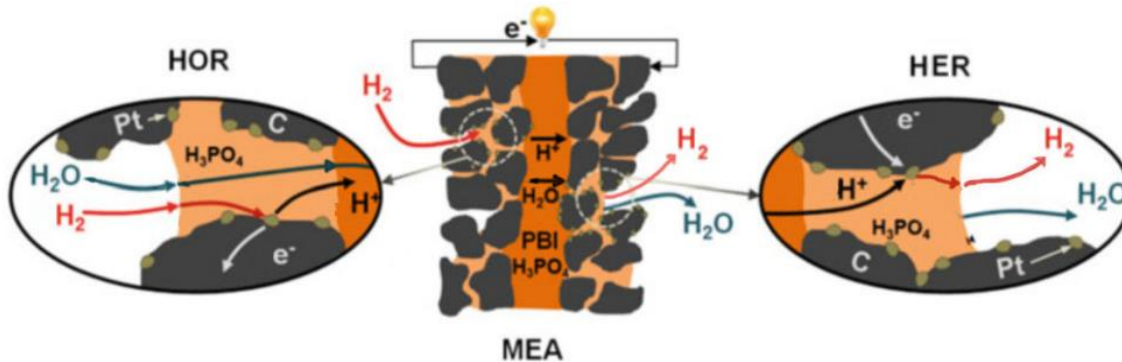


Figure 2.15 Schematic of HT-PEM in EHP operation at MEA level. Modified from [128].

As in LT-PEM system, platinum based electrocatalysts are employed at the electrodes due to their high affinity for HOR and HER in acidic media [83] [129]. Unlike LT-PEM where a ionomeric binder provides proton conduction in the electrodes, there is no solid ionomer in HT-PEM, instead relying on aqueous phosphoric acid in the catalyst layer to provide the proton conduction[130]. Due to the higher conductivity of pure phosphoric acid relative to PA-PBI, and the low gas permeability of PA-PBI, the addition of PBI as a binder in the electrode phase tends to negatively impact cell performance[131]. Instead the state of the art is the addition of a hydrophobic binder to the electrode, either PVDF or most commonly PTFE, to facilitate the formation of hydrophobic domains that allow better gas transport and encourage thin film type formations of phosphoric acid in macropores[132]. Some efforts have been made to integrate phosphonic acid ( $\text{H}_3\text{PO}_3$ ) ionomers, but the relatively low conductivity of phosphonic acid particularly in dry condition is a challenge[133].

The amount of phosphoric acid present in the catalyst layer is a critical parameter for PA-PBI HT-PEM. The addition of phosphoric acid to the electrode phase reduces the ohmic losses associated with proton transport through the electrodes and enhances electrode kinetics with greater interfacial area between proton conducting phase and platinum sites, at least up to a point. At excessive amounts of phosphoric acid, electrode flooding can occur, blocking gas from entering the catalyst entirely and inhibiting cell performance particularly at high current densities [134] [135].

In addition to physically occluding platinum surfaces, phosphoric acid also blocks platinum in a physiochemical manner. Phosphoric acid anions, primarily in the form of biphosphate anions  $\text{H}_2\text{PO}_4^-$ , are known to strongly adsorb to platinum surface[136] much like sulfonate anion

poisoning in LT-PEM electrodes[137]. In LT-PEM however, the molar ratio of sulfonic acid to Pt is around 0.1 to 1 in the catalyst layer [138] while in PA-PBI HT-PEM it is around an order of magnitude higher at 6-10 mol PA per Pt [139]. In combination with a more mobile  $\text{H}_3\text{PO}_4$  phase relative to the solid-phase bound sulfonic acid in LT-PEM ionomers, the presence of aqueous phosphoric acid in the HT-PEM electrodes leads to substantial inhibition of catalytic activity of platinum that has to be compensated for by utilizing much higher platinum loadings ( $> 0.5 \text{ mg Pt cm}^{-2}$ ) than LT-PEM ( $> 0.1 \text{ mg Pt cm}^{-2}$ )[140][141][142].

HT-PEM EHPs have been demonstrated in several applications, largely pertaining to hydrogen gas separations rather than pure hydrogen compression. Kim et al. demonstrated the separation of  $\text{H}_2$  from simulated molten carbon fuel cell (MCFC) anode exhaust with a composition of 20%  $\text{H}_2$  and 80%  $\text{CO}_2$  by volume using an HT-PEM EHP[143]. Several studies have demonstrated the stable long-term operation (4000 + hours) and separation of high-purity hydrogen gas (up to 99.99 % vol  $\text{H}_2$ ) from simulated reformat gases composed of varying ratios of  $\text{H}_2$ ,  $\text{CO}_2$ ,  $\text{CO}$ , and  $\text{CH}_4$  [127][144][145][146][147]. Notably Jiang et al. showed operation with reformat gas at 300 psi feed and 300 psi product with very minimal permeation of  $\text{CO}/\text{CO}_2/\text{CH}_4$  impurities and attributed high overpotentials at elevated pressures to increased  $\text{CO}/\text{CO}_2$  adsorption on Pt surfaces due to elevated pressures[145]. For hydrogen gas separations from low hydrogen volumetric content in natural gas, Vermaak et al. published HT-PEM EHP performance data down to 20%  $\text{H}_2$  in methane and showed that methane acted solely as a diluent as was observed in LT-PEM EHP[148][101].

As a device for gas separation, the HT-PEM EHP is uniquely suited to separate hydrogen gas from particularly pernicious gas impurities such as  $\text{CO}$  and  $\text{CO}_2$  that are often present with hydrogen gas as a consequence of steam methane reforming or other hydrocarbon reforming processes used to produce hydrogen. In fuel cell operation, HT-PEMFC demonstrated high tolerance to  $\text{H}_2\text{S}$  species in excess of 5 ppm, exceeding typical  $\text{H}_2\text{S}$  concentrations in pipeline natural gas of around 3 ppm of net sulfur compounds[149]. Currently, there are limited studies on low  $\text{H}_2$  concentrations (20% and below by volume) in any scenario, let alone blended with methane or natural gas that explore the application of HT-PEM EHP to hydrogen separation from hydrogen natural gas blends. Due to challenges with the trace impurities in natural gas faced by LT-PEM EHPs, HT-PEM EHP may have a role to play if it can show similar

performance aspects to LT-PEM EHP in H<sub>2</sub>/CH<sub>4</sub> blends and then translate that performance to H<sub>2</sub>/natural gas blends.

### 2.2.3 Recent developments in High-Temperature Proton Exchange Membranes and Ionomers

Currently there exists a nascent fuel cell industry surrounding the application of PEM fuel cells to electrify powertrains that are difficult to meet with battery based powertrains alone such as heavy-duty vehicles and aircraft. As a result, there is renewed interest in high temperature PEM fuel cell technology in spite of the relative technological immaturity to LT-PEM based fuel cells due to their enhanced thermal stability, better heat rejection, and higher tolerance to varying humidification[150]. For example, very recently ZeroAvia reported a record breaking fuel cell stack power module of with a record breaking power density of 2.5 kW/kg based on HTPEM for use in aviation[151].

A primary challenge for PA-PBI based HT-PEM systems, particularly in fuel cells, is the sensitivity to acid replacement by water over time that is further exacerbated by dynamic operation, in particular with the thermal cycling associated with start-up and shut-down events[152]. In 2016, an alternative HT-PEM membrane based on ion-pair coordination of biphosphate anions rather than acid-base interactions with phosphoric acid was proposed to address these issues of acid retention and water tolerance[111]. The ion-pair membrane was based on a polyphenylene structure with a benzyl trimethylammonium (BTMA) salt group, typically what would be employed for alkaline exchange membrane-based fuel cells upon introduction of OH<sup>-</sup> groups, but upon interaction with phosphoric acid leads to a complete deprotonation into biphosphate anion form that remains strongly coordinated with the BTMA group. Overall, the QAPOH-PA displayed a higher degree of PA uptake than PA-PBI on a per base moiety basis, a low degree of water uptake per mol of phosphoric acid and a higher overall solids content in the polymer due to a lower overall number of base moieties and lower total volume of PA and water uptake. Figure 2.16 displays the improved operating window of the QAPOH-PA over PA-PBI, with QAPOH-PA exhibiting over 500 thermal cycles from 80 to 160 °C with little loss in conductivity – a test that saw PA-PBI reach failure in 60 cycles.

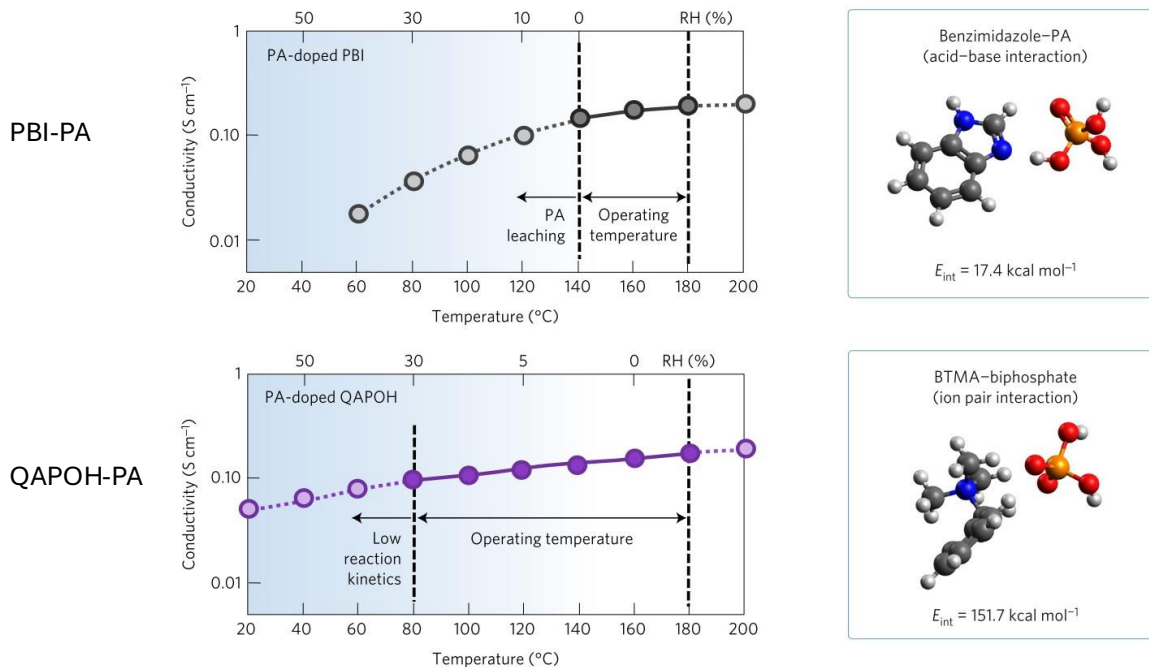


Figure 2.16 Comparison of effective operation window and of fuel cells based on PA-PBI and QAPOH-PA HT-PEM (left). Interaction energy between base moiety and phosphoric acid dopant (right).

In 2011, a research group at the University of Stuttgart published a phosphanated poly(pentafluorostyrene) (PWN) as a high temperature polymer proton conductor with high thermal stability and conductivity exceeding that of Nafion<sup>®</sup> and other comparable phosphanated polymers for temperatures over 100 °C in 1 atm water vapor atmosphere[153][154]. In the absence of water however, the conductivity of phosphonic acid is relatively low ( $< 0.001 \text{ S/cm}$ ) particularly when compared to phosphoric acid, and while PWN was determined to have improved resistance to anhydride formation, its anhydrous conductivity is still significantly lower than phosphoric acid  $0.004 \text{ S/cm}$ [155]. The enhanced water tolerance of the QAPOH-PA HT-PEM facilitated the synergistic integration of such phosphonic acid based ionomers in an ion-pair based HT-PEMFC. The ion-pair HT-PEMFC system comprised of a QAPOH-PA HT-PEM with PWN ionomers showed stable operation from 120 to 240 °C at high current densities beyond what PA-PBI based HT-PEMFC could sustain and reaching peak power densities of  $480 \text{ mW cm}^{-2}$  exceeding what industry standard PA-PBI based HT-PEMFC was currently capable of [155].

In a bid to further improve low temperature performance ( $< 120\text{ }^{\circ}\text{C}$ ) of ion-pair based HT-PEMFC, Nafion® ionomer was introduced alongside PWN ionomer in the electrodes. The ionomer blend unexpectedly produced enhanced performance not only at sub  $120\text{ }^{\circ}\text{C}$  conditions but also in dry condition at temperatures exceeding  $160\text{ }^{\circ}\text{C}$ [156]. DFT calculations and NMR measurements indicated that the PFSA group of Nafion® could protonate the phosphonic acid group of the PWN at the phosphonic oxygen site enhancing the acidity of the phosphonic acid resulting in a significantly higher proton conductivity and a suppression of phosphonic acid anhydride formation [157]. These ‘protonated’ phosphonic acid based electrodes exhibited power densities competitive with LT-PEM fuel cells (Figure 2.17) while improving the overall durability of the ion-pair based HT-PEMFC[157][158][159].

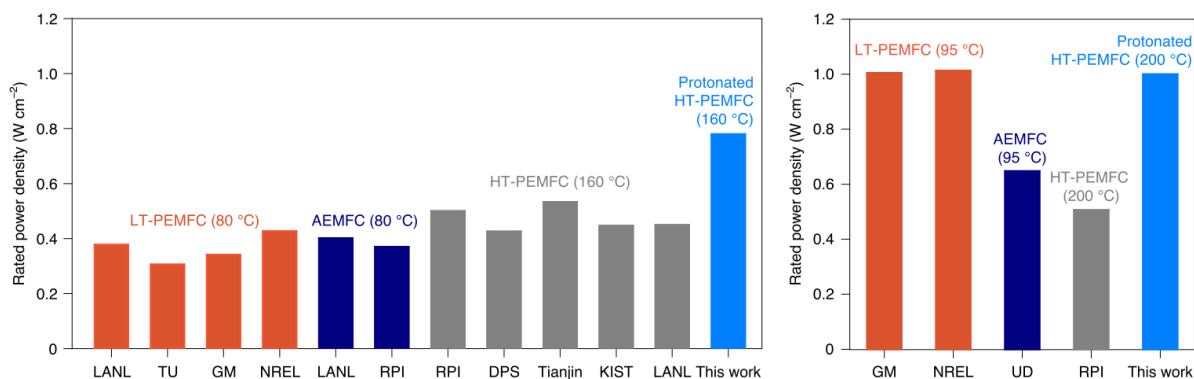


Figure 2.17 Rated power density of Ion-pair HT-PEMFC (‘This work’) compared to other existing polymer electrolyte fuel cell technologies. Reproduced from [157].

Now undergoing commercialization, ion-pair based HT-PEM technology could be a viable alternative to the PA-PBI based materials that have been dominant since their introduction in 1995. To date, only fuel cell operation has been studied with these materials. The ability to operate at higher temperatures, the enhanced acid retention and mechanical properties, and the implementation of a solid ionomer phase in the electrodes rather than a solely aqueous proton conducting phase, could make ion-pair materials an attractive alternative for HT-PEM EHP as well.



## Chapter 3      Goal & Objectives

The goal of this Ph.D. is to investigate the potential of high temperature proton exchange membrane (HT-PEM) based electrochemical hydrogen pump (EHP) technology to meet the demanding requirements of extracting fuel cell quality hydrogen gas from low concentration hydrogen in natural gas infrastructure. It is evident that HT-PEM EHP based on phosphoric acid doped polybenzimidazole (PA-PBI) has not been evaluated experimentally as a gas separation device for low H<sub>2</sub> volumetric content (<20% by volume) gas feeds, nor is there much fundamental understanding at the cell level for PA-PBI based HT-PEM EHP in these limited reactant gas feed conditions. Additionally, the viability of recent material developments in ion-pair HT-PEM and ionomeric binders in HT-PEM EHP operation is of interest as a viable alternative to conventional PA-PBI.

To complete this goal, the following objectives were developed:

**Objective 1:** Conduct ongoing and continuous literature review on topics concerning H<sub>2</sub> gas separation technologies, EHP technologies, and topics surrounding HT-PEM.

**Objective 2:** Experimentally evaluate conventional PA-PBI in HT-PEM EHP for H<sub>2</sub>/CH<sub>4</sub> gaseous blends at low H<sub>2</sub> concentrations to determine its suitability for application in H<sub>2</sub>/natural gas blends.

**Objective 3:** Develop a detailed physical model of the PA-PBI based HT-PEM EHP that accounts for mass transport limitations, phosphoric acid phase distribution, and effects of humidification to enhance understanding of HT-PEM EHP operation in low concentration H<sub>2</sub>/CH<sub>4</sub> blends.

**Objective 4:** Construct an HT-PEM EHP based on ion-pair HT-PEM materials and study the performance and stability of these materials in EHP operating conditions.

**Objective 5:** Demonstrate the separation of hydrogen gas from real pipeline natural gas/hydrogen blends using HT-PEM EHP and evaluate the impact that gaseous impurities have on HT-PEM EHP stability and performance.

## Chapter 4 Approach

Here, the tasks necessary to accomplish each objective are outlined.

### **Objective 1: Conduct ongoing and continuous literature review on topics concerning H<sub>2</sub> gas separation technologies, EHP technologies, and topics surrounding HT-PEM.**

Complete a thorough literature review of progress to date on hydrogen gas separation technologies with careful consideration of the underlying physics and how that could inform that optimal approach to the dissertation goal. Conduct ongoing and continuous literature review on EHP technologies and fundamental HT-PEM research particularly concerning materials development, characterization techniques, and physical modelling.

### **Objective 2: Experimentally evaluate conventional PA-PBI in HT-PEM EHP for H<sub>2</sub>/CH<sub>4</sub> gaseous blends at low H<sub>2</sub> concentrations to determine its suitability for application in H<sub>2</sub>/natural gas blends.**

The following tasks were planned to meet this objective:

- i) Construction of a HT-PEM test stand capable of operating single-cell EHP over long time-scales and evaluating HT-PEM materials using electrochemical techniques and evaluating HT-PEM EHP as a gas separation device using in-line gas analyzers.
- ii) Develop the capability to produce HT-PEM membrane electrode assemblies (MEA) that match current state-of-the-art performance by a thorough literature review of techniques and best practices and subsequent benchmarking of HT-PEM cells.
- iii) Optimize HT-PEM MEA for HT-PEM EHP performance by varying MEA parameters and operating conditions (acid content in electrodes, feed gas humidification).
- iv) Introduce H<sub>2</sub>/CH<sub>4</sub> gas blends to the HT-PEM EHP and evaluate the performance

### **Objective 3: Develop a detailed physical model of the PA-PBI based HT-PEM EHP that accounts for mass transport limitations, phosphoric acid phase distribution, and effects of humidification to enhance understanding of HT-PEM EHP operation in low concentration H<sub>2</sub>/CH<sub>4</sub> blends.**

The goal of this objective is to provide a similar depth of understanding to critical cell parameters to HT-PEM such as acid distribution in the MEA that has been extensively studied in HT-PEM fuel cells and to a much lesser extent in EHP configurations.

To meet this objective the following tasks were outlined:

- i) Development of a physical 2-D model of a PA-PBI HT-PEM EHP that could account for the impact of varying MEA acid content, humidification, and H<sub>2</sub> concentrations.
- ii) Development of operando X-ray CT HT-PEM cell to attempt to image acid distribution in the MEA during operation under humidified and non-humidified conditions and support development of physical model by measurement of physical parameters.
- iii) Validation of physical model with experimental results from Objective 2.
- iv) Parametric sweep of HT-PEM model to identify limiting factors in performance

**Objective 4: Construct an HT-PEM EHP based on ion-pair HT-PEM materials and study the performance and stability of these materials in EHP operating conditions.**

To meet this objective the following tasks were outlined:

- i) Develop the capability to produce protonated phosphonic acid base gas diffusion electrodes, an effective process for doping of QAPOH-PA membranes, and the subsequent assembly of ion-pair HT-PEM MEAs
- ii) Modify the HT-PEM test stand for high humidification testing for proper characterization of ion-pair HT-PEM MEAs and develop ion-pair MEA conditioning and testing protocols that produce consistent results
- iii) Characterize basic performance of ion-pair HT-PEM in EHP in a systematic fashion, isolating the contribution of ionomeric binder and ion-pair HT-PEM to cell performance by testing ion-pair HT-PEM in ionomeric and non-ionomeric MEA. Vary electrode parameters such as ionomer quantity, ionomer ratio and type of ionomer to determine optimal composition for EHP.
- iv) Utilize MEA characterization techniques such as cyclic voltammetry, electrochemical impedance spectroscopy (EIS) and distribution of relaxation times (DRT) to better

differentiate limiting factors in ion-pair HT-PEM MEA stability and performance in EHP.

**Objective 5: Demonstrate the separation of hydrogen gas from real pipeline natural gas/hydrogen blends using HT-PEM EHP and evaluate the impact that gaseous impurities have on HT-PEM EHP stability and performance.**

To meet this objective the following tasks were outlined:

- i) Connect a medium pressure natural gas line to a sulfur removal device and then to the HT-PEM test stand gas mixer.
- ii) Test ion-pair and PA-PBI in natural gas/H<sub>2</sub> blends and compare to methane/H<sub>2</sub> blends to assess whether gaseous impurities present have significant impact on HT-PEM EHP.
- iii) From these results, assess overall suitability for HT-PEM EHP for H<sub>2</sub>/natural gas separations compared to other gas separation technologies.

## **Chapter 5      Experimental Characterization of PA-PBI based HT-PEM EHP for the separation of low H<sub>2</sub> content Methane/H<sub>2</sub> gas mixtures**

### **5.1 Introduction**

This section focuses on the experimental assessment of PBI-PA based HT-PEM EHP for separating fuel cell quality hydrogen gas from methane blends at concentrations of 20% by volume and below. For this study, conventional PA-PBI membranes as opposed to sol-gel type PA-PBI membranes were selected as they exhibited sufficient proton conductivity while exhibiting superior mechanical strength for the relatively harsh operating environment of HT-PEM EHP at low hydrogen concentration feeds. The performance of two different gas diffusion electrodes sets, one based on carbon paper and the other on carbon cloth, is examined in the HT-PEM EHP. The influence of varying phosphoric acid content in the electrodes is experimentally assessed as well and the optimal amount is determined. This optimal MEA is finally evaluated for H<sub>2</sub> gas separation in non-compression and co-compression operating regimes and the purity of H<sub>2</sub> product obtained is examined.

### **5.2 Experimental Materials**

#### **5.2.1 HT-PEM EHP test stand for gas separation**

The HT-PEM EHP experiments are carried out on a high temperature electrochemical test stand built for evaluation of proton exchange membrane based fuel cells and electrochemical hydrogen pumps. The HT-PEM EHP test stand consisted of PID-based temperature controls, a backpressure unit, potentiostat for electrochemical measurements (Gamry 5000), a series of mass flow controllers for fuel gas mixing on the anode and for sweep, purging, or oxidant gas on the cathode, and a high flow rate evaporator type gas humidifier for humidification of dilute hydrogen gas anode feeds. Figure 5.1 outlines the gas line connections of the HT-PEM test stand.

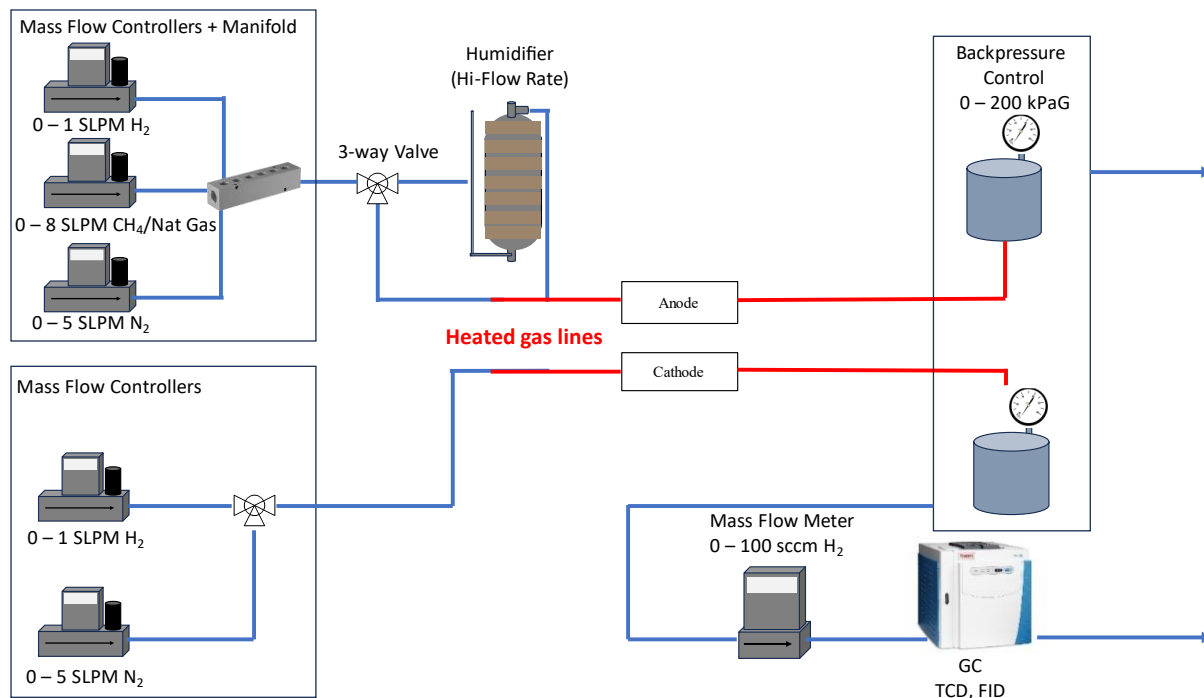


Figure 5.1 Test stand for PA-PBI HT-PEM EHP testing

Temperatures were controlled via four channels of PID controllers for the cell hardware, humidifier bottle, anode inlet heating, and anode/cathode exhaust line heating. Line heating at the anode inlet and anode/cathode exhaust outlets was set to 20 °C over humidifier temperature set point at all times to prevent water condensate in the lines that can cause pressure fluctuations in the cell during experiments.

A high flow rate humidifier was built in-house and consisted of a stainless steel pressure vessel, wrapped in heating tape and ceramic insulation. A ¼” stainless steel tube was inserted through the top of the tube and welded shut at the end, then milled into a porous structure for the last 2 inches of the tube length, sitting ½” from the bottle of the pressure vessel. Deionized water at 18.2 Mohm-cm resistivity is fed from a Milli-Q system through a water feed tube at the bottom of the pressure vessel alongside a k-type thermocouple inserted through the bottom of the pressure vessel to measure water temperature. The humidified gas exits through a stainless steel tube plumbed at the top of the vessel. The structure of the humidifier forces gas to bubble through the water heated to the desired saturation temperature of the gas feed. Humidification was verified up to 2 SLPM flow rates by in-line humidity probe (Vaisala HMP7).

Mass flow controllers on the anode consisted of 1 SLPM H<sub>2</sub> (Brooks 5850i), 8 SLPM CH<sub>4</sub> (Brooks 5851e), 5 SLPM N<sub>2</sub> (Brooks 5850e) with outlets plumbed to a gas mixing manifold. The

outlet of the manifold is three-way valved to enter the humidifier bottle or bypass for dry gas operation. On the cathode side two flow controllers are situated consisting of 1 SLPM H<sub>2</sub> (Brooks 5850i) and 5 SLPM N<sub>2</sub> (Brooks 5850e) directly plumbed to the cathode inlet of the cell. The 5 SLPM N<sub>2</sub> cathode flow controller is valved upstream to provide N<sub>2</sub> gas for inerting or air for oxidant feeds in fuel cell testing. Gas pressure in the cell is controlled by a backpressure unit that can independently control anode and cathode backpressure up to 200 kPa gauge and serves as a gas cooling condensate trap. Anode and cathode cell hardware inlet pressures are viewable by pressure gauge.

An in-line gas chromatograph (ThermoFisher Trace 1300) sampled cathode effluent gas from the HT-PEM EHP. A molsieve 5A column with nitrogen carrier gas separated gas samples drawn in from an automated 400 uL gas sample valve that were analyzed by thermal conductivity detector (TCD) with N<sub>2</sub> reference gas and a flame ionization detector running on H<sub>2</sub>/Air. Cathode effluent was sampled from 1/8" line from the exhaust following the backpressure unit and was further dried through a column of Drierite ® before entering the GC column.

All gases used were of the ultra high-purity (UHP) degree provided by AirGas (>99.995% vol. primary constituent).

### 5.2.2 Phosphoric Acid Doped Polybenzimidazole (PA-PBI) Membranes

Fumapem AP-30 (Fumatech BWT GmbH) polybenzimidazole (PBI) copolymer was purchased from Fuel Cell Store to serve as the proton conducting membrane (PEM). 5.25 cm<sup>2</sup> segments were cut and weighed in dry condition to obtain dry weight prior to doping in phosphoric acid. PBI membranes were placed in ACS Reagent Grade 85% weight ortho-phosphoric acid aqueous solution (Sigma-Aldrich P/N 695017) at room temperature for 72 hours whereupon they were weighed to assess the percentage weight of acid added and the acid doping level (ADL) of the membranes following the doping procedure.

$$\%wt_{H_3PO_4} = \frac{m_{PBI,doped} - m_{PBI,dry}}{m_{PBI,doped}} \quad (Eq. 5-1)$$

$$ADL_{PBI} \left[ \frac{mol H_3PO_4}{mol} \right] = \frac{(m_{PBI,doped} - m_{PBI,dry})}{m_{PBI,dry} / MW_{PBI}} \quad (Eq. 5-2)$$

Doped PBI membranes exhibited a transition to a more gel-like structure and some swelling. The typical %wt of phosphoric acid following 72 hours doping procedure was 68-70% wt H<sub>3</sub>PO<sub>4</sub>

corresponding to 6-7 mol PA/PBI which is typical of conventional PBI doping procedures[160][117].

### 5.2.3 Gas Diffusion Electrodes & MEA Assembly

Gas diffusion electrodes based on carbon paper type gas diffusion layer (GDL) Freudenberg H23C2 were prepared with catalyst inks containing 40% Pt nanoparticles on carbon black (HiSpec 4000) and PTFE (DuPont™ Teflon® PTFE DISP30). Pt/C was mixed with PTFE dispersion in a ionomer to carbon ratio (I/C) of 0.2, the mixture was dispersed in a water/1-propanol solvent system of 25:75 wt water:1-propanol and a solids content of the dispersion of 20 mg C/mL solvent. The ink slurry was sonicated for 1 hour in ice bath and then drop-cast on 5 cm<sup>2</sup> GDLs sitting on vacuum hot plate set at 60 °C with targeted loading of 1 mg Pt cm<sup>2</sup>. Fabricated GDEs were further dried in oven at 200 °C to remove any remaining surfactant due to its presence in the DISP30 PTFE dispersion. Loadings were verified by gravimetric measurement of GDL before electrode deposition and following oven drying.

De Nora carbon cloth type gas diffusion electrodes were provided by Technologie De Nora for HT-PEM EHP and fuel cell testing. The loading of the 1 mg Pt cm<sup>-2</sup> De Nora GDEs were verified by X-ray fluorescence (XRF) and found to be within 2% of the rated platinum loading across five randomized measurements. The structure of the De Nora GDEs were analyzed ex-situ via X-ray micro-computed tomography (micro-CT) at Argonne National Lab (ANL) Advanced Photon Source (APS). A higher density micro porous layer (MPL) type region was found interwoven through the carbon cloth gas diffusion layer (GDL) structure (Figure 5.2). The catalyst layer thickness was on average 80 μm and was stated to contain PTFE by the OEM but further details on the exact composition of the catalyst layer were not provided.



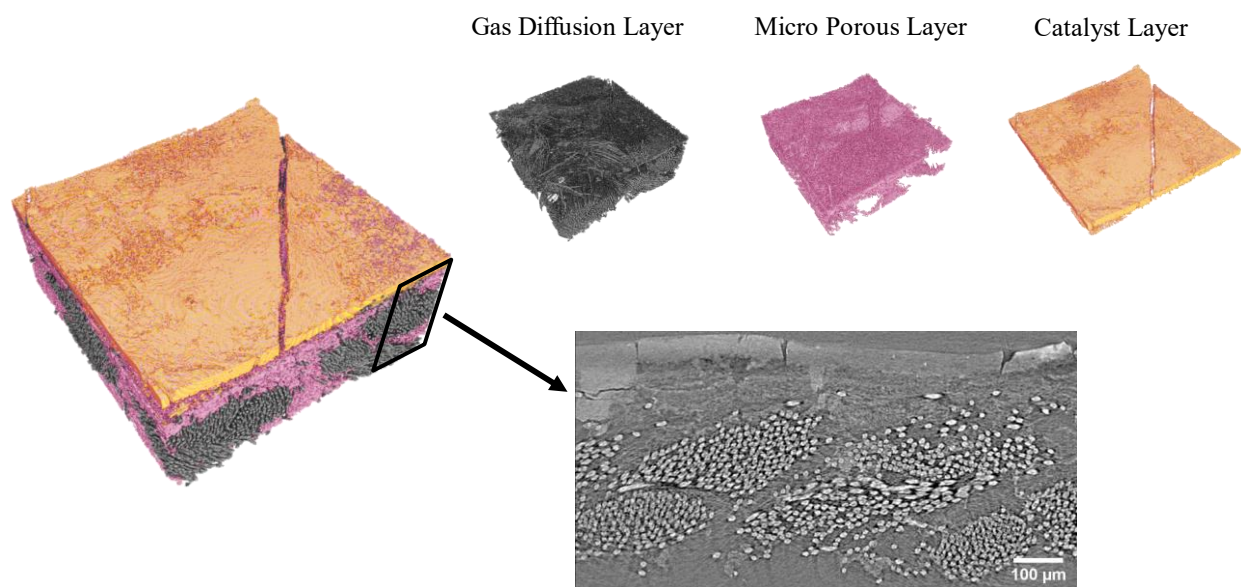


Figure 5.2 X-Ray CT of De Nora gas diffusion electrodes with loading of 1 mg Pt cm<sup>2</sup>.

Membrane electrode assemblies (MEA) were constructed with the phosphoric acid (PA) doped PBI membranes by sandwiching two 5 cm<sup>2</sup> identical gas diffusion electrodes on each side. An equivalent amount of phosphoric acid (85% wt H<sub>3</sub>PO<sub>4</sub>) was drop-cast on each electrode surface prior to assembly in varying amounts to characterize the impact of phosphoric acid content in the catalyst layer and determine the optimal amount of electrolyte phase in the electrode for HT-PEM EHP operation. Table 5-1 outlines the MEAs characterized in this section.

Table 5-1 Physical characteristics of Freudenberg and De Nora based GDEs for HT-PEM EHP

Gas Diffusion Electrodes tested in HT-PEM EHP MEAs		
	Freudenberg	De Nora
Pt Loading [mg Pt cm <sup>-2</sup> ]	1	1
Hydrophobic Binder	PTFE	PTFE
I/C Ratio	0.2	n/a
Catalyst Layer Thickness* [um]	72	80
GDL thickness [um]	255	440

Compression [% Thickness GDL]	20	50
Acid Content [mg H <sub>3</sub> PO <sub>4</sub> cm <sup>-2</sup> ]	0, 10, 20, 40	0, 10, 20, 40

The MEA consisting of two GDEs and the PA-PBI membrane is framed by PTFE gaskets totaling a thickness of 180  $\mu\text{m}$  for Freudenberg GDEs and 195  $\mu\text{m}$  for De Nora GDEs plus a 1 mil (25.4  $\mu\text{m}$ ) thick Kapton frame as a sub-gasket. The single cell 5 cm<sup>2</sup> MEA was mounted in a Scribner fuel cell fixture with 5 cm<sup>2</sup> serpentine graphite flow fields, and bolts were torqued to 10 Nm. The entire assembly is described below in Figure 5.3.

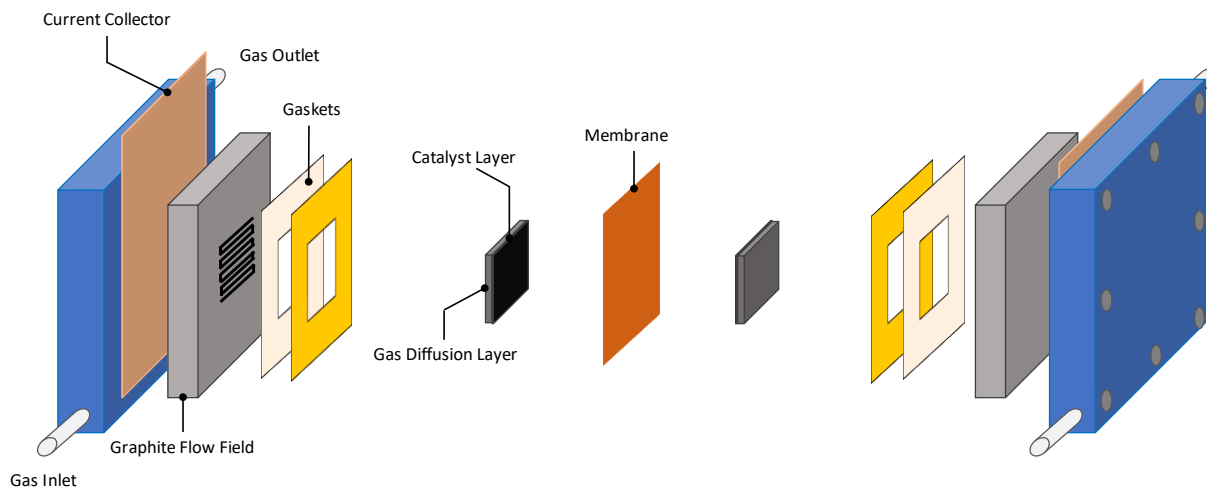


Figure 5.3 5 cm<sup>2</sup> cell assembly.

## 5.3 Experimental Methods

### 5.3.1 Cell Start-Up & Conditioning

Upon assembly, the cell is heated to 160C with dry nitrogen flowing on anode and cathode at ambient pressures. At 160 C, 0.2 SLPM of humidified hydrogen is supplied to the anode at a relative humidity of 1.2%, corresponding to a humidifier bottle temperature of 40 C, and 0.1 SLPM of dry hydrogen is flowed at the cathode as a sweep gas. Prior to testing the HT-PEM EHP was conditioned by current hold at 0.2 A cm<sup>-2</sup> for 4 hours.

Pure H<sub>2</sub> anode feed EHP operation was performed initially to characterize MEA performance due to acid content in the electrodes. Backpressure was set to 80 kPaG at both anode and cathode with 0.2 SLPM humidified H<sub>2</sub> gas at the anode (T<sub>sat</sub> = 40 °C) and 0.1 SLPM dry H<sub>2</sub> sweep gas at

the cathode to maintain cathode backpressure at low current condition holds. Polarization curves were taken in galvanostatic condition following 4 hour conditioning, Galvanostatic holds of 10 minutes per point were repeated three times from low to high current to generate pol curves. EIS measurements were similarly repeated 3 times, taken at 100 mA with an amplitude of 10% following the 100 mA current hold.

### 5.3.2 H<sub>2</sub>/CH<sub>4</sub> Gas Separation

MEAs with the identified best performance with respect to electrode acid content were tested in H<sub>2</sub>/CH<sub>4</sub> blend anodic feeds to assess the HT-PEM EHP for gas separation suitability.

Polarization curves were collected in a like manner to pure H<sub>2</sub> characterization- galvanostatic for 10-min duration holds with EIS collected at 100 mA. Anode and cathode gas flows consisted of 1.0 SLPM net flow at the anode for hydrogen/methane blends of 20,10, and 2% H<sub>2</sub> by volume were humidified to T<sub>sat</sub> = 40 °C and 0.1 SLPM dry H<sub>2</sub> sweep gas. Backpressure was varied for an equal pressure operation case – both anode and cathode set to 80kPaG, and a H<sub>2</sub> co-compression case with anodic pressure set to 40 kPaG and cathode pressure at 80 kPaG.

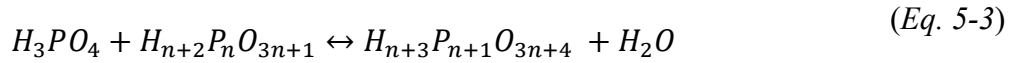
GC measurements of the cathode effluent were taken at 30-minute galvanostatic condition above 1 amp at which sweep gas was not needed to maintain cathodic backpressure due to sufficient hydrogen evolution rates.

Gas cross-over in the HT-PEM EHP of H<sub>2</sub> was characterized by limiting current measurements and validated with mass flow metering on the outlet[161]. 0.3 SLPM of humidified hydrogen (T<sub>sat</sub> = 40C) and dry nitrogen were flowed at the cathode and anode respectively, with the limiting current measured at 0.5 V determining H<sub>2</sub> gas cross-over. Cross-over of CH<sub>4</sub> gas was characterized in HT-PEM EHP by combination of GC-FID measurements and cathode outlet mass flow metering with 0.3 SLPM humidified methane and 0.3 SLPM dry nitrogen flowing on opposite sides of the HT-PEM EHP and no current applied.

## 5.4 Results & Discussion

Water vapor was introduced to the anode feeds as some amount of water is needed to maintain sufficient hydration of the phosphoric acid in the electrodes and membrane to ultimately prevent phosphoric acid species from undergoing transition to lower conductivity pyrophosphoric acid

species through a dimerization process (Eq. 5-3) resulting in diminished proton conductivity [112] and greater degree of phosphoric acid species adsorption on Pt surfaces and thus lower reaction kinetics [162]. Unlike in HT-PEMFCs, for water to be introduced in the phosphoric acid phase it must be introduced in the anode gas due to lack of gas flow in cathode for typical outlet only cathode operating condition of EHP.



Daletou et al. demonstrated that the dimerization process of phosphoric anhydrides can be reversed with sufficient vapor pressure increasing with temperature[163]. At 160 °C this vapor pressure is around 7 kPa, corresponding roughly to a relative humidity of 1.2% and a  $T_{sat}$  of 40 °C for an environment at 160 °C. These equilibrium vapor pressures at which EQ is reversed can be observed to lie between vapor pressures of aqueous phosphoric acid solutions of 0 to 1 % weight water content at the same temperatures (Figure 5.4).

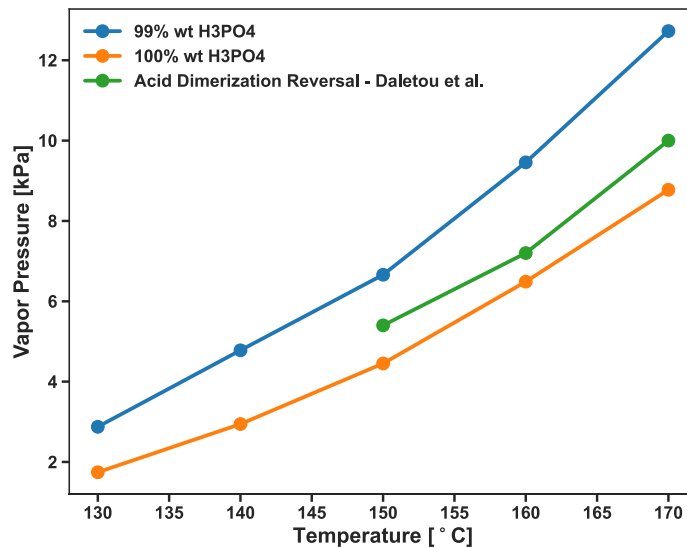


Figure 5.4 Temperature vs. vapor pressure of water for equilibration of 99 and 100% wt  $H_3PO_4$  phosphoric acid and observed reversal of dimerization of phosphoric acid species at anhydrous conditions from Daletou et al [163].

Further humidification would lead to increasing conductivity of the phosphoric acid phase and thus better conductivity in the HT-PEM EHP however increased water content has implications for the long-term stability of the HT-PEM EHP due to acid replacement by water[152]. For this study, minimum RH needed to prevent acid dimerization is selected as an optimal approach, with

similar RH values observed in other HT-PEM EHP studies employing phosphoric acid doped PBI membranes[126][127]. Dry operation of HT-PEM EHP for gas separation has been observed, but largely for CO<sub>2</sub> containing gas mixtures, which could potentially introduce water through a secondary reverse water gas-shift[143][145][164].

HT-PEM EHPs were constructed with GDEs based on Freudenberg H23C2 carbon paper GDLs as well as De Nora carbon cloth GDLs, with varying amounts of 85% wt H<sub>3</sub>PO<sub>4</sub> drop-cast to electrode surface prior to assembly to provide the proton-conducting phase in the catalyst layer. The polarization behavior and Nyquist plot of electrochemical impedance spectroscopy (EIS) of HT-PEM EHP as a function of this additional electrode acid content is described in Figure 5.5 for the former and Figure 5.6 for the latter.

Across both cases, at lower amounts of drop-cast acid content, activation polarization is greater as is apparent from the larger *iR*-corrected polarization losses and higher *R*<sub>ct</sub> values. *iR*-corrected polarization curves are calculated from the high frequency resistance (HFR) recorded with galvanostatic EIS at 0.02 A cm<sup>-2</sup>, as HFR was found to not vary with current density or potential appreciably in the HT-PEM EHP.

$$E_{ir} = E_{cell} - iR_{HFR} \quad (Eq. 5-4)$$

Higher HFR values were observed for lower acid content which could be attributed to diminished contact between electrode and membrane proton conducting phases. At very high acid loadings, mass transport limitations begin to appear as observed at the high current density regime for GDEs drop-cast with 40 mg H<sub>3</sub>PO<sub>4</sub> cm<sup>-2</sup>.

## Freudenberg H23C2 GDE

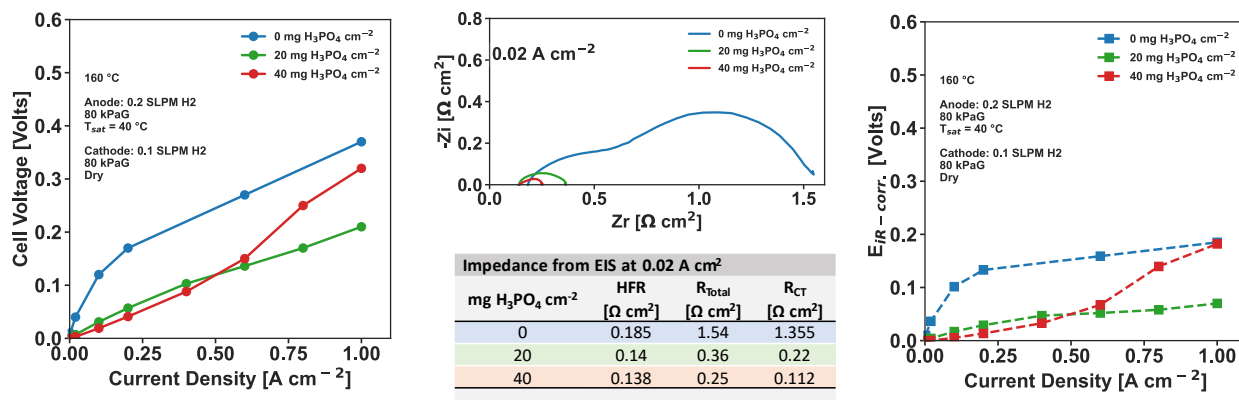


Figure 5.5 Polarization curve (left), EIS with impedance values (middle), and  $iR$ -corrected polarization curves (right) for varying amounts of phosphoric acid added to Freudenberg type gas diffusion electrodes for PBI-PA HT-PEM EHP

De Nora based GDEs displayed consistently lower HFR suggesting a better contact between GDE surface and the PBI-PA membrane with the softer carbon cloth type GDL. At the highest acid contents, charge transfer resistance from EIS analysis,  $R_{CT}$  associated with the remaining impedance after subtracting the HFR, is comparable between the two electrodes and a similar inflection point in mass transport type overpotentials in polarization curve occurs. As both electrodes are close in thickness and use a similar Pt/C catalyst, the total void fraction that acid can occupy is similar in value and thus the amount of acid required to reach a flooded electrode state is similar in value. The actual pore size distribution and hydrophobicity in the electrode phase is not known for either and would play a role in wettability of pores, but flooded condition would occur at high enough acid contents regardless.

## De Nora GDE

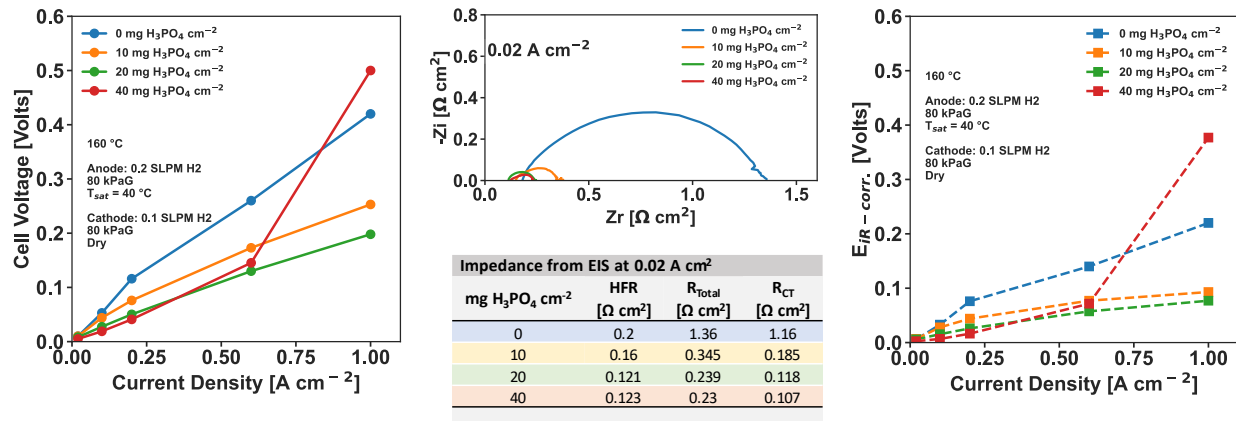


Figure 5.6 Polarization curve (left), EIS with impedance values (middle), and  $iR$ -corrected polarization curves (right) for varying amounts of phosphoric acid added to De Nora type gas diffusion electrodes for PBI-PA HT-PEM EHP

Electrode acid content does occupy a ‘goldilocks zone’ with respect to the HT-PEM EHP performance, which was similarly found to occur around 20 mg H<sub>3</sub>PO<sub>4</sub> cm<sup>-2</sup> drop-cast amount. This does align with findings around HT-PEMFC based on similar MEA structures which also found optimal electrode acid contents that lied between dry and flooded phosphoric acid electrode conditions[134].  $iR$ -corrected polarization curves show that kinetic improvements do seem to continue at increasingly high acid contents, but the current limiting behavior at high overpotentials with high acid content at 40 mg H<sub>3</sub>PO<sub>4</sub> cm<sup>-2</sup> would be prohibitive in performance to the desired gas separation application of the HT-PEM EHP.

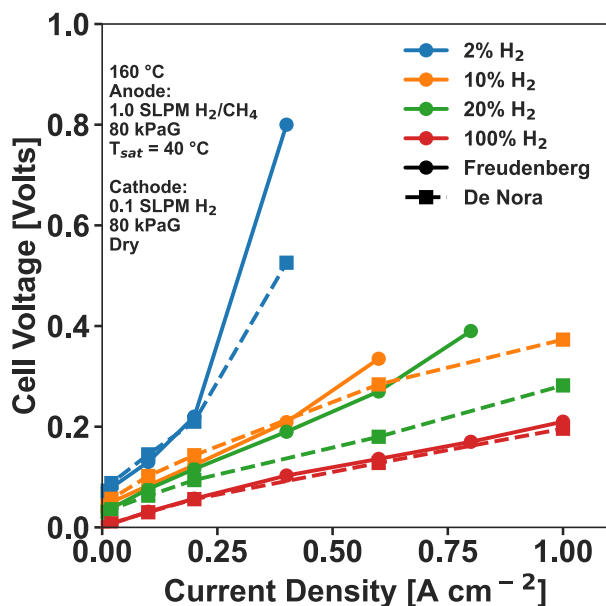
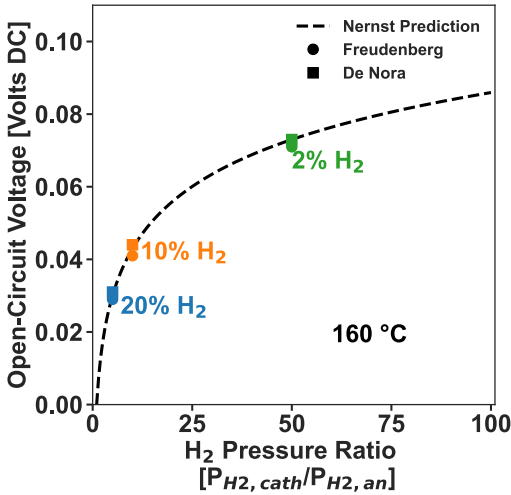


Figure 5.7 HT-PEM EHP polarization curves for Freudenberg and De Nora GDEs for H<sub>2</sub>/CH<sub>4</sub> gas separations.

The HT-PEM EHPs with Freudenberg and De Nora type gas diffusion electrodes at the optimal acid loading of 20 mg H<sub>3</sub>PO<sub>4</sub> cm<sup>-2</sup> were tested in H<sub>2</sub>/CH<sub>4</sub> gaseous blends for low H<sub>2</sub> volumetric concentrations of 2, 10, and 20% by volume H<sub>2</sub> in CH<sub>4</sub> to mirror the expected near-term limits of H<sub>2</sub> gas content in natural gas infrastructure. The pure H<sub>2</sub> EHP performance is relatively comparable between the two and the primary distinction is more apparent in the mass transport limiting conditions introduced by the low H<sub>2</sub> gas content polarization at current densities beyond 0.2 A cm<sup>-2</sup>. Evidently, the carbon cloth De Nora GDEs is better suited to reactant gas transport and overall has a superior microstructure for HT-PEM EHP in gas separation.





Theoretical Separation Efficiency no co -compression			
% vol H <sub>2</sub>	Nernst Voltage [Volts DC]	Minimum Sep. Eff [kWh/kg]	% Lower Heating Value H <sub>2</sub>
20	0.03	0.802	2.41%
10	0.043	1.150	3.45%
2	0.073	1.952	5.86%

Figure 5.8 Nernst potential prediction versus observed open-circuit voltage in H<sub>2</sub>/CH<sub>4</sub> separation and corresponding minimum theoretical separation efficiency.

Dilution of feed H<sub>2</sub> gas leads to an increase of voltage at the zero net current condition or open-circuit voltage (OCV) which aligns accordingly with the predicted voltage from Nernst equation for a H<sub>2</sub>/H<sub>2</sub> concentration cell.

$$OCV = \frac{RT}{2F} \ln \left( \frac{P_{H_2,c}}{P_{H_2,an}} \right) \quad (Eq. 5-5)$$

This OCV represents the theoretical minimum separation efficiency of the HT-PEM EHP for the given pressure ratio and temperature. For gas separation process without pressurization of the cathode above anodic pressure or a co-compression processes where in H<sub>2</sub> product from the cathode leaves at a higher total pressure than the anode feed, the separation of H<sub>2</sub> gas mixtures at 20, 10, and 2% volume H<sub>2</sub> takes up to 2.4, 3.5, and 5.86 % respectively, of the associated lower heating value (LHV) of the separated H<sub>2</sub> gas.

HT-PEM EHP based on the De Nora GDEs were further examined for H<sub>2</sub>/CH<sub>4</sub> gas separation in terms of the influence of equal pressure versus co-compression operation. The polarization behavior of the HT-PEM EHP with backpressure of 80 kPaG at both anode and cathode, corresponding to a compression ratio of P<sub>r</sub> = 1, compared to an anodic backpressure of 40 kPaG versus cathode at 80 kPaG, P<sub>r</sub> = 1.27, is shown below in Figure 5.9.

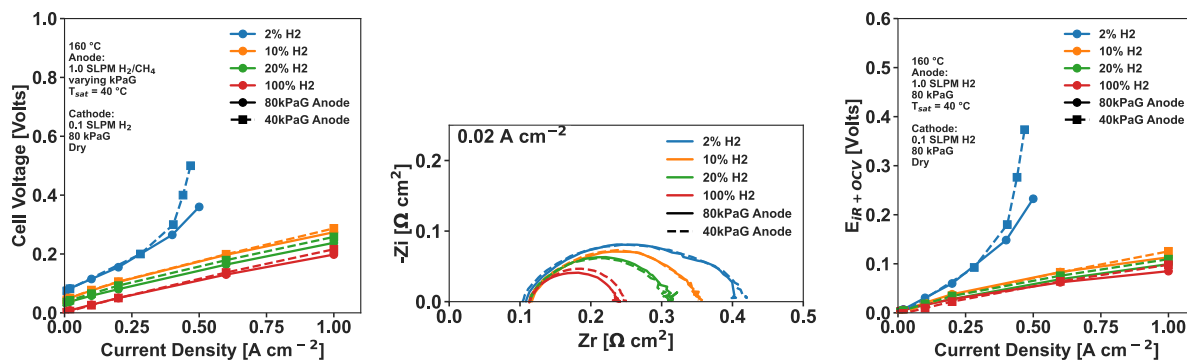


Figure 5.9 Polarization curve, Nyquist plot of EIS at  $0.02 \text{ A cm}^{-2}$ , and  $iR + OCV$  corrected polarization behavior of the HT-PEM EHP with De Nora GDE for  $\text{H}_2/\text{CH}_4$  gaseous mixtures at equal pressure operation and co-compression operation.

Mass transport limitations were solely observed for the ultra-dilute case of 2%  $\text{H}_2$ , for which the theoretical limiting current density is  $0.57 \text{ A cm}^{-2}$ . When operating in co-compression, the maximum observed current of  $0.48 \text{ A cm}^{-2}$ , is 85% of the theoretical limit. Due to the higher anodic pressure driving reactant transport and higher local reactant concentration, the equal pressure case was able to reach current densities of  $0.53 \text{ A cm}^{-2}$ , 93% of the theoretical limit. This suggests that the utilization of higher pressure gas streams such as high pressure distribution level natural gas infrastructure (upwards of 200 psig)[165] would have a beneficial effect to a degree over ambient systems. Correcting for  $iR$  and open-circuit potential demonstrates that the kinetic and mass transport related effects at 2%  $\text{H}_2$  are appreciable across the entire range of current density, while the overpotential difference between 10 and 20%  $\text{H}_2$  cases approaches 100%  $\text{H}_2$ . The primary driver in potential difference between these cases then is due to a

thermodynamic effect associated with the electrochemical potential difference in hydrogen concentration captured by the Nernst potential.

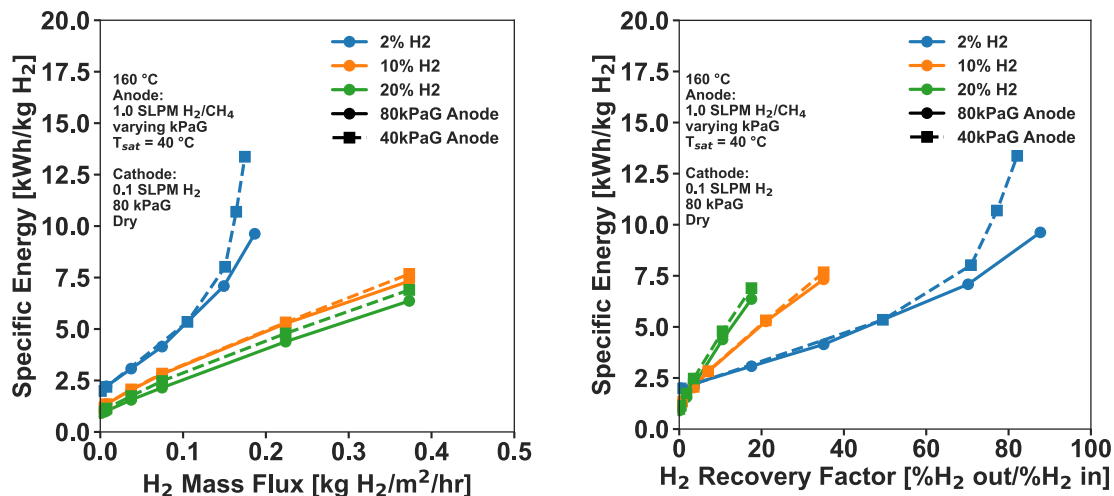


Figure 5.10 Specific energy consumption of H<sub>2</sub> separation for equal compression and co-compression of H<sub>2</sub>/CH<sub>4</sub> blends in PA-PBI based HT-PEM EHP

The HT-PEM EHP performance in gas separation can be characterized in terms of gas separation efficacy, namely the specific energy of gas separation defined here as the electrical power consumption of the electrochemical reactions in the HT-PEM EHP divided by H<sub>2</sub> flux in kg H<sub>2</sub>/hr. H<sub>2</sub> mass flux defined as the mass flux per area of the membrane surface is plotted against specific energy, effectively re-casting polarization data in terms of the gas separation efficacy. Due to the strong dependence of the cell potential on the current density, the specific energy cost of separation scales up quickly with increasing mass flux.

Another metric for H<sub>2</sub> flux is the hydrogen recovery factor (H<sub>2</sub>RF) taken as the percentage of H<sub>2</sub> leaving the cathode out of the dilute anode feed. Intriguingly the specific energy cost scales quickly with H<sub>2</sub>RF for less dilute mixtures, with a H<sub>2</sub>RF of 10% resulting in a separation efficiency of ~5 kWh/kg H<sub>2</sub> for a 20% volume H<sub>2</sub> feed while a 2% H<sub>2</sub> feed achieves ~3 kWh/kg H<sub>2</sub> for the same H<sub>2</sub>RF. For reference, state-of-the-art pressure swing adsorption (PSA) separation scales poorly into sub-25% H<sub>2</sub> containing mixtures and was determined to require approximately 20 kWh/kg H<sub>2</sub> for separation of 10 % H<sub>2</sub> from methane blend [78].

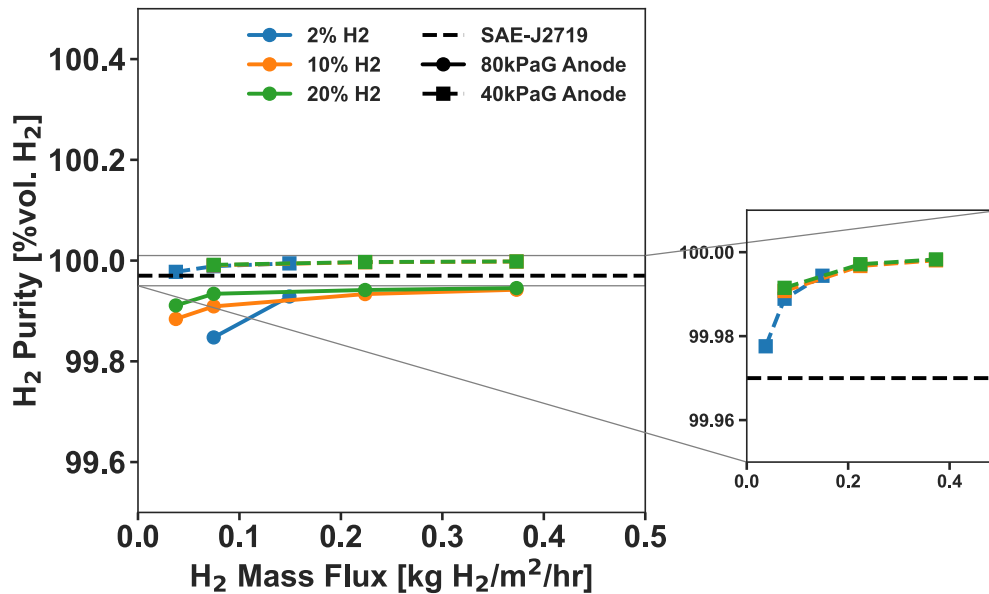


Figure 5.11 Cathode effluent H<sub>2</sub> purity for HT-PEM EHP operation in H<sub>2</sub>/CH<sub>4</sub> blends for equal pressure and co-compression gas separation modes.

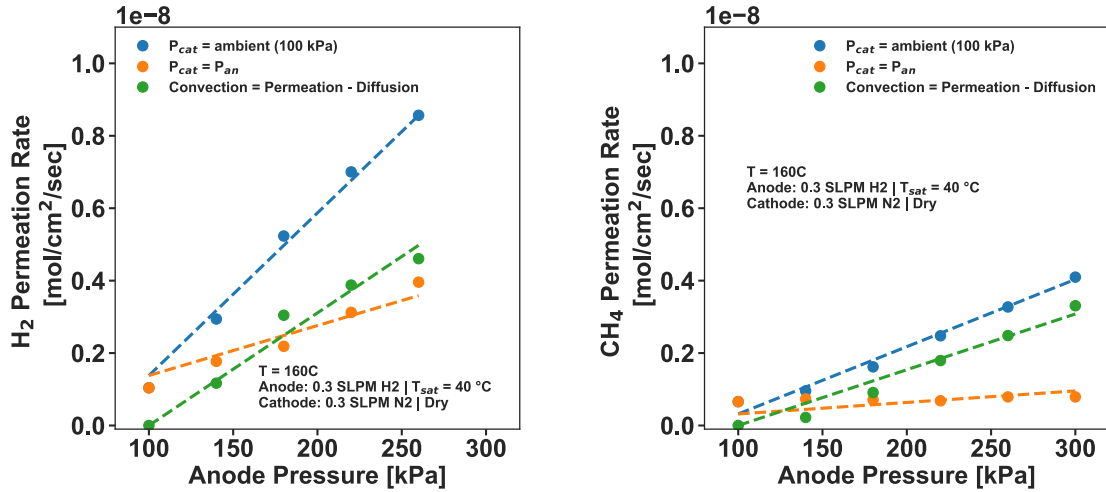
In-line GC measurements of cathode effluent during the H<sub>2</sub>/CH<sub>4</sub> separation testing at equal pressure and in co-compression operation was carried out to detect impurities in the H<sub>2</sub> gas stream. Figure 5.11 shows the H<sub>2</sub> purity from GC analysis with respect to the H<sub>2</sub> mass flux. Fuel cell electric vehicle fueling standards (FCEV) set by the Society of Automotive Engineers (SAE) in SAE-J2719 specify minimum hydrogen purity of 99.97% by volume, and a maximum hydrocarbon concentration of 2 μmol/mol or 99.998% H<sub>2</sub> purity in balance against CH<sub>4</sub> at most. However, methane is an exception in that the sum of Methane, Nitrogen, and Argon must not exceed 100 ppm. In equal pressure operation, the highest attainable purity was approximately 99.95% for high flux for the 20 and 10 % H<sub>2</sub> separation cases. The relatively high methane gas concentrations on the cathode side result partially from the pressure gradient favoring anode to cathode; while the backpressure is set to equal amounts 80 kPaG the high flow rate of 1.0 SLPM on the anode compared to no-sweep gas conditions at the cathode leads to an appreciable pressure drop from anode inlet to outlet of ~30 kPaG. In the co-compression case, the pressure gradient from anode to cathode favors a high pressure on the cathode side across anode inlet and outlet. The resulting improvement in cathode purity is evident with upwards of 99.994% H<sub>2</sub>

purity achieved well in excess of the 99.97% purity requirement and meeting the methane only hydrocarbon requirement.

Gas cross-over measurements of H<sub>2</sub> and CH<sub>4</sub> gases were taken at conditions relevant to the operation of the HT-PEM EHP at 160C, anode humidification of 1.2% RH, and dry cathode. In the controlled cross-over measurements, lower and equal flow rates at the anode and cathode could be employed to mitigate the impact of pressure drop from inlet to outlet across the membrane. The measured permeability rates (Figure 5.12) were used to determine permeability coefficients. Permeation rates are attributed to a contribution from diffusive transport due to concentration gradients of gaseous species from one side of the membrane to the other as well as a convective transport contribution due to bulk gas movement by total pressure gradient across the membrane. The convection permeation coefficient,  $\varepsilon_{dp}$ , is determined as the difference between the measured total permeation rate due to absolute pressure differential and the diffusion transport permeation rate,  $\varepsilon_{diff}$ , due to partial pressure differential alone [166],

$$\dot{n}_{CH_4,perm} = \varepsilon_{diff,CH_4} \frac{P_{c,CH_4} - P_{a,CH_4}}{t_{mem}} + \varepsilon_{dp,CH_4} \frac{P_c - P_a}{t_{mem}} \quad (Eq. 5-6)$$

$$\dot{n}_{H_2,perm} = \varepsilon_{diff,H_2} \frac{P_{c,H_2} - P_{a,H_2}}{t_{mem}} + \varepsilon_{dp,H_2} \frac{P_c - P_a}{t_{mem}} \quad (Eq. 5-7)$$



Permeability Coefficients of H <sub>2</sub> and CH <sub>4</sub> in PA-PBI HT-PEM EHP		
	H <sub>2</sub>	CH <sub>4</sub>
$\epsilon_{diff}$ [mol/cm/s/pa]	8.28E-17	1.91E-17
$\epsilon_{conv}$ [mol/cm/s/pa]	1.87E-16	9.24E-17

Figure 5.12 Permeation rates of H<sub>2</sub> (top left) and CH<sub>4</sub> (top right) as a function of anode pressure for net pressure differential permeation and partial pressure differential only. Fitted diffusive and convective permeation coefficients (bottom).

Measurements of the H<sub>2</sub> permeation rates were comparable to rates reported by the literature for a PBI membrane with a similar level of acid doping content [167], as well as permeation rates reported by Wainwright et al. [107]. H<sub>2</sub> permeation rates reported in literature for PFSA membranes such as Nafion® 112 in operating conditions relevant to EHP cells (~100% RH, 20 – 60 C) are within range of observed H<sub>2</sub> permeation rates for HT-PEM EHP [161][168][169][170]. Nordio et al. published methane permeation rates through a LT-PEM EHP based on a Nafion® 112 that showed a higher permeation rate of  $1.5 \times 10^{-8}$  mol/cm<sup>2</sup>/sec compared to  $0.4 \times 10^{-8}$  mol/cm<sup>2</sup>/sec in the HT-PEM EHP at 300 kPaG [169].

Benchmarking the effectiveness of the HT-PEM EHP as a means of H<sub>2</sub> separation in low H<sub>2</sub> concentration CH<sub>4</sub>/natural gas blends is challenging due to a lack of separation technologies that can effectively operate at such low H<sub>2</sub> contents and produce sufficiently high purity hydrogen that would meet fuel cell quality standards. Other EHP studies have been carried out in methane mixtures at 20% [169][102][148] and 10% H<sub>2</sub> [102] volumetric content. Figure 5.13 displays the comparison in efficacy in terms of polarization with LT-PEM EHP based on Nafion® membranes as well as an HT-PEM EHP study utilizing pyridine structure HT-PEM membrane.

Due to differences in stoichiometry, mass transport limiting effects are apparent in the other studies that used relatively limited anode flow rates in their experiments.

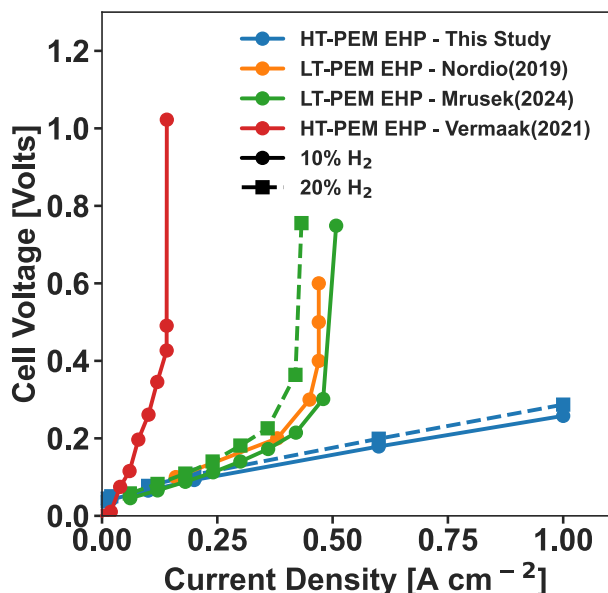


Figure 5.13 Comparison of EHP performance with published EHP performance for low %  $H_2$  in  $CH_4$  blends. Data reproduced from Nordio et al., 2019[169], Mrusek et al., 2024[102], and Vermaak et al., 2021 [148].

It was observed that in the ohmic limited regime before mass transport impacts, the HT-PEM EHP is comparable in performance to LT-PEM EHP operated in their preferred operating conditions at ambient pressures. LT-PEM EHP are a more mature EHP technology that is commercially available for electrochemical compression applications[171][95][86]. Their usage in gas separation has long been considered due to simplicity of a single-stage gas separation step through EHP and the maturity of the LT-PEM technology[103][169][172][173][174]. A limiting factor in their deployment is their sensitivity to  $CO_2$ , which is present in natural gas, as a progenitor to CO and subsequent platinum catalyst poisoning at low temperatures[104] as well as the high cross-over rates of  $CO_2$  in Nafion® systems due to the high water content and high solubility of  $CO_2$  gas in water[102][175][176] while PBI type membranes have shown orders of magnitude lower  $CO_2$  permeability[177] making them a potentially better candidate for natural gas and  $H_2$  blend separations.

Another potentially viable alternative achieving high purity H<sub>2</sub> from low concentration blends is a hybrid separation system. Such approaches have been studied in which the synergies between conventional molecular sieve type membrane separation, adsorption based separation techniques based on temperature swing (TSA) and pressure swing (PSA) processes, and EHP type technologies are examined to model a viable approach. HyLyPure was one of the more promising proposed systems in this vein, in which H<sub>2</sub>/CH<sub>4</sub> gas blends were separated into high purity H<sub>2</sub> streams. A series of compressors and membranes handled the initial separation stages, terminated by a PSA process to reach the final high purity requirements, with the modelled system ultimately able to produce >99.97% H<sub>2</sub> purity from gas streams as low as 1% vol H<sub>2</sub> concentration.

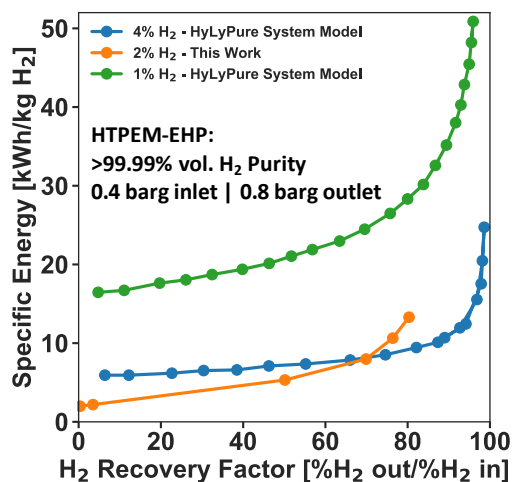
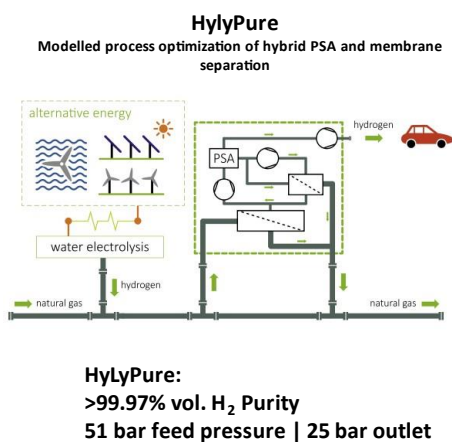


Figure 5.14 Specific energy of separation comparison of PBI-PA HT-PEM EHP against HyLyPure hybrid separation system for ultra-low H<sub>2</sub> concentration separations from H<sub>2</sub>/CH<sub>4</sub> blends.

Comparing the performance of the HyLyPure system to the HT-PEM EHP experiments, in terms of electrical consumption of the HT-PEM EHP the amount of energy needed to separate 2% vol. H<sub>2</sub> at 99.99% H<sub>2</sub> product purity is lower by a significant degree for low H<sub>2</sub>RF (< 50%) than the 4% vol. H<sub>2</sub> case in HyLyPure. Another distinction is the ability of the HT-PEM EHP to gain



pressure through the separation process versus the 26 bar pressure loss through the HyLyPure separation process due to the need to drop pressure through the membrane and PSA processes.

## 5.5 Summary & Conclusions

Very limited examples of effective approaches to separate fuel cell grade H<sub>2</sub> from low volumetric H<sub>2</sub> content H<sub>2</sub>/CH<sub>4</sub> blends (<20% volume H<sub>2</sub>) exist in the literature due to the challenging, stringent requirements for H<sub>2</sub> purity and the complexity that such a process would entail. EHP based separation potentially provides a simpler, single-stage approach to H<sub>2</sub> gas separation from these challenging mixtures. HT-PEM EHP based on PA-PBI proposed due to their lower humidification requirements, higher impurity tolerance due to high temperature operation, and lower gas permeability through the membrane phase for a higher purity product, compared to the more technologically mature LT-PEM EHP based on PFSA membrane materials e.g. Nafion®.

PA-PBI HT-PEM EHP based on conventional PBI imbibing process were studied and found to require some degree of humidification to perform well. Gas diffusion electrodes were prepared with hydrophobic PTFE binder based on Freudenberg H23C2 carbon paper GDL and compared to commercial De Nora carbon cloth based gas diffusion electrodes with a similar hydrophobic binder electrode composition.

The addition of phosphoric acid by drop-casting on the electrode surface prior to construction of the MEA was found to improve the HT-PEM EHP performance for both GDEs considered and the optimal amount of additional acid was identical. Initial performance improvement was attributed to improved membrane-electrode contact due to slight reductions in HFR and improved electrode performance through improvements in catalyst site availability and enhanced proton conductivity due to the higher phosphoric acid phase content. Further addition of acid leads eventually to continuing improvement in electrode kinetics but also an increase in voltage at higher current densities due to impeded reactant mass transport due to acid flooding.

H<sub>2</sub>/CH<sub>4</sub> blends down to 2% by volume H<sub>2</sub> were found to be viable, demonstrating the lowest concentration H<sub>2</sub>/CH<sub>4</sub> separation in EHP in literature to date. By elevating the cathode pressure above the anode pressure, co-compression of separated H<sub>2</sub> gas can be accomplished with very

little overpotential over the equal pressure separation case outside of conditions approaching Faradaic limiting currents where higher anode pressures have a strong effect by improving the diffusion limited reactant transport. Due to higher cathodic pressures, the purity of the H<sub>2</sub> gas on the cathode was improved appreciably by limiting pressure-driven transport of gaseous impurities such as CH<sub>4</sub> across the membrane, with H<sub>2</sub> purities exceeding 99.99% for a 2% by volume H<sub>2</sub> content inlet demonstrated. Separation efficiencies for 2% vol H<sub>2</sub> of 2-6 kWh/ kg H<sub>2</sub> for H<sub>2</sub>RF up to 50% were competitive with hybrid conventional gas separation systems proposed in the literature, and the HT-PEM EHP performance was comparable to LT-PEM EHP for 10 and 20% H<sub>2</sub>/CH<sub>4</sub> separation processes. Gas cross-over characterization of the HT-PEM MEA at operating conditions indicated comparable H<sub>2</sub> gas cross-over rates to Nafion® based systems and lower cross-over rates of CH<sub>4</sub>.

## Chapter 6      Operando X-Ray CT of PA-PBI based HT-PEM EHPs

X-ray imaging via synchrotron light source is a powerful diagnostic technique for studying the morphology of electrochemical cells during operation. Operando X-ray imaging in HT-PEM fuel cells has been deployed extensively to study the distribution of phosphoric acid throughout the MEA structure. Radiographic studies, where a time-series of 2-D images either in-plane or through-plane is gathered and the X-ray transmittance is analyzed, have been deployed on operando HT-PEMFC cells characterize the composition and distribution of phosphoric acid at varying current densities[178][179][180]. X-ray computed tomography (CT) generates three-dimensional volumes by reconstruction of 1000s of two-dimensional image slices taken via X-ray during the 180-degree rotation of a sample. This technique has been applied operando in HT-PEMFC to a limited extent to also quantify the distribution of phosphoric acid through the MEA as a function of current density[181][182][183][184], and is also employed ex-situ through sample preparation post-mortem [185].

In HT-PEMFC, phosphoric acid migration occurs by the carrying of a fraction of the protonic current by phosphoric acid anions,



as protons transport from anode to cathode proportional to the current density of the fuel cell, the small fraction of migration current carried by the phosphate anion results in a net migration of phosphoric acid to the anode. X-ray computed tomography of the anode GDL in operando HT-PEMFC shows a redistribution of phosphoric acid to the anode GDL and channels (Figure 6.1) [183].

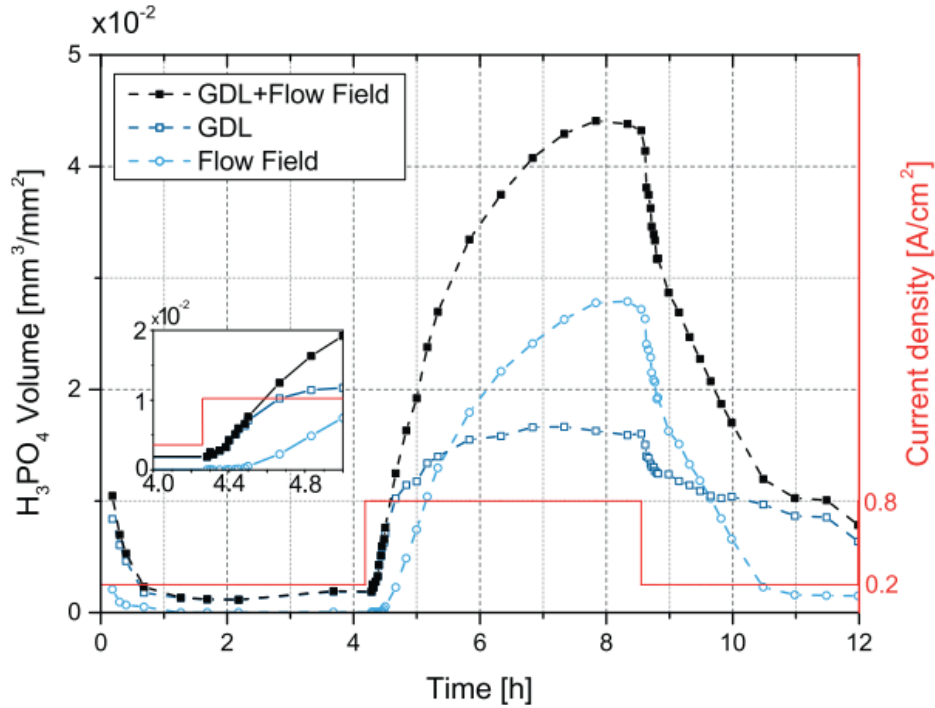


Figure 6.1 Re-distribution of phosphoric acid to the anode GDL/flow field in HT-PEMFC with increasing current density. Reproduced from [183].

X-ray CT was further utilized to quantify the transference number of the phosphate anions,  $t_{H_2PO_4^-}$ ,

$$t_{H_2PO_4^-} = \frac{i^-}{i^- + i^+} \quad (\text{Eq. 6-2})$$

And found it to be roughly on the order of  $10^{-3}$  to  $10^{-5}$  depending on the initial acid content of the MEA[181].

In HT-PEMFC, the water content of the hygroscopic phosphoric acid phase varies with current density due to generation of water as a result of the oxygen reduction reaction at the cathode. In radiographic studies, membrane swelling as a result of high current density operation was observed and correlated to water uptake[178], while in another X-ray CT study in similar conditions membrane thinning was observed[183]. The phase separation of water, phosphoric acid and carbon materials in X-ray imaging shows significant overlap making significant

quantification of the relative volumes of the three when all are present a difficult exercise from X-ray CT alone [182]. Given that increasing current densities in HT-PEMFC coincides with an increase in water content of the hygroscopic phosphoric acid phase, it is difficult to delineate the contributions of acid migration and water uptake to changes in the volume occupied by phosphoric acid in MEA.

In HT-PEM EHP, the water content of the phosphoric acid phase is independent of the current density, and instead relies on the introduction of external humidification of the anode and/or cathode feed gases. In this section, an operando X-Ray micro-CT cell for HT-PEM EHP operation is constructed and tested at synchrotron light source. MEAs with varying acid content are considered and the influence of current density and humidification of the cell on the microstructure in HT-PEM EHP operating conditions (160 °C) is studied.

## **6.1 Experimental Materials**

The design of the operando X-ray CT HT-PEM EHP hardware is derived from previous work of Zenyuk group at University of California, Irvine for the study of LT-PEM electrolyzer and fuel cells[186][187]. The end plates are constructed of aluminum, gaseous connections are made with stainless steel tube fittings, and two copper current collectors are mounted between the end plates and graphite flow fields. Four cartridge heaters are inserted into the cell to reach operating temperatures of 160 °C, with a thermocouple inserted into the top of the aluminum plate to control temperatures via PID. Graphite flow fields triple parallel channel configuration and with 1 x 1 mm channels.

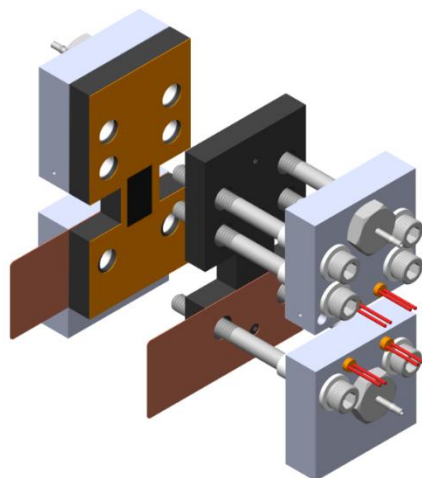


*Figure 6.2 HT-PEM EHP Operando cell hardware*

1 cm<sup>2</sup> membrane electrode assemblies were prepared with De Nora GDE following the procedure outlined in section 5.2.3. In brief, Fumapem AP-30 PBI membranes were doped in 85% wt ortho-phosphoric acid at room temperature overnight for 24 hours. De Nora gas diffusion electrodes (1 mg Pt cm<sup>-2</sup>) were drop-cast with varying amounts of phosphoric acid prior to MEA assembly. 220 μm PTFE gaskets limited the GDE compression to 50% thickness as was found to be optimal in 5 cm<sup>2</sup> cell testing. Table 6-1 describes the characteristics of the MEAs for the X-ray CT operando study.

*Table 6-1 MEA composition for operando HT-PEM EHP cells*

<b>MEA Composition Operando X-Ray Cells</b>	
Membrane	Fumapem AP-30
ADL [mol PA/mol PBI]	6.8 – 7.1
Electrode Acid Loading [mg PA cm <sup>-2</sup> ]	0, 20, 40
GDE	De Nora Carbon Cloth

The X-ray CT study was carried out at the Lawrence Berkeley National Laboratory (LBNL) Advanced Light Source (ALS) synchrotron facility beamline 8.3.2. The beamline is outfitted with a 50 μm LuAg:Ce scintillator, with 2x, 5x, 10x lenses, a double multilayer monochromator and a CSMOS PCO Edge camera. For the tests conducted, a 26 keV beam energy was used with 10x magnification resulting in a depth of field of 1.65 mm and voxel resolution of 0.65 μm. With these settings, 180 degree X-ray scans took approximately 6 minutes per scan.

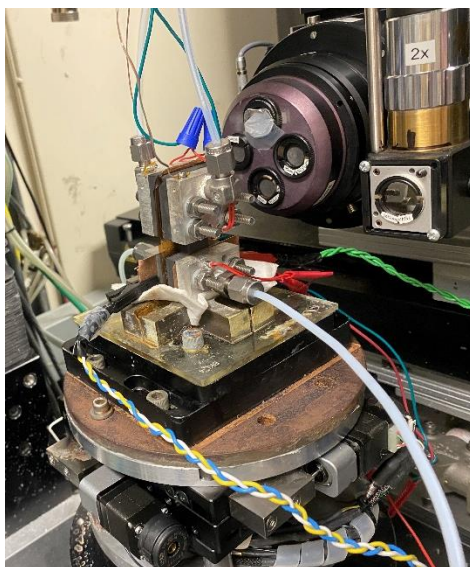


*Figure 6.3 Operando HT-PEM EHP cell mounted on X-ray CT stage at ALS beamline 8.3.2*

Figure 6.3 shows the HT-PEM EHP operando cell mounted on the beamline stage immediately prior to scanning. A Gamry 1000 potentiostat was used to carry out electrochemical measurements. Hydrogen gas was fed by needle valve to anode and cathode at 50 sccm, and during humidification the anode line was fed through a gas humidifier bottle with PID temperature controls. Great care was taken to arrange gas and electrical lines so that the cell could rotate freely during the 6 minute scan period.

## **6.2 Experimental Methods**

Operando cells were pre-conditioned before X-ray scanning by galvanostatic hold at  $0.2 \text{ A cm}^{-2}$  for 30 minutes at the given humidification condition to achieve equilibration, according to observed equilibration time for acid distribution in similar studies[184][180]. Following equilibration, polarization curve and electrochemical impedance spectroscopy were obtained. Operation in dry gas feed and with an anodic humidification of  $T_{\text{sat}} = 40 \text{ }^\circ\text{C}$  ( $P_v = 7.4 \text{ kPa}$ , Rel. Humidity = 1.2%) were carried out for each cell. For a given cell and humidification condition, the HT-PEM EHP was scanned in X-ray CT at open-circuit, and at galvanostatic holds of  $0.2$  and  $0.6 \text{ A cm}^{-2}$ .

### 6.3 Results & Discussion

Of the three cells brought to the beamline, the 0 mg PA cm<sup>-2</sup> and 20 mg PA cm<sup>-2</sup> electrode acid content cells were characterized and imaged due to time constraints. Figure 6.4 shows the polarization response of the two operando cells and compares them to the 5 cm<sup>2</sup> bench scale results in Chapter 5. The operando cell HT-PEM EHP successfully showed comparable polarization response to the 5 cm<sup>2</sup> bench hardware.

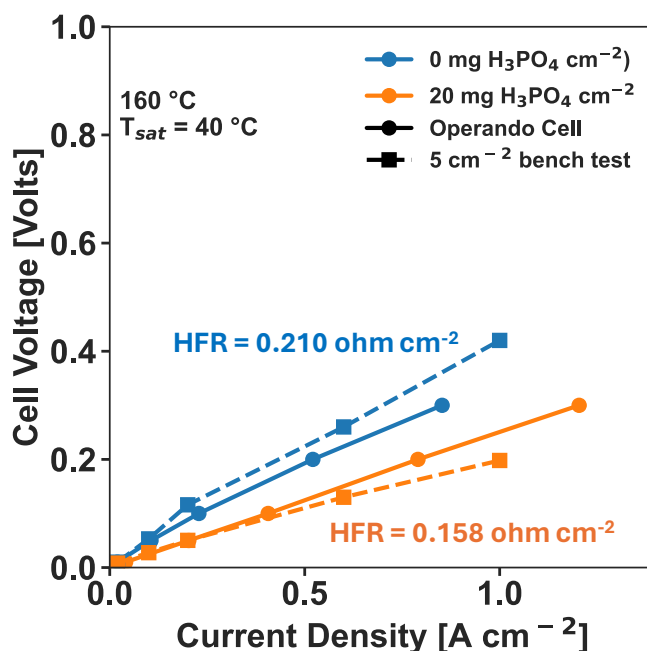


Figure 6.4 Polarization curves of operando HT-PEM EHP compared to 5 cm<sup>2</sup> MEA bench tests.

HFR measured from EIS at 0.02 A cm<sup>-2</sup> indicated that the HFR was slightly higher than the standard bench testing, which is less pronounced at the 0 mg PA cm<sup>-2</sup> condition where the operando cell polarization was slightly better. At low acid conditions the electrode impedance is a significant source loss and the influence of higher HFR is not as prominent.

Figure 6.5 shows a slice from the X-ray CT reconstruction of the HT-PEM EHP with 0 mg PA cm<sup>-2</sup> electrode content for both dry and then humidified operation. The separate phases of GDL, catalyst layer, membrane, channel, and porous graphite plates are readily visible. While some droplets of aqueous phosphoric acid are visible in the channel phases, the thresholding of phosphoric acid in the porous domains was not possible due to lack of contrast for the imaging conditions employed.



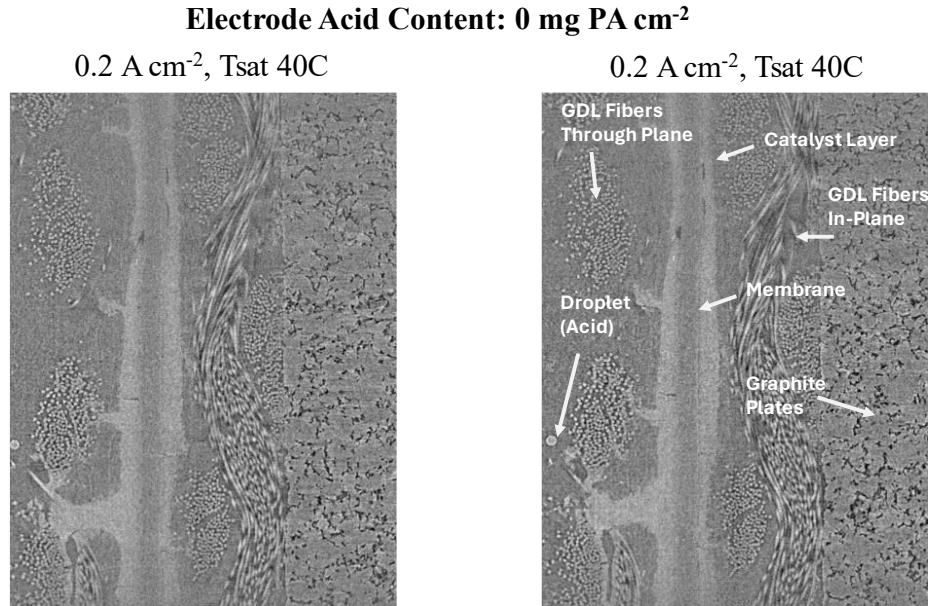


Figure 6.5 Representative slice of X-Ray CT reconstruction of HT-PEM EHP cell.

The membrane phase was thresholded for all scans to characterize the average thickness of the membrane in-situ with and without humidification and with respect to current applied. TABLE outlines the average through plane thickness of the membrane for the operating conditions scanned at. In conclusion, no appreciable swelling or thinning of the membrane phase was observed when going between dry and humid operation and for changing current densities as was observed in some cases for HT-PEMFC. The MEA with higher acid content in the electrodes did exhibit a slightly higher membrane thickness however the membrane thickness is within the range of observed ex-situ thickness for the Fumapem AP-30 membranes post PA-doping (~50 to 65 um).

Table 6-2 Membrane thickness of operando cell for varying operating conditions

<b>Membrane phase thickness [um]</b>				
Current Density [A cm <sup>-2</sup> ]	0 mg PA cm <sup>-2</sup>		20 mg PA cm <sup>-2</sup>	
	Dry	T <sub>sat</sub> = 40	Dry	T <sub>sat</sub> = 40
0	51	50	57	55
0.2	51	52	56	56
0.6	50	50	54	54

## 6.4 Summary & Conclusions

Hardware for the study of operando HT-PEM EHP based on PA-PBI was developed and successfully operated at HT-PEM EHP operating conditions (160 °C, humidified hydrogen gas feed) at a synchrotron light source. The performance of the operando cells was comparable to bench scale tests with commercial MEA cell fixtures using the same MEA materials.

Due to the very similar transmission characteristics of the carbon, phosphoric acid, and water present in the porous domains, the thresholding and quantification of phosphoric acid in these domains was not feasible for the images obtained. Some insight was gleaned into the membrane phase behavior in operando suggesting that the membrane does not swell appreciably during typical HT-PEM EHP operation by introduction of humidity.

## **Chapter 7      Two-Dimensional Model of PA-PBI based HT-PEM EHP for gas separation**

### **7.1 Introduction**

Physics based modelling of electrochemical cells is a useful tool for obtaining an intuitive understanding of the underlying processes governing cell performance. With this understanding obtained, models can be used to inform future cell design, optimize operating conditions, and integrate into system level models for testing out various scenarios. Furthermore, such models can be a useful tool for cutting down on the cost and time associated with continuous prototype development.

In HT-PEM based on PA-PBI, physical models have been used extensively in the study of HT-PEM fuel cells. At the cell level, simulations of HT-PEMFC have granted insight into kinetic limitations that plague performance such as the impacts of gas solubility in phosphoric acid on ORR kinetics [188][189][190][191][192] and the impact of CO co-adsorption from using reformat hydrogen gas [193][194][195][196]. Factors affecting the distribution of phosphoric acid throughout the cell and its impact on fuel cell performance have been addressed to a great extent in literature as well, such as cell compression [197][198] and varying acid content in MEA construction [199][200][191]

Of primary interest to HT-PEM EHP is a greater understanding of mass transport characteristics. Very few HT-PEM models attempt to implement gas cross-over through the membrane phase [201], as it is generally low in the PA-PBI phase, or to describe water uptake and transport through the membrane phase [202][203], both crucial parameters for obtaining high purity hydrogen product in the HT-PEM EHP. Furthermore, the distribution of and composition of phosphoric acid in HT-PEM EHP likely differs from HT-PEM fuel cell. In HT-PEM EHP water is introduced solely through the humidification of a gas stream and then transported to the electrolyte phase at the anode, rather than being generated within the cathode as in HT-PEM fuel cell. This leads to greater water contents at the outlet of the HT-PEMFC, with decreasing  $\text{H}_3\text{PO}_4$  concentration at higher currents as more water is generated. The distribution and composition of

phosphoric acid in the cell affects the kinetic performance, the local conductivity of the electrode and membrane phases, and the mass transport characteristics of the porous domains. These effects have been captured by physical simulation of HT-PEM fuel cell, but not in HT-PEM EHP which generally lacks in simulation based studies.

## **7.2 Modelling Methodology and Description**

The model in this work is developed to capture the performance of the HT-PEM EHP for separation of low percentage hydrogen volumes blended in methane. For modelling of HT-PEM EHP for gas separation applications, a 2-D ‘along-the-channel’ geometry is considered with separate domains for channel (CHN), gas diffusion layer (GDL), catalyst layer (CL), and membrane phases (MEM) (Figure 7.1). The along-the channel geometry allowed for mass transport losses associated with reactant depletion in low hydrogen concentration feeds to be considered. The physics of the model is implemented in COMSOL Multiphysics (version 5.6), with Matlab® implemented for iterating over parametric sweeps and post-processing of the model outputs through Matlab®.

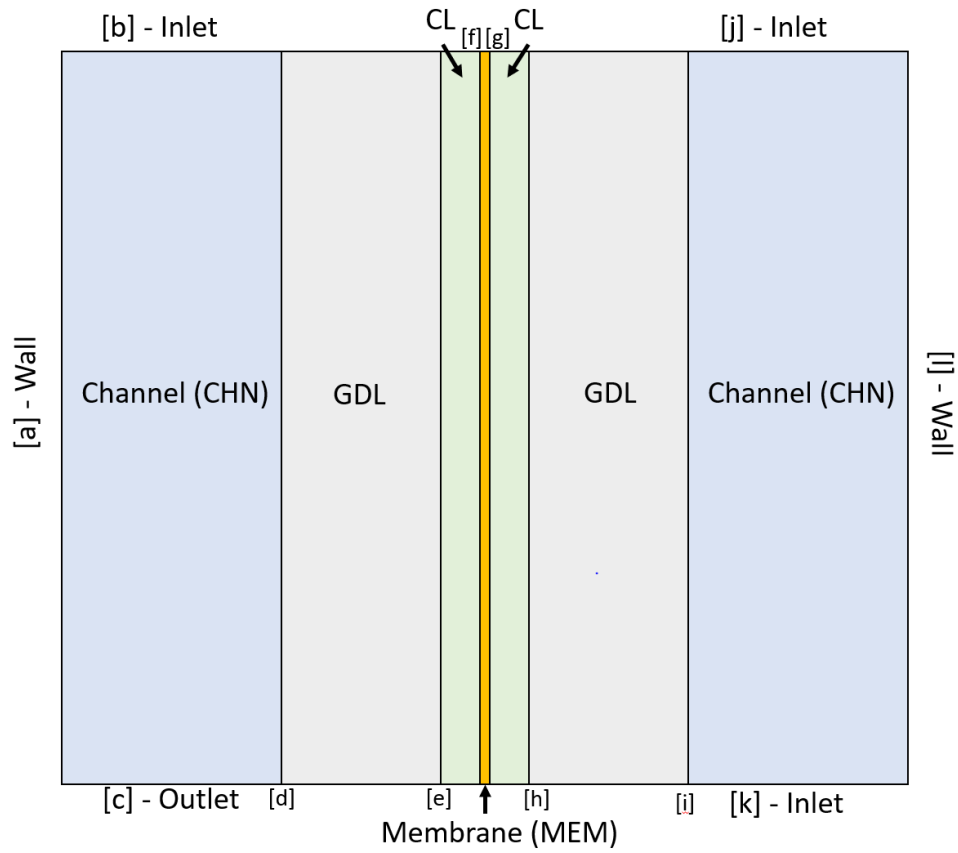


*Figure 7.1 HT-PEM EHP model geometry and domains*

The EHC model is governed by several equations including conservation of energy, mass, ionic charge, and electronic charge. These relations and their corresponding domains in the model are outlined in Table 7-1.

Table 7-1 Governing equations of HT-PEM EHP model by domain

Governing Equations of Model by Domain			
Variable	Governing Equation	Domain	
Gas Pressure	$\nabla p = \nabla \cdot \left[ \mu(\nabla \mathbf{u} + (\nabla \mathbf{u})^T) - \frac{2}{3} \mu(\nabla \cdot \mathbf{u}) \mathbf{I} \right]$	CHN	(Eq. 7-1)
Gas Pressure	$\mathbf{u} = -\frac{\kappa}{\mu} \nabla p$	GDL, CL	(Eq. 7-2)
Gas Flux	$\nabla \cdot (\rho \mathbf{u}) = Q_m$	CHN, GDL, CL	(Eq. 7-3)
Gas Mass Fraction	$\nabla \cdot \left( -\rho \omega_i \sum_k D_{ik,eff} (\nabla x_k + \frac{1}{p} (x_k - \omega_k) \nabla p) \right) + \rho \omega_k \mathbf{u} = R_i$	CHN, GDL, CL	(Eq. 7-4)
Phosphoric Acid Mass Fraction	$\rho \omega_i \sum_k D_{ik} \nabla x_k = R_i$	CL, MEM	(Eq. 7-5)
Ionic Current	$\nabla i_2 = i_{rxn}$	CL, MEM	(Eq. 7-6)
Ionic Potential	$i_2 = -\sigma_{eff,2} \nabla \Phi_2$	CL, MEM	(Eq. 7-7)
Electronic Current	$\nabla i_1 = -i_{rxn}$	GDL, CL	(Eq. 7-8)
Electric Potential	$i_1 = -\sigma_{eff,1} \nabla \Phi_1$	GDL, CL	(Eq. 7-9)
Temperature	$\rho \mathbf{u} C_p \nabla T - k_{eff} \nabla \cdot (\nabla T) = Q$	CHN, GDL, CL, MEM	(Eq. 7-10)

### 7.2.1 Gaseous Species Transport

Gaseous species in the channel domains are governed by the conservation of momentum ((Eq. 7-1) and conservation of mass (Eq. 7-3) for laminar flow as defined by Navier-Stokes equations. Gaseous mixtures are assumed to follow ideal gas behavior and mixture physical properties such as viscosity and diffusivity were assumed to follow Lennard-Jones mixture behaviors based on kinetic theory of gases. Velocity in the x- and z- directions were assumed to be negligible relative to the y-direction flow.

$$\nabla p = \nabla \cdot \left[ \mu(\nabla \mathbf{u} + (\nabla \mathbf{u})^T) - \frac{2}{3} \mu(\nabla \cdot \mathbf{u}) \mathbf{I} \right] \quad (\text{Eq. 7-1})$$

$$\nabla \cdot (\rho \mathbf{u}) = Q_m \quad (\text{Eq. 7-3})$$

Conservation of momentum for Newtonian fluid with no forcing term determines the pressure gradient  $\nabla p$  according to the cross-section averaged velocity,  $\nabla \mathbf{u}$ , and the dynamic viscosity  $\mu$ . For the conditions in the HT-PEM EHP, the density of the gas phase,  $\rho$  is well described by the ideal gas law. Dynamic viscosity for a three-gas mixture system was determined by approximation based on kinetic theory of gases [204],

$$\phi_{12} = \left(\frac{1}{8}\right)^{\frac{1}{2}} \left(1 + \frac{M_1}{M_2}\right)^{-\frac{1}{2}} \left(1 + \left(\frac{\mu_1}{\mu_2}\right)^{\frac{1}{2}} \left(\frac{M_2}{M_1}\right)^{\frac{1}{4}}\right)^2 \quad (\text{Eq. 7-11})$$

$$\mu = \frac{x_1 \mu_1}{x_1 + \phi_{1-2} x_2 + \phi_{1-3} x_3 + \dots} + \frac{x_2 \mu_2}{x_2 + \phi_{1-2} x_1 + \phi_{2-3} x_3 + \dots} \quad (\text{Eq. 7-12})$$

Where  $\phi$  is a dimensionless quantity calculated from the constituents of the binary gas pair molecular weight  $M$ , and the pure gas phase dynamic viscosity (Table 7-2).

Table 7-2. Dynamic viscosities of gaseous components

Pure Gas Viscosity			
Viscosity	H <sub>2</sub>	CH <sub>4</sub>	H <sub>2</sub> O(v)
$\mu$ [uPa s]	8.39	11.13	8.02

In the porous domains of the GDL and CL, convective mass flux is governed by Darcy's Law and conservation of mass,

$$\mathbf{u} = -\frac{\kappa}{\mu} \nabla p \quad (\text{Eq. 7-2})$$

$$\nabla \cdot (\rho \mathbf{u}) = Q_m \quad (\text{Eq. 7-3})$$

Where  $\kappa$  is the absolute permeability of the porous media, described by a Carman-Kozeny permeability model which correlates the absolute permeability to the representative diameter  $d_{CK}$  of a overlapping fiber in a porous packed structure of randomly overlapping rod like structures and the total porosity of the structure,  $\varepsilon$  [205][206]. The empirical constant  $k_{CK}$  is not easily derived as it varies strongly with the geometry of the flow paths, with values here taken from literature on carbon cloth type GDL permeability[207] and Pt/C electrode structures[208]. In this case  $d_{CK}$  is correlated instead to the characteristic pore size of the associated porous subdomain as described in the dissertation work of Balliet[209].

$$\kappa = \frac{d_{CK}^2 \varepsilon^3}{16k_{CK}(1 - \varepsilon^2)} \quad (\text{Eq. 7-2})$$

Table 7-3 lists the values employed for the characteristic diameter  $d_{CK}$  and the porosity values, noting that the porosity in the catalyst layer is a function of phosphoric acid volume fraction,  $\phi_{PA-H2O,CL}$  as outlined further in section 7.2.4

*Table 7-3 Carmen-Kozeny parameter values for permeability coefficient calculation in Darcy's Law*

Parameter	GDL	CL
Diameter, $d_{CK}$	2.5	0.5 [208]
Constant, $k_{CK}$	1 [207]	10 [208]
Porosity, $\varepsilon$	0.65	$0.5 - \phi_{PA-H2O,CL}$

Diffusive mass transport occurs in all gas species domains (channel, GDL and CL) and is described by the combination of conservation of species from the Stefan-Maxwell equation (first term on the left-hand side of (Eq. 7-4)) and the conservation of mass (second term on the left-hand side of (Eq. 7-4)) where  $\omega_k$  and  $x_k$  are the mass and mol fraction of a gas component  $k$ , and  $\omega_i$  is the mass fraction of the gas species  $i$ , in question.



$$\nabla \cdot \left( -\rho \omega_i \sum_k D_{ik,eff} (\nabla x_k + \frac{1}{p} (-\omega_k) \nabla p) \right) + \rho \omega_i \mathbf{u} = R_i \quad (\text{Eq. 7-4})$$

The effective binary diffusion coefficient,  $D_{ik,eff}$ , is obtained by the Bruggeman approach to from the Stefan-Maxwell binary diffusion coefficients.

$$p D_{ik,eff} = \varepsilon^{3/2} D_{ik} \quad (\text{Eq. 7-13})$$

The binary diffusion coefficients,  $D_{ik}$ , for a three component gas system  $i$ ,  $k$ , and  $j$  are tabulated according to methods described in Bird et al. [210], where the diffusion coefficient  $D_{ik}$  has to be related to the Stefan-Maxwell binary diffusion coefficients  $\mathfrak{D}_{ik}$  due to the form of (Eq. 7-4).

$$D_{ik} = \frac{\frac{\omega_i(\omega_k + \omega_j)}{x_i \mathfrak{D}_{kj}} + \frac{\omega_k(\omega_i + \omega_j)}{x_k \mathfrak{D}_{ij}} - \frac{\omega_j^2}{x_j \mathfrak{D}_{ik}}}{\frac{x_i}{\mathfrak{D}_{ik} \mathfrak{D}_{ij}} + \frac{x_k}{\mathfrak{D}_{ik} \mathfrak{D}_{kj}} + \frac{x_j}{\mathfrak{D}_{ij} \mathfrak{D}_{kj}}} \quad (\text{Eq. 7-14})$$

The Stefan-Maxwell binary diffusion coefficients are determined from kinetic theory of gases assuming ideal gas behavior of the mixture,

$$p \mathfrak{D}_{ik} = 0.001853 \sqrt{T^3 \left( \frac{1}{M_i} + \frac{1}{M_k} \right) \frac{1}{\sigma_{ik}^2 \Omega_{\mathfrak{D},ik}}} \quad (\text{Eq. 7-15})$$

Where the parameter  $\sigma_{ik}$  represents the binary collision diameter from Chapman-Enskog kinetic theory for ideal gases estimated from,

$$\sigma_{ik} = \frac{1}{2} (\sigma_i + \sigma_k) \quad (\text{Eq. 7-16})$$

The collision integral for diffusivity,  $\Omega_{\mathfrak{D},ik}$ , is adapted from curve fitting in [211], as a function of the reduced temperature  $T_r$ ,

$$T_r = \frac{k_B T}{\epsilon_{ik}} \quad (\text{Eq. 7-17})$$

$$\Omega_{\mathcal{D},ik} = \frac{1.06036}{T_r^{0.15610}} + \frac{0.19300}{\exp(0.4763T_r)} + \frac{1.03587}{\exp(1.52996T_r)} + \frac{1.76474}{\exp(3.89411T_r)} \quad (\text{Eq. 7-18})$$

Where  $k_B$  is the Boltzmann constant and  $\epsilon_{ik}$  is characteristic energy of the Lennard-Jones parameters calculating by mixing rule,

$$\epsilon_{ik} = \sqrt{\epsilon_i + \epsilon_k} \quad (\text{Eq. 7-19})$$

Table 7-4 lists the relations for the binary diffusion coefficients implemented in the model as a empirical curve fitting by power rule for simplicity of implementation of the values derived by the method outlined above.

*Table 7-4 Binary diffusion coefficient of gaseous species correlation implemented in HT-PEM EHP model.*

Model implementation of binary diffusion coefficients	
Binary Gas Pair	$p\mathcal{D}_{ik}$ [bar cm <sup>2</sup> sec <sup>-1</sup> ]
H2-CH4	$0.001037T^{1.65639}$
H2-H2O	$0.0000797T^{1.656107}$
CH4-H2O	$0.0000357T^{1.656994}$

Boundary conditions are set at the anode and cathode inlet for gas pressure and velocity as well as the mass fractions of gaseous species H<sub>2</sub>, CH<sub>4</sub>, and water vapor, v, (Table 7-5).

*Table 7-5 Gaseous Species Transport Boundary and Initial Conditions.*

Boundary and Initial Conditions for Gaseous Species Transport			
Equation	Boundary Condition	Boundary	Initial Condition
(Eq. 7-1 Eq. 7-2)	$P = P_{outlet}$	[c] & [k] (Channel Outlet)	$P = P_{outlet}$
(Eq. 7-1 Eq. 7-2)	$\mathbf{u} = \frac{1}{A_{CHN}} \frac{\dot{n}RT}{P}$	[b] & [j] (Channel Inlet)	$\mathbf{u} = \frac{1}{A_{CHN}} \frac{\dot{n}RT}{P}$
(Eq. 7-1 Eq. 7-2)	No-Slip	[a] & [l] (Channel Wall) [d] & [i] (GDL/CHN interface)	
(Eq. 7-3)	$P = P_{[d], P_{[i]}}$	[d] & [i] (GDL/CHN interface)	$P = P_{outlet}$

(Eq. 7-3)	No Flow	[e] & [h] (CL/CHN interface)	
(Eq. 7-4)	$\omega_{CH_4} = \frac{M_{CH_4}[x_{CH_4,dry}(1 - \omega_v)]}{\sum_i M_i x_{i,init}}$	[b] & [j] (Channel Inlet)	$\omega_{CH_4} = \frac{M_{CH_4}[x_{CH_4,dry}(1 - \omega_v)]}{\sum_i M_i x_{i,init}}$
(Eq. 7-4)	$\omega_v = \frac{M_v \frac{P_{sat}}{P} RH_{init}}{\sum_i M_i x_{i,init}}$	[b] & [j] (Channel Inlet)	$\omega_v = \frac{M_v \frac{P_{sat}}{P} RH_{init}}{\sum_i M_i x_{i,init}}$
(Eq. 7-4)	$\omega_{H_2} = 1 - \omega_{CH_4} - \omega_v$	[b] & [j] (Channel Inlet)	$\omega_{H_2} = 1 - \omega_{CH_4} - \omega_v$

$\omega_{CH_4}$  is set as a model input on dry molar basis  $x_{CH_4,dry}$  and water vapor mass fraction,  $\omega_v$ , is initialized from relative humidity,  $RH_{init}$ , and the gaseous mass fractions are bounded by unity condition, and this is used to solve for  $\omega_{H_2}$ ,

$$\omega_{CH_4} = \frac{M_{CH_4}[x_{CH_4,dry}(1 - \omega_v)]}{\sum_i M_i x_{i,init}} \quad (Eq. 7-20)$$

$$\omega_v = \frac{M_v \frac{P_{sat}}{P} RH_{init}}{\sum_i M_i x_{i,init}} \quad (Eq. 7-21)$$

$$\omega_{H_2} = 1 - \omega_{CH_4} - \omega_v \quad (Eq. 7-22)$$

Gas velocity,  $u$ , is calculated from a defined molar flow rate  $\dot{n}$  and divided by channel cross-sectional area to define the average gas velocity.

$$\mathbf{u} = \frac{1}{A_{CHN}} \frac{\dot{n}RT}{P} \quad (Eq. 7-23)$$

Channel outlets are defined for pressure to match with controlled backpressure in experiments. Initial conditions reflect inlet & outlet boundary conditions. No-slip conditions are applied for Navier-Stokes equations at the channel wall and GDL boundary. The pressure calculated in the channels provides the initial condition and as well as the boundary condition at the channel + GDL interface for Darcy's Law in the GDL and CL, with a no flow condition applied at all other boundaries of the GDL+CL phase.

Source terms appear in both conservation of mass in the form of  $Q_m$  and conservation of species as  $R_i$ . In the channel and gas diffusion layer, no mass sources exist and thus the source terms are only relevant in the catalyst layer phase. Table 7-6 shows the value of source terms for these two equations in the catalyst layer.

Table 7-6 Source terms for gaseous species transport equations in the catalyst layer

Source terms of gaseous species transport equations in CL	
Equation	Source Terms
(Eq. 7-4)	$R_{H_2} = \dot{m}_{rxn} + \dot{m}_{H_2,cross}$
(Eq. 7-4)	$R_{CH_4} = \dot{m}_{CH_4,cross}$
(Eq. 7-4)	$R_v = \dot{m}_{evap}$
(Eq. 7-2)	$Q_m = \dot{m}_{rxn} + \dot{m}_{H_2,cross} + \dot{m}_{CH_4,cross} + \dot{m}_{evap}$

Hydrogen gas is generated at the cathode and consumed at the anode due to hydrogen evolution (HER) and hydrogen oxidation (HOR) reactions respectively, which is described by the  $\dot{m}_{rxn}$  term,

$$\dot{m}_{rxn} = \frac{M_{H_2} i_{rxn}}{nF} \quad (Eq. 7-24)$$

Where  $n$  is the mol of electrons,  $e^-$ , that participate in the electrochemical reaction,  $F$  is Faraday's constant of  $96485 \text{ C mol}^{-1}$ , and  $i_{rxn}$  is the current density in  $\text{A cm}^{-2}$  associated with the rate of reaction.

Water vapor enters and leaves the aqueous phosphoric acid phase in the catalyst layer and membrane domains and is accounted for by the  $\dot{m}_{evap}$  term, which is further elucidated on in section 7.2.4 .

Cross-over of gaseous species occurs through the membrane phase and is implemented here as a local source/sink term in the catalyst layer phase,  $\dot{m}_{H_2,cross}$  for each gaseous species,

$$\text{Anode: } \dot{m}_{CH_4, cross} = \varepsilon_{diff, CH_4} M_{CH_4} \frac{P_{c, CH_4} - P_{a, CH_4}}{t_{mem}} + \varepsilon_{dp, CH_4} M_{CH_4} \frac{P_c - P_a}{t_{mem}} \quad (\text{Eq. 7-25})$$

$$\text{Cathode: } \dot{m}_{CH_4, cross} = -\varepsilon_{diff, CH_4} M_{CH_4} \frac{P_{c, CH_4} - P_{a, CH_4}}{t_{mem}} - \varepsilon_{dp, CH_4} M_{CH_4} \frac{P_c - P_a}{t_{mem}} \quad (\text{Eq. 7-26})$$

$$\text{Anode: } \dot{n}_{H_2, cross} = \varepsilon_{diff, H_2} M_{H_2} \frac{P_{c, H_2} - P_{a, H_2}}{t_{mem}} + \varepsilon_{dp, H_2} M_{H_2} \frac{P_c - P_a}{t_{mem}} \quad (\text{Eq. 7-27})$$

$$\text{Cathode: } \dot{n}_{H_2, cross} = -\varepsilon_{diff, H_2} M_{H_2} \frac{P_{c, H_2} - P_{a, H_2}}{t_{mem}} - \varepsilon_{dp, H_2} M_{H_2} \frac{P_c - P_a}{t_{mem}} \quad (\text{Eq. 7-28})$$

Where the cross-over rate is described as a net flux contribution of convective transport and diffusive transport[166] due to Fick's Law (diffusive) and Darcy's Law (convective, porous media) fluid flow and the permeability coefficients  $\varepsilon_{diff}$  and  $\varepsilon_{dp}$  are taken from permeability measurements from the HT-PEM EHP for operating conditions of 160 °C and humidity of 1.2%. Net cross-over rates are bound to be non-negative. Transport of water vapor membrane is assumed to be negligible and instead the dominant mode of water transport is considered as diffusive transport of condensed water in the aqueous phosphoric acid phase.

*Table 7-7 Permeability coefficients for gaseous species cross-over*

Permeability Coefficients of H <sub>2</sub> and CH <sub>4</sub> in PA-PBI HT-PEM EHP		
	H <sub>2</sub>	CH <sub>4</sub>
$\varepsilon_{diff}$ [mol/cm/s/pa]	8.28E-17	1.91E-17
$\varepsilon_{conv}$ [mol/cm/s/pa]	1.87E-16	9.24E-17

## 7.2.2 Conservation of Electronic Charge

Transport of electrons is described by the conservation of charge according to,

$$\nabla i_1 = -i_{rxn} \quad (\text{Eq. 7-8})$$

The electron current density  $i_1$  is a function of the electronic potential  $\Phi_1$  and the effective electron conductivity  $\sigma_{eff,1}$ .

$$i_1 = -\sigma_{eff,1} \nabla \Phi_1 \quad (Eq. 7-8)$$

The value of  $\sigma_{eff,1}$  is a function of the material electron conductivity  $\sigma_1$  and the volumetric content of the solid phase of the domain  $\phi_s$  with Bruggeman coefficient correction factor.

$$\sigma_{eff,1} = \sigma_1 \phi_s^{3/2} \quad (Eq. 7-8)$$

Electron conducting phases include the carbon materials in the GDL and CL phases, and the boundary and initial conditions for conservation of electronic charge varies depending on if the HT-PEM EHP is operated in a potentiostatic (constant potential) or galvanostatic (constant potential) mode. Table 7-8 lists boundary and initial conditions for potentiostatic conditions deployed in this chapter.

*Table 7-8 Potentiostatic boundary and initial conditions for conservation of electrons*

Boundary and Initial Conditions for Cons. Of Electronic Charge			
Boundary Condition	Boundary	Initial Condition	Domain
$\Phi_1 = E_{app}$	[d] (Anode CHN/GDL interface)	$\Phi_1 = E_{app}$	Anode GDL, CL
$\Phi_1 = 0$	[i] (Cathode CHN/GDL interface)	$\Phi_1 = 0$	Anode GDL, CL
No Flux	[f] & [g] (GDL/membrane interface)		

Sources and sinks of electronic current occur solely in the catalyst layer due to the electrochemical reactions described by Butler-Volmer equation (see section 7.2.5 )

*Table 7-9 Source terms for conservation of electrons*

Source terms for conservation of electrons	
Domain	Source Terms
GDL	$i_{rxn} = 0$
(Eq. 7-4 CL	$i_{rxn} = i_{HOR}$
Cathode CL	$i_{rxn} = i_{HER}$

### 7.2.3 Conservation of Protons

Conservation of protons solves for the ionic current density  $i_2$ ,

$$\nabla i_2 = i_{rxn} \quad (Eq. 7-6)$$

Proton conducting phases consist of the aqueous phosphoric acid phase present in the catalyst layer subdomain as well as the phosphoric acid doped PBI in the membrane subdomain. Ionic potential is calculated as,

$$i_2 = -\sigma_{eff,2} \nabla \Phi_2 \quad (Eq. 7-8)$$

Where the effective conductivity  $-\sigma_{eff,2}$  is a function of the conductivity of the pure aqueous phosphoric acid (PA-H<sub>2</sub>O) phase and the volume fraction of the PA-H<sub>2</sub>O phase in the domain.

For the membrane this equation takes the form,

$$\sigma_{eff,2,mem} = 0.42 \sigma_{PA} \phi_{PA,mem}^{2.1} \quad (Eq. 7-29)$$

Where  $\sigma_{PA}$  is the conductivity of pure aqueous phosphoric acid phase, and  $\phi_{PA,mem}$  is the volume fraction of phosphoric acid in the PBI membrane,

$$\phi_{PA,mem} = \frac{(ADL_{PA} - 1.25)V_{m,PA}}{(ADL_{PA}V_{m,PA}) + V_{m,PBI}} \quad (Eq. 7-30)$$

The acid doping level,  $ADL_{PA}$ , is a consequence of the temperature and duration of the phosphoric acid membrane doping process[114] and is the ratio of mol of PA to mol of PBI polymer repeating unit (RPU).  $ADL$  is calculated from gravimetric measurements pre and post membrane doping process.  $V_m$  is the molar volume of phosphoric acid and PBI polymer.

In the catalyst layer, a Bruggeman equation corrected conductivity is employed,

$$(Eq. 7-31)$$

Where the phosphoric acid volume  $\phi_{PA,CL}$  can vary during operation and is expanded upon in section 7.2.4 – see (Eq. 7-35).

The conductivity of PA doped PBI membranes display a dependence on temperature, relative humidity, and the  $ADL$  of the membrane [112][167][203]. The conductivity of pure aqueous phosphoric acid  $\sigma_{PA}$  depends strongly on the temperature and water content [212]. Pure aqueous phosphoric acid conductivity has been tabulated by a number of studies in good agreement as a

function of the %wt of ortho-phosphoric acid and temperature[212][213][214]. In the high temperature and dry operating conditions, bulk aqueous phosphoric can exceed 100% wt H<sub>3</sub>PO<sub>4</sub> basis due to the generation of and subsequent loss of water from H<sub>3</sub>PO<sub>4</sub> species after the free water has largely evaporated out[163].

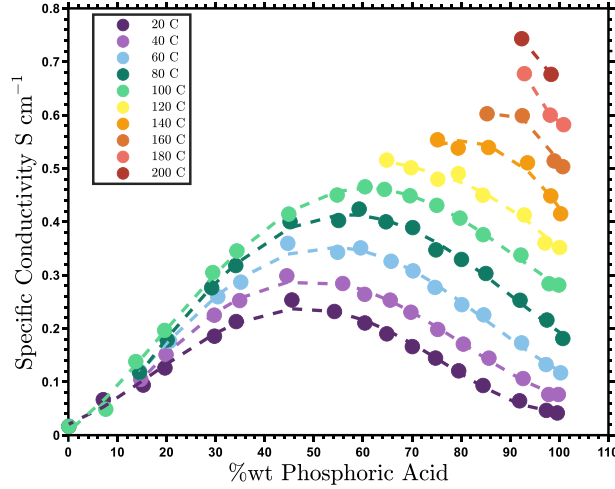


Figure 7.2 Conductivity of aqueous phosphoric acid as function of temperature and %wt H<sub>3</sub>PO<sub>4</sub>. Reproduced from [212]

PA-PBI based HT-PEMFC and EHP operate at high temperatures in the range of 150-170 °C at dry or low humidity conditions where phosphoric acid anhydrides can form with lower proton conductivity than ortho-phosphoric (H<sub>3</sub>PO<sub>4</sub>) and water systems. Due to water replacement degradation of phosphoric acid in the PBI membranes, high humidification operation is not viable in HT-PEM and as such the % wt H<sub>3</sub>PO<sub>4</sub> at 160 °C is typically greater than 95% such that the proton conductivity of pure phosphoric acid is roughly 0.5 – 0.6 S cm<sup>-1</sup> and in PA-PBI membrane the conductivity is roughly one order of magnitude lower typically.

Data from Chin & Chang was curve fitted to generate an empirical description of  $\sigma_{PA}$  for implementation in the COMSOL model,

$$\sigma_{PA} = aT + b \quad (Eq. 7-32)$$

$$a = -0.0426\omega_{PA}^3 + 0.0972\omega_{PA}^2 - 0.0718\omega_{PA} + 0.0208 \quad (Eq. 7-33)$$

$$b = -0.6305\omega_{PA} - 0.4647 \quad (Eq. 7-34)$$



The boundary and initial conditions for (Eq. 7-6 & (Eq. 7-8 consist of no flux at the GDL boundaries and a null initial condition for ionic potential across CL and membrane domains (Table 7-10). Source and sink of ionic current occurs due to electrochemical reactions HOR and as shown in Table 7-11.

*Table 7-10 Boundary and Initial conditions for conservation of ionic current*

<b>Boundary and Initial Conditions for Cons. Of Protonic Charge</b>			
<b>Boundary Condition</b>	<b>Boundary</b>	<b>Initial Condition</b>	<b>Domain</b>
No Flux	[e] & [h] (GDL/CL interface)	$\Phi_2 = 0$	CL, MEM

*Table 7-11 Source and sink terms for conservation of ionic current.*

<b>Source terms for conservation of electrons</b>	
<b>Domain</b>	<b>Source Terms</b>
MEM	$i_{rxn} = 0$
(Eq. 7-4 CL	$i_{rxn} = i_{HOR}$
Cathode CL	$i_{rxn} = i_{HER}$

#### 7.2.4 Aqueous Phosphoric Acid Phase

A liquid phase consisting of water and phosphoric acid is present in the membrane and catalyst layer. The PBI membrane is doped to a high degree of phosphoric acid content that contains free acid, and in some cases phosphoric acid is also added to the catalyst layer prior to assembly to enhance the proton conducting pathways from electrodes to membrane phase. During operation of the EHP the density of the aqueous phosphoric acid phase changes with varying temperature and water content. This phenomenon contributes to a transfer of phosphoric acid between the highly imbibed PBI membrane and the catalyst layer. Additionally, some migration occurs in the form of phosphate anions ( $H_2PO_4^-$ ) which forms  $H_3PO_4$  at the anode in increasing amounts proportional to the current, although the overall magnitude of this anion current is typically <0.01% of the total ionic current[181].

The volume fraction of phosphoric acid in the catalyst layer can vary significantly as a function of the initial acid content  $m_{PA,CL}$  in  $mg\ PA\ cm^{-2}$ , and the transfer of acid between catalyst and membrane phase due to changes in density of the phosphoric acid phase,  $\Delta m_{PA-H_2O,mem}$ ,

$$\phi_{PA,CL} = \frac{0.2m_{PA,CL} + 0.5\Delta m_{PA,mem}}{\rho_{PA}\omega_{PA}V_{CL}} \quad (Eq. 7-35)$$

$$\Delta m_{PA,mem} = \Delta(\rho_{PA}\omega_{PA})V_{mem}\phi_{PA,mem} \quad (Eq. 7-36)$$

Where the 0.5 in front of the  $\Delta m_{PA,mem}$  term reflects a symmetric movement of PA expanded out of the membrane into anode and cathode. The 0.2 term preceding  $m_{PA,CL}$  is a fitting term for the amount of acid that is transferred from the electrode surface into the catalyst layer pores upon assembly as described in 5.2.3 , rather than the majority of acid that is squeezed through the sides of the MEA into the gaskets or through the CL and entering the GDL and channels.

Phosphoric acid loss by evaporation is assumed to be negligible due to the low phosphoric acid vapor pressure for the temperatures considered[213][215]. In addition, it is assumed that the membrane phase does not increase in thickness or swell in volume during operation of the EHP. Previously it has been observed that water absorption into the doped PBI membranes, for the regime of humidity encountered in this study, does not lead to observable swelling in the operando CT operation (section 6.3 ) and in previous studies on water absorption of PA-doped PBI membranes[167].

The flux of liquid water through the aqueous phosphoric acid phase in the catalyst layer and membrane is of interest to describe the net water transport from the humidified anode to the cathode side where a dry H<sub>2</sub> gas product is desirable. There exist some numerical studies of HT-PEMFC that incorporate membrane water transport, however all vary widely in implementation either through permeation transport of the water vapor through empirical fitting[163][216][202] while another did employ diffusive transport of liquid water but with a ‘fictitious’ diffusivity coefficient[203].

The diffusion transport of liquid phase phosphoric acid and water species is implemented in the model by conservation of species using Fick’s 1<sup>st</sup> law,

$$\rho\omega_i \sum_k D_{ik} \nabla x_k = R_i \quad ((Eq. 7-5))$$

In an analysis by Lang et al. [217] experimental measurements of  $D_{H_2O-PA}$  demonstrated the fitting of Wilke and Chang's [218] correlation for diffusion coefficients in dilute solutions to their own measurements of  $D_{H_2O-PA}$  as well as other studies' [219][220] (Figure 7.3).

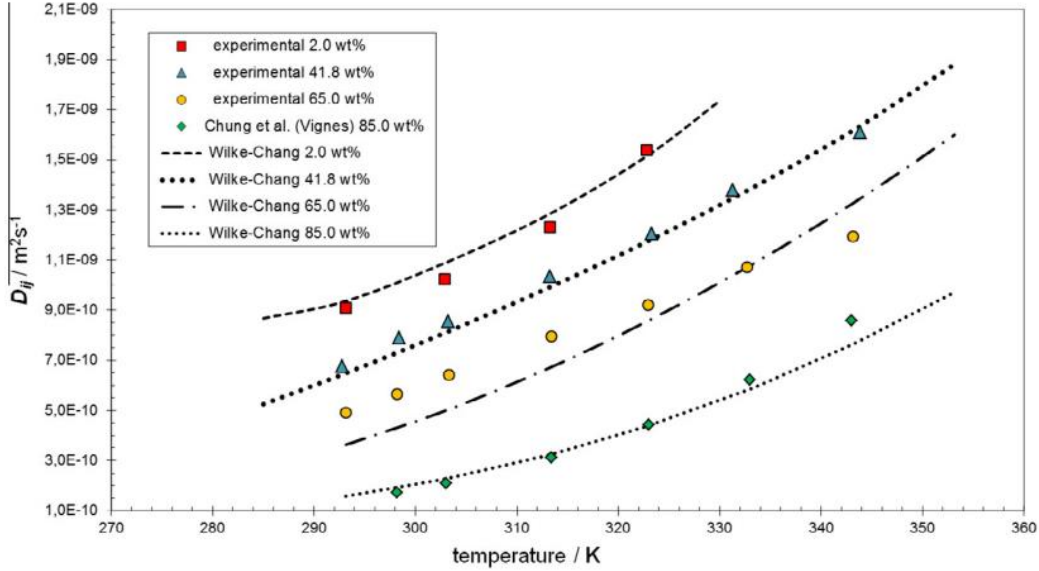


Figure 7.3 Experimental measurements of binary diffusion coefficients of pure  $H_2O$ -Phosphoric Acid. Reproduced from [217]

The Wilke-Chang correlation for estimating the diffusion coefficient is,

$$D_{H_2O-PA} = 7.4 \times 10^{-8} \frac{(\Phi M_{H_2O-PA})^{0.5} T}{\eta V_{PA}} \quad (Eq. 7-37)$$

Where  $M_{H_2O-PA}$  is the mean molecular weight of the mixture,  $\Phi$  is an association factor obtained from fitting to experiments,  $\eta$  is the mixture dynamic viscosity and  $V_{PA}$  is the molar volume of phosphoric acid. Plugging in the fitting values from [217] and using dynamic viscosity measurements of aqueous phosphoric acid in [212] the model implementation becomes,

$$D_{H_2O-PA} = 8.457 \times 10^{-9} \frac{T}{\eta(T, \omega_{PA})} \quad (Eq. 7-38)$$

Where the mixture dynamic viscosity is interpolated from the values tabulated in [212].

The boundary and initial conditions for (Eq. 7-5) are outlined in Table 7-12.

*Table 7-12 Boundary and initial conditions for aqueous phosphoric acid phase conservation of species*

Boundary and Initial Conditions for Aqueous Phosphoric Acid Phase cons. of species			
Boundary Condition	Boundary	Initial Condition	Domain
No Flux	[e] & [h] (GDL/CL interface)	$\omega_{PA} = \omega_{PA,init}$	CL, MEM
		$\omega_L = 1 - \omega_{PA,init}$	CL, MEM

Water present in vapor form in the gaseous phases can condense to and from the aqueous phosphoric acid phase of the catalyst layers and membrane. The water vapor pressure of aqueous phosphoric acid has been measured empirically with respect to varying concentrations and temperature[213][215][217]. These data were interpolated to determine the vapor pressure  $P_{v,PA}$  as a function of weight fraction and temperature (Figure 7.4).

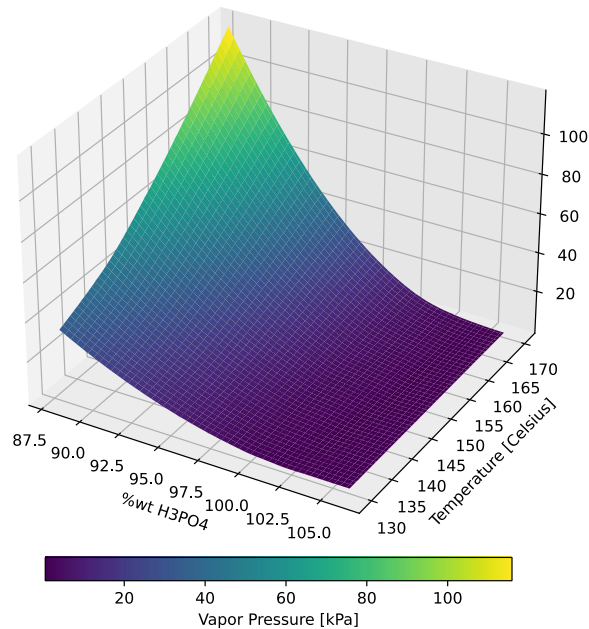


*Figure 7.4 Water vapor pressure of aqueous phosphoric acid solutions*

A Hertz-Knudsen evaporation-condensation relation characterizes the exchange of water between vapor and aqueous phases (Eq. 7-39). The local pressure differential between the vapor pressure of the aqueous phosphoric acid phase and the vapor pressure in the adjacent gas phase is the driving force for the phase change.  $A_{PC}$  is a coefficient describing the surface to volume ratio of the phase change surface in the porous domains and  $k_v$  is the rate constant. The rate constant  $k_v$  in this case was simplified to a collision frequency based solely on Maxwell-Boltzmann velocity distribution and condensation/evaporation coefficients with value of unity (Eq. 7-40)[221]. The rate of water phase change is the sole source term for (Eq. 7-5 as outlined in Table 7-13.

$$R_v = A_{PC} k_v (P_{v,PA} - P_v) \quad (\text{Eq. 7-39})$$

$$k_v = \sqrt{\frac{M_{H_2O}}{2\pi RT}} \quad (\text{Eq. 7-40})$$

Table 7-13 Source terms for aqueous phosphoric acid phase conservation of species

Source Term (s) Aqueous Phosphoric Acid Phase cons. of species	
Domain	Source Terms
CL	$R_i = R_v$
Mem	$R_i = 0$

## 7.2.5 Electrode Kinetics

Butler-Volmer relation describes the reaction rates in terms of current density  $i_{rxn}$  of hydrogen oxidation (HOR) and hydrogen evolution (HER) occurring at the anode and cathode catalyst layers respectively,

$$i_{rxn} = i_{0,HOR} \left[ \left( \frac{P_{H_2,an}}{P_{ref}} \right)^{\gamma_{HOR}} \exp \left( \frac{\alpha_{a,HOR} F \eta_{act}}{RT} \right) - \exp \left( \frac{-\alpha_{c,HOR} F \eta_{act}}{RT} \right) \right] \quad (\text{Eq. 7-41})$$

$$i_{rxn} = i_{0,HER} \left[ \exp \left( \frac{-\alpha_{c,HER} F \eta_{act}}{RT} \right) - \left( \frac{P_{H_2,c}}{P_{ref}} \right)^{\gamma_{HER}} \exp \left( \frac{\alpha_{a,HER} F \eta_{act}}{RT} \right) \right] \quad (\text{Eq. 7-42})$$

Where the electrode overpotential  $\eta_{act}$  is a function of the electronic and ionic potentials as well as the standard potential of reaction  $U_{HOR}$ ,

$$\eta_{act} = \Phi_1 - \Phi_2 - U_{HOR} \quad (Eq. 7-43)$$

The exchange current density  $i_0$  depends on the geometry of the electrode  $R_{cat}$  and a blocking factor related to phosphoric acid volumetric content in the electrode,  $\Theta_{active}$  [134].

$$i_0 = i_{0,ref} R_{cat} \Theta_{active}(\phi_{PA}) \quad (Eq. 7-44)$$

The reference exchange current density,  $i_{0,ref}$ , for HOR and HER are adapted from Arrhenius type relationship from fuel cell literature [208].

$$i_{0,ref} = 215 \exp\left(\left(-\frac{E_{act}}{RT}\right)\left(1 - \frac{T}{T_{ref}}\right)\right) \quad (Eq. 7-45)$$

Which give values of  $i_{0,ref}$  of 0.3 A cm<sup>-2</sup> at 160 °C for the parameters used in Table 7-14.

Detailed studies on HOR/HER rates on Pt electrodes in acidic environments exist for RDE but are constrained by mass-transport limiting currents lead to lower HOR/HER exchange current densities than MEA conditions [138][129]. In MEA efforts have been made to characterize HOR/HER exchange current densities in detail in LT-PEM EHP set-up, at temperatures up to 90 °C where exchange current densities of 0.6 A cm<sup>-2</sup> were observed for Butler-Volmer type kinetics [83]. A strong dependence on temperature for exchange current density indicates that more detailed study is likely needed to accurately account for kinetic losses in HT-PEM conditions.

$$R_{cat} = \Theta_{block} \frac{6L_{cat}}{\rho_{Pt} d_{Pt} t_{CL}} \quad (Eq. 7-46)$$

$R_{cat}$  describes the available surface area of platinum catalyst as a function of the total platinum loading  $L_{cat}$  in mg Pt cm<sup>-2</sup>, the density and average diameter of platinum particles  $\rho_{Pt}$  and  $d_{Pt}$  respectively, and the thickness of the electrode  $t_{CL}$ . A blockage factor  $\Theta_{block}$  describes the number of unavailable platinum sites, typically taken as a number near unity [134].

The pressure coefficient  $\gamma$  and the anodic and cathodic transfer coefficients  $\alpha_a$  and  $\alpha_c$  are constrained by the limiting condition,

$$\frac{\gamma}{\alpha_a + \alpha_c} = \frac{1}{2} \quad (\text{Eq. 7-47})$$

At zero current density, the net electrode overpotentials predicted by the Butler-Volmer equation should be equivalent to the predicted potential by the Nernst equation. Taking the limit at  $i_{rxn} = 0$ , the Butler-Volmer equations give,

$$\eta_{act,HOR} = \frac{\gamma_{HOR}}{\alpha_{a,HOR} + \alpha_{c,HOR}} \frac{RT}{F} \ln \left( \frac{P_{H2,an}}{P_{ref}} \right) \quad (\text{Eq. 7-48})$$

$$\eta_{act,HER} = \frac{\gamma_{HER}}{\alpha_{a,HER} + \alpha_{c,HER}} \frac{RT}{F} \ln \left( \frac{P_{H2,c}}{P_{ref}} \right) \quad (\text{Eq. 7-49})$$

Where the net potential of an electrochemical cell is,

$$E_{cell} = E_{red} - E_{ox} = \eta_{act,HER} - \eta_{act,HOR} = \frac{\gamma_{HER}}{\alpha_{a,HER} + \alpha_{c,HER}} \frac{RT}{F} \ln \left( \frac{P_{H2,c}}{P_{H2,an}} \right) \quad (\text{Eq. 7-50})$$

Which can be equivalent to the Nernst equation for hydrogen concentration electrochemical cell, for the standard hydrogen potential of  $E^0 = 0$ ,

$$E_{cell} = E^0 + \frac{RT}{2F} \ln \left( \frac{P_{H2,c}}{P_{H2,an}} \right) \quad (\text{Eq. 7-51})$$

Detailed study of Butler-Volmer kinetics fitting to HOR and HER in pump set-up indicate reasonable fits for  $\alpha_a + \alpha_c = 1$  and for  $\alpha_a + \alpha_c = 2$ , unlike typical assumptions symmetric transfer coefficients typically assumed of  $\alpha_a = \alpha_c = 0.5$  [222]. It is hypothesized that at higher overpotential a change in reaction pathway occurs due to a switch in rate determining step meaning that the transfer coefficients is a function of overpotential [83]. Sensitivity analysis of the transfer and pressure coefficients was conducted and found to be significant with respect to electrode overpotential, with one example for a 10% H<sub>2</sub> anode overpotential for both  $\alpha_a + \alpha_c = 1$  and  $\alpha_a + \alpha_c = 2$  show in Figure 7.5. The latter demonstrated the best fit particularly at higher overpotentials as predicted by the literature and was selected as the constraint for the model.

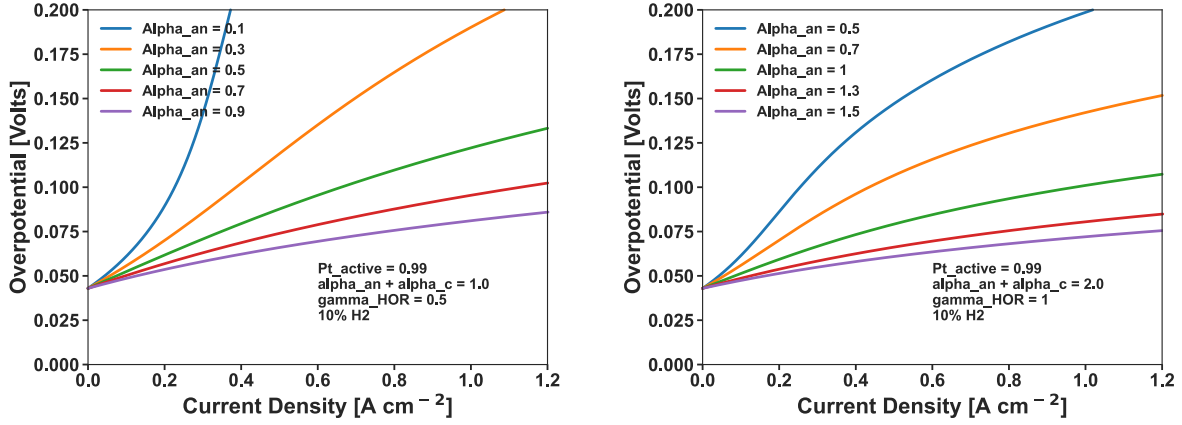


Figure 7.5 Influence of transfer coefficient and pressure coefficient on predicted electrode overpotential of HOR/HER by Butler-Volmer equation.

In the HT-PEM EHP, the catalyst layer is comprised of platinum nanoparticles supported on carbon particles, a hydrophobic binder (PTFE or PVDF) and aqueous phosphoric acid, with the latter providing the proton conducting phase in lieu of an ionomeric binder typical in LT-PEM cells. Some fraction of the porous phase is occupied by the aqueous phosphoric acid, giving the following relation for porosity as a function of phosphoric acid volume fraction  $\phi_{PA,CL}$ , and  $\phi_{S,CL}$ , the solid fraction content.

$$\varepsilon_{CL} = 1 - \phi_{PA,CL}(T, m_{PA}) - \phi_{S,CL} \quad (\text{Eq. 7-52})$$

The presence of phosphoric acid leads to an inactivation of platinum catalyst observed as an inhibition of electrode kinetic performance due to adverse effects of phosphate anion adsorption on Pt surfaces and gas transport blockage by aqueous phosphoric acid in which the solubility of gases is 1-2x order magnitude lower than water which would be present in the analogous LT-PEM electrodes. Ideally, there some amount of phosphoric acid is present to provide proton conducting pathways to and from the reaction sites at platinum carbon junctions that connect to the membrane phase and remain accessible to reactants. Figure 7.6 illustrates the structure of the HT-PEM EHP with the morphology of the catalyst layer and the impacts of increasing electrode



acid content on the availability of reaction sites.

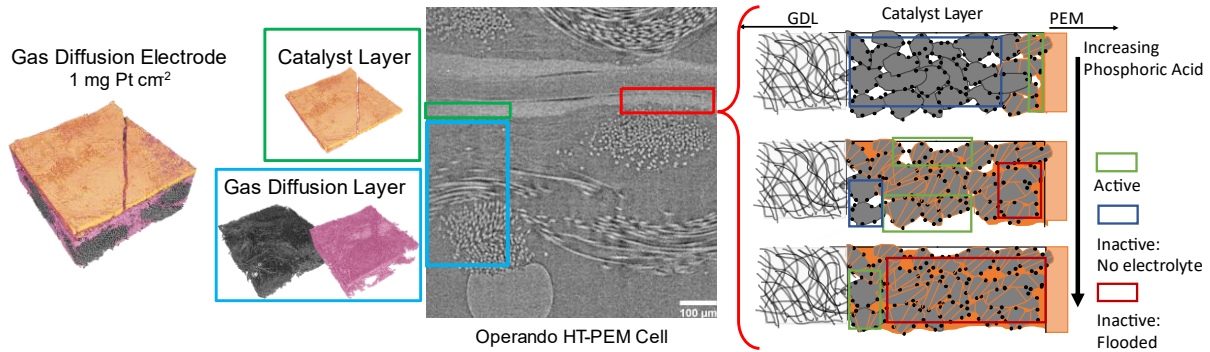


Figure 7.6 HT-PEM EHP structure: GDE structure from x-ray CT (left), MEA structure from operando x-ray CT (middle), illustration of catalyst layer structure with increasing volume fractions of phosphoric acid (right)

Kazdal et al. proposed the  $\Theta_{active}$  term to describe the net effect of the phosphoric acid content on the electrode kinetics for a HT-PEMFC using E-tek carbon cloth electrodes that are similar in structure to the De Nora GDEs examined in this study [134]. At low volume fractions of PA, the smaller capillaries are assumed to fill first and then the larger pore domains are wetted while remaining accessible to gases. It is proposed that this leads to the optimal reaction interface, while further addition of acid begins to fill up the larger pores impeding gas transport and occluding platinum surfaces.

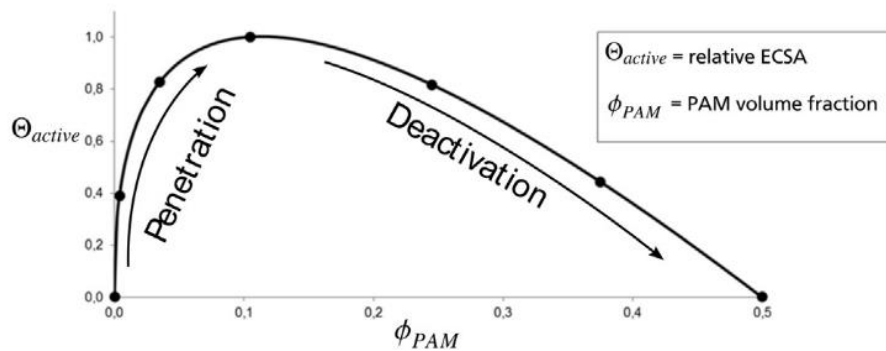


Figure 7.7 Correlation between activity coefficient  $\Theta_{active}$  and phosphoric acid volume fraction in the catalyst layer. Reproduced from [134].

Properties for equations pertaining to electrode kinetics are given below in Table 7-14.

Table 7-14 Properties for Butler-Volmer kinetics of HOR and HER

Butler-Volmer Kinetic Properties		
Property	Value	Source
$E_{act}$ [J mol <sup>-1</sup> ]	16000	[222]
$T_{ref}$ [K]	298.15	
$P_{ref}$ [Bar]	1.0	
$\rho_{Pt}$ [kg m <sup>-3</sup> ]	21450	
$\Theta_{block}$	0.99	[134]
$\alpha_a   \alpha_c$ *	1.0   1.0	[83]
$\gamma^*$	1.0	[83]
$U_{HOR}$ [V]*	0	[223]

\*HOR and HER values are equal

## 7.2.6 Conservation of Energy

Conservation of energy is considered across all domains, written in a general form as,

$$\rho \mathbf{u} C_p \nabla T - k_T \nabla \cdot (\nabla T) = Q \quad (\text{Eq. 7-10})$$

The first term on the left-hand side is associated with convective heat transfer occurring in the channels, and the second term is the conduction occurring throughout. Thermal equilibrium is maintained across domains.  $Q$  represents the heat source and sink terms.

Convection heat transfer in the channel consists of the velocity term solved by Navier-Stokes (section 7.2.1 ). The mixture averaged density,  $\rho$ , and specific heat capacity at constant pressure  $C_p$ . Assuming ideal gas properties,

$$\rho_{CHN} = \frac{p}{RT} \sum_j y_j M_j \quad (\text{Eq. 7-53})$$

$$C_{p,CHN} = \sum_j \omega_j C_{p,j} \quad (\text{Eq. 7-54})$$

Conduction in the channel occurs through gaseous phase, where the thermal conductivity of the gaseous mixture is estimated in a like manner to viscosity,

$$k_{T,CHN} = \sum_j \frac{y_j k_{T,j}}{\sum_k y_k \phi_{j,k}} \quad (\text{Eq. 7-55})$$

$$\phi_{j,k} = \left(\frac{1}{8}\right)^{\frac{1}{2}} \left(1 + \frac{M_j}{M_k}\right)^{-\frac{1}{2}} \left(1 + \left(\frac{k_{T,j}}{k_{T,k}}\right)^{\frac{1}{2}} \left(\frac{M_k}{M_j}\right)^{\frac{1}{4}}\right)^2 \quad (\text{Eq. 7-56})$$

In the gas diffusion layers (GDL) there are two phases through which heat can be conducted – gas and solid. Accordingly, the density and specific heat capacity is taken as a volume-averaged value between the solid and gaseous phases,

$$\rho_{GDL} = \varepsilon_{GDL} \frac{p}{RT} \sum_j y_j M_j + \rho_{S,GDL} \phi_{S,GDL} \quad (\text{Eq. 7-57})$$

$$C_{p,GDL} = \varepsilon_{GDL} \sum_j \omega_j C_{p,j} + C_{p,S} \phi_{S,GDL} \quad (\text{Eq. 7-58})$$

Where  $\varepsilon$  is the porosity of the GDL domain, and  $\phi_S$  is the volume fraction of the solid phase.

Thermal conductivity of the GDL is assumed to act as a combination of bulk phase thermal conductivity and the gaseous phases,

$$k_{T,GDL} = \varepsilon_{GDL}^{1.5} k_{T,gas} + k_{T,s} \phi_{S,GDL}^{1.5} \quad (\text{Eq. 7-59})$$

Where the thermal conductivity of the gaseous mixture phase,  $k_{T,gas}$ , is calculated according to (Eq. 7-55) and the exponent factor 1.5 corresponds to a tortuosity correction of  $\varepsilon^{-0.5}$ .

In the catalyst layer phase, the addition of a third phase of aqueous phosphoric acid adds an additional term but is otherwise solved in a likewise manner to the GDL thermal properties,

$$\rho_{CL} = \varepsilon_{CL} \frac{p}{RT} \sum_j y_j M_j + \rho_{CL} \phi_{S,CL} + \rho_{PA} \phi_{PA,CL} \quad (\text{Eq. 7-60})$$

$$C_{p,CL} = \varepsilon \sum_j \omega_j C_{p,j} + C_{p,S} \phi_S + C_{p,PA} \phi_{PA,CL} \quad (\text{Eq. 7-61})$$

$$k_{T,CL} = \varepsilon_{CL}^{1.5} k_{T,gas} + k_{T,S} \phi_{S,CL}^{1.5} + k_{T,PA} \phi_{PA,CL}^{1.5} \quad (\text{Eq. 7-62})$$

In the membrane domain, the thermal properties are assumed to be attributed entirely to the PBI membrane and volume fraction of phosphoric acid,

$$\rho_{mem} = \rho_{PBI} \phi_{PBI} + \rho_{PA} \phi_{PA,mem} \quad (\text{Eq. 7-63})$$

$$C_{p,mem} = C_{p,PBI} \phi_{PBI} + C_{p,PA} \phi_{PA,mem} \quad (\text{Eq. 7-64})$$

$$k_{T,mem} = k_{T,PBI} \phi_{PBI,mem}^{1.5} + k_{T,PA} \phi_{PA,mem}^{1.5} \quad (\text{Eq. 7-65})$$

Table 7-15 summarizes the relevant material properties of  $C_p$ ,  $k_T$ , and  $\rho$  used to calculate the energy balance.

*Table 7-15 Material thermal properties*

Thermal Properties for Conservation of Energy							
Property	H2	CH4	H2O(v)	GDL(s)	CL(s)	PBI	PA
$C_p$ [J g <sup>-1</sup> K <sup>-1</sup> ]	14.48[224]	2.3[224]	1.9[224]	0.71[208]	0.71[208]	1.05	1876.3[224]
$k_T$ [W m <sup>-1</sup> K <sup>-1</sup> ]	0.17[225]	0.06[225]	0.02[225]	3[209]	3[209]	0.2[209]	0.5[226]
$\rho$ [kg m <sup>-3</sup> ]	Ideal Gas	Ideal Gas	Ideal Gas	1800[209]	2200[209]	1800	1880

The source term  $Q$ , consists of ohmic heating  $Q_{ohm}$ , in the GDL, CL and membrane domains. In the CL, the heat of reaction,  $Q_{rxn}$ , is accounted for along with the heating/cooling associated with the phase change of water  $Q_v$ . The source terms are outlined in Table 7-16.

Table 7-16 Source terms for conservation of energy

Source Terms for Conservation of Energy			
Domain	Q_ohm	Q_rxn	Q_v
CHN	---	---	---
GDL	$\frac{i_1^2}{\sigma_{1,eff}}$	---	---
	$\frac{i_1^2}{\sigma_{1,eff}} + \frac{i_2^2}{\sigma_{2,eff}}$	$i_{rxn}(\eta_{act} + \Pi_h)$	$-\Delta H_v R_v$
MEM	$\frac{i_2^2}{\sigma_{2,eff}}$	---	---

Where  $\Pi_h$  is the Peltier coefficient for HOR, resolved by the empirical correlation[227]

$$\Pi_h = -\frac{0.012T}{T_t} \quad (Eq. 7-66)$$

and  $T_t$  is the triple point temperature of H<sub>2</sub>O.

Boundary and initial conditions for conservation of energy are outlined below in Table 7-17. Generally, the cell temperature setpoint is defined as the initial condition for all domains. The cell is assumed to behave as well insulated at the walls, and the inlet gases are assumed to be pre-heated to cell operating temperature.

Table 7-17 Boundary and initial conditions for conservation of energy

Boundary and Initial Conditions for Conservation of Energy			
Boundary Condition	Boundary	Initial Condition	Domain
$\mathbf{n} \cdot \mathbf{Q} = 0$ (insulated)	All outer boundaries	$T = T_{cell}$	All
$T = T_{inlet} = T_{cell}$	[b] & [j] Channel Inlets		
$T = T_{cell}$	All outer boundaries except Inlets		

### 7.2.7 Voltage Breakdown by Spatially Normalized Power-Losses

Power-loss voltage breakdown analysis is a post-processing technique that allows for the deconvolution of voltage loss in the cell under study by considering the rates of energy loss

defined by physical equations and averaged over the relevant dimensional space. This energy loss, or power loss, can then be divided by the average cell current to obtain the voltage loss for that region and equation [228][229]. The strength of this approach as compared to other voltage breakdown loss techniques is the ability to extract the voltage losses from a simulation output without the need for additional simulation such as in subtractive voltage breakdown techniques where simulations are run without sources of voltage loss to identify the magnitude of other sources.

The underlying principle of the power-loss voltage breakdown approach and its implementation in conventional electrochemical MEA models is presented in Gerhardt et al.[229] and is briefly outlined below. Power-loss voltage breakdown is based on the definition of a power density vector  $p_k$ ,

$$p_k = i(\Phi_k - \Phi_k^{ref}) \quad (Eq. 7-67)$$

Where  $\Phi_k$  is the potential with respect to a reference potential,  $\Phi_k^{ref}$ . In other words, the power density is the product of current density  $i$ , and the potential. Power-loss or in other words, waste heat, can be defined as the divergence of  $p_k$ ,  $\Delta \cdot p_k$ , and thus the voltage loss  $\Delta V_k$  can be determined from the integration of the power loss and divided by the average current density  $i_{cell}$ ,

$$\Delta V_k = \frac{\int \nabla \cdot p_k}{i_{cell}} \quad (Eq. 7-68)$$

By divergence theorem equating the flux out of the volume as a surface integral, for the surface  $S_k$  of a volume element  $v_k$ ,

$$\int \mathbf{i} \cdot \Phi_k dv_k + \int (\Phi_k - \Phi_k^{ref}) \nabla \cdot \mathbf{i} dv_k = \int \mathbf{p} \cdot \mathbf{n} dS_k = i_{cell} \Delta V_k \quad (Eq. 7-69)$$

Which gives us our relation for the voltage loss  $\Delta V_k$  in terms of volume elements as a function of the power loss normalized to the cell current density,  $i_{cell}$ .

$$\Delta V_k \equiv \frac{\int \mathbf{i} \cdot \Phi_k dv_k}{i_{cell}} + \frac{\int (\Phi_k - \Phi_k^{ref}) \nabla \cdot \mathbf{i} dv_k}{i_{cell}} \quad (Eq. 7-70)$$

Where the first term of (Eq. 7-70) relates to ohmic losses. For the case of proton conduction in the HT-PEM EHP where the ionic potential voltage drop is described by ohms law,

$$i_2 = -\sigma_{eff,2} \nabla \Phi_2 \quad (Eq. 7-8)$$

The ohmic losses of the catalyst layer (CL) and membrane (MEM) due to ion transport can be re-written as,

$$\Delta V_{ohm} \equiv \frac{\int -\sigma_{eff,2} \mathbf{i}_2 \cdot \mathbf{i}_2 dv}{i_{cell}} \quad (Eq. 7-71)$$

$i_2$  is the local ionic current density, and the above relation takes a similar form to the Ohm's law relation for power,  $P = I^2 R$ .

The second term of (Eq. 7-70) relates to kinetic and mass-transport overpotentials due to the electrochemical reactions considered. For an overpotential  $\eta_{act} = \Phi_1 - \Phi_2 - U^0$ , this reduces to the following voltage loss for a given reaction at an electrode,

$$\Delta V_{electrode} \equiv \frac{\int i_{rxn} \eta_{act} dv_{CL}}{i_{cell}} \quad (Eq. 7-72)$$

To parse out the contribution of kinetics and mass-transport, two overpotentials can be defined as follows,

$$\eta_{act} = \eta_{surf} + \eta_{conc} \quad (Eq. 7-73)$$

Where  $\eta_{surf}$  is referred to as the surface overpotential and provides the kinetic voltage loss when plugged into (Eq. 7-72) and  $\eta_{conc}$  likewise provides mass transport related voltage losses. Since mass-transport overpotentials are well defined as the loss associated with a change in reactant concentration at the electrode surface,  $\eta_{conc}$  is directly defined in terms of voltage loss for the model in a general form for Butler-Volmer type kinetics involving a concentration C, of reactant k, as,

$$\eta_{conc} = \frac{RT\gamma}{\alpha F} \ln \left( \frac{C_k}{C_{k,ref}} \right) \quad (Eq. 7-74)$$

Then,

$$\Delta V_{mass\ transport,k} = \frac{\int i_{rxn} \frac{RT\gamma}{\alpha F} \ln\left(\frac{C_k}{C_{k,ref}}\right) dv_{CL}}{i_{cell}} \quad (Eq. 7-75)$$

And for kinetic overpotential  $\eta_{surf}$ ,

$$\eta_{surf} = \eta_{act} - \eta_{conc} \quad (Eq. 7-76)$$

And,

$$\Delta V_{kinetic} = \frac{\int i_{rxn}(\eta_{act} - \eta_{conc}) dv_{CL}}{i_{cell}} \quad (Eq. 7-77)$$

Table 7-18 lists the implementation of the above voltage-loss breakdown equations in the 2-D space of the HT-PEM model for the relevant sources of overpotential and relevant relations.

*Table 7-18 Power-loss voltage breakdown equations in model*

Voltage-loss breakdown equations by source	
Parameter	Equation
Membrane Ohmic Loss	$\frac{1}{L_{CHN} i_{cell}} \int_0^{L_{CHN}} \int_0^{t_{mem}} \frac{i_2^2}{\sigma_{2,eff}} dx dy$
Anode Ohmic Loss	$\frac{1}{L_{CHN} i_{cell}} \int_0^{L_{CHN}} \int_0^{t_{CL,an}} \frac{i_2^2}{\sigma_{2,eff}} dx dy$
Cathode Ohmic Loss	$\frac{1}{L_{CHN} i_{cell}} \int_0^{L_{CHN}} \int_0^{t_{CL,cat}} \frac{i_2^2}{\sigma_{2,eff}} dx dy$
Anode Kinetic Loss	$\frac{1}{L_{CHN} i_{cell}} \int_0^{L_{CHN}} \int_0^{t_{CL,cat}} i_{rxn} \eta_{act} dx dy - OCP_{an} - \Delta V_{MT,an}$
Cathode Kinetic Loss	$\frac{1}{L_{CHN} i_{cell}} \int_0^{L_{CHN}} \int_0^{t_{CL,cat}} i_{rxn} \eta_{act} dx dy - OCP_{cat}$
Anode Mass Transport	$\frac{1}{L_{CHN} i_{cell}} \int_0^{L_{CHN}} \int_0^{t_{CL,an}} i_{rxn} \frac{RT\gamma}{\alpha F} \ln\left(\frac{P_{H2}}{P_{H2,inlet}}\right) dx dy$



## 7.3 Results & Discussion

### 7.3.1 Model Validation with Varying Operating Conditions

The model was initially validated on varying operating conditions by sweeping the temperature of the EHP at 100% H<sub>2</sub> operation and as well as validation against the varying %H<sub>2</sub> concentration cases. Dimensions and model parameters for these initial validation cases are outlined in Table 7-19. The model physical parameters are based on the De Nora GDE based HT-PEM EHP MEAs examined in Chapter 5 further informed by the operando X-ray CT experiments in Chapter 6

*Table 7-19 Simulation parameters for HT-PEM EHP model*

Simulation Properties of HT-PEM EHP	
Property	Value
Area [cm <sup>2</sup> ]	5
Channel Length [m]	0.295
Channel Height [mm]	0.8
Channel Width [mm]	1
Gas Diffusion Layer (GDL) Thickness [mm]	0.38
Catalyst Layer (CL) Thickness [mm]	0.08
Membrane Thickness [mm]	0.06
ADL [mol PA mol <sup>-1</sup> PBI RPU]	7
Catalyst Loading [mg Pt cm <sup>-2</sup> ]	1.0
m <sub>PA,CL</sub> [mg PA cm <sup>-2</sup> ]	20

The HT-PEM EHP model showed good agreement with respect to varying temperatures at 100% H<sub>2</sub> anodic feeds for the temperature range of 140 to 160 °C for a fixed saturation temperature at the anode corresponding to 1.2, 1.6 and 2.0 % relative humidity. When varying the concentration of H<sub>2</sub> at the anode feed, the HT-PEM EHP model can capture the shift in open-circuit voltage due to concentration polarizations as well as the limiting current density at extremely limited cases such as 2% vol. H<sub>2</sub>.

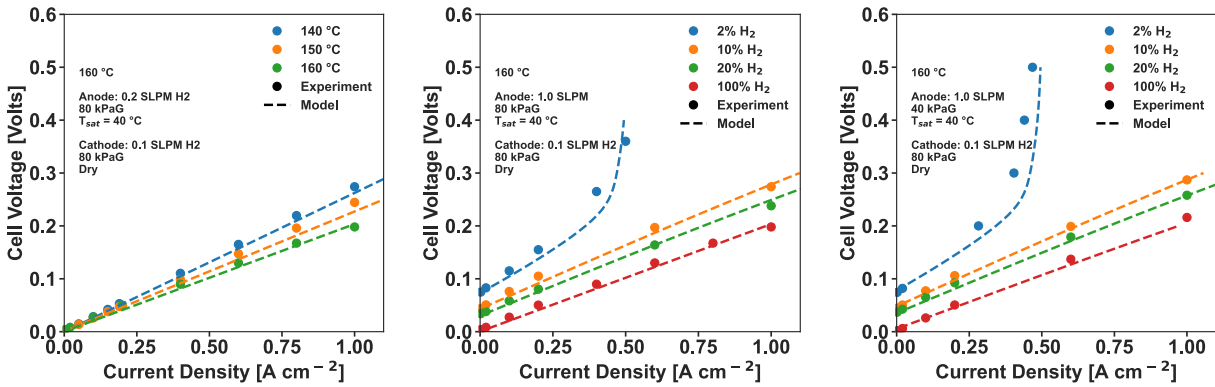


Figure 7.8 HT-PEM EHP model agreement with polarization curves from experiments.

There was some non-ideality in the MEA testing for the 2 % vol. H<sub>2</sub> case as it approaches limiting currents that suggests a greater limiting permeability in one of the phases. One possibility is the presence of phosphoric acid in the GDL phase, which is not considered in the model but is certainly a reality in the HT-PEM EHP. Due to the low solubility of gases in phosphoric acid, the presence of phosphoric acid in the GDL phase would be expected to effectively reduce the porosity and contribute to mass transport overpotentials.

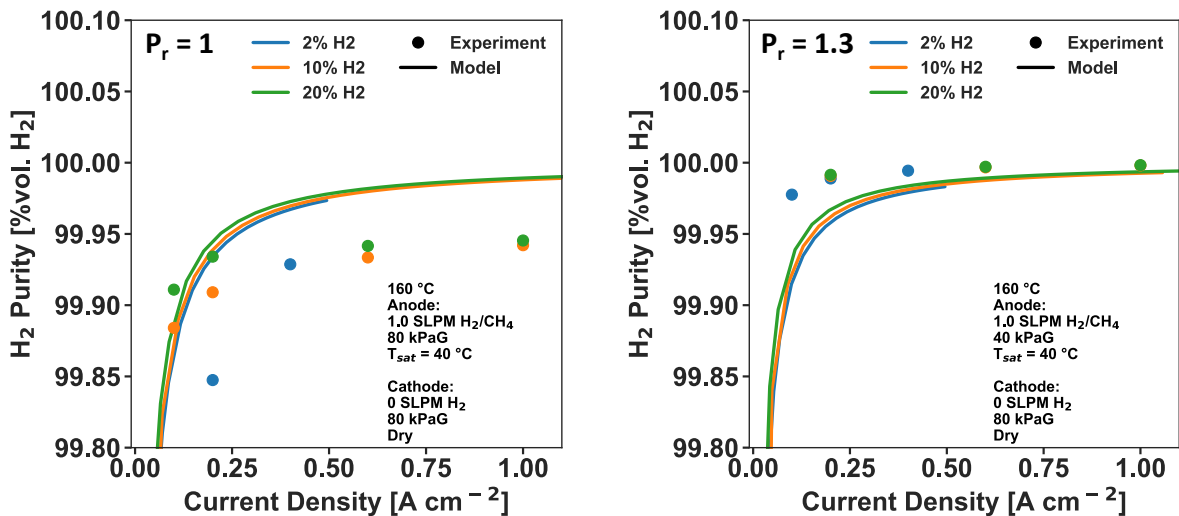


Figure 7.9 HT-PEM EHP model agreement with cathode outlet purity measurements.

The outlet purity measurements taken by GC-FID was compared as well to the empirically derived model prediction for the case of balanced back pressure (Figure 7.9, left) at 80 kPaG as well as the co-compression case at a compression ratio of  $P_r = 1.3$  for backpressures of 40 kPaG anode against 80 kPaG cathode (Figure 7.9, right). The model over predicts the H<sub>2</sub> purity at the cathode outlet for balanced pressure scenario while the co-compression scenario does show a

closer fit particularly at the higher current density where purity levels off. Both cases struggle to match at the low current density regime, likely due to difficulties in measuring at low current densities due to the low faradaic production rate of H<sub>2</sub> and the need to operate at pressure to feed the in-line GC a reasonable sample volume. Pressure drop across the cell hardware in experiments was higher than what is predicted by the model, which simulates the flow field as a straight channel of equivalent length to the serpentine flow field length. While back-pressure is defined, the average pressure across the channel from inlet to higher is higher than the back-pressure especially on the anode side where the flow rate is relatively (1 SLPM). With this limitation, prediction of methane cross-over and thus over-prediction of H<sub>2</sub> purity at the cathode would be expected of the model. For the case of co-compression, where the absolute pressure gradient favors the convective permeation of gas from cathode to anode, the convective permeation of methane may be under-predicted relative to the diffusive transport of methane.

### 7.3.2 Influence of humidification and operating pressure on H<sub>2</sub> product purity

In experiments with the HT-PEM EHP involving the separation of H<sub>2</sub> from CH<sub>4</sub>, the purity of the cathode outlet has been determined on a dry basis due to the drying needed upstream of the GC to maintain the integrity of the column and detectors that could be adversely affected by water vapor. While the cathode of the HT-PEM EHP is 'dry' in terms of the lack of humidified cathodic gas feed, there is some water present due to the transport of water from the humidified anode to the cathode side that ultimately affects the H<sub>2</sub> purity.

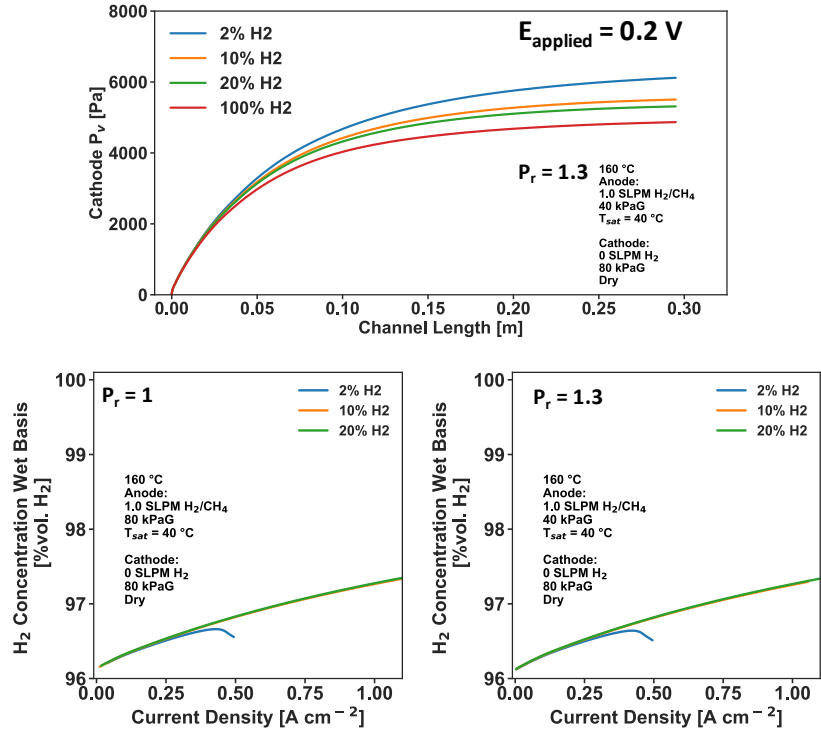


Figure 7.10 Water vapor pressure in along the length of the cathode channel, inlet at channel length = 0 (Top). H<sub>2</sub> volumetric content at the cathode outlet before drying as a function of current density.

Figure 7.10 shows the vapor content in the cathode as a function of the channel length as water evaporates from the aqueous phosphoric acid phase into the cathode. At a fixed cell voltage of 0.2 V, the vapor pressure at the cathode does increase with decreasing H<sub>2</sub> anodic feeds. This is due to the difference in current density at a given potential, as exemplified in the correlation between current density and outlet H<sub>2</sub> purity on wet basis, which only deviates slightly for the case of limiting current density operation in 2% H<sub>2</sub> basis due to the increasing concentration of current density and thus HOR and HER reactions closer to the inlet at the higher anodic over potentials. These results suggest that the water content of the cathode for HT-PEM EHP, which relies on some humidification at the anode to maintain reasonable performance, is not negligible when considering the H<sub>2</sub> purity of the H<sub>2</sub> cathode product.

It was previously demonstrated that H<sub>2</sub> purity post drying from the HT-PEM could exceed ISO14687-2 standards of 99.97% H<sub>2</sub> purity for FCEV fueling requirements, however with the balance impurity being solely methane, the purity was not sufficient in terms of the 2 ppm total hydrocarbons (THC) requirement. In terms of methane alone, the case of 10% and 20% H<sub>2</sub> at a

compression ratio of  $P_r = 1.3$  does meet the maximum concentration requirement of 100 ppm  $\text{CH}_4$ , suggesting further co-compression is required to meet methane requirements for the 2%  $\text{H}_2$  case. The model is used to extend this analysis for the cases measured and displays the limit in ppm  $\text{CH}_4$  on a dry basis for the cathode outlet and the benefits of even slight cathodic pressurization in minimizing the  $\text{CH}_4$  content.

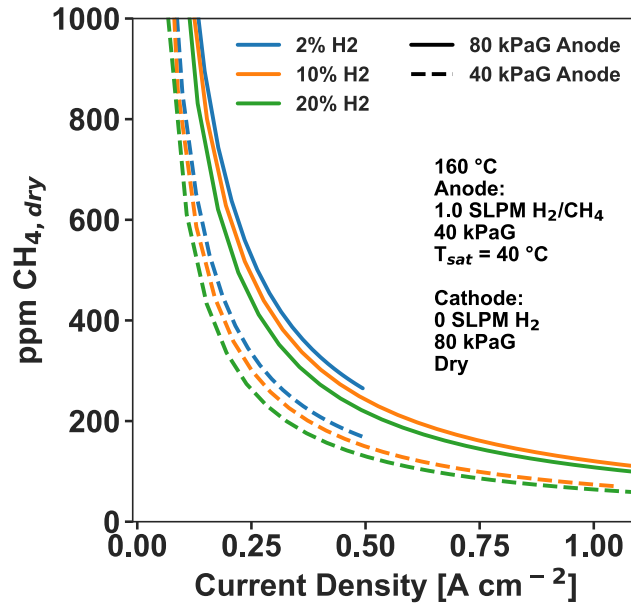


Figure 7.11 Methane concentration in cathode outlet on dry basis as function of current density for compression ratio of 1 and 1.3.

The effect of even slight pressurization of the cathode is significant – at 20%  $\text{H}_2$  anodic feed, the methane content of the cathode is 86 ppm for equal pressure scenario and drops to 52 ppm when running a compression ratio of 1.3 cathode to anode. It is also apparent that extending the current density for the 2% vol  $\text{H}_2$  case by increasing the stoichiometry of the HOR reaction, through net flow rate, would likely be beneficial for  $\text{H}_2$  purity assuming that the associated increase in pressure drop at the anode would not lead to a significant increase in cross-over of methane.

### 7.3.3 Voltage loss breakdown analysis

Voltage loss breakdown analysis (section 7.2.7) can be used to garner greater insight into the dominant sources of overpotential and thus where changes in operating condition or material properties could be valuable to future implementation of HT-PEM EHP in this application.

Figure 7.12 shows this practice applied to two extremes for 2%  $\text{H}_2$  anode feed concentration and for the 100%  $\text{H}_2$  case.

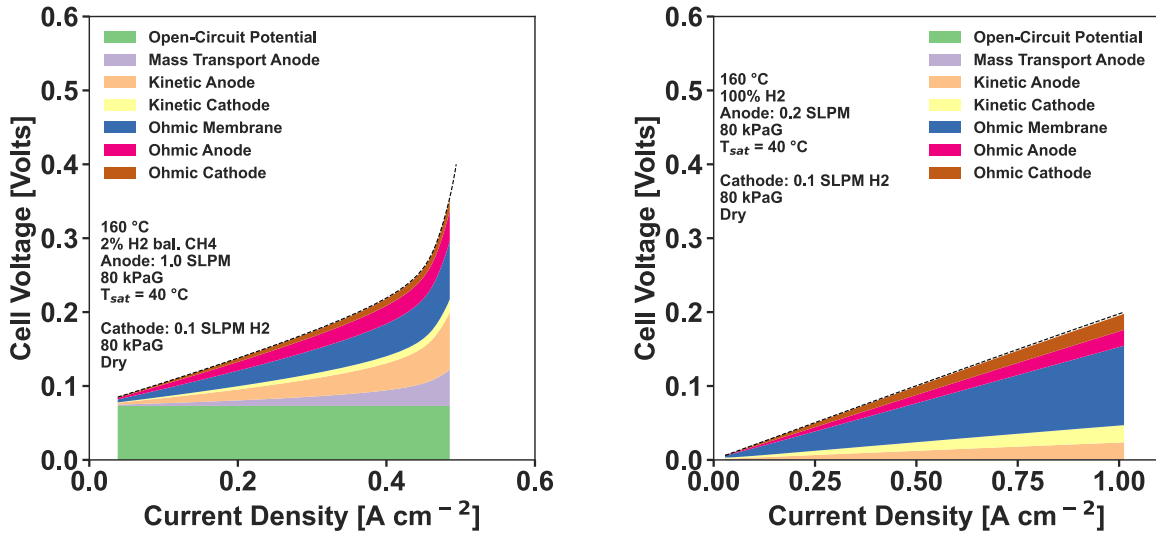
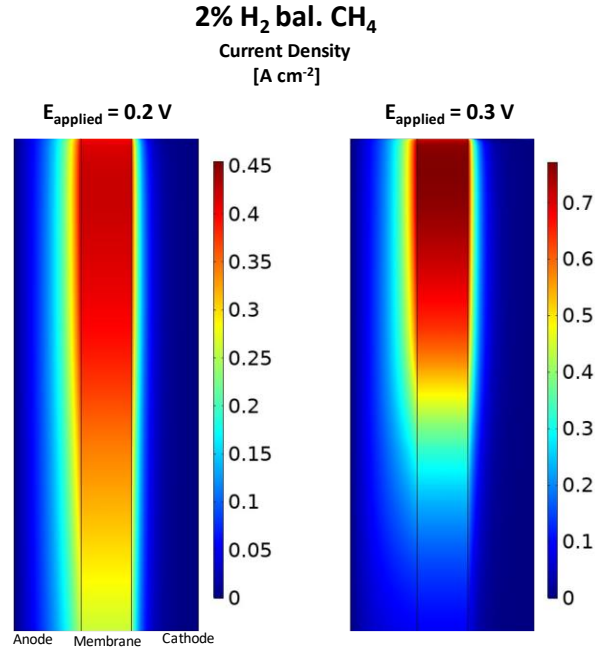


Figure 7.12 Voltage loss breakdown analysis for 2% and 100% H<sub>2</sub> anode feeds.

For both cases, the ohmic losses largely through the membrane is a significant source of overpotential, suggesting that the further improvement of the electrode and membrane proton conductivity would provide the greatest benefit to increasing the efficiency of the separation process. In the 2% H<sub>2</sub> gas feed case, it is apparent that open-circuit potential, even at the higher end of feasible applied current, contributes an appreciable amount to the net cell voltage, highlighting the thermodynamic limitations of gas separation and compression inherent in the process.

Kinetic losses at the anode are much higher than at the cathode for the 2% H<sub>2</sub> case, which is unexpected. Typically, one would expect the greater part of the discrepancy in anodic overpotential compared to cathodic overpotential to be ascribed to an increase in mass-transport overpotential. This can be attributed in part due to a limitation in the power-loss voltage analysis related to the use of spatial integration over regions with high discrepancies in current density distribution.



*Figure 7.13 Current density distribution in membrane and catalyst layers in HT-PEM EHP model at 2% H<sub>2</sub>.*

Figure 7.13 shows the current density distribution of the HT-PEM EHP for a 2% H<sub>2</sub> feed case where practical limiting current densities are reached. It can be observed that even for the 0.2 V case, where the polarization curve has yet to show a non-linear response indicating mass-transport losses beginning to dominate, the current density distribution shifts to the inlet as the reaction rate increases with applied potential. A large part of the current density as well is apportioned to a small region right next to the membrane-electrode interface, leaving large spatial regions where there is near-zero current density in the electrodes. At a higher potential of 0.3 V where very little current increase is obtained for higher potentials due to a depletion of reactants, this effect becomes very pronounced and begins to impact the accurate calculation of voltage breakdown sources including ohmic type losses. Thus, the attribution of significantly higher anode kinetic losses over cathode kinetic losses is a non-physical result from the obfuscation of losses that should be related more to mass-transport voltage loss. This limitation of the technique only seems to be relevant for 2% H<sub>2</sub> by volume for the cases studied here, as that is the only scenario in which the spatial distribution of current density is significantly distributed with many regions of near-zero current that can result in non-physical integration results.

Voltage loss breakdowns predicted from the model for the two compression ratios ( $P_r=1$  and 1.3) and for 2, 10, 20, and 100%  $H_2$  gas feeds tested in MEA are presented below in Figure 7.14 for applied cell potentials of 0.1 and 0.2 V. Assuming ideal faradaic efficiency, these voltages correspond to electrical consumption of 2.7 and 5.3 kWh/kg  $H_2$ , which is 8.02 and 16.05% of the LHV of the separated  $H_2$  gas respectively.

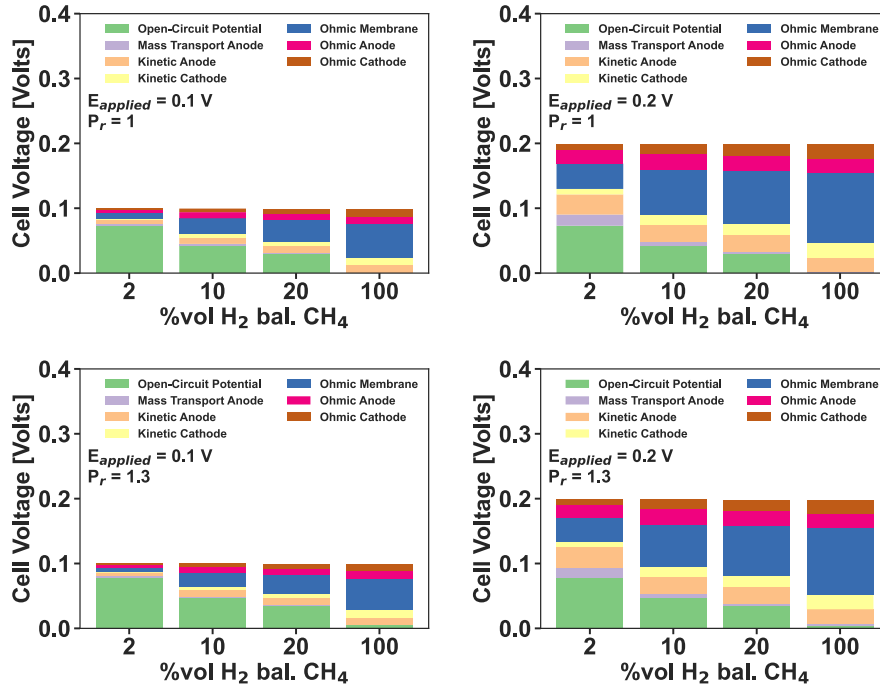


Figure 7.14 Voltage loss breakdowns at 0.1 and 0.2 V cell potentials for tested compression ratio and varying  $H_2$  concentrations.

For the 2%  $H_2$  case, operation at 0.1 V is dominated by thermodynamic limitations, thus there is very little room for improvement. At increasing hydrogen contents, ohmic losses are dominant, although kinetic losses are still present. At 0.2 V of applied potential, while ohmic losses are still very dominant, kinetic losses are also an appreciable source of overpotential despite using relatively high platinum loadings of  $1 \text{ mg Pt cm}^{-2}$ . This is emblematic of a key issue with HT-PEM EHP due to the presence of significant phosphoric acid electrolyte. The reduction of phosphoric acid electrolyte does not improve the performance, and thus an alternative approach to the proton conducting phases in the electrodes is desirable in the long-term for the advancement of the technology. At 10%  $H_2$  thermodynamic and membrane ohmic losses are pre-eminent, while at higher concentrations ohmic losses generally dominate.



### 7.3.4 Influence of increasing compression ratios on HT-PEM EHP

Higher compression ratios are considered for the 10% and 2% H<sub>2</sub> concentration cases and the apparent impacts on separation efficiency and cost are examined. At 10% H<sub>2</sub> feed (Figure 7.15) the increase in potential and separation cost is very minimal for increasing compression ratio from 1.3 to 3. The bulk of the separation cost comes from the penalty in overpotential that is largely a function of hydrogen production rather than the concentration at the feed, assuming that the HT-PEM EHP is not nearing reactant starvation conditions, and thus it is almost always worth compressing hydrogen as it is separated. Faradaic efficiency is highly sensitive to compression ratio at low current density operation, and thus impacts the real separation efficiency appreciably, but only at very low current densities.

In bench tests, 10% H<sub>2</sub> feed was able to meet 100 ppm CH<sub>4</sub> maximum purities requirements from FCEV fueling requirements at high current density (1 A cm<sup>-2</sup>). At higher compression ratios, the effective current density at which this is feasible is lower dramatically due to inhibited methane cross-over. At  $P_r = 3$ , the limitation of the implementation of cross-over in this model is apparent as the predicted methane concentration goes to zero due to large permeation rates from cathode to anode, a non-physical result pertaining to an edge case that requires further experimental characterization and analysis. Water content in the cathode H<sub>2</sub> is diluted with increasing cathode pressure, but still requires the downstream removal of water from the HT-PEM EHP before meeting hydrogen fuel cell quality standards.

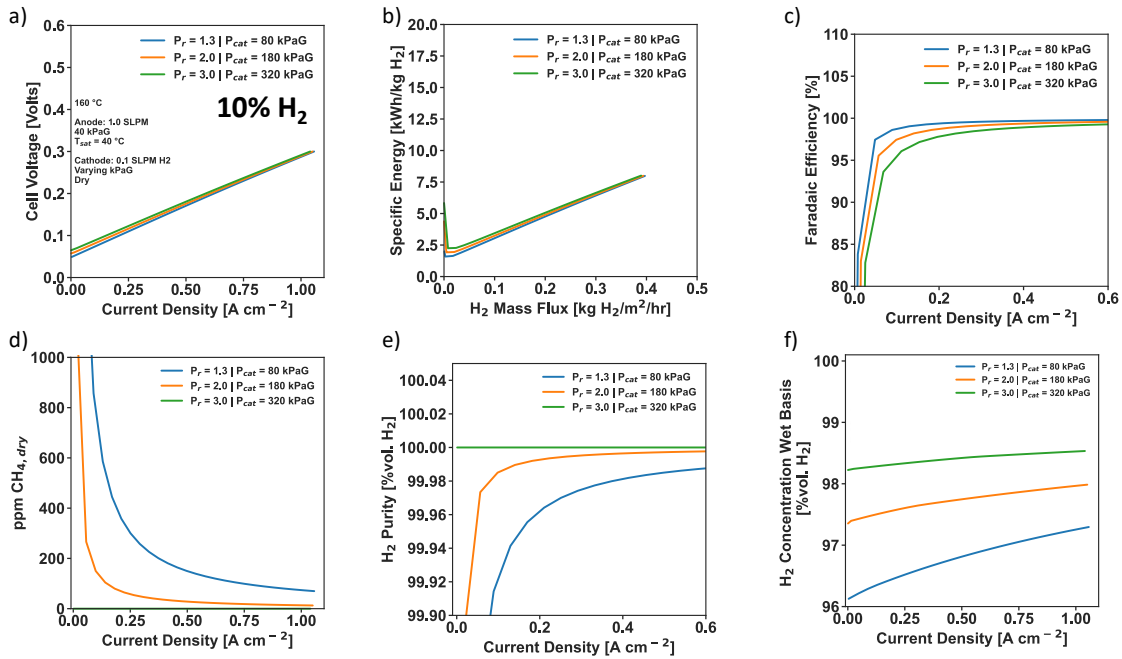


Figure 7.15 Varying compression ratio for 10% H<sub>2</sub> feed in HT-PEM EHP.

At 2% H<sub>2</sub> feed, separation cost and voltage climb more rapidly with hydrogen production rate, and the sensitivity to faradaic efficiency is higher due to the limit in maximum current density and thus maximum hydrogen production rate. While purities in excess of 99.99% H<sub>2</sub> were obtained at  $P_r = 1.3$ , the maximum methane concentration requirements are not met until  $P_r > 2$ , and only at current densities approaching the limit for  $P_r = 2$ , thus requiring ~10% of H<sub>2</sub> LHV to meet fuel cell quality standards from a 2% H<sub>2</sub> feed.

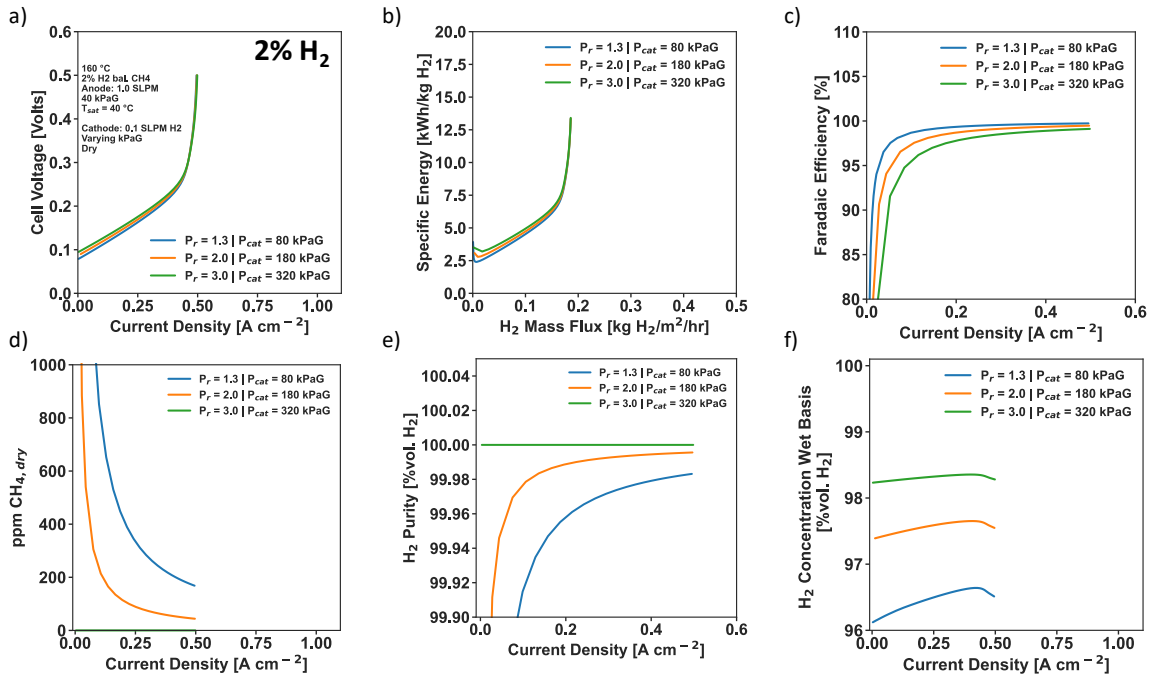


Figure 7.16 Varying compression ratio for 2% H<sub>2</sub> feed in HT-PEM EHP

Voltage loss break-down analysis for the two cases examined above highlight the thermodynamic limitations at these low hydrogen concentrations. Achieving appreciable flux requires reasonable overpotential beyond open-circuit potential to ultimately justify the material costs of the HT-PEM EHP. At 0.1 V, very little material improvements would provide significant reduction in overpotential due to the low current densities achieved, 0.05 and 0.2 A cm<sup>-2</sup> for 2 and 10% H<sub>2</sub> respectively. Increasing compression ratio further exacerbates this issue, but also offsets the need for downstream compression which could be more energetically intensive if done in a separate mechanical compression process. At 0.2 V, the influence of additional compression is minimal relative to other losses such as ohmic and kinetic sources which are largely unaffected by compression ratios up to P<sub>r</sub> = 3.

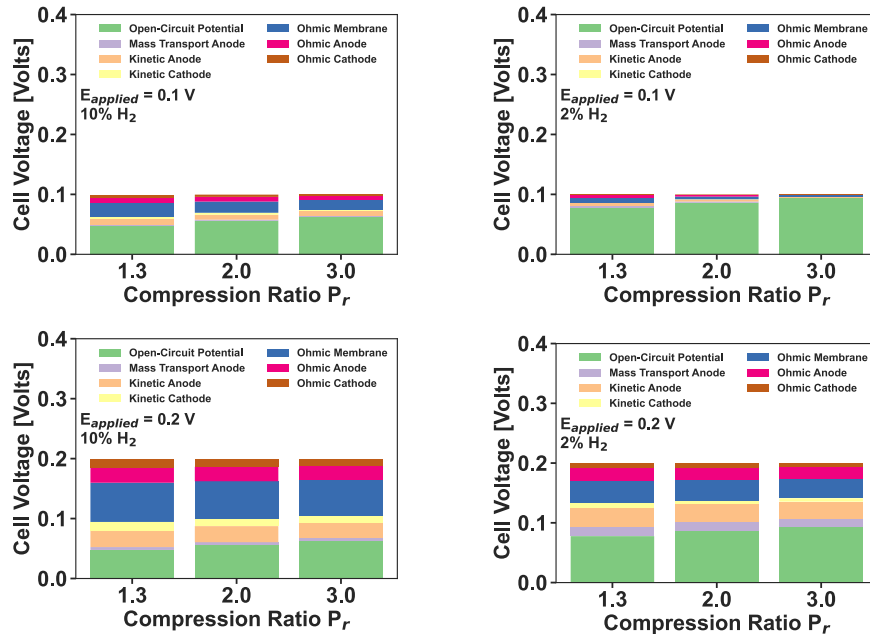


Figure 7.17 Voltage loss breakdown of increasing compression ratio for 2 and 10%  $H_2$  at 0.1 and 0.2 V cell voltage.

### 7.3.5 Influence of electrode acid content on HT-PEM EHP

As demonstrated in bench scale testing in  $5\text{ cm}^2$  MEAs, there is a consistent influence on HT-PEM EHP polarization and degree of phosphoric acid imbibed into the electrode phase. Here, the model is exercised to validate the acid phase relations employed against experimental data.

Figure 7.18 shows the agreement between model and MEA testing for acid content up to  $20\text{ mg PA cm}^{-2}$ . While data was gathered up to  $40\text{ mg PA cm}^{-2}$  in MEA, the inclusion of this much acid physically in the model exceeds the effective pore volume of the catalyst layer and is thus not a valid value for the simulation boundaries. In testing, this much acid exhibited mass transport limitations suggesting flooding of the catalyst layer and likely appreciable acid movement into the GDL and channel as well as laterally squeezed out through gasket layers. The model is bounded by the requirement that no acid leaves the catalyst layer and membrane phases and is thus not able to capture this effect.

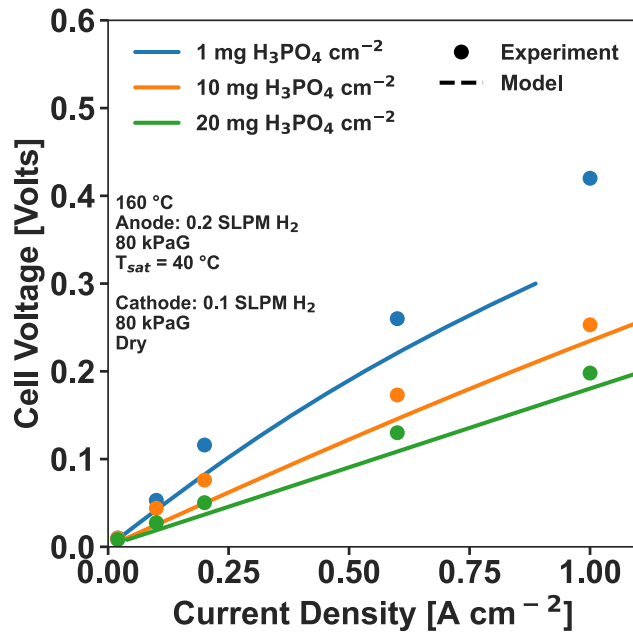


Figure 7.18 Validation of varying electrode acid content with experimental polarization curves.

The agreement for the lower acid content cases is reasonably in line with experimental measurements. The influence of lower acid contents on higher overpotentials is shown, with the characteristic non-linear polarization attributed to higher kinetic overpotentials apparent in the experimental data and in the model. Voltage loss break-down (Figure 7.19) in the model predicts that increasing phosphoric acid contributes to reductions in overpotential first by improving the kinetics of the electrode phases. Further addition of acid as a more positive influence on ohmic overpotentials. At 20 mg PA cm<sup>-2</sup>, some mass transport over potential begins to be observed, but it is very small at 1 to 3 mV, portending what happens with further addition of phosphoric acid to the electrodes.

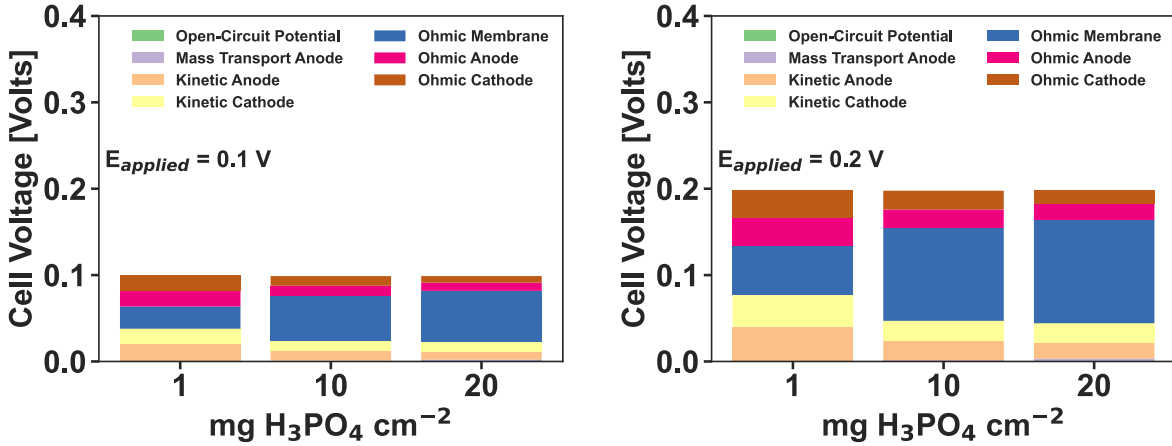


Figure 7.19 Voltage loss breakdown of varying acid electrode content.

Kazdal et al. demonstrated that the distribution of acid and its composition along the channel of an HT-PEM fuel cell was most concentrated at the anode inlet (Figure 7.20 right). In HT-PEMFC, the expansion of the phosphoric acid phase with increasing water content has been shown to increase the performance through improvement proton conductivity[163] and in other cases decrease the performance due to loss of ECSA from excessive phosphoric acid volume[135] or from reduction in partial pressure of reactants and phosphoric acid leaching[203].

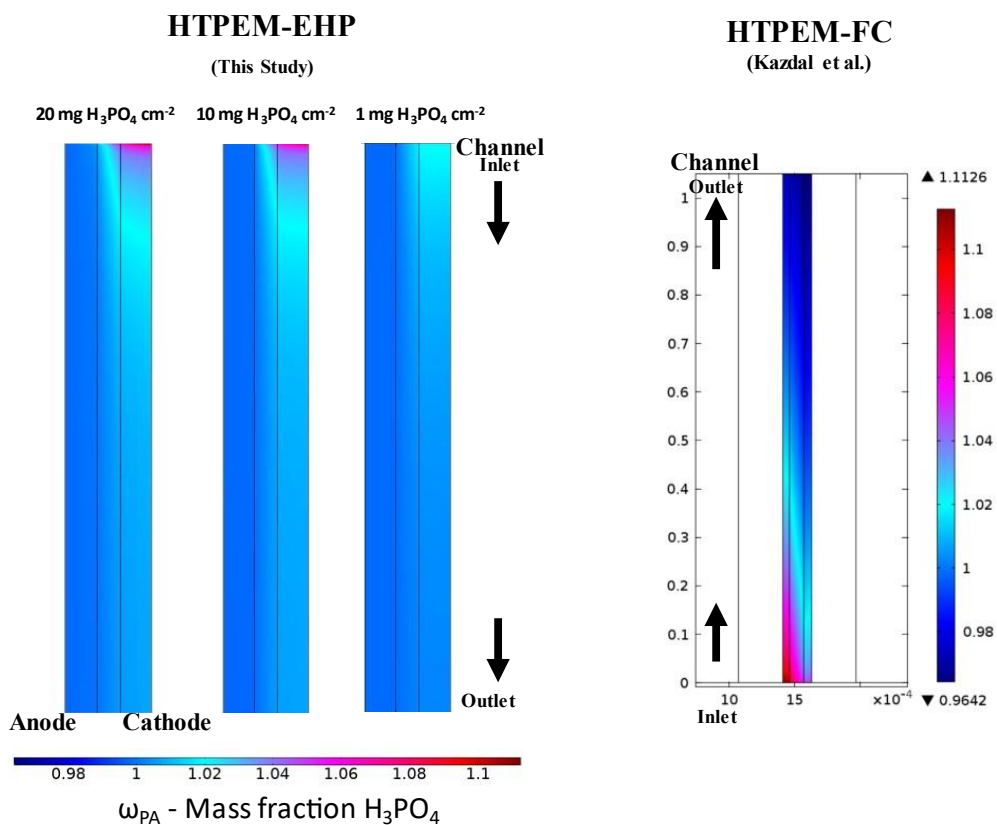


Figure 7.20 Acid distribution of HT-PEM EHP and HT-PEMFC[134].

For HT-PEM EHP (Figure 7.20 LEFT), where the water content and thus distribution of acid is more controllable these effects are not as significant as the distribution of acid is relatively more uniform as is the composition. Furthermore, the negative effect of PA leaching at high current densities is also not as much of a concern as the water content is independent of current density.

## 7.4 Summary & Conclusions

A two-dimensional physical model of a PBI-PA based HT-PEM EHP was implemented in COMSOL with an along-the channel geometry configuration and detailed descriptions of gaseous species transport, water and phosphoric acid phase properties, and the impact of phosphoric acid on the electrochemical properties of the catalyst layers. Very little literature

concerning HT-PEM EHP simulation at this degree of detail exists to date, and hopefully the model will help to inform further work in HT-PEM EHP for gas separation.

The model successfully captured the effects of mass transport limitations due to dilute H<sub>2</sub> gas feeds and the sensitivity of electrode polarization to electrode acid content. Gas cross-over and membrane water transport, while not considered in many HT-PEMFC models, is of great interest to HT-PEM EHP operation. Gas cross-over was implemented with empirical determined coefficients based on cross-over measurements of H<sub>2</sub> and CH<sub>4</sub> in MEA and implemented as a source/sink type mass transfer. This method of implementation ran into limitations at very high compression ratios effective cross-over rates of methane reached near-zero values that are non-physical. Water transport was modelled based on bulk aqueous phosphoric acid properties. The predicted transfer of these gaseous impurities showed that limited compression was needed to largely eliminate the presence of methane impurities in the cathode, but water vapor will generally be present in appreciable amounts requiring downstream drying of hydrogen product gas before further compression and utilization in processes requiring high purity, fuel cell quality hydrogen.

The voltage losses associated with compression of H<sub>2</sub> while separating hydrogen gases was shown to be relatively minimal as overpotential in large part occurs due to ohmic, followed by kinetic losses which were relatively unaffected by increasing cathodic pressures. At very low H<sub>2</sub> concentrations of 2% H<sub>2</sub> by volume, the co-compression of H<sub>2</sub> during gas separation does add appreciable separation costs due to the high thermodynamic penalty and the limited amount of hydrogen production as reactant starvation regimes are reached, and the relatively larger impact of parasitic hydrogen loss to hydrogen back-diffusion.

The model also highlights the appreciable difference in acid phase to HT-PEMFC, where the water content of the phase is entirely tunable by the degree of gas humidification. This can circumvent many concerns regarding PA leaching and reduced HT-PEM performance due to excessive swelling of the PA phase, while taking advantage of the enhanced proton conductivity and inhibited PA anhydride formation from the introduction of relatively low amounts (~1 to 2% relative humidity) of humidification.



## **Chapter 8      Stability and performance of Ion-Pair HT-PEM for EHP application**

### **8.1 Introduction**

To determine whether the promising characteristics of HT-PEM electrochemical cells based on ion-pair membranes, exemplified in HT-PEMFC testing, can also prove promising for HT-PEM EHP cells in natural gas separation application, the behavior of the ion-pair membrane in a EHP environment needs to first be assessed in terms of stability and performance. In the earliest publication of QAPOH-PA in HTPEM FC, the ion-pair membrane was paired with ion-pair based ionomeric binder that utilizes phosphoric acid as the conductive medium in the electrode akin to PBI based HT-PEMFC. In this configuration the ion-pair based HTPEM-FC was able to demonstrate superior stability in humid and lower temperature conditions, and comparable performance with superior stability at 160 °C in highly humidified conditions to PBI based HT-PEMFC. In non-humidified conditions, the ion-pair MEA performance was severely impacted, whereas PBI based HT-PEMFC performance was minimally impacted.

State-of-the-art HT-PEMFCs based on a QAPOH-PA ion-pair membranes have shown the necessity of utilizing ionomeric binder based on phosphonic acids in the electrodes to attain performance that is comparable to PBI-based HT-PEMFC[155]. Most recently researchers were able to demonstrate that a combination of sulfonic acid based ionomer, such as Nafion®, blended with a phosphonic acid based ionomer phosphanated polypentafluorostyrene (referred to as ‘PWN’) can achieve further performance improvements[157].

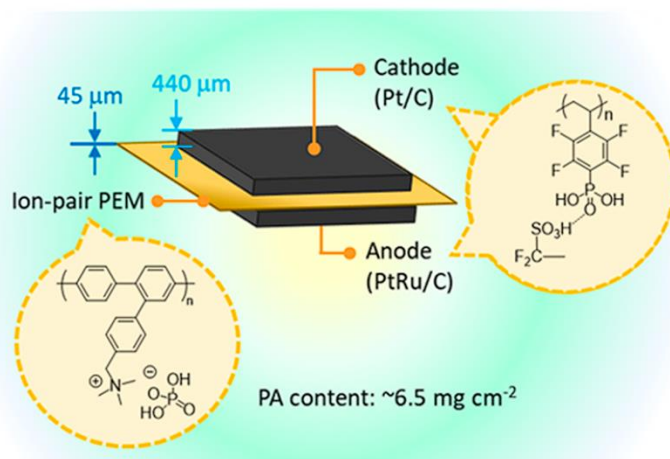


Figure 8.1 Ion-pair HT-PEM MEA with protonated phosphonic acid electrodes. Reproduced from [158].

In HT-PEM EHP conditions, the water content of the MEA environment is solely controlled through the humidification of gas flows into the cell. It is thus important to understand the interaction between humidification of the gas streams and the ion-pair based MEAs for HT-PEM EHP. To isolate the membrane characteristics of the ion-pair in HT-PEM EHP, an ion-pair based MEA is first examined using non-ionomeric gas diffusion electrodes GDE. For comparison, ionomeric GDEs containing a blend of Nafion®/PWN ionomer akin to those employed in comparable fuel cell literature are examined in like manner to ascertain the role of the ionomer in the performance and stability of the HT-PEM EHP.

## 8.2 Experimental Materials

### 8.2.1 Membrane

Orion CMX membranes are acquired in Br<sup>-</sup> form and prepared for HT-PEM application through a series of ion exchange processes. First the membrane is immersed in 1M NaCl solution for 1 hr to exchange to Cl<sup>-</sup> form, which was recommended by the manufacturer intended to improve the mechanical stability of the polymer before exchanging to OH<sup>-</sup> form. The membrane is rinsed with DI water thoroughly and then immersed in 1M NaOH solution overnight to convert to OH<sup>-</sup> form. In the final step, the membranes are again rinsed with DI water before immersion in 85% weight ortho-phosphoric acid solution in a sealed container that is placed in an oven at 65 °C for 3 days to convert to the biphosphate anion ion-pair form for HT-PEM use (Figure 8.2).

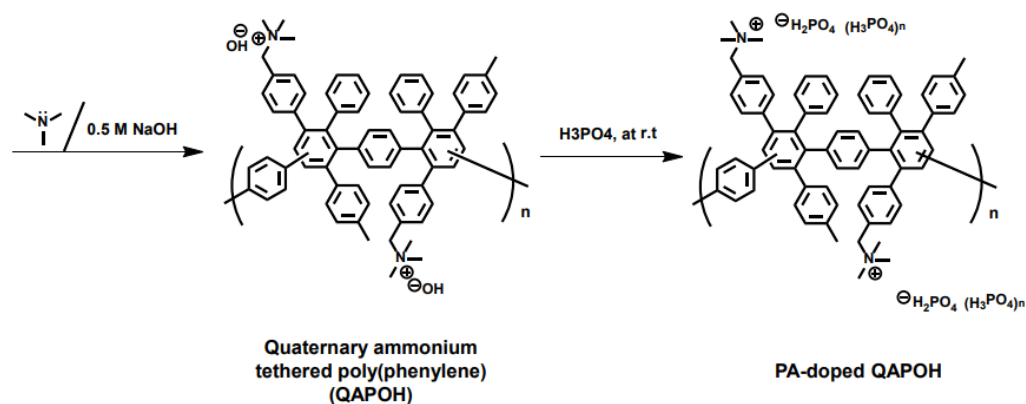


*Figure 8.2 Ion exchange process for QAPOH membrane from OH<sup>-</sup> to biphosphate anion form[230].*

### 8.2.2 MEA Assembly

Electrode coating was prepared using 47% wt Pt/C platinum supported on carbon catalyst (Tanaka Precious Metals TEC10E50E) or 75% wt PtRu/C (Johnson-Matthey HiSpec 12100), phosphonated polypentafluorostyrene ionomer with 62% degree phosphonation (PWN62) provided by Atanasov group in powder form, and commercially available Nafion® ionomer dispersion (Nafion® D5211). Nafion® ionomer was isolated from the original solvent system by vacuum oven and then re-dispersed in at 5% wt in anhydrous N-Methyl-2-Pyrrolidone (NMP) solution system and sonicated in ice bath until fully dispersed. PWN62 was similarly dispersed at 5% wt in NMP solution and sonicated until fully dispersed. PWN62 and Nafion® dispersion was blended in 1:1 wt ratio and sonicated for 1 hour. Catalyst inks were prepared by dispersion of Pt/C catalyst into NMP solvent and the PWN62/Nafion® ionomer blend to attain an I/C ratio of 0.65 for Pt/C and 0.3 for PtRu/C corresponding to ~10% wt ionomer in the electrodes. The resulting ink was ball milled for at least 24 hours followed by 30 minutes of bath sonication before spray-coating on to gas diffusion layer (Figure 8.3). CeTech WS1011 carbon cloth gas diffusion layers (380 μm thickness) with microporous layers were coated by air spray-gun with targeted loading of 1.0 mg Pt cm<sup>-2</sup>. Final platinum loading of the GDEs were verified by gravimetric and X-ray fluorescence measurements.

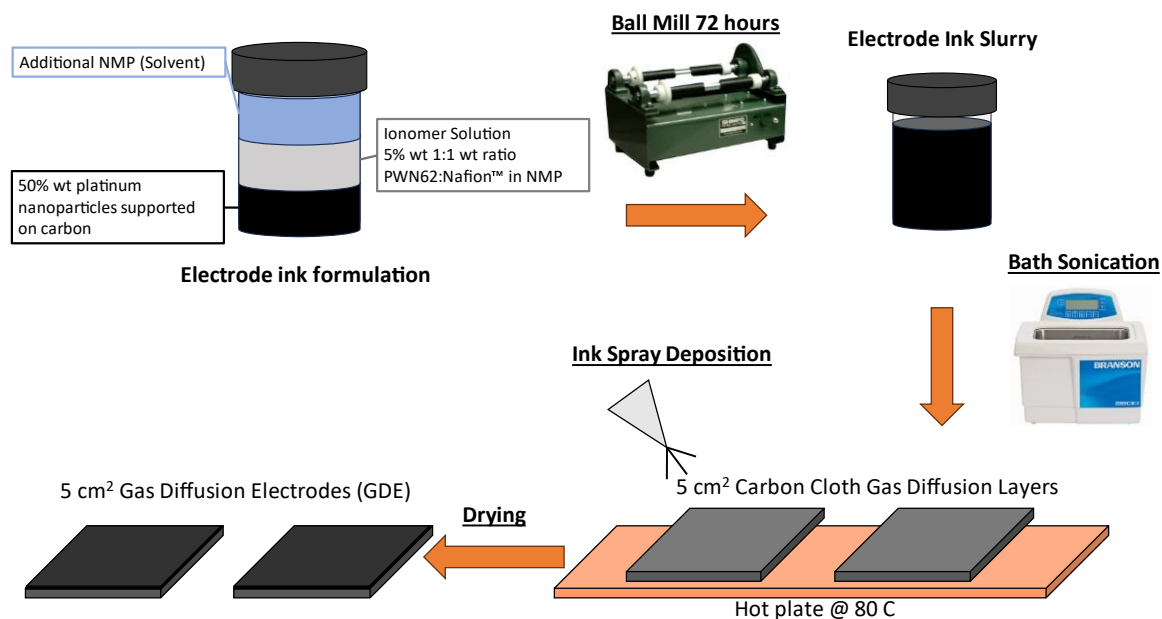


*Figure 8.3 Ionomeric GDE fabrication process*

For the non-ionomeric GDEs, 5 cm<sup>2</sup> gas diffusion electrodes are provided by Tecnologie De Nora consisting of Pt/C electrodes and carbon cloth with an MPL structure embedded in the GDL and hydrophobic binder. The platinum loading of the electrodes is 1 mg Pt cm<sup>-2</sup> for anode and cathode side measured by X-ray Fluorescence.

For MEA assembly, Kapton sub-gaskets are framed around the membrane and reinforced PTFE gaskets control the compression of the GDEs to 50%. No phosphoric acid is added to the electrodes before assembly as is typically employed with low acid doping (ADL) level PBI membranes that do not squeeze sufficient phosphoric acid from the membrane to the electrodes for optimal performance such as the Fumapem AP-30 membranes employed in Chapter 5. This makes the construction approach more akin to sol-gel based PBI membranes such as Celtec® P-1000 HT-PEMs with ADL in excess of 37 mol PA/mol RPU. All phosphoric acid electrolyte in the catalyst layer for proton conduction is thus solely provided by leaching of acid from the membrane phase from compression at time of assembly followed by further re-distribution of acid throughout operation. Since the starting thickness of the ion-pair membrane is minimal at around 45 μm post acid doping, and the ion-pair has high acid retention characteristics[158], the acid content of the electrode phase is expected to be relatively low compared to PBI HT-PEM.

The MEA is mounted in Fuel Cell Technologies high temperature cell hardware which is then plumbed to the HT-PEM test stand.

### 8.2.3 Ion-Pair HT-PEM EHP Test Stand

The HT-PEM test stand employed in Chapter 5 was utilized with slight modifications for ion-pair testing (see 5.2.1 An additional humidifier based on Nafion® coils (Fuel Cell Technologies) was added to the cathode gas feed with dry gas bypass. Humidity probes (Vaisala HMP7) were added to the anode and cathode outlets preceding the back-pressure water dropouts.

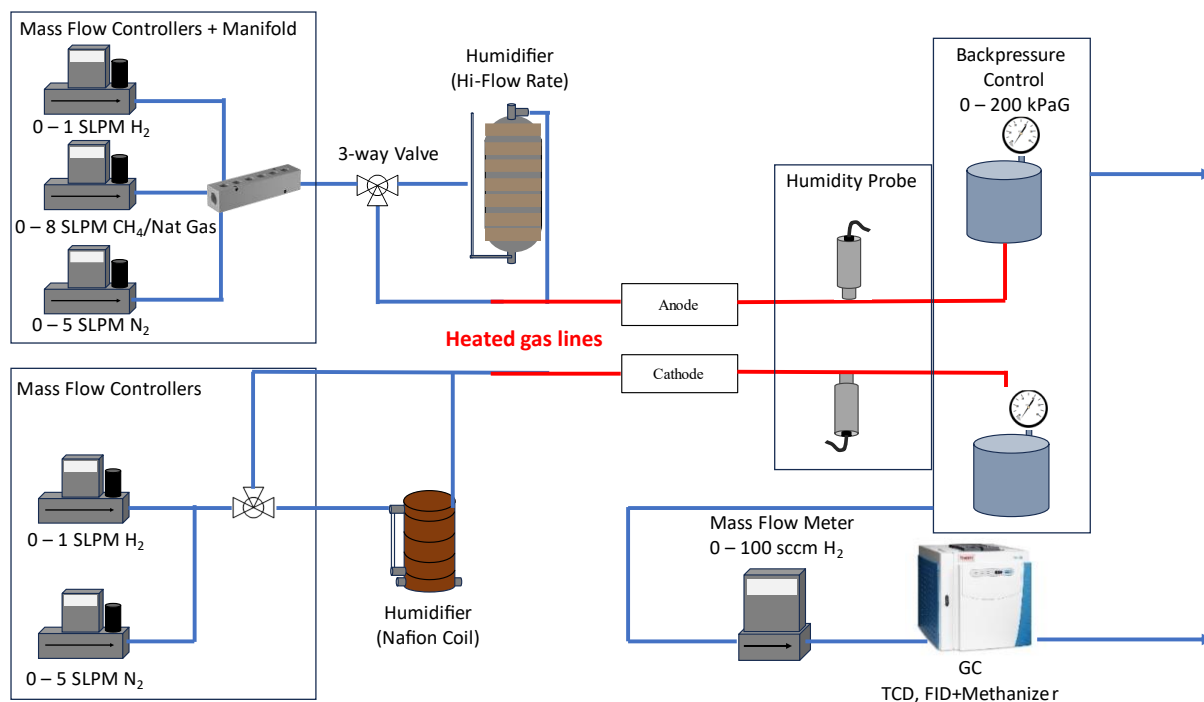


Figure 8.4 Test stand for HT-PEM EHP testing modified for Ion-pair HT-PEM.

A methanizer unit (Restek) was added to the GC upstream of the FID system to enable the detection of CO<sub>2</sub> by FID unit and to enhance sensitivity to CO for natural gas separation testing.

## 8.3 Experimental Methods

### 8.3.1 Cyclic Voltammetry

Cyclic voltammetry techniques can be employed to provide further insight into the individual electrode environment. A typical cyclic voltammogram of a platinum surface is shown below in

Figure 8.5 where hydrogen underpotential deposition region,  $H_{\text{upd}}$  can be observed in the  $\sim 0.05$  V to 0.4 V vs. RHE range and platinum oxide formation and subsequent reduction can be seen around the 0.8 V vs. RHE region.

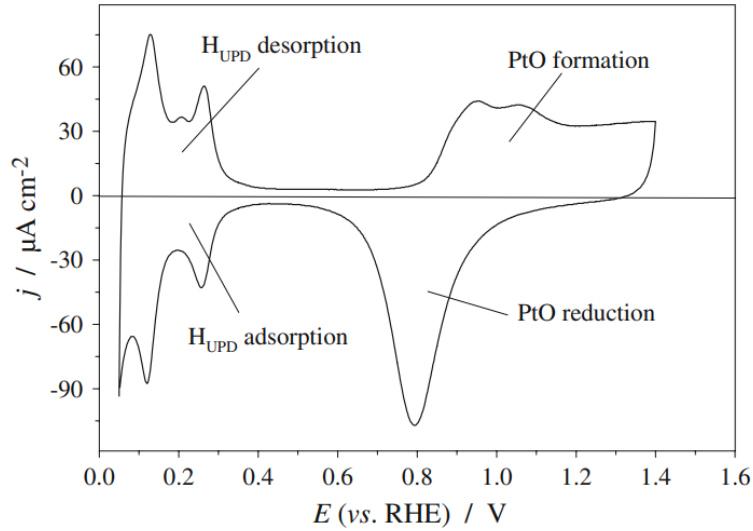
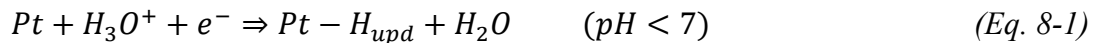


Figure 8.5 A cyclic-voltammetry profile for Pt(poly) obtained in 0.05 M

$H_2SO_4(aq)$  at  $T=298$  K and recorded at a scan rate of  $s=50$   $mV s^{-1}$ . Reproduced from [231]

The  $H_{\text{upd}}$  region describes the charge associated with the deposition of H species on a Platinum electrode surface preceding the onset of hydrogen evolution reaction (HER). In acidic media the reaction occurs as follows,



giving rise to a relatively convenient method of estimating electrochemically active surface area of platinum surface through measuring this  $H_{\text{upd}}$  charge signature[232]. By integration of the measured current response in the  $H_{\text{upd}}$  region, subtracting out pseudocapacitive current associated with double layer charging, a net charge  $Q_H$  can be obtained that can be correlated to a monolayer of hydrogen atom species adsorbed to available Pt surface.

$$Q_H = \frac{\int i dE}{\nu} \quad (Eq. 8-2)$$

From  $Q_H$  the ‘real’ active area or electrochemical active surface area ‘ $A_{real}$ ’ can be determined,

(Eq. 8-3)

$$A_{real} = \frac{Q_H}{Q_{H,s}}$$

Where  $Q_{H,s}$  is the charge density of the bulk Pt surface, often taken as  $210 \mu\text{C cm}^{-2}$  for MEA studies[233].

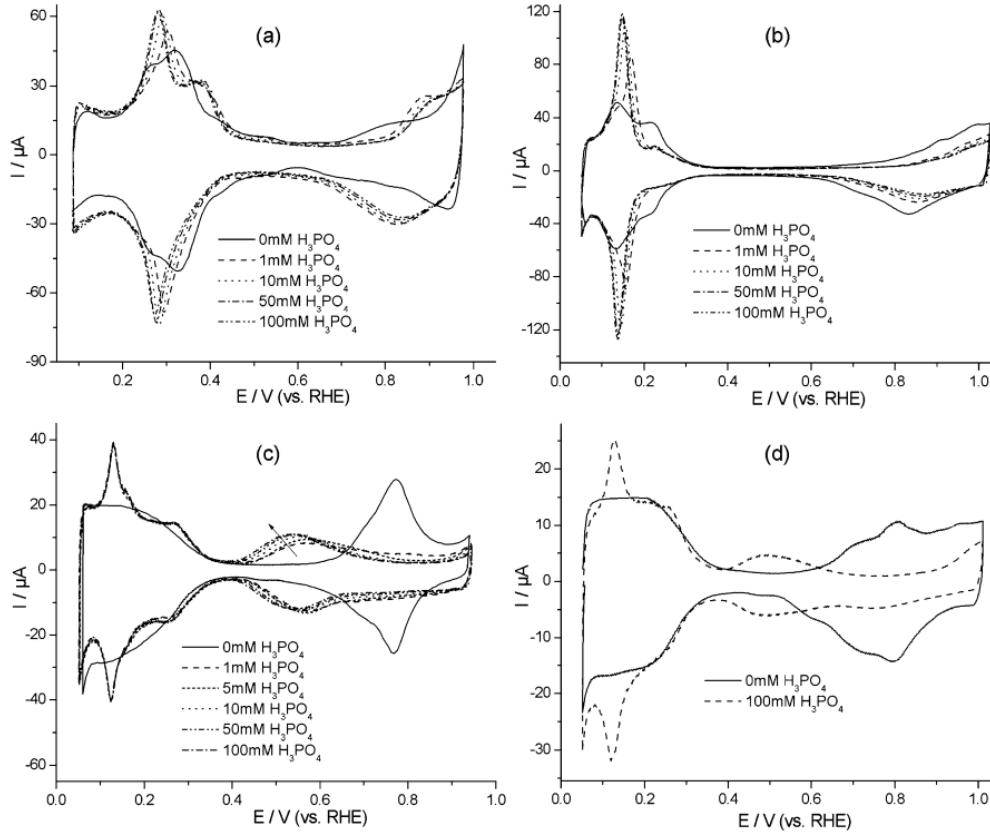
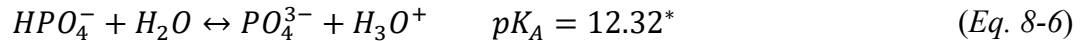
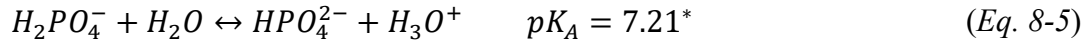


Figure 8.6 Cyclic voltammograms of (a) Pt(100), (b) Pt(110), (c) Pt(111) and (d) PtSn(111) electrodes in  $0.1 \text{ M HClO}_4$  with the addition of various amounts of  $\text{H}_3\text{PO}_4$  (shown as figure legends). Potential scan rate  $50 \text{ mV s}^{-1}$ . Reproduced from [234].

When studying the  $H_{\text{upd}}$  region for HT-PEMFC, there are a few mitigating factors that complicate an accurate assessment of  $Q_H$  from cyclic voltammetry. He et al. studied the influence of increasing concentrations of aqueous  $\text{H}_3\text{PO}_4$  on single crystal Pt interfaces in rotating disk electrode set-up and observed new CV features in some cases around the  $0.4 \text{ V}$  to  $0.6 \text{ V}$  vs. RHE potential mark with the introduction of small amounts of  $\text{H}_3\text{PO}_4$  to the aqueous

electrolyte and proposed adsorption of phosphate ( $H_2PO_4^-$ ) anions as the underlying mechanism [234] (Figure 8.6). This is supported by in-situ photoelectrochemical analysis that showed the strong adsorption of phosphate anions on platinum surface, increasing at potentials below 0.5 V associated with the shift of adsorbed  $H_3PO_4$  molecules to phosphate anion  $H_2PO_4^-$  [136]. A specialized high temperature RDE set-up employed by Lin et al. for the study of platinum catalysts in concentrated phosphoric acid electrolyte showed suppression of this phosphate anion voltametric signature could occur due to the presence of  $H_3PO_3$  that forms at potentials below 0.4 V vs. RHE[235].

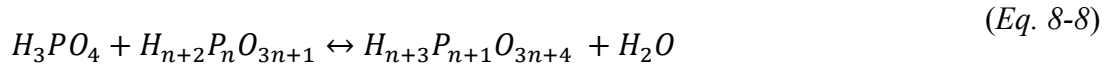
The effect of strongly adsorbed phosphate species on platinum surfaces with respect to hydrogen adsorption in the low potential range is significant[236], furthermore in elevated temperatures relevant to HT-PEM operation ( $\sim 160$  °C) the surface saturation of  $H_2$  is not well understood. In HT-PEM MEA, the phosphoric acid concentration is high ( $>95\%$  wt  $H_3PO_4$  equivalent) leading to a lower degree of ionization of  $H_3PO_4$  (favoring the right-hand side of (Eq. 8-4)) and a larger number of low-conductivity polyphosphoric acid species are formed[237][238].



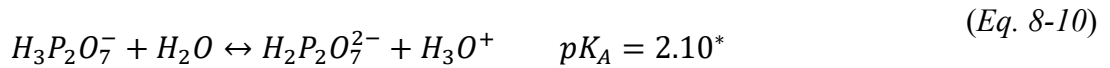
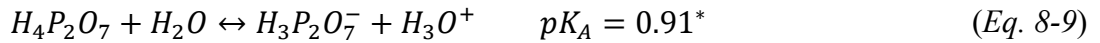
\* $pK_A$  values at 25 °C

In these high phosphoric acid concentration regimes where the condensation reactions to form polyphosphoric acid species occur ((Eq. 8-7)), platinum surface coverage has been observed to reduce even further suggesting that these condensed phosphoric acid species can further contribute to platinum surface blocking[162].





Polyphosphoric acid species ionize into diphosphoric, a relatively strong proton donor, with a higher pKa value than the phosphate anion corresponding to ortho-phosphoric acid ((Eq. 8-9))[239][240]



\*pK<sub>A</sub> values at 25 °C

The competitive adsorption of phosphate species along with the enhanced superposition of faradaic currents for HER over H<sub>upd</sub> region occurring more readily at high temperature makes H<sub>upd</sub> unreliable in HT-PEM for ECSA estimations. An alternative approach for MEA based studies of ECSA is to employ CO stripping techniques taking advantage of the strong binding characteristics of CO with platinum surfaces. Carbon monoxide is introduced to the electrode of interest at a low positive potential range ensuring monolayer coverage of the surface, followed by a stripping step of CO oxidation at potential ranges. CO stripping has been employed to some success in phosphoric acid doped PBI based HT-PEM MEAs, however additional consideration had to be taken for competing oxidation of phosphoric acid reactions at high positive potentials (<0.55 V vs. RHE) when measuring the CO stripping signal and for the lower surface coverage of CO at elevated temperatures[13][14].

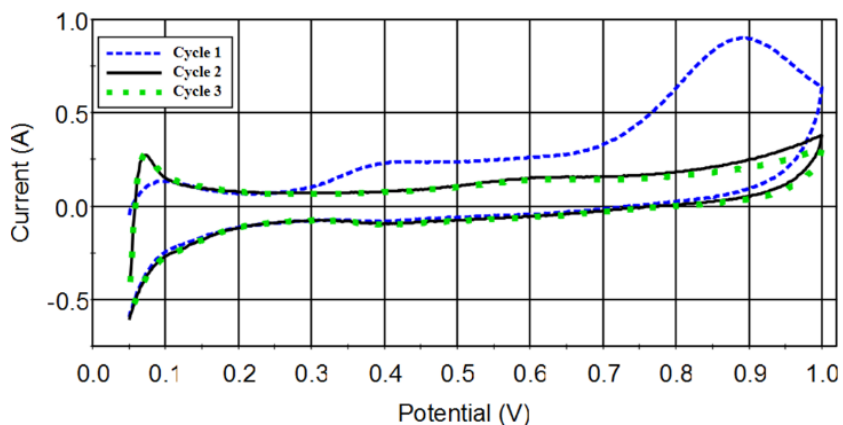
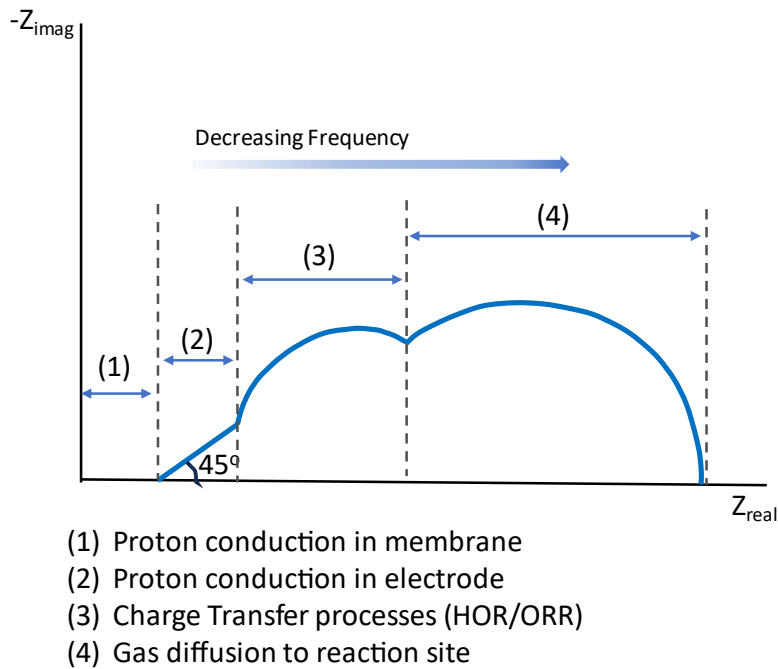


Figure 8.7 Cyclic Voltammogram of PBI based HT-PEM EHP after operation in dry condition at 160 °C for 72 hours. Reproduced from [243]

In PBI based HT-PEM EHP oxidation currents correlated with phosphate species have been observed in initial cycles of CV after extended operation in high phosphoric acid concentration conditions (160 °C,  $T_{\text{sat}} < 28$  °C) (Figure 8.7). This feature was accompanied by recovery of  $H_{\text{upd}}$  signature on subsequent cycles and recovery of EHP performance, suggesting an oxidation of strongly adsorbing phosphate or diphosphoric acid species[243].

### 8.3.2 Electrochemical Impedance Spectroscopy

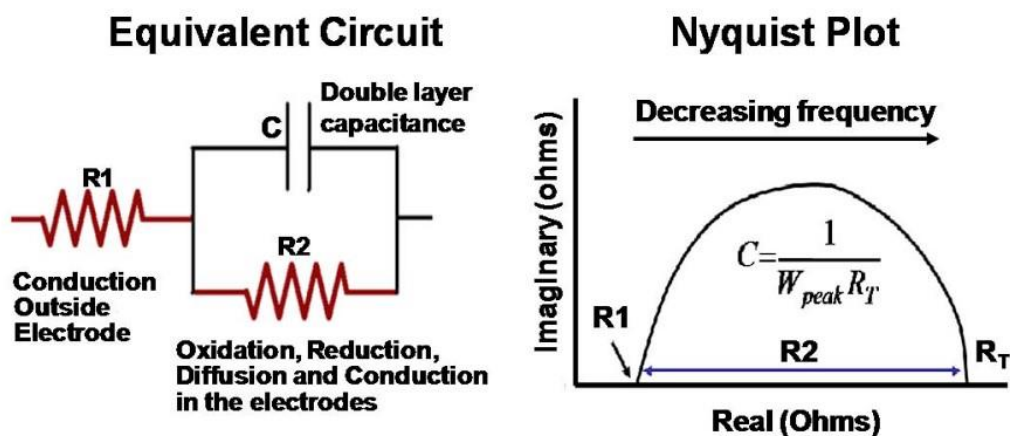
Electrochemical impedance spectroscopy (EIS) is a technique that takes advantage of the range of time scales at which different steps of electrochemical reactions occur at the interface between electrode surface and electrolyte. EIS employs an alternating current (AC) sine wave superimposed over a fixed DC signal and sweeps the frequency of the sine wave from high frequency to low. EIS data is commonly represented in the form of a Nyquist plot (Figure 8.8).



*Figure 8.8 Representative Nyquist Plot of PEM Fuel Cell EIS*

At high frequencies, only resistive elements such as electron conduction through the electronic phase and proton conduction through the continuous electrolyte phase, in this case the proton exchange membrane, show a fast enough response to the AC signal. Proton conduction through tortuous pathways in the electrode environment and then the charge transfer behind the electrode reactions begin to register and ultimately at lower frequencies gas mass transport timescales begin to become relevant.

For non-ohmic losses, frequency dependent response from AC impedance techniques can provide useful information about the electrode environment in MEA studies. Interpretation of the data relies on mechanistic models to interpret and thus requires a systematic approach to identify the different underlying mechanisms differentiated by time-domain.



$R_1$  = 'High Frequency Resistance' (HFR)

$R_2$  = 'Charge Transfer Resistance' ( $R_{CT}$ )

*Figure 8.9 Simplified Randles circuit for interpretation of EHP EIS Data*

Equivalent circuit models are typically employed to assign impedance values to various underlying processes. In EHP, the charge transfer processes of hydrogen oxidation reaction (HOR) and hydrogen evolution reaction (HER) often overlap due to their comparable kinetics. The Simplified Randles circuit is one of the simplest equivalent circuit models applied to electrochemical cell modelling, consisting of a resistor in series with a R-C circuit element (Figure 8.5). The resistance of the series resistor, the high frequency resistance 'HFR', describes the ohmic losses associated with the impedance of the membrane phase and electronic phases and the resistor in the R-C circuit describes all impedances associated with the electrodes. This delineation provides a quick way to qualitatively assess the relative contribution to overall MEA impedance from its components, albeit in a coarse manner that combines a number of charge and mass transfer processes at both electrodes into one charge transfer resistance ' $R_{CT}$ '.

$R_{CT}$  growth is observable when operating PBI based HT-PEM EHP in relatively dry conditions. In the dissertation work of Buelte[243][162], it was observed that platinum surface coverage growth rate increased at lower humidity anode feeds. It was further hypothesized then, that phosphoric acid anhydride species consisting of polyphosphoric acids, were a major contributing

factor to performance drop-off of the HT-PEM EHP due to adsorbing species as their concentration is dependent on the water content of the phosphoric acid phase which decreases with the relative humidity of the adjacent gas phase. In the ion-pair membrane environment, higher relative humidity can be introduced to a much greater extent without the occurrence of irreversible acid-water replacement degradation of the phosphoric acid present in the membrane phase[158]. This allows a probing of a phosphoric acid electrolyte electrode environment in a HT-PEM at higher humidities than was previously practical in PBI based HT-PEM EHP studies.

### 8.3.3 Distribution of Relaxation Times

Distribution of relaxation (DRT) times provides an alternative to selecting a specific equivalent circuit model comprised of a number of RC circuit elements, out of a multitude of circuit configurations that could provide a good fit to EIS data. Instead, the system is assumed to be comprised of an infinite number of RC circuit elements each with their own time constant with distinct relaxation processes occurring across different time constants. The impedance response is represented instead as a distribution of these relaxation times with respect to frequency or time domain, and the distribution of the impedance across these domains can provide greater insight and ability to differentiate the underlying physio-chemical mechanisms occurring in the electrochemical system[244][245][246].

The impedance response,  $Z$ , of the DRT model of the system can be displayed in a relatively simple form as a distribution of a function  $g(\tau)$  vs the relaxation times  $\tau$ [247],

$$Z(f) = R_{\infty} + \int_0^{\infty} \frac{g(\tau)}{1 + i2\pi f\tau} d\tau \quad (\text{Eq. 8-11})$$

Where  $R_{\infty}$  represents the non-zero real ohmic resistance of the electrochemical system, and the integration of the function  $g(\tau)$  with respect to  $\tau$  the impedance contribution from the time constant dependent relaxation processes. Since EIS responses are taken on log scale with respect to the frequency range measured over, the DRT response and the relaxation time distribution function are more commonly represented as[248],

$$Z(f) = R_{\infty} + \int_{-\infty}^{\infty} \frac{\gamma(\ln \tau)}{1 + i2\pi f\tau} d\ln\tau \quad (\text{Eq. 8-12})$$

Where the  $\gamma$  function is equivalent to  $\tau g(\tau)$  and the primarily goal of the DRT analysis is to obtain a reasonable estimation of the  $\gamma(\ln \tau)$  function.

Distribution of relaxation times has been applied in electrochemical system characterization across a wide range of systems, notably in solid oxide fuel cell[249][250][246] and Li-Ion battery characterization[251][252]. Recently, some efforts have been made in the application of DRT to HT-PEMFC cells based on PA-PBI[253][140][254][255] and EHP configuration[255][256]. Table 8-1 lists off the frequency domains at which appreciable impedance responses were observed for HT-PEM in PA-PBI and the physio-chemical mechanisms that were associated with them.

*Table 8-1 Literature Survey of DRT frequency domains in HT-PEM fuel cells & H<sub>2</sub> Pump*

HTPEM DRT Frequency Domains by Physio-chemical Response – [Hz]						
Type of Cell	Mass Transport	Cathode/ORR	Anode/HOR	Cathode/HER	Electrode H+ Conduction	Source
Fuel Cell	≤ 2	2 - 60	100 - 1000	-	1000 - 5000	[253]
Fuel Cell	-	10 - 100	≥ 100	-	-	[254]
Fuel Cell + H <sub>2</sub> Pump	≤ 1	30	100 - 20000	100 - 20000	100 - 20000	[255]
Fuel Cell	-	15 - 150	≥ 150	-	≥ 150	[140]
H <sub>2</sub> Pump	0.1 - 10	-	10 - 100	100 - 1000	≥ 10000	[256]

### 8.3.4 Cell Start-Up and Conditioning

The HT-PEM EHP is initially heated under dry nitrogen flow to 40 °C. At 40 °C hydrogen is fed to the anode at 0.2 SLPM while the cathode is fed 0.2 SLPM nitrogen flow. Linear sweep voltammetry from 0 to 0.6 V at 5 mV/sec is used to assess initial shunt and cross-over characteristics of the cell. Following this, cyclic voltammetry is taken at both anode and cathode. The electrode under examination is fed nitrogen gas at 0.2 SLPM for 5 minutes while the reference electrode is fed hydrogen at 0.2 SLPM. Prior to the cyclic voltammogram

measurement the nitrogen gas feed to the working electrode is shut-off to mitigate influence on the cyclic voltammogram features from local nitrogen convection.

Following initial characterization, the cell is heated to 160 °C at 0.2 SLPM H<sub>2</sub> at the anode and 0.1 SLPM H<sub>2</sub> cathode. Once the cell temperature settles, the anode is initially humidified to a dewpoint temperature ( $T_{\text{sat}}$ ) of 80 °C corresponding to a vapor pressure of 47.15 kPa corresponding to optimal conditions for the ion-pair based HT-PEMFC testing[111] and the anode and cathode are pressurized to 40 kPaG for break-in.

### 8.3.5 Stability Characterization of Ion-Pair HT-PEM EHP

In conventional HT-PEM, the local vapor pressure at the electrodes and the cell temperature directly influences the composition of the phosphoric acid electrolyte and consequently greatly influences the performance and stability. The QAPOH-PA ion-pair HT-PEMs extend the viable range of relative humidity and temperatures beyond what was reasonable for conventional PA-PBI based HT-PEM systems. To assess the stability of the ion-pair HT-PEM in EHP, the humidification varied at the anode H<sub>2</sub> feed during pump operation, and in some cases on the cathode side as well, to observe changes in the stability and performance. Figure 8.10 outlines the stability and performance characterization procedure for the two HT-PEM cells under

consideration.

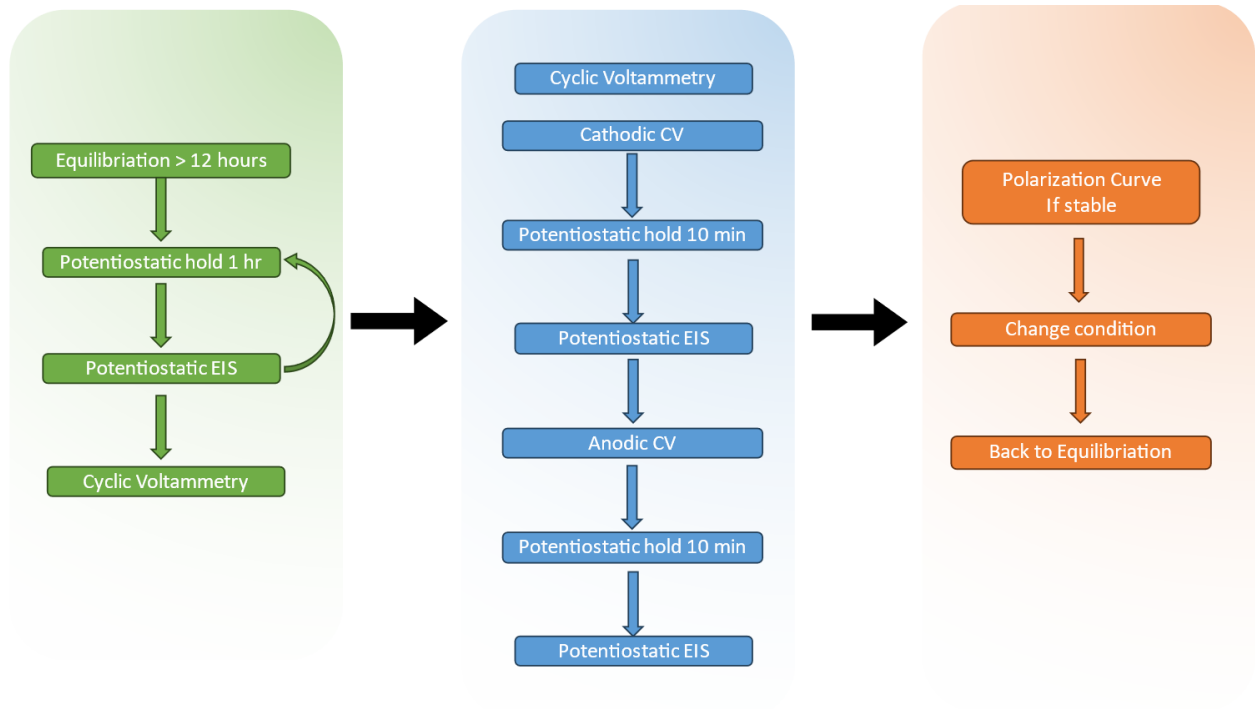


*Figure 8.10 Stability testing procedure for Ion-pair HT-PEM EHP testing.*

Prior to potentiometry, the EHP is equilibrated overnight for at least 12 hours at the operating conditions, this equilibration time is primarily for considerations of relative humidity step changes when changing the humidification of the anode gas feed and/or the cell temperature. Following equilibration, the EHP is held under potentiostatic hold at 0.1 V with EIS taken periodically every hour at 0.1 V with an AC amplitude of 5 mV and frequency range from 200,000 Hz to 0.01 Hz. This condition is held until the voltage response for at least 8 hours.



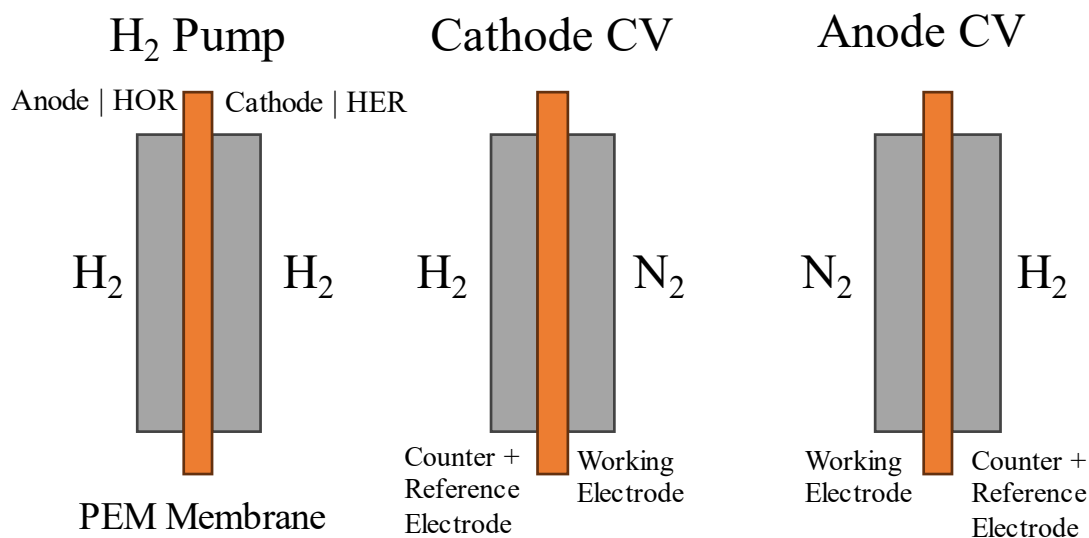


*Figure 8.11 Gas and electrode configuration for Ion-pair HT-PEM EHP operation and cyclic voltammetry measurements.*

Cyclic voltammetry is performed following potentiostatic holds to probe the electrode environment. The electrode of interest is fed nitrogen gas and treated as the working electrode while the remaining electrode continues hydrogen gas flow to serve as a RHE. To maintain electrode environment to the same as the potentiostatic hold condition, the anode remains humidified at the relevant condition and the cathode gas remains a dry feed. During cyclic voltammetry, nitrogen gas flow is cut to the working electrode.

Cathodic CV is measured first, followed by a short 10-minute potentiostatic hold to stabilize the system for EIS measurement. The process is then repeated for an anodic CV. If the system is stable in the measured condition, polarization curves are taken before changing humidification and/or temperature.

EIS data is fitted to a simplified Randles circuit with an additional series inductor to account for inductance of the cables and instrumentation[257]. The circuit can be represented schematically as follows,

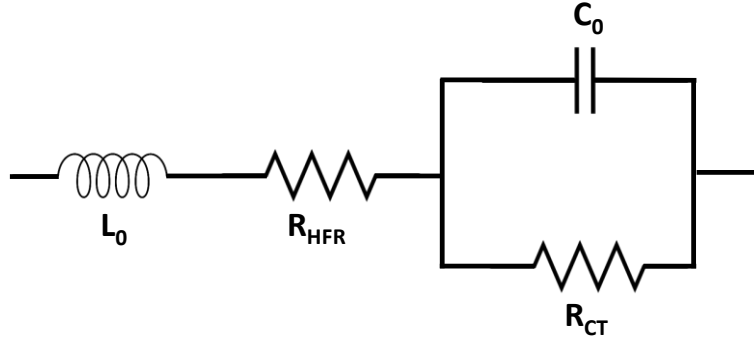


Figure 8.12 Simplified Randles equivalent circuit model with additional inductor element for EIS data interpretation.

With the values of interest HFR and  $R_{CT}$  fitted to the model with (Eq. 8-13) by a Levenberg-Marquardt least squares minimization.

$$Z = j\omega L_0 + R_{HFR} + \frac{1}{j\omega C_0 + \frac{1}{R_{CT}}} \quad (\text{Eq. 8-13})$$

## 8.4 Results & Discussion

### 8.4.1 Non-Ionomeric Gas Diffusion Electrodes

The stability of the HT-PEM EHP under varying humidified gas conditions are initially examined by potentiostatic experiments. A voltage hold of 0.1 V is utilized to operate at appreciable current densities while still being able to perform electrochemical impedance spectroscopy every hour. The EIS spectrum gathered from these humidification tests are displayed below in Figure 8.13. Humidification of  $T_{sat} = 80\text{ }^\circ\text{C}$  is selected as an upper boundary based on previously reported stability of the QAPOH-PA membrane at these high humidities. Additionally, measurements at  $T_{sat} = 40\text{ }^\circ\text{C}$  is of interest as it corresponds to the minimum humidification level before which pure phosphoric acid phase begins to dehydrate, making it the typical operating humidity for PBI-based HT-PEM EHP. Lastly, dry gas feed stability is probed.

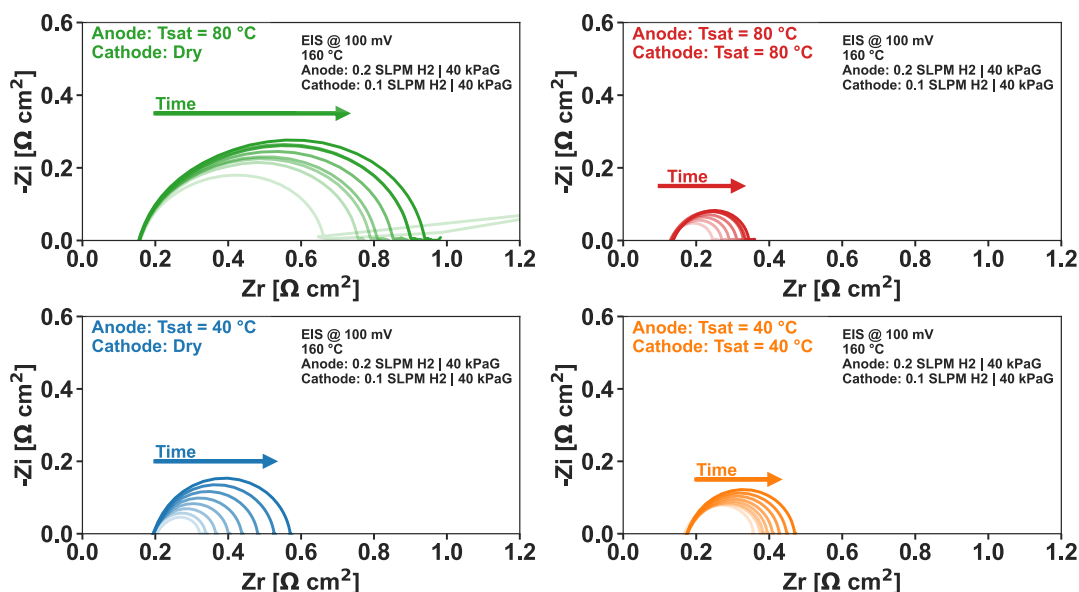


Figure 8.13 EIS of non-ionomeric Ion-Pair HT-PEM in potentiostatic stability testing.

Initially, the HT-PEM EHP was operated with humidified anode feed of  $T_{\text{sat}} = 80\text{ }^{\circ}\text{C}$  and dry cathode feed. Even at this high level of humidification, the electrode impedance characterized by  $R_{\text{CT}}$  is high to start and grows over time. A cleaning cyclic voltammetry protocol was employed after 8 hours of stability testing for all humidity conditions. For the initial case of  $T_{\text{sat}} = 80\text{ }^{\circ}\text{C}$ , the CV protocol was employed at the start of test but did not seem to have a large impact on initial performance. Despite this, the recovery upon carrying out the cyclic voltammetry protocol was appreciable, with a current density increase of  $0.1\text{ A cm}^{-2}$  to  $0.2\text{ A cm}^{-2}$  following cathodic cyclic voltammetry sweeps and climbing to approximately  $0.6\text{ A cm}^{-2}$  following the anodic sweep (Figure 8.14).

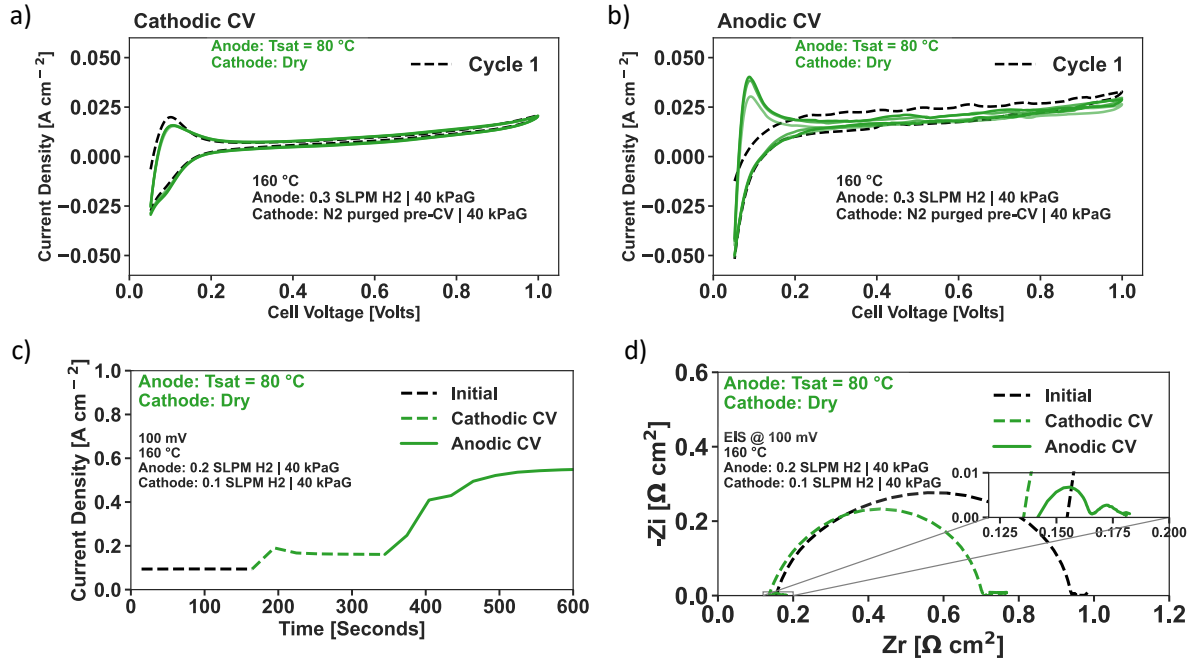


Figure 8.14 Effect of cyclic voltammetry on non-ionomeric HT-PEM EHP at anode feed  $T_{sat} = 80$  deg C. a) Cathodic CV and b) anodic CV, c) shows the amperometric response before and following anodic and cathodic CV d) EIS spectrum before and following cathodic and anodic CV.

During the cathodic sweep, no observable increase in catalytic surface area is apparent from the  $H_{upd}$  region. EIS scans indicate a slight reduction in HFR and appreciable reduction in  $R_{CT}$  following the cathodic sweep. The subsequent anodic sweep displays a growth in  $H_{upd}$  across the cycles, with the following EIS measurement showing reduction in  $R_{CT}$  indicating near-zero electrode impedance and minimal shift in HFR.

Extracted HFR and  $R_{CT}$  values from EIS measurements during 0.1 V potentiostatic measurements are collated below for the different humidification scenarios. In all cases HFR settles in the first hour, but  $R_{CT}$  fails to stabilize for any condition. In the cases of humidification of both gas streams, the rate of  $R_{CT}$  growth is inhibited relative to the sole anodic humidification case. Except for the initial operation post start-up, preceding any cyclic voltammetry steps, at  $T_{sat} = 80$  °C, the starting point of  $R_{CT}$  is relatively equivalent for all cases following the cyclic voltammetry cleaning procedure indicating that the mechanism of electrode impedance increase is largely reversible.

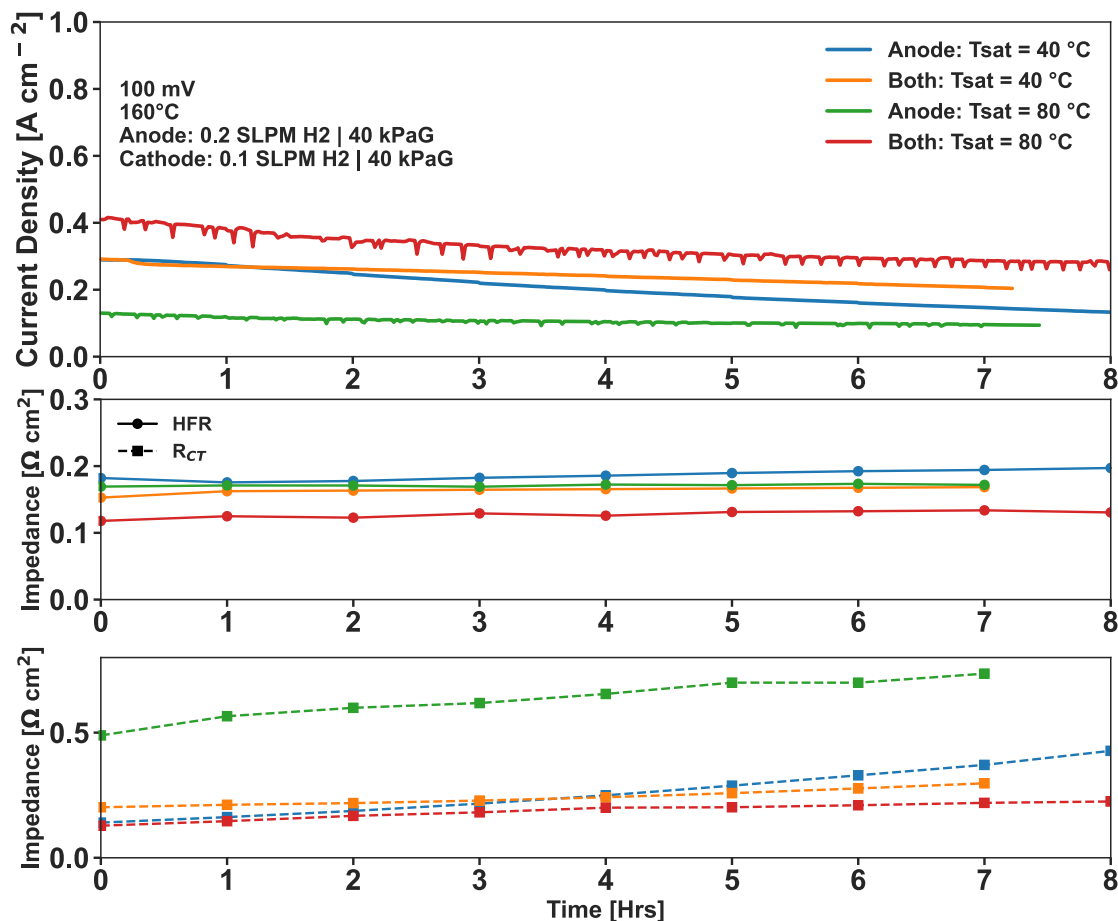


Figure 8.15 Amperometric response of non-ionomeric HT-PEM EHP at 0.1 V over time with HFR and  $R_{CT}$  measured hourly.

Across all cases of humidification testing, the cathodic CV sweep shows minimal  $H_{upd}$  change, and results in some slight reduction in HFR and  $R_{CT}$  (Figure 8.16). Proceeding the anodic sweep, the electrode impedance is near-zero in most cases, apart from anode humidified at  $T_{sat} = 40\text{ }^{\circ}\text{C}$ . This trend is reminiscent of the observed reversible electrode impedance decay when operating PBI based HT-PEM EHP at saturation temperatures below  $T_{sat} = 28\text{ }^{\circ}\text{C}$  at  $160\text{ }^{\circ}\text{C}$  [243]. There was no readily discernable charge signature outside of the hydrogen underpotential deposition region that could be associated with side electrochemical redox reactions although the signature for phosphoric acid oxidation is weak even in an RDE set-up[235] and formation of phosphonic acid and the subsequent formation of anhydride could be a possible driver for this impedance growth and the reversibility after cycling anodic and cathodic potential up to 1 V vs RHE.

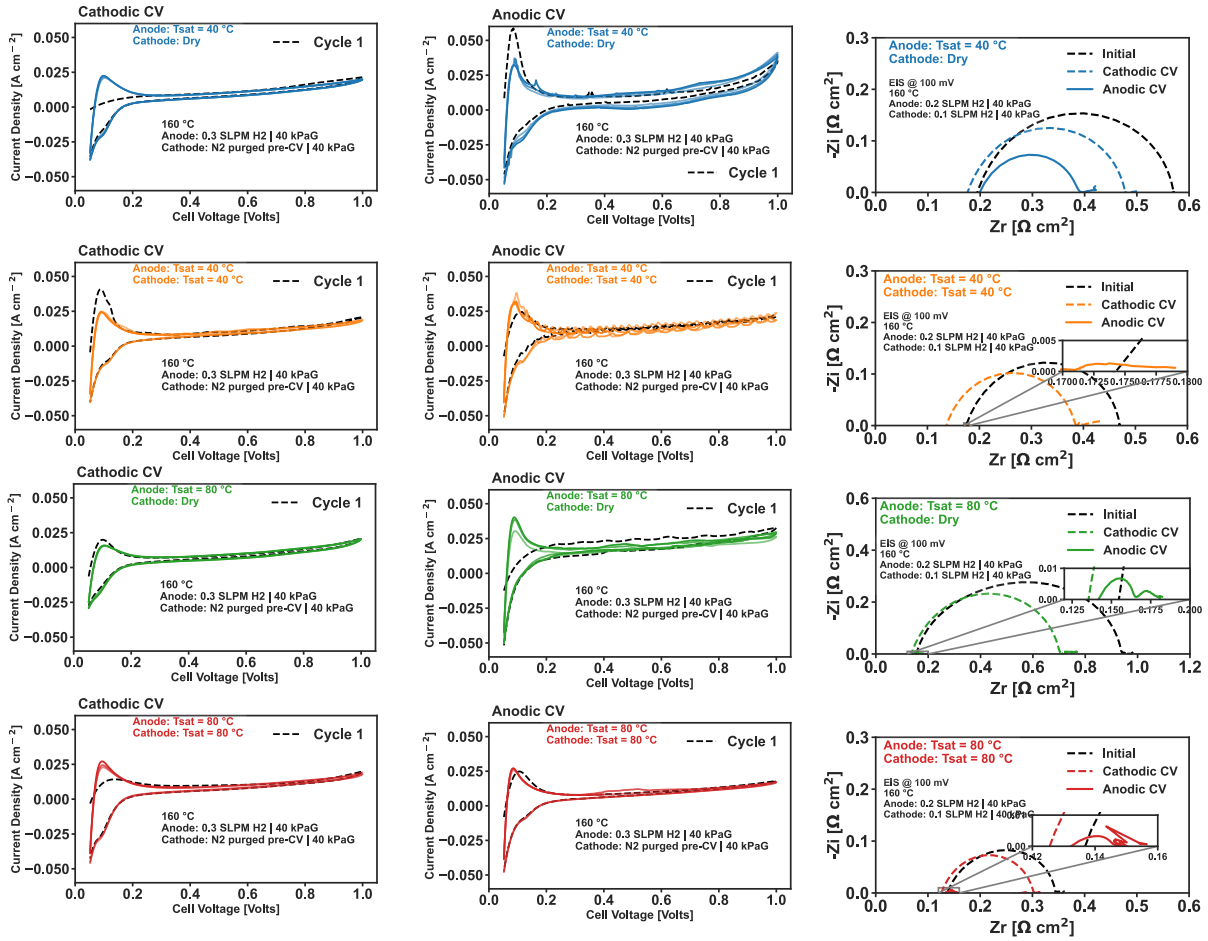


Figure 8.16 Cathodic & anodic CVs and EIS response preceding and following CV measurements for non-ionomeric ion-pair HT-PEM EHP

The operation of EHP in lieu of any humidification is desirable for simpler balance of plant and higher purity of product for gas separation applications. Dry operation data of the QAPOH-PA in MEA is not widely studied, as HTPEM-FC operation involves the local generation of water and thus the MEA environment is not entirely anhydrous. Dry gas feed operation in EHP mode only contains water present from the initial aqueous phosphoric acid present, and some water can be generated from the dehydration of phosphoric acid to pyrophosphoric acid species.

Stability of the dry operation of the QAPOH-PA with no ionomeric binder is shown below in. HFR largely stabilizes after the first several hours, with the step change in rate around the 2-hour mark coinciding with the up-tick of  $R_{ct}$  growth rate. This step change could correlate to

dehydration of the phosphoric acid electrolyte and the onset of condensation reactions ((Eq. 8-8)) as remaining water is formed from existing  $\text{H}_3\text{PO}_4$  mark although not completely.  $R_{CT}$  growth is an order of magnitude beyond what was previously observed for the humidified cases. Notably, the cathodic CV sweep led to a large increase in  $R_{CT}$ , although the total current response did not increase much in magnitude due to the already high overall impedance. Following the anodic CV sweep,  $R_{CT}$  drops appreciably while HFR is only minimally impacted. Cyclic voltammograms show that the electrode environment is greatly reduced in terms of activity towards hydrogen electrochemistry in the dry condition.

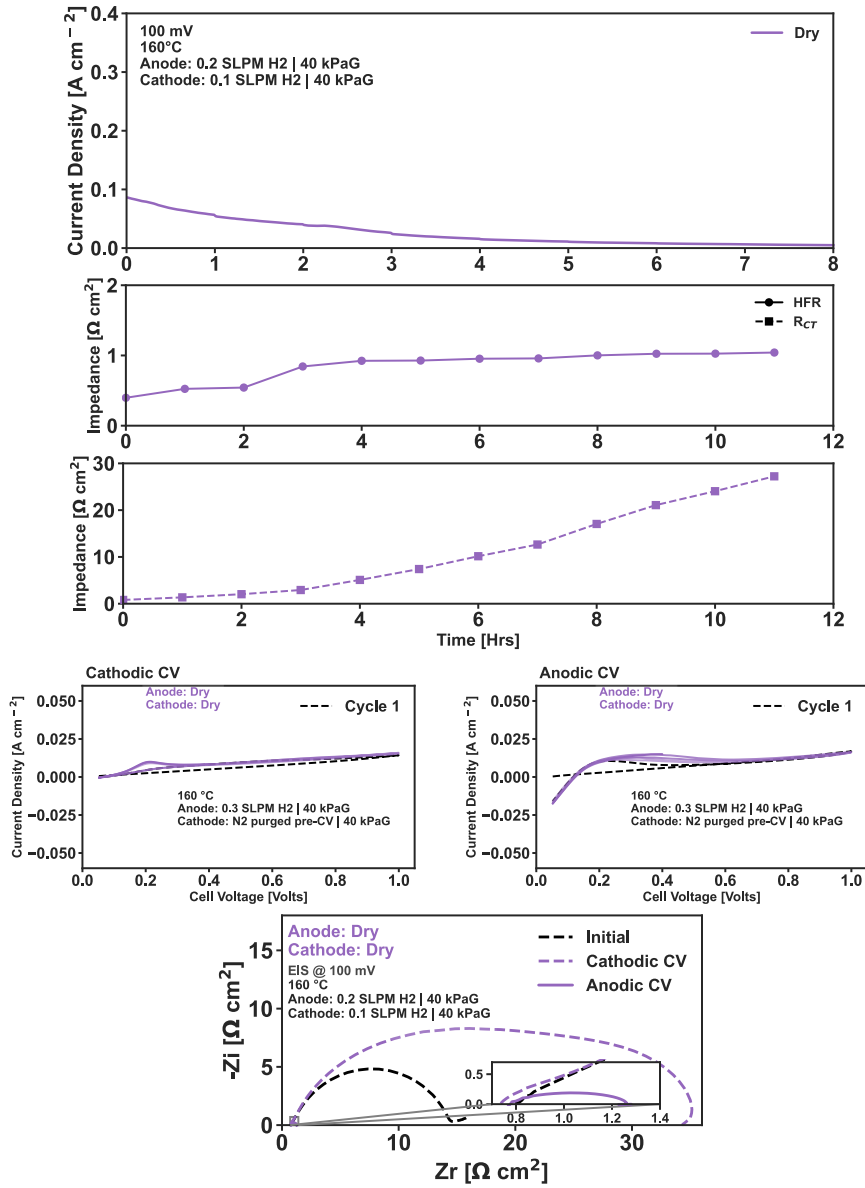


Figure 8.17 Characterization of dry operation of non-ionomeric ion-pair HT-PEM EHP

The impact of CV cleaning sweeps on the varying relative humidity cases is summarized below in Figure 8.18. Dry operation of the QAPOH-PA is likely untenable due to a large increase in HFR indicating an increase in the membrane-electrolyte phase resistance which is signature of the complete dehydration of phosphoric acid electrolyte and potential further conversion of phosphoric acid species to pyrophosphoric acid species with lower intrinsic proton conductivity. Except for the initial  $T_{sat} = 80\text{ }^{\circ}\text{C}$  anode humidification case,  $R_{CT}$  value growth rate and initial



value is higher for lower humidification cases indicating that the presence water contributes significantly to reduce electrode impedance. Humidification of both anode and cathode led to lower overall  $R_{CT}$  growth rate relative to the solely anodic humidification, indicating appreciable cathodic contribution to overall cell impedance that is similarly sensitive to humidification.

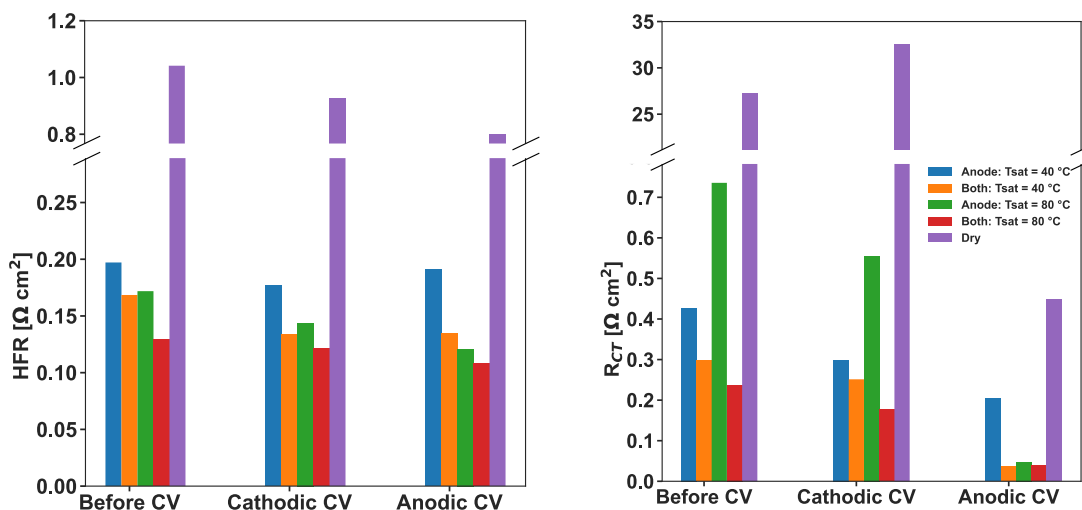
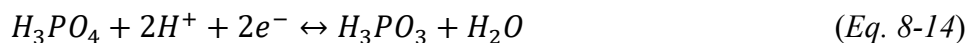


Figure 8.18 Bar chart summary of HFR and  $R_{CT}$  change due to cyclic voltammetry for non-ionic ion-pair HT-PEM EHP

The slight variation in HFR with humidity is due to the dependence of phosphoric acid electrolyte conductivity on water content in the membrane phase and is largely unaffected by the application of CV. Dramatic growth in  $R_{CT}$  at increasing dry conditions and its reversibility with potential cycling indicates that polyphosphoric acid species that form at lower water content are likely contribute to electrode blocking, and that the formation of their ionized form is reversible. Another possibility is the formation of phosphonic acid  $\text{H}_3\text{PO}_3$ , which is favorable at lower potentials (Eq. 8-14) and readily forms low conductivity anhydrides in low water conditions.



To further elucidate the underlying mechanisms behind the cleaning effect of cathodic and anodic cyclic voltammetry sweeps, the upper vertex of the cyclic voltammograms were varied to isolate a potential window at which the recovery effect largely occurs. Conditions for this vertex study are fixed solely to anodic humidification at  $T_{\text{sat}} = 40^\circ\text{C}$ , and the selected vertexes of interest are applied cell voltages of 0.5, 0.7, and 0.9 volts. The ‘pre-conditioning’ hold at 0.1 V for these conditions before the cyclic voltammograms was relatively consistent and showcased the reversibility of the  $R_{\text{CT}}$  growth mechanism (Figure 8.19). The potentiostatic hold following the 0.5 V vertex CV and preceding the 0.7 V vertex CV started at a higher  $R_{\text{CT}}$  value due to a limited recovery from the 0.5 V vertex CV (Figure 8.20).

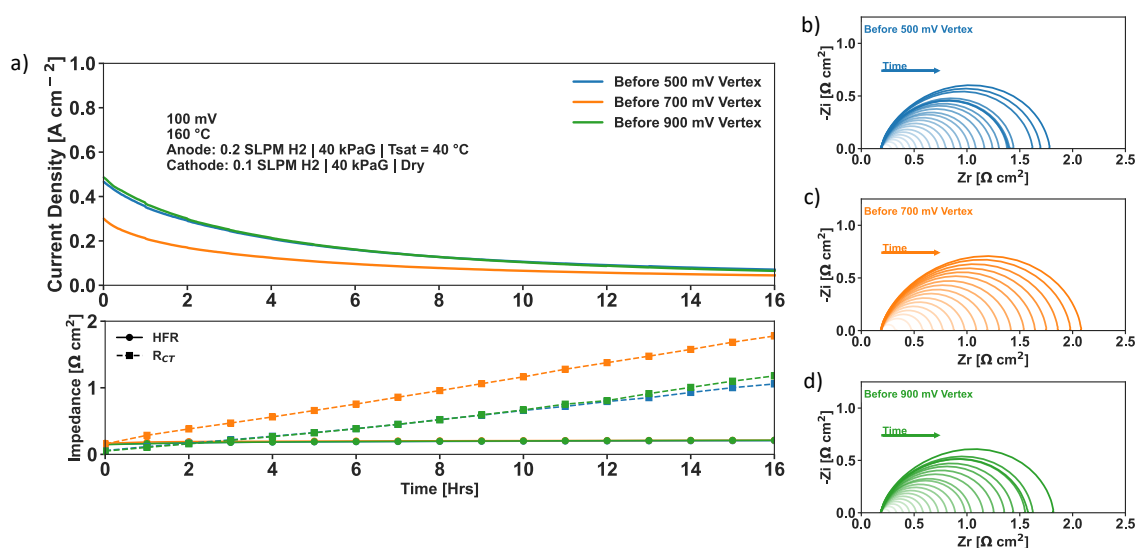


Figure 8.19 Cyclic voltammetry vertex variation on non-ionomeric ion-pair HT-PEM EHP. a) 0.1V potentiostatic hold and HFR/ $R_{\text{CT}}$  change with respect to time b-d) EIS spectra for potentiostatic hold.

Repeated CV cycles show an incremental increase in  $H_{\text{upd}}$  recovery for all cases of cathodic direction CV, and all cases save for the 0.9 V vertex sweep in the anodic direction. As was the case for the RH variation study, the cathodic CV does initially start with minimal  $H_{\text{upd}}$  region. This is likely due to the relatively dry cathode environment as this was not the case when both sides were humidified to  $T_{\text{sat}} = 40^\circ\text{C}$ . Generally, the  $T_{\text{sat}} = 40^\circ\text{C}$  anode condition for the

potentiostatic hold ends with largely suppressed  $H_{\text{upd}}$  for anode as well that is more readily recovered upon anodic sweep of at least 0.7 V vertex.

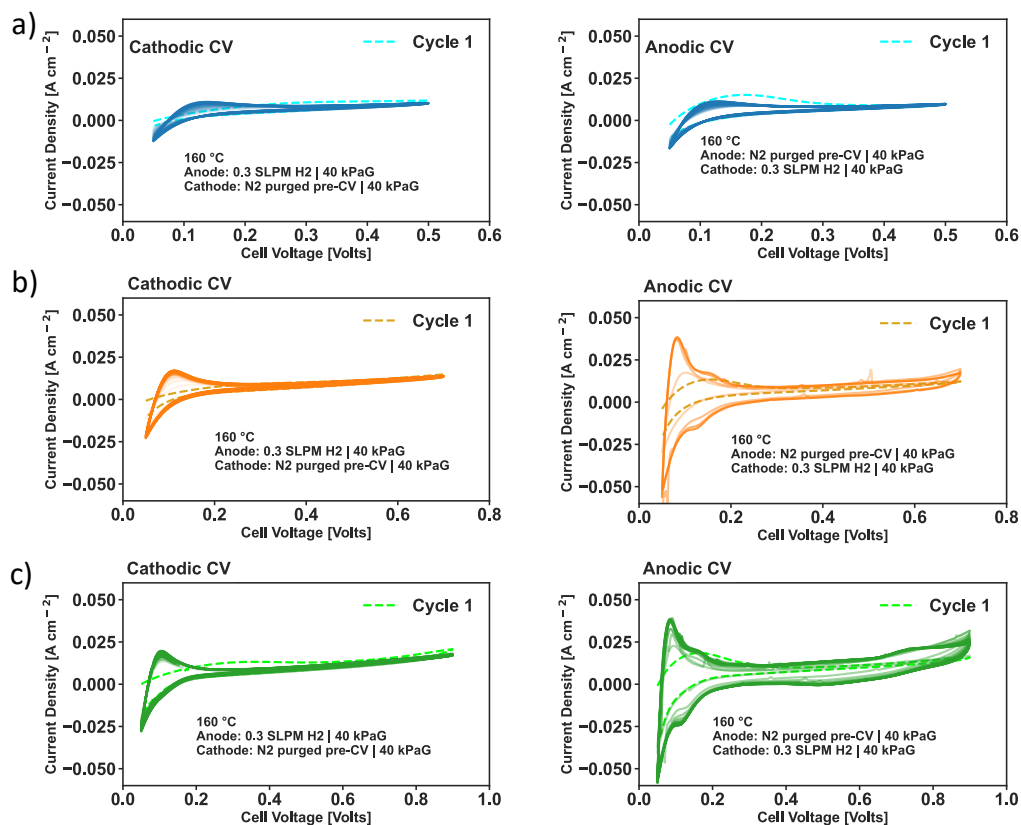


Figure 8.20 Varying vertex CVs for non-ionomeric ion-pair HT-PEM EHP, transparency of CVs corresponding to cycle number a) 0.5 V vs. RHE peak vertex b) 0.7 V vs. RHE vertex c) 0.9 V vs. RHE vertex

The magnitude of the vertex of the sweep and its impact on  $H_{\text{upd}}$  at the end of test is more pronounced for the anode but still shows a similar trend on the cathodic side (Figure 8.20). A corresponding reduction in  $R_{\text{CT}}$  relative to the applied vertex can be observed for anodic and cathodic sweep. HFR also shows a slight reduction corresponding to the magnitude of the CV vertex applied, although this variation is quite low.

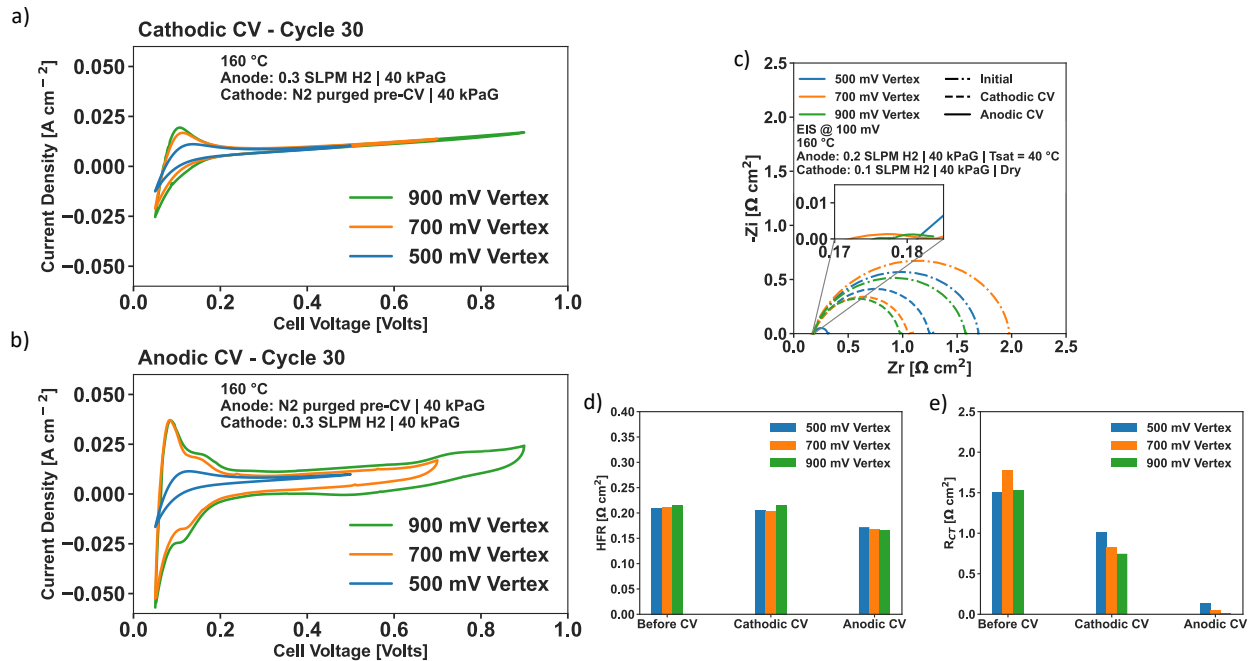


Figure 8.21 a) Anodic and b) cathodic recovery CV vertex variation in non-ionomeric GDE ion-pair HT-PEM EHP. c) EIS spectra preceding and following cathodic and anodic CV d-e) HFR and  $R_{CT}$  values fitted EIS data

There is appreciable reversal in cell impedance when taking cyclic voltammetry at 0.5 V vs. RHE when compared to CV with vertex above 0.7 V vs. RHE. In high-temperature RDE experiments in concentrated phosphoric acid an oxidation current was notably present but only after polarizing the electrode for some time (Figure 8.22). This current could be replicated in ‘fresh’ phosphoric acid by the addition of phosphonic acid lending credence to the formation of phosphonic acid (H<sub>3</sub>PO<sub>3</sub>) from concentrated phosphoric acid solution under lower electrode polarization (<0.6 V vs. RHE) with the apparent electrochemical oxidation of this phosphonic acid occurring at roughly 0.6 V vs. RHE[235]. This is supported by spectroscopy studies that found the formation of phosphonic acid under polarized and non-polarized conditions and suggested a chemical mechanism of formation of phosphonic acid and an electrochemical oxidation of phosphonic acid to phosphoric acid at high anodic potentials[258]. Sugishima et al. demonstrated that the electrochemical reduction of phosphoric acid to phosphonic acid was the most likely source of this impurity and similarly found that phosphonic acid underwent oxidation to phosphoric acid at high anodic potentials[259][260]. It is ultimately unclear whether the

formation of phosphonic acid occurs electrochemically or chemically but the oxidation of phosphonic acid does seem to occur at potentials higher than 0.6 V vs. RHE (Figure 8.22) and is the likeliest source of  $R_{CT}$  growth and recovery in the non-ionomeric GDE ion-pair HT-PEM cell here.

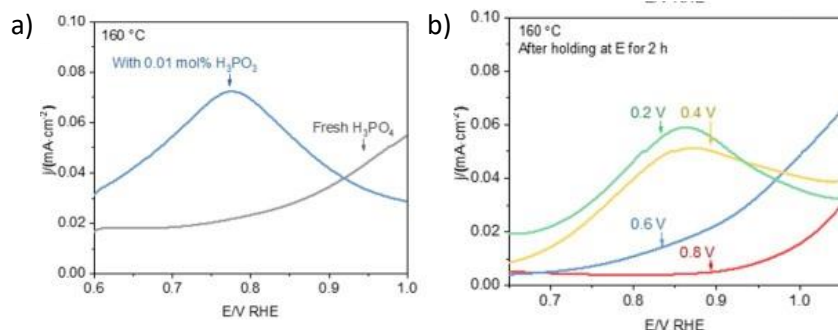


Figure 8.22 High temperature RDE in pure phosphoric acid on platinum electrode. Reproduced from [235].

Anodic cyclic voltammetry displayed impedance recovery at anodic  $T_{sat}$  as high as 80 °C corresponding to a relative humidity of 7.6%. In neat phosphoric acid this would correlate to ~92% wt H<sub>3</sub>PO<sub>4</sub> mixture [213], a much lower concentration than typically encountered in HT-PEM due to PA-PBI being intolerant to excess water content. Phosphoric acid anhydrides have not been observed to form below 95% wt H<sub>3</sub>PO<sub>4</sub> [239][214]. At this weight concentration the formation of phosphoric acid anhydrides are not the primary source of electrode poisoning and is more likely due to the formation of phosphonic acid at the low anodic potentials employed in HT-PEM EHP.

Stability of the ionomer-free ion-pair based MEA improved with the reduction of temperature for fixed anodic humidity feed of  $T_{sat} = 40$  °C, corresponding to relative humidity of 3.6% and 1.2% at 120 °C and 160 °C respectively. At 120 °C, the formation of phosphoric acid anhydrides in PBI doped PA is not favorable with anodic humidity feed of  $T_{sat} = 40$  °C. Additionally the formation of phosphonic acids at low potentials is strongly temperature dependent and falls off appreciably at 120 °C [235].

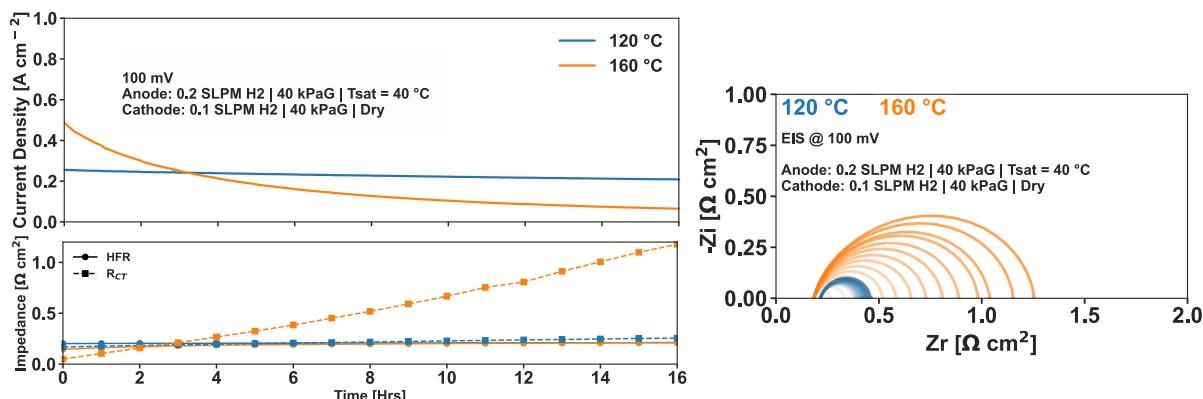


Figure 8.23 Potentiostatic stability and EIS of non-ionomeric GDE ion-pair HT-PEM EHP at 120 and 160 °C at anodic humidification of  $T_{sat} = 40$  °C.

At 120 °C, HFR does see a slight reduction to a stable value from 0.18 ohm cm<sup>2</sup> at 160 °C to 0.2 ohm cm<sup>2</sup>.  $R_{CT}$  growth is much lower relative to the 160 °C case but is still not able to stabilize for the timescales observed here, in which the relatively monotonic increase is observed.

Ultimately, the dependence of  $R_{CT}$  growth on humidity and temperature would suggest that electrode hydration plays a major role in the impedance growth of the electrode environment for the ionomer free ion-pair based HT-PEM EHP. While phosphoric acid anhydrides and their ionized forms could play a major role in electrode poisoning, reversible  $R_{CT}$  growth is observed at conditions unfavorable to the formation of phosphoric acid anhydrides and furthermore shows reversibility when cycling to anodic potentials in excess of 0.7 V vs. RHE corresponding to roughly the voltage range at which phosphonic acid undergoes oxidation to phosphoric acid. It is likely then that the major source of electrode ‘poisoning’ is due to phosphonic acid formation.

#### 8.4.2 Ionomeric Gas Diffusion Electrodes

The ion-pair HT-PEM EHP utilizing GDEs containing Nafion®/PWN ionomeric binder showed a definite improvement in potentiostatic stability with respect to degree of anodic humidification and showed a similar trend at dry conditions. Again, initial humidification was set at  $T_{sat} = 80$  °C solely on the anode hydrogen gas feed, followed by humidification of both anode and cathode at  $T_{sat} = 80$  °C. Both scenarios exhibited a similar trend in EIS response indicating stable performance with slight reductions in  $R_{CT}$  over time. At the lower humidification case of  $T_{sat} = 40$  °C on the anode, the trend was reversed showing an increase in  $R_{CT}$  over time. To probe the

effective stable humidity range, an additional measurement point of anode humidity feed was taken at  $T_{\text{sat}} = 60\text{ }^{\circ}\text{C}$  which eventually stabilized after some electrode impedance growth.

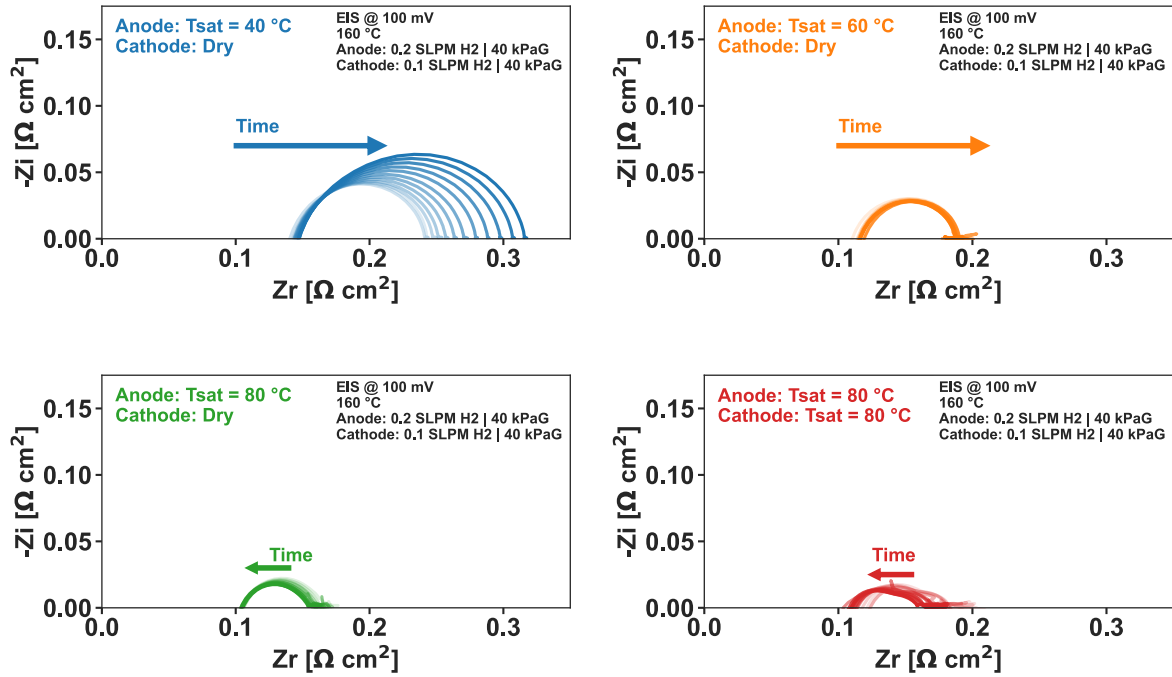


Figure 8.24. EIS of Nafion®/PWN ionomeric GDE Ion-Pair HT-PEM in potentiostatic stability testing.

The amperage response is greatest initially for the solely anodic humidification  $T_{\text{sat}} = 80\text{ }^{\circ}\text{C}$  case, after 12 hours of potentiostatic hold, the anode and cathode humidified case of  $T_{\text{sat}} = 80\text{ }^{\circ}\text{C}$  reached parity with the anodic only case. The initial disparity in current response between anodic and both anodic and cathodic humidification is observed to be related to an initially higher HFR rather than associated with any electrode impedance differences suggesting that the humidification of the anode alone provides sufficient hydration to the cathode to promote cathodic charge transfer processes.

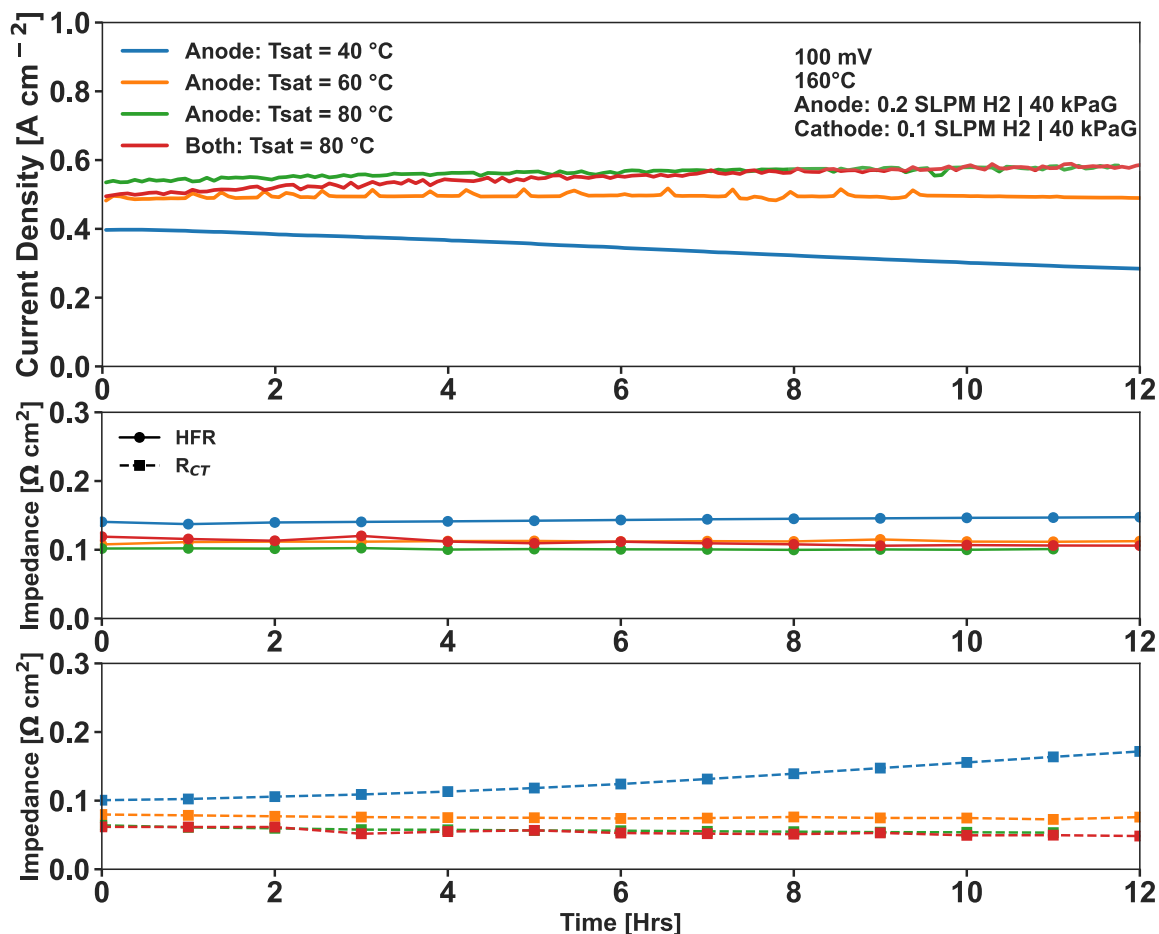


Figure 8.25 Amperometric response of Nafion®/PWN ionomeric GDE HT-PEM EHP at 0.1 V over time with HFR and  $R_{CT}$  measured hourly.

For the lower anode humidification cases of  $T_{sat} = 60\text{ °C}$  and  $T_{sat} = 40\text{ °C}$ , a stronger dependence on  $R_{CT}$  with humidity change occurred rather than HFR as was observed similar to the no-ionomer case.  $T_{sat} = 40\text{ °C}$  failed to equilibrate with respect to  $R_{CT}$  within the 12 hour test period and showed appreciable reduction in current response relative to the other cases – 47% reduction relative to  $T_{sat} = 80\text{ °C}$ .  $T_{sat} = 60\text{ °C}$  showed a slight increase in impedance resulting in a difference in amperometric response of  $58\text{ mA cm}^2$  at 0.1 V compared to  $T_{sat} = 80\text{ °C}$  at 12 hours of potentiostatic stability hold.

Cyclic voltammograms following potentiostatic stability measurements were relatively symmetric for the anodic and cathodic cases. For stabilized conditions, the potential sweep in neither the anodic or cathodic direction did not impact impedance and thus demonstrate any performance recovery. Anodic direction sweeps lead to higher impedances for these cases,



although the magnitude of the increase was relatively small and reversible following further potentiostatic operation.

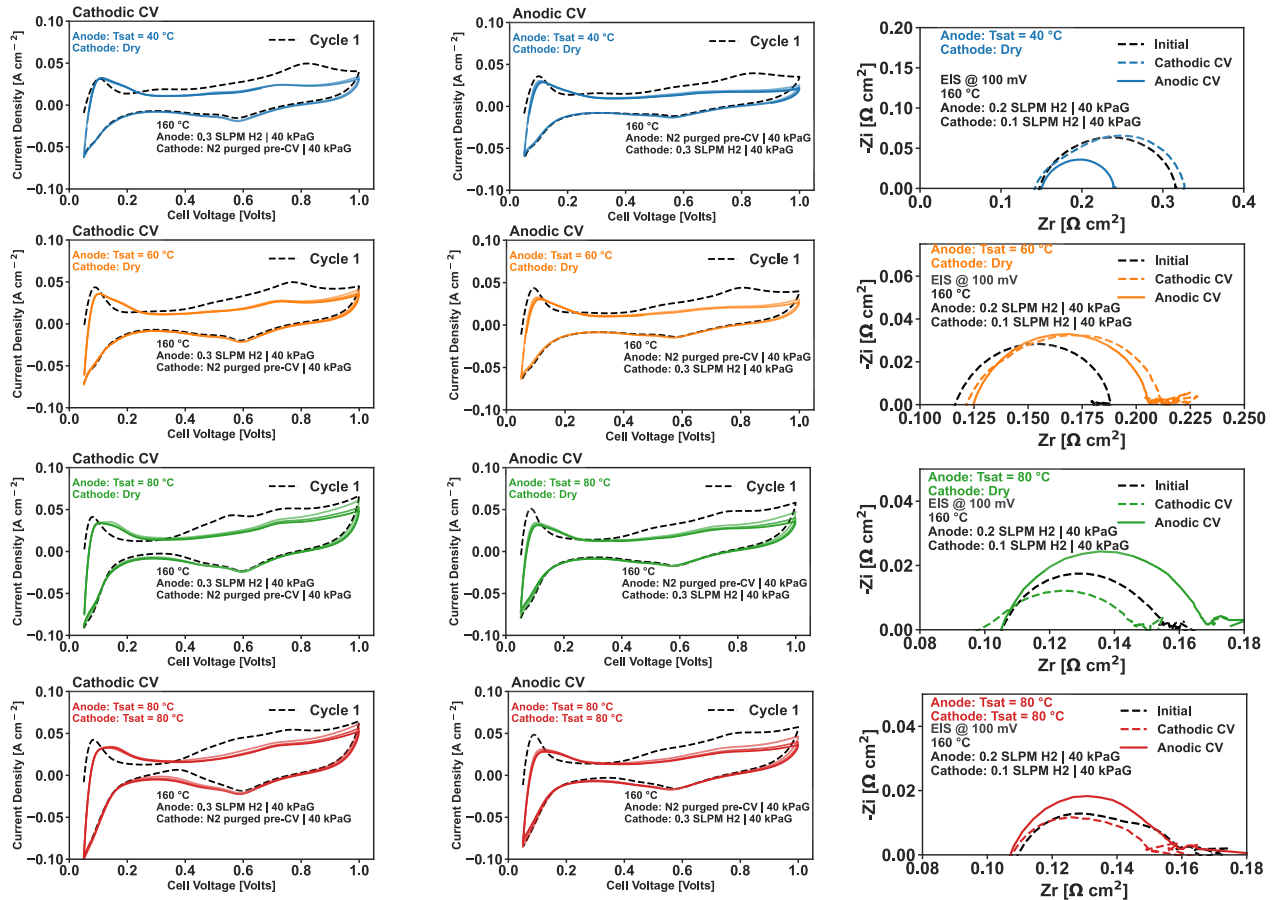


Figure 8.26 Cathodic & anodic CVs and EIS response preceding and following CV measurements for Nafion®/PWN ionomeric ion-pair HT-PEM EHP.

At  $T_{\text{sat}} = 40\text{ }^{\circ}\text{C}$  where a  $R_{\text{CT}}$  growth pattern is observed, the anodic potential sweep did lead to a recovery of the charge transfer impedance to near-initial conditions. This further supports the notion that the lower humidity condition  $R_{\text{CT}}$  growth is related to an electrochemically adsorbed species on the platinum surface that is part of the  $\text{H}_3\text{PO}_4/\text{H}_2\text{O}$  electrolyte phase. At lower humidities, the contribution of the proton conducting ionomeric phase is potentially less relative to the PA- $\text{H}_2\text{O}$  electrolyte phase and thus similar mechanisms encountered in the no-ionomer case emerge. Additionally, some contribution could come from the formation of phosphoric and phosphonic acid anhydrides in the aqueous electrolyte phase, the latter of which would be similarly reversible through cyclic voltammetry as was observed in the non-ionomeric GDE case. Phosphonic and sulfonic acid in the ionomeric phase is not expected to readily form

anhydrides per DFT analysis[155][157].

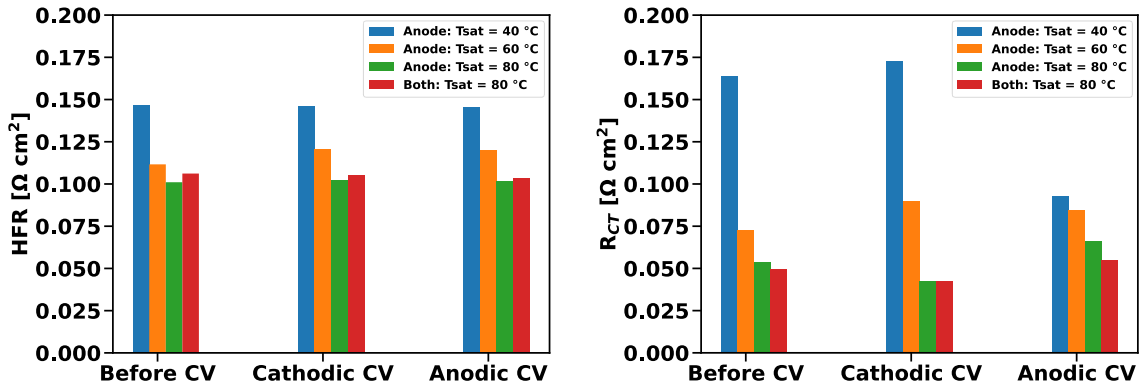


Figure 8.27 Bar chart summary of HFR and  $R_{CT}$  change due to cyclic voltammetry for Nafton®/PWN ionomeric ion-pair HT-PEM EHP

HFR is not impacted in any appreciable manner following cyclic voltammetry in any case of humidification as opposed to the higher humidification cases without ionomeric binder, indicating that the HFR shifts are related to the aqueous phosphoric acid electrolyte.

One of the potential advantages of the high phosphoric acid retention capabilities of the ion-pair is the potential for long-term stable operation at temperatures exceeding 160 °C. At cell temperatures of 160 °C, an anode feed humidification of  $T_{\text{sat}} = 80$  °C was found to operate in a stable manner in EHP in the previous section which agrees with AST studies of similar ion-pair MEA in HTPEM-FC operation that indicates this degree of humidification was viable for long-term operation (2500 + hrs)[158]. In the same study, anhydrous HT-PEMFC at 200 °C was found to lose performance over time for the same AST protocol, however measurements of acid content post AST indicated no loss of acid associated with the performance loss indicating that the performance loss could be related to reversible MEA dehydration.

To assess this same effect at elevated temperatures in the HT-PEM EHP configuration, the anodic humidification of  $T_{\text{sat}} = 80$  °C is utilized at elevated cell temperatures up to 200 °C (Figure 8.28). For all cases, some time is needed for stable operation regime to be reached.

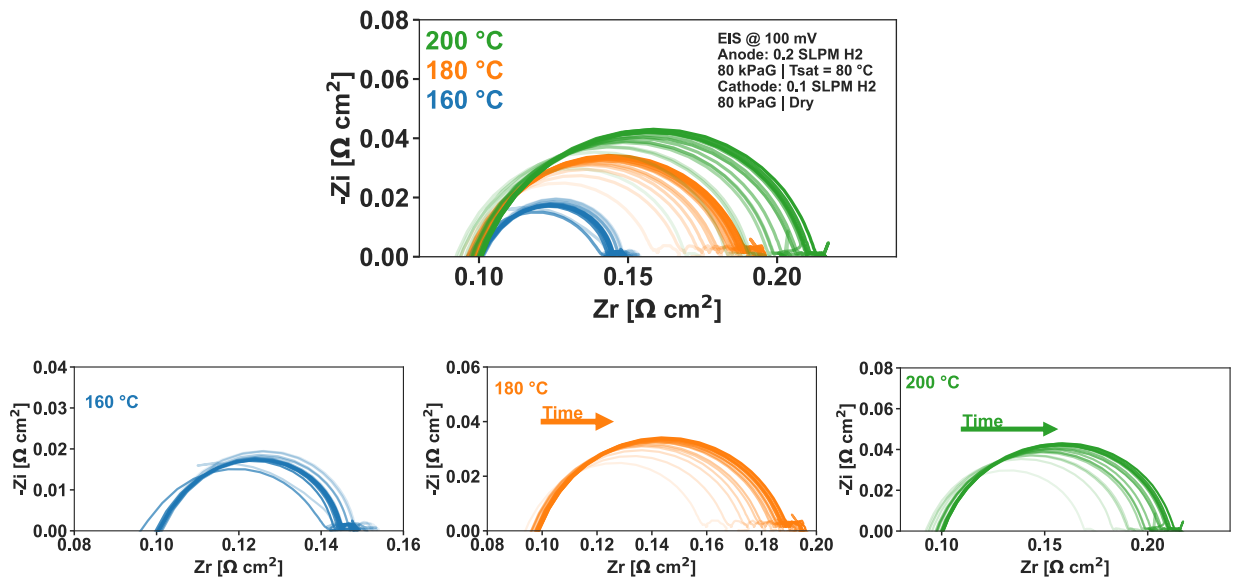


Figure 8.28 EIS stability data of Nafion®/PWN ionomeric GDE ion-pair HT-PEM operating at high temperatures 160/180/200 °C.

At elevated temperatures, the kinetics of the HOR/HER is expected to improve as well as the intrinsic proton conductivity of the ion conducting materials per thin film ex-situ conductivity studies[111][157]. Here the opposite trend is observed (Figure 8.29). Initially, HFR at elevated temperatures improves once the cell reaches temperature. Over time, the HFR value increases eventually equilibrating to approximately 0.097 ohm cm<sup>2</sup> for all cases. The initial decrease of HFR can be attributed to the QAPOH-PA membrane conductivity increase at elevated temperature that is subsequently balanced out by the reduction in water content in the membrane phase as the equilibrium between the fixed water vapor pressure from the anode feed and the increased water vapor pressure of the aqueous phosphoric acid phase is reached. This effect is consistent for both elevated temperature cases.

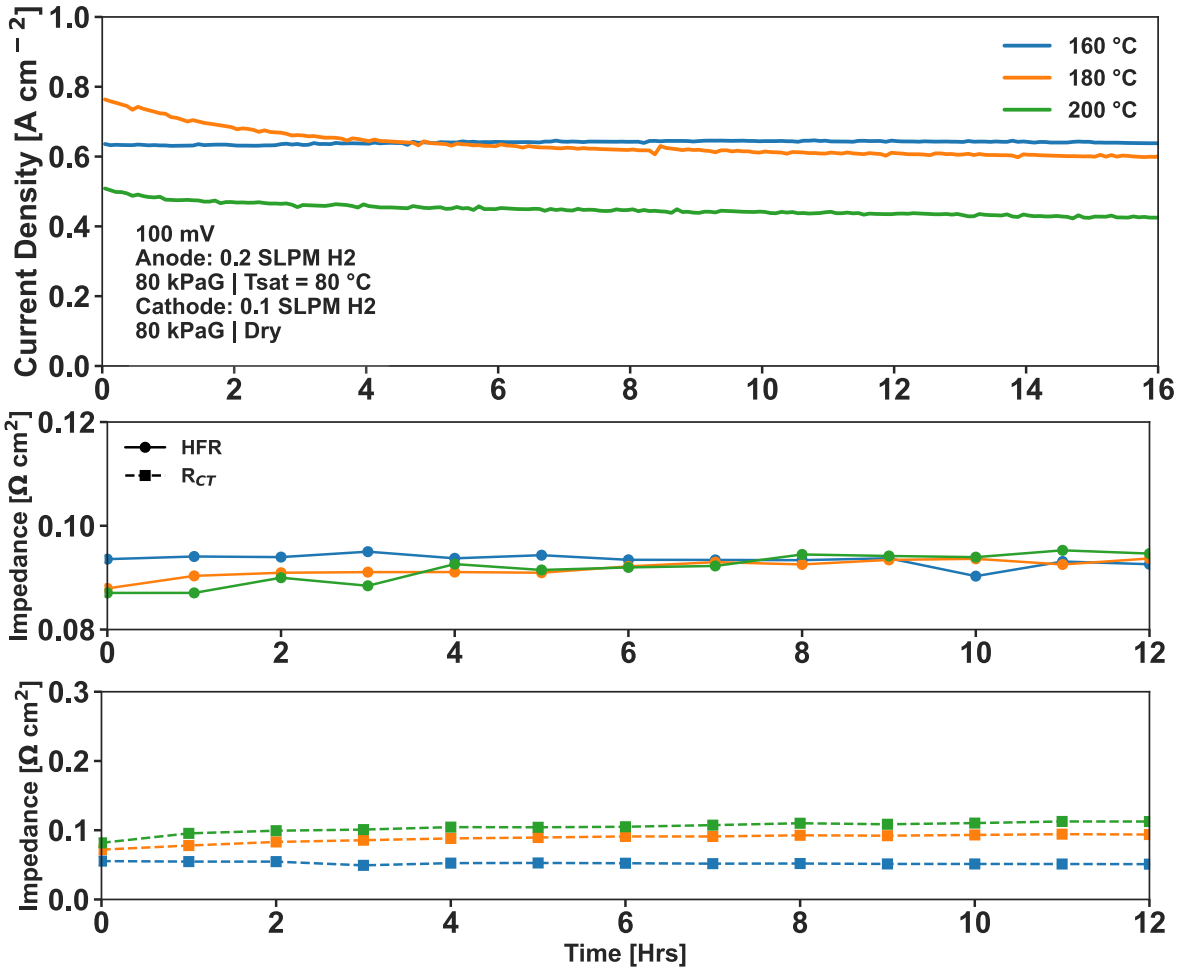


Figure 8.29 16-hour potentiostatic stability of Nafion®/PWN ionomeric GDE Ion-pair HT-PEM EHP at elevated temperatures 160/180/200 °C with HFR and R<sub>CT</sub> trends.

Ultimately, increase in electrode impedance characterized by R<sub>CT</sub> is the major factor impacting the reduction in current for the potentiostatic measurement at elevated temperatures. Sulfonic and phosphonic acid ionomers present in the MEA are known to be highly sensitive to humidity for conductivity [155]. While one of the roles of the sulfonic acid ionomer (Nafion® in this case) is to inhibit the formation of phosphonic acid anhydrides[157], phosphonic acid itself still has higher intrinsic proton conductivity at elevated water content as is the case for PFSA based ionomers such as Nafion®.

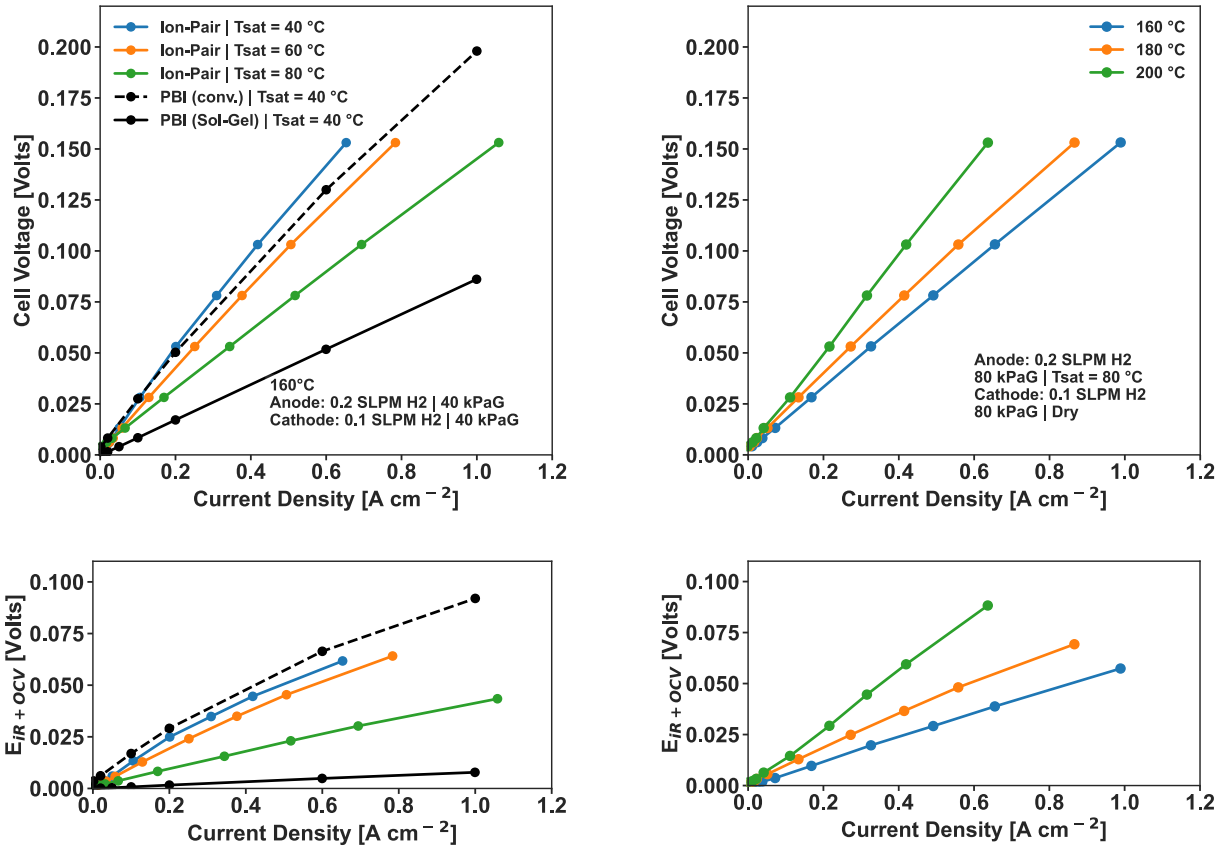


Figure 8.30 Polarization curves and Ir-Corrected polarization curves of Nafton®/PWN ionomeric GDE Ion-pair HT-PEM EHP with respect to humidity at 160 °C and respect to temperature at anode  $T_{sat} = 80$  °C. Comparisons to conventional and sol-gel PBI HT-PEM EHP.

For stable conditions in the ionomeric MEA, the polarization curve characterizations provide some insight into the relative performance impacts of humidification and cell temperature. In Figure 8.30, the trend with RH in terms of improved current response is apparent, with current at cell voltage of 0.15 V roughly doubling from 0.6 A cm<sup>-2</sup> to 1.05 A cm<sup>-2</sup> by increase humidification from  $T_{sat} = 40$  °C to  $T_{sat} = 80$  °C corresponding to an RH of 1.2% to 7.5% respectively. Correcting for HFR and the OCV shift due to dilution of anode hydrogen with additional water vapor, the increase in impedance due to non-ohmic losses can be observed to be appreciable, supporting the notion that humidity plays a large role in both membrane resistance as well as electrode impedance. Comparing the impact of humidity to PBI based membranes, for an equivalent humidification regime typical of PBI at RH = 1.2% for 160 deg C the ion-pair with ionomeric binder performs poorly with respect to polarization relative to conventional PBI with

ADL on the order of 7 mol PA/mol PBI studied in Chapter 5, and notably worse than a sol-gel style PBI HT-PEM based on Celtec membranes with an ADL on the order of ~37 mol PA/mol PBI. At high humidities the performance of the ion-pair membrane approaches sol—gel style PBI current response but is still limited in large-part by the electrode impedance.

### 8.4.3 Distribution of Relaxation Times & Non-ionomeric vs. Ionomeric GDEs in Ion-pair EHP

EIS data gathered on the non-ionomeric and ionomeric ion-pair HT-PEM EHP cells in the preceding sections are processed to produce the distribution of relaxation times function  $\gamma$  (Eq. 8-11). The DRTtools open-source project is used to compute the DRT function through the Tikhonov regularization approach[261][262][263]. Efforts were made to reduce inductive elements in the measurement elements such as stranding current carrying and sense cables on the Gamry potentiostat[257] however inductive behavior was exhibited throughout measurements, particularly at high frequencies. To offset this influence an inductor is added to the DRT function equation (Eq. 8-15).

$$Z(f) = j\omega L_0 + R_\infty + \int_{-\infty}^{\infty} \frac{\gamma(\ln \tau)}{1 + i2\pi f\tau} d\ln\tau \quad (\text{Eq. 8-15})$$

The selection of the regularization parameter  $\lambda$  is crucial to the proper evaluation of DRT function[264]. Lower values of the regularization parameter reflect the EIS spectra more accurately and thus provide a ‘sharper’ set of peaks, however this can also lead to a number of ‘artificial peaks’. A robust method for then for selecting the regularization parameter is through increasing the value of the parameter until the sum of squared residuals (SSR) no longer decreases with the fitted DRT spectrum[265][256][262]. A number of DRT spectrum were swept through increasing  $\lambda$  values and the SSR response was plotted (Figure 8.31) and a regularization parameter of  $10^{-3}$  was found reasonable.

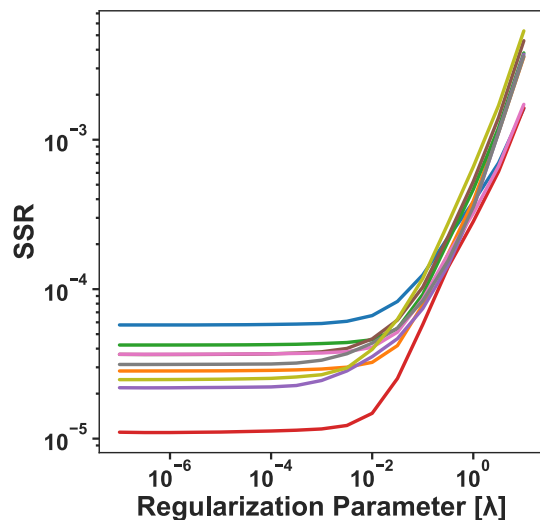


Figure 8.31 Selection of regularization parameter for DRT analysis based on sum of squared residuals analysis.

Impedance peaks in the DRT functions and their proposed associated underlying physio-chemical processes are displayed in Figure 8.32. Table 8-2 outlines the frequency ranges applied to these peaks.

Table 8-2. DRT frequency domains for Ion-pair HT-PEM EHP

DRT Assigned Frequency Domains - [Hz]				
P1   GDE H+	P2   HER	P3   HOR	P4   Mass Trans.	P5   Low Freq.
$\geq 80000$	10000 - 80000	150 - 10000	0.1 - 150	$\leq 0.1$

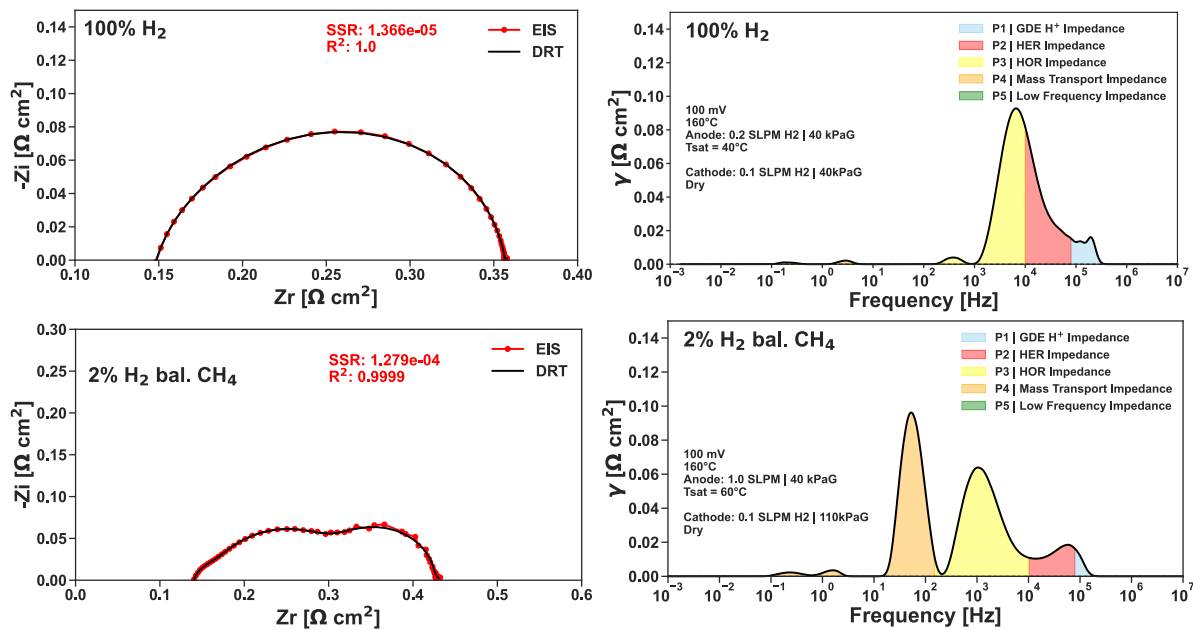


Figure 8.32 Example DRT spectrum of Nafion®/PWN ionomeric GDE ion-pair HT-PEM with peaks identified.

Two examples of DRT spectrum used to inform identification of these processes are included. Peaks were selected based on physical intuition through observing the response due to variations of humidity, cell temperature, and different gas feed concentrations. Peaks P3 and P4 are associated with anodic kinetics of hydrogen oxidation and with mass transport limiting behavior as their growth is observed with dilution of the anodic gas. P3 still appears in non-mass transport limiting conditions and was observed to grow in lower anodic humidification and was directly influenced by anodic recovery CV and cathodic recovery CVs had minimal influence. P2 corresponding to HER, occurring at slightly higher frequencies than the HOR reaction as was observed in another study in HT-PEM EHP[256]. P2 is similarly visible in all cases like P3 but does not tend to change with dilution of the anodic feed and does grow with lower anodic humidification. Water content in the cathode is entirely dependent on the membrane transport of water from the anode, so it is reasonable that cathodic HER reaction rate would respond to changing anodic humidity. feed results in a growth of impedance in the low frequency range assigned to mass transport loss as well as a growth in the frequency range assigned to HOR impedance relative to higher concentration H<sub>2</sub> feeds. There is some difficulty in separating the relatively fast processes of HOR and HER particularly in EHP conditions where anode and



cathode are similar such as 100% H<sub>2</sub> feed to the anode, however the deviation in the peaks is very much apparent when diluting the anodic H<sub>2</sub> feed. P1 is assigned to proton conduction in the electrodes which occurs at very high frequencies and is generally very low as is expected and decreases with higher humidity due to the high conductivity of the ionomeric phases and phosphoric acid electrolyte with higher water content. Very low frequency peaks are assigned to a separate region P5 which are not well understood in LT and HT-PEM literature. One theory is that acid migration contributes to formation of these peaks in HT-PEM.

To further elucidate the observed electrode impedance growth, EIS data gathered is processed to generate DRT functions for the non-ionomeric and Nafion®/PWN ionomeric GDE case of the ion-pair HT-PEM EHPs. Figure 8.33 shows this comparison for 0.1 V potentiostatic hold in the anode humidification condition of T<sub>sat</sub> = 40 °C where both cases of exhibited a growth of R<sub>CT</sub> impedance over time starting from a ‘fresh’ condition where anodic potential was cycled up to 1.0 V vs. RHE in cyclic voltammetry preceding the potentiostatic hold test.

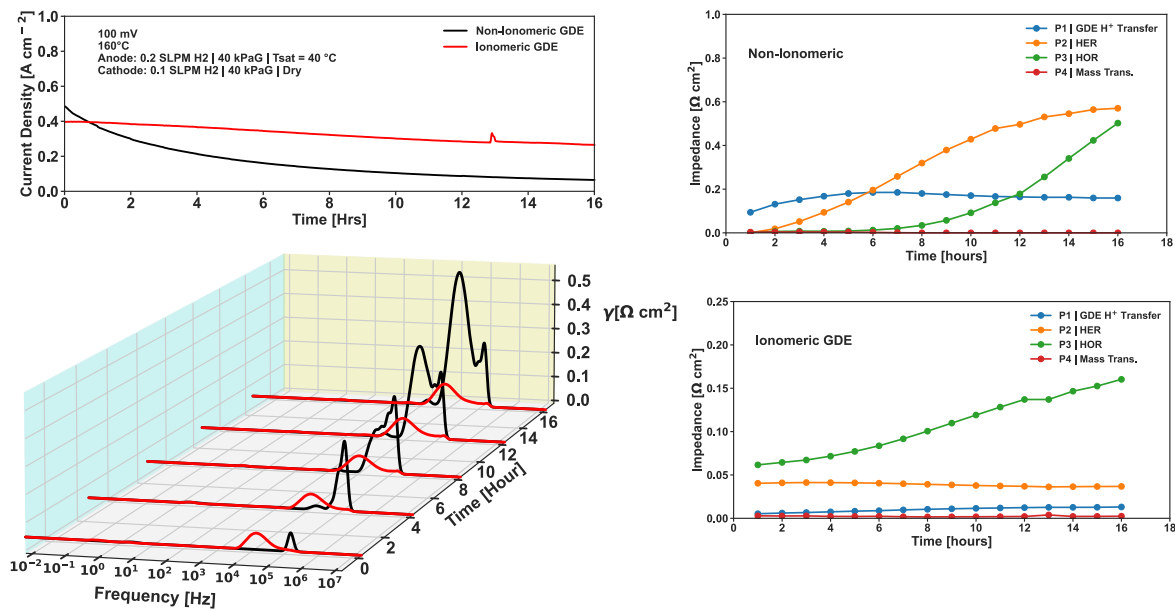


Figure 8.33 DRT function time-series for 0.1 V potentiostatic hold with EIS taken hourly, comparing non-ionomeric vs ionomeric GDE ion-pair HT-PEM stability

In the non-ionomeric GDE, the only real impedance initially occurs at very high frequencies largely attributed to proton conduction in the GDE. Impedance growth shifts towards lower frequencies, with HER growing more quickly followed by rapid increase of HOR while the GDE

H<sup>+</sup> conduction impedance levels off within the first several hours. This is consistent with the settling time of the HFR and likely corresponds with the equilibration of the phosphoric acid electrolyte composition. After the settling of P1 and HFR, an increase in HOR related peaks indicate a reduction in kinetic activity. As previously noted, delineating impedance between HOR and HER is difficult in symmetric conditions, although given the presence of dry H<sub>2</sub> sweep flow at the cathode, it is reasonable that phosphoric acid anhydride formation would occur more rapidly at the cathode side.

Overall electrode impedance of the Nafion®/PWN ionomeric GDE is lower by an order of magnitude after some stabilization time. Higher frequency impedance associated with GDE H<sup>+</sup> conduction and HER reactions are largely unaffected and a consistent growth in HOR impedance at the anode side occurs. The impedance increase is much slower than the non-ionomeric case indicating suppression of the poisoning mechanisms. Notably, higher frequency impedance associated with H<sup>+</sup> conduction and HER kinetics are constant in these conditions.

DRT functions of EIS spectra recorded preceding and between cathodic and anodic cyclic cycling up to 1.0 V vs. RHE are presented for the non-ionomeric (Figure 8.34) and ionomeric (Figure 8.35) ion-pair HT-PEM EHP below. Notably in both cases, the cathodic CV has relatively less impact on recovery, with a larger change occurring in impedance attributed to HER at the cathode rather than the lower frequency range HOR. This is in line with phosphonic acid formation contributing to electrode poisoning, as a cathodic potential sweep would not reverse any phosphonic acid formation at the anode, solely the cathode. The reduction in HOR impedance in the non-ionomeric case following the cathodic CV case is difficult to draw a conclusion from, given that there is likely significant overlap between the two reactions' frequency domains. The fact remains that the cathodic CV has a larger impact on HER side.

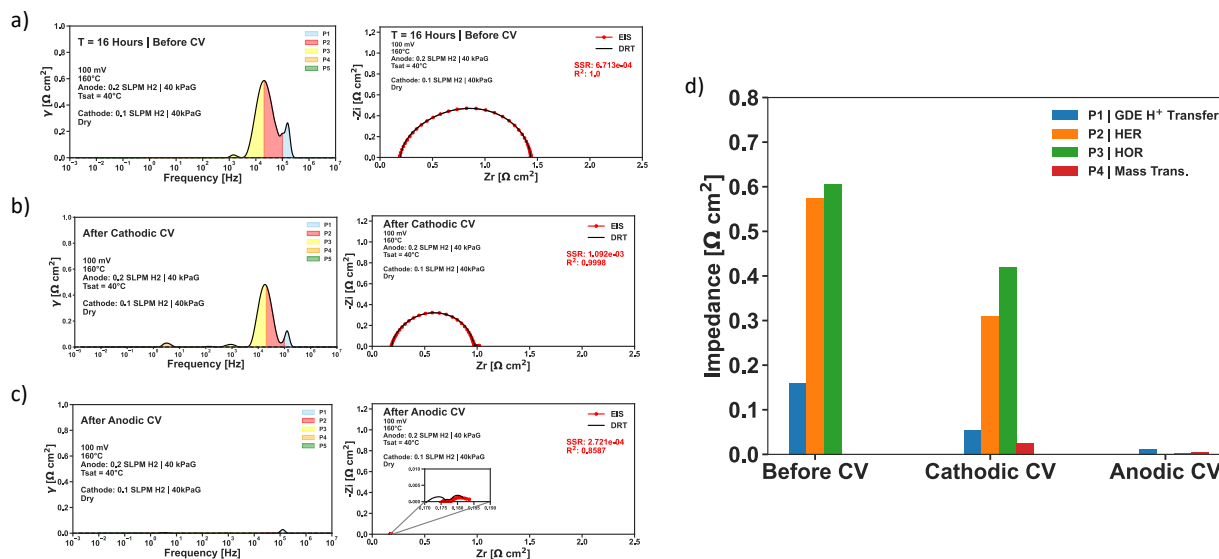


Figure 8.34 Non-ionomeric ion-pair HT-PEM EHP 0.1 V a) Before CV b) following cathodic CV c) following anodic CV DRT function with respect to frequency and DRT-Nyquist fit. d) Total impedance contribution by mechanism from DRT.

Anodic CV has a significant impact on both ion-pair HT-PEM EHP cases. The HOR domain impedance, along with any appreciable impedance outside of the highest frequency domain, following anodic CV is non-existent in the absence of ionomer. In the case of the Nafion®/PWN ionomer ion-pair HT-PEM EHP, the ‘minimum’ anode impedance post anodic CV is higher which is reasonable given the baseline concentration of phosphonic acid present in the form of the PWN binder as well as potential sulfonic acid poisoning from Nafion®.

Regardless of the stability provided by the addition of the Nafion®/PWN ionomeric phase in the electrodes, the ion-pair HT-PEM EHP system is still unable to reach reasonable stability at anodic humidification of  $T_{\text{sat}} = 40$  °C as compared to PBI-PA based HT-PEM EHP with phosphoric acid electrolyte in the electrode. The limiting factor in this stability appears to be anodic poisoning that is reversible through cycling to anodic potentials above 0.7 V, suggesting that the formation of phosphonic acid species in the phosphoric acid electrolyte phase may contribute to this electrode poisoning. Higher humidification stability can be achieved with the ionomeric GDE with electrode impedance remaining sensitive to humidification degree.

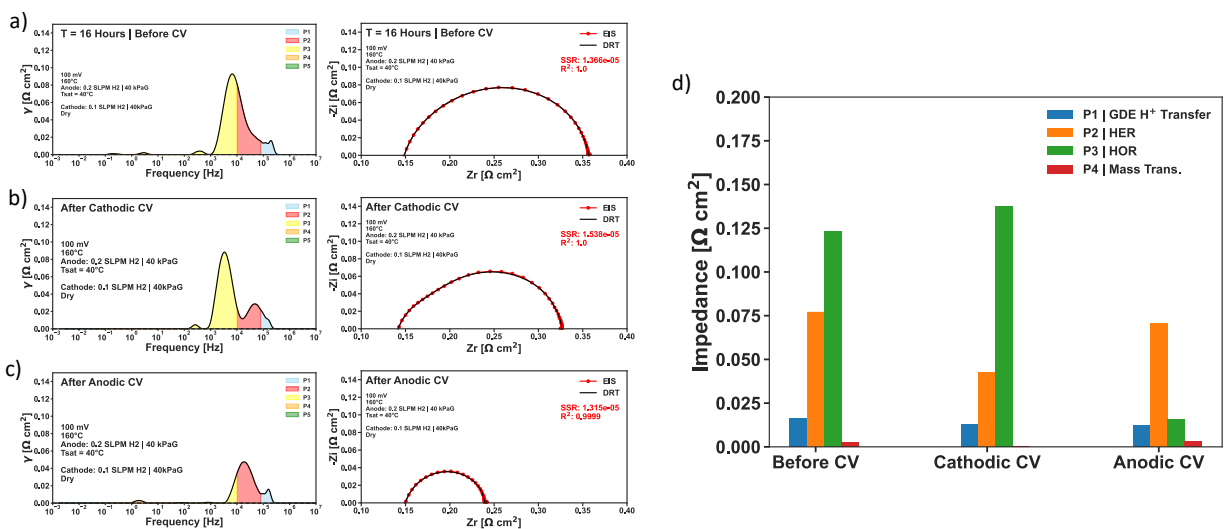


Figure 8.35 Nafton®/PWN ionomeric ion-pair HT-PEM EHP 0.1 V a) Before CV b) following cathodic CV c) following anodic CV DRT function with respect to frequency and DRT-Nyquist fit. d) Total impedance contribution by mechanism from DRT.

#### 8.4.4 Performance of Ion-pair HT-PEM EHPs with bimetallic PGM catalyst for HOR and HER

Ultimately for the application of the ion-pair based HT-PEM EHPs to gas separation processes, it is crucial to better understand the feasible operating windows of the EHP cell and the optimal performance within this window. In the previous section it was apparent that the addition of a blend of Nafion® and phosphanated polypentafluorostyrene ionomeric binders to a carbon supported platinum electrode enabled a stable ion-pair HT-PEM based EHP system at temperatures up to 200 °C. The performance and stability of ionomeric GDEs with the ion-pair HT-PEM was strongly correlated with water vapor content in the anodic feed, particularly with respect to charge transfer impedances relating to performance limitations in the electrodes.

In this section, the analysis of the stability of the ion-pair HT-PEM is expanded beyond the analysis comparing the ion-pair HT-PEM with and without ionomeric binder blends. The addition of PtRu bimetallic PGM catalyst supported on carbon - ‘PtRu/C’, is considered at both anode and cathode as a possible route for further performance improvement by inhibition of phenyl group adsorption from the PWN and platinum interacting in the electrodes. A wider range of temperature and relative humidity is studied to better elucidate the optimal operation point for the ion-pair based HT-PEM EHP. EIS and DRT analysis are utilized to delineate the impacts of

temperature and RH on the Pt/C and PtRu/C electrodes across physical mechanisms attributed to different frequency domains.

One possible explanation for limiting electrode performance is the impact of aromatic type hydrocarbons on platinum surfaces in acidic conditions. In the presence of hydrogen, platinum is known to contribute to the hydrogenation of aromatic hydrocarbons such as benzene and phenyl rings [266]. Furthermore, hydrogenated aromatics have been shown to adsorb to platinum surfaces in acidic conditions at low potentials relevant to HOR overpotentials [267]. Such aromatic hydrocarbons are structurally similar to the fluorophenyl ring backbone of the PWN ionomeric binder. The influence of phenyl group poisoning on platinum surfaces in alkaline exchange membrane fuel cell (AEMFC) electrode performance has been observed as a major contributing factor to disparities across AEMFC literature in performance particularly with respect to inhibited HOR kinetics [268]. The degree of this inhibition varied depending on the phenyl backbone structure of the ionomer employed [269]. For AEMFC ionomers where HOR kinetics on Pt were inhibited, bimetallic PGM catalysts were found to inhibit the adsorption of phenyl type structures on the Pt-surface with Pt-Ru catalysts consistently showing the best improvement over solely platinum based catalysts [270][271].

Kim et al. in their investigation of the ion-pair based HT-PEM combined with Nafion® + PWN ionomeric binder electrodes for HT-PEMFC applications determined that phenyl group adsorption poisoning was a significant factor in the anode electrode environment [157]. This was surmised from MEA measurements with an equivalent phosphonic acid content calculated from electrode composition and compared against RDE mass activity measurements for phosphoric acid and phosphonic acid (Figure 8.36a). Ex-situ RDE measurements of Pt/C and PtRu/C catalysts in phosphonic acid solutions showed an improvement in mass activity for PtRu/C for HOR supporting the usage of PtRu/C for HOR in HT-PEMFCs containing the PWN binders (Figure 8.36b).

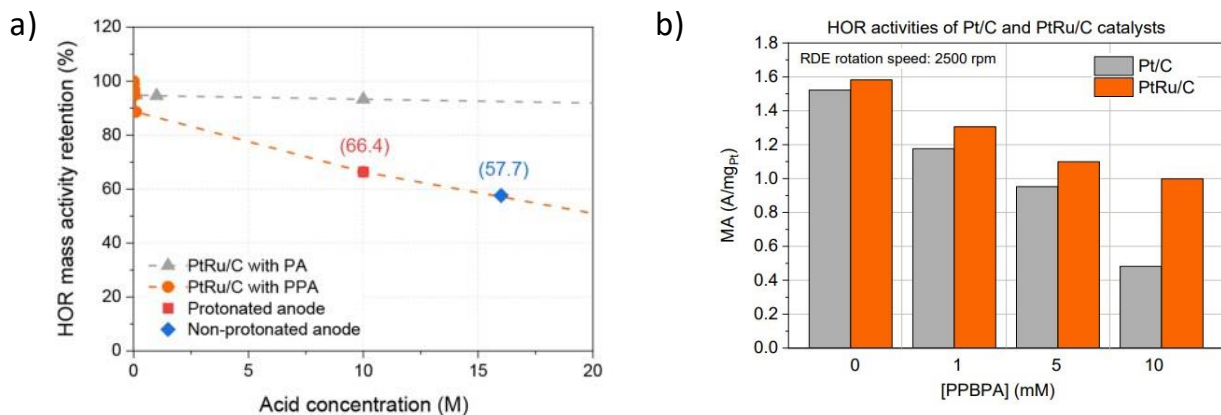


Figure 8.36 a) HOR mass activity of PtRu/C in RDE with phosphoric acid (PA) and pentafluorophenyl phosphonic acid (PPA) and in ion-pair HT-PEMFC MEA with PWN ionomeric binder ('non-protonated anode') and Nafion®/PWN ionomeric binder ('protonated anode') with equivalent acid concentration. B) HOR mass activity in RDE of Pt/C vs. PtRu/C as a function of perfluoro-1,4-phenylene bis(phosphonic acid) concentration. Reproduced from [157].

Three MEAs were considered for comparison (Table 8-3). MEA2 and MEA3 were constructed to examine the impact of PtRu/C each consisted of one PtRu/C and one Pt/C based electrode, with the PtRu/C electrode serving as the anode in MEA2, and the Pt/C electrode serving as the anode in MEA3.

Table 8-3. MEA composition for PtRu/C vs. Pt/C study in Ion-pair HT-PEM EHP

MEA compositions for Ion-Pair HT-PEM EHP Bimetallic Catalyst Comparisons					
MEA#	Membrane	Anode Catalyst (Gravimetric XRF)	Cathode Catalyst (Gravimetric XRF)	Anode Ionomer	Cathode Ionomer
MEA1	QAPOH-PA	Pt/C [TEC10E50E] 1.05   0.98 mg Pt cm <sup>-2</sup>	Pt/C [TEC10E50E] 0.97   0.998 mg Pt cm <sup>-2</sup>	I/C = 0.3 1:1 wt PWN/ Nafion	I/C = 0.3 1:1 wt PWN/ Nafion
MEA2	QAPOH-PA	PtRu/C [HiSpec 12100] 1.15   1.18 mg Pt cm <sup>-2</sup>	Pt/C [TEC10E50E] 1.12   1.08 mg Pt cm <sup>-2</sup>	I/C = 0.65 1:1 wt PWN/ Nafion	I/C = 0.3 1:1 wt PWN/ Nafion
MEA3	QAPOH-PA	Pt/C [TEC10E50E] 0.98   1.01 mg Pt cm <sup>-2</sup>	PtRu/C [HiSpec 12100] 0.94   0.89 mg Pt cm <sup>-2</sup>	I/C = 0.3 1:1 wt PWN/ Nafion	I/C = 0.65 1:1 wt PWN/ Nafion

In similar fashion to potentiostatic stability measurement in the previous section, MEAs were conditioned at each temperature and relative humidity setting by potentiostatic hold at 0.05 V for

at least 16 hours. During conditioning relative humidity was controlled by bubbler type gas humidifier on the anode gas feed side with an H<sub>2</sub> gas flow rate of 0.2 SLPM H<sub>2</sub> while the cathode was flowing at 0.1 SLPM H<sub>2</sub> dry to maintain a constant hydrogen pressure at low current densities. Back pressure was set to 40 kPa gauge on both sides for all tests. Cyclic voltammograms were taken before conditioning following a 10-minute equilibration time as the feed-in humidity settles and once again following the conditioning and characterization. EIS spectra were recorded at conditioning potential every hour.

Polarization curves displaying the performance of the HT-PEM EHP with symmetric Pt/C electrodes at 160 °C is compared to the MEAs with bimetallic PtRu/C electrocatalyst at the anode with Pt/C cathode, and PtRu/C cathode with Pt/C anode for varying anodic humidities from T<sub>sat</sub> = 60 °C to T<sub>sat</sub> = 80 °C (Figure 8.37). In some cases, the maximum measurement point of 0.15 V was beyond the current range of the potentiostat. The baseline case of Pt/C is displayed here at 160 °C for T<sub>sat</sub> = 60 °C and T<sub>sat</sub> = 80 °C as a point of comparison for the PtRu/C MEAs.

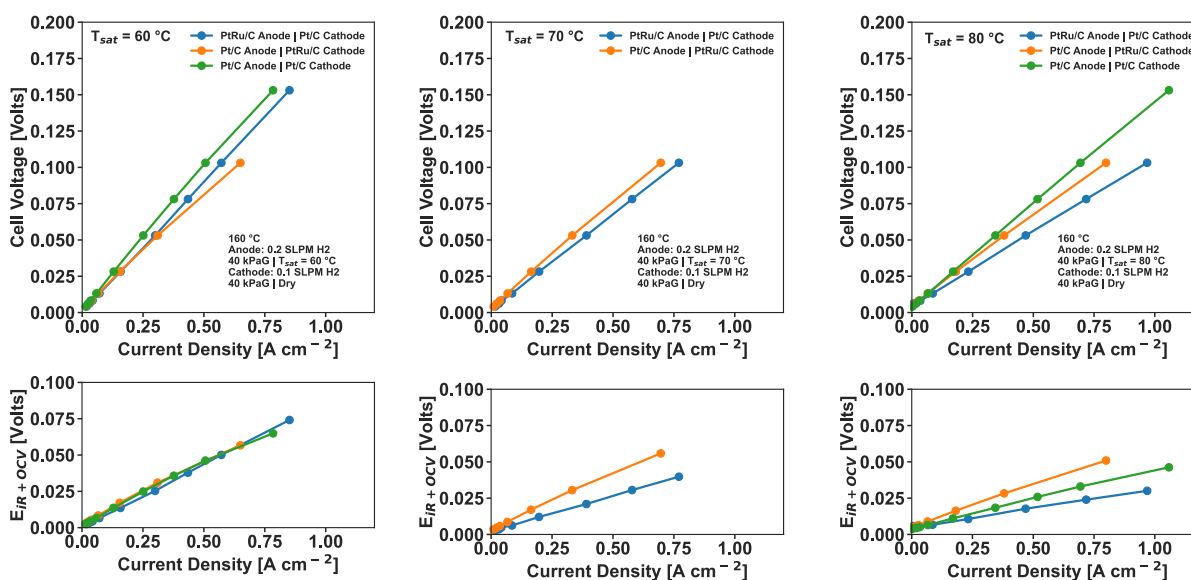


Figure 8.37 Polarization and  $iR$ -corrected polarization curves of ion-pair HT-PEM EHP with Pt/C and PtRu/C electrodes at 160 °C from anode  $T_{sat} = 60$  °C to  $T_{sat} = 80$  °C

In all cases the polarization response was higher for the MEAs containing the PtRu/C at either anode or cathode, with the anodic PtRu/C demonstrating the strongest performance characteristics. Correcting for OCV and HFR ohmic potential loss, the polarization response for

the MEA with PtRu/C cathode is not lower than the comparison cases for any humidification regime, and is higher at the high humidification case than the base case of solely Pt/C.

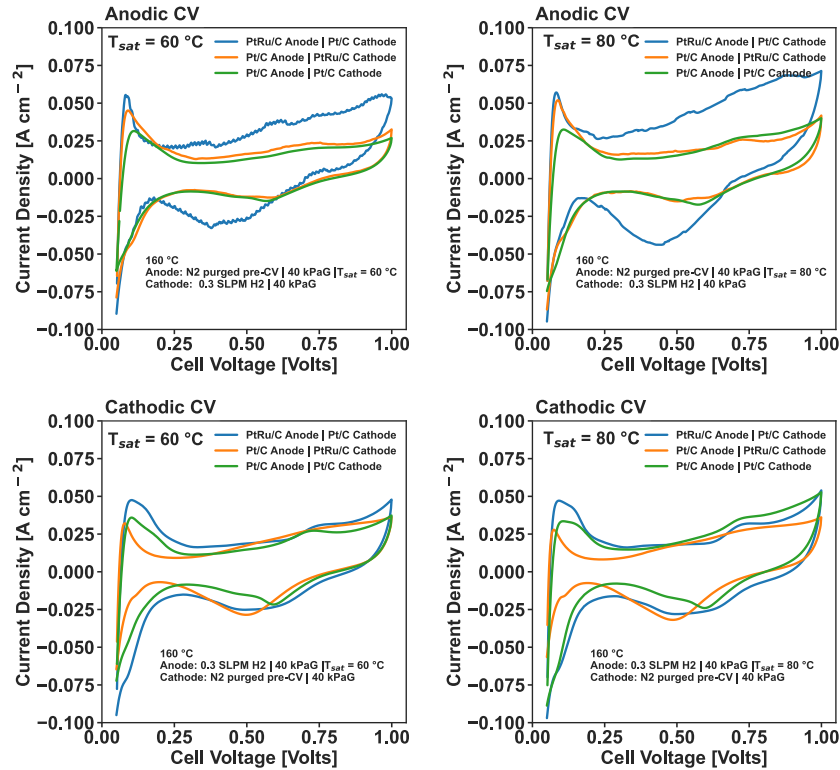


Figure 8.38 Anodic and Cathodic cyclic voltammograms of Pt/C vs. PtRu/C electrodes at 160 °C for anodic humidification of  $T_{sat} = 60\text{ °C}$  and  $T_{sat} = 80\text{ °C}$

Cyclic voltammograms recorded following stabilization and polarization curves at both anode and cathode are displayed above in Figure 8.38. Anodic CVs experienced issues associated with water condensation in gas lines following gas flow cut-off of the humidified gas feed during the cyclic voltammograms measurement most notably for the MEA utilizing PtRu/C in the anode that were later rectified by increasing the time between gas cut-off and subsequent cyclic voltammogram measurement.

With respect to varying relative humidity there was very little variation in cyclic voltammogram features. The differentiating features of the PtRu/C and Pt/C catalysts are more clearly observed in the cathodic CVs due to the lack of humidified gas feed. The features indicating  $H_{upd}$  region of the PtRu/C catalyst as well as the apparent double layer capacitance suggest lower magnitudes of both for the PtRu/C catalyst, the latter potentially attributable to the total carbon content of the



PtRu/C electrode being lower for the same platinum loading. There is a feature occurring roughly in the 0.3 to 0.6 V region in the reduction direction and the 0.6 – 0.8 V in the oxidation direction that could be correlated with electrochemical reduction and oxidation of phosphonic acid from aqueous phosphoric acid electrolyte present in the electrodes (Eq. 8-14). The reduction feature is most prominent in the PtRu/C case. The greater magnitude could be a result of lower double layer capacitance for masking less of the reduction reaction in the PtRu/C electrodes or correlated with the volumetric content of aqueous phosphoric acid and the concentration of water in this phase.

Impedance spectroscopy and distribution of relaxation time analyses of the 160 °C comparison provide some further insight into the influence of increasing relative humidity at the anode. Figure 8.39 displays the DRT fitted EIS data along with the associated log normalized DRT impedance spectrum. HFR values of the ion-pair HT-PEM varied to an extent with the Pt/C electrodes only MEA sitting at relatively higher HFR for all cases and the PtRu/C cathode MEA displaying markedly lower HFR. These slight variation in HFR for the QAPOH-PA at fixed operating conditions is similarly observed in comparable MEAs in published fuel cell literature[158]. The PtRu/C anode MEA shows the greatest sensitivity to anode relative humidity, showing significantly lower charge transfer resistance at relative humidities exceeding 2% over the comparison cases.

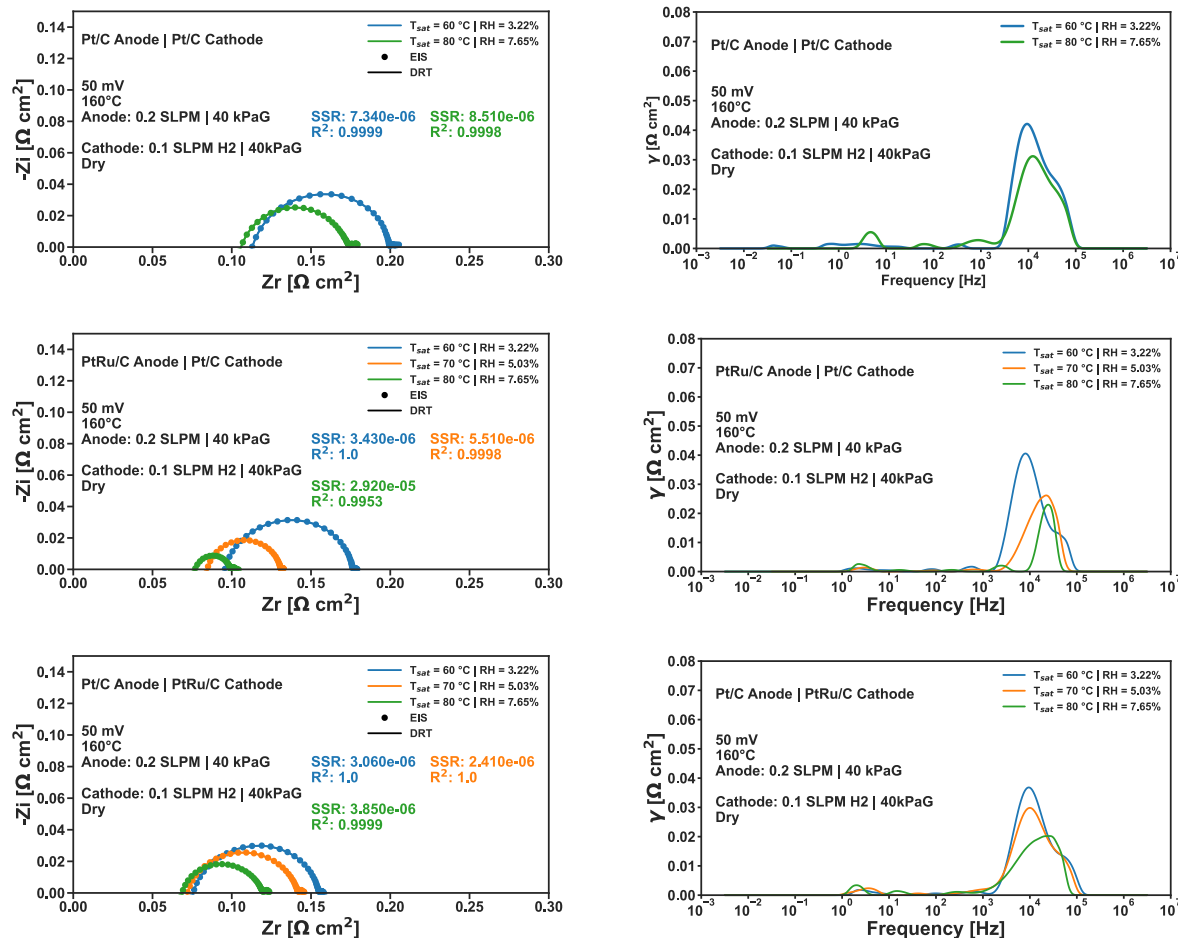


Figure 8.39 EIS and DRT and associated DRT function at 50 mV of Ion-pair HT-PEM EHP with Pt/C and PtRu/C electrodes at 160 °C with varying anodic humidification.

Breaking down the impedances further by the frequency domains (Table 8-2), we can attribute the largest variations to reduction in impedances associated with HOR, P3, due to increasing anode relative humidity. Figure 8.40a highlights the difficulty for 100% H<sub>2</sub> EHP operation in differentiating the P3 and P2 domains related to HOR and HER respectively, so there is some uncertainty associated with the exact delineation and the differentiation between the two is somewhat qualitative. In cases where the anode is mass transport limited, the HOR impedances are more clearly shifted to a lower frequency domain with respect to the HER (Figure 8.32).

There are some small contributions at the highest frequency domain P1, associated with GDE proton transfer, that quickly falls off at increasing relative humidity which aligns with expectations on the ionomer blend conductivity with respect to the water content. In most cases,

the higher frequency portion of the charge transfer impedance associated with the P2/HER is largely unaffected, only slightly reduced at increasing relative humidity at the anode.

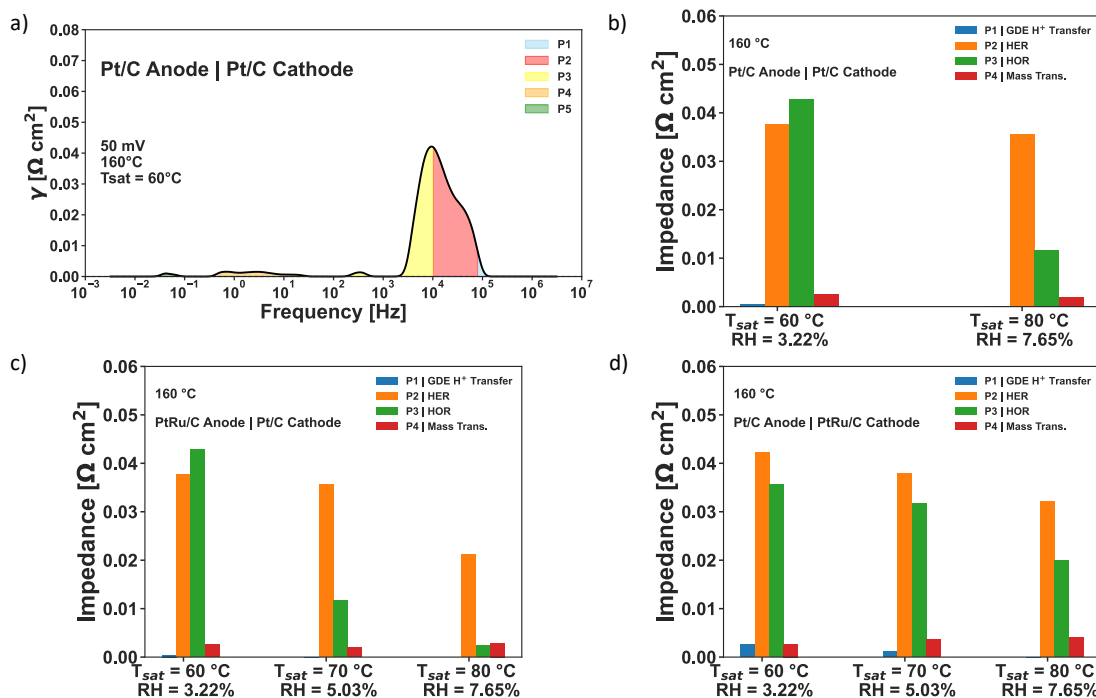


Figure 8.40 a) DRT with frequency domains highlighted for 100% H<sub>2</sub> operation b)-d) Impedance contributions calculated from DRT analysis at 50 mV for Pt/C and PtRu/C electrodes at 160 °C with varying anodic humidification.

The PtRu/C anode showed the greatest reduction in HOR impedance with increasing relative humidity when compared to MEAs with Pt/C anode. Due to the lower carbon content of the PtRu/C electrodes, the electrode structure is thinner and overall smaller volume could help to explain the higher sensitivity to changes in water content due to local anode humidity changes. Table 8-4 shows the combined P2+P3 impedance values from Figure 8.40, which illustrates the lower overall impedance for MEAs containing a PtRu/C electrode and the lowest combined impedance occurring in the PtRu/C anode with the only outlier at the RH = 3.22% condition due to the great humidity sensitivity.

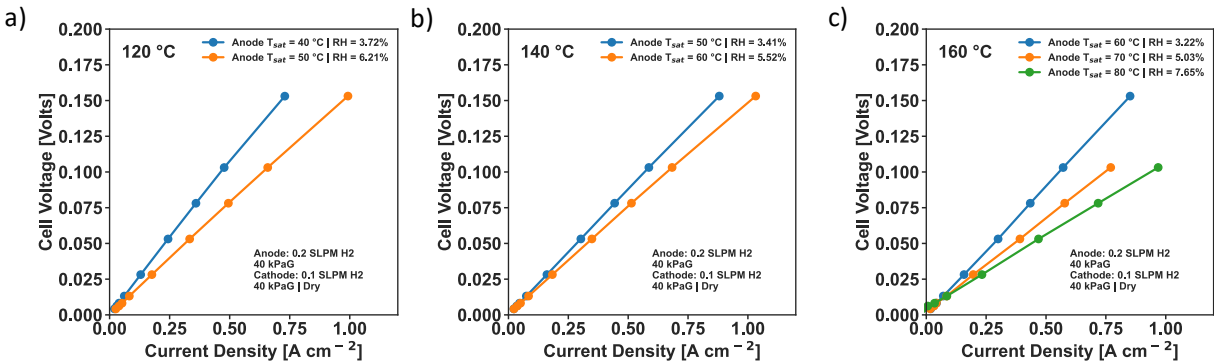
Table 8-4 DRT analysis of HOR + HER impedance contributions combined.

160 °C   P2+P3 Impedance - Combined HOR+HER Kinetics			
Anode   Cathode	3.22% RH [Ω cm <sup>2</sup> ]	5.03% RH [Ω cm <sup>2</sup> ]	7.65% RH [Ω cm <sup>2</sup> ]
Pt/C   Pt/C	0.0893	--	0.0708
PtRu/C   Pt/C	0.0805	0.0473	0.0236
Pt/C   PtRu/C	0.0778	0.0697	0.0520

One of the benefits of the ion-pair HT-PEM as compared to conventional PBI based HT-PEM is its apparent ability to operate at lower temperatures and higher humidities due to the enhanced water tolerance. Thermodynamically this can be favorable for HT-PEM EHP operation as lower temperatures lead to more efficient isothermal compression and electrochemical compression. Conversely major sources of overpotential such as reaction kinetics, the conductivity of proton conducting phases, and mass transport are expected to favor high temperature operation.

The influence of polarization response for the PtRu/C electrode ion-pair EHPs are measured at temperatures down to 120 °C for a humidity window between ~3 and ~8% relative humidity (Figure 8.41). At lower operating temperatures the positive effect from relative humidity on polarization remains, although slightly less pronounced, particularly for Pt/C anode which already exhibited a lower relative humidity dependence on its performance.

### PtRu/C Anode | Pt/C Cathode



### Pt/C Anode | PtRu/C Cathode

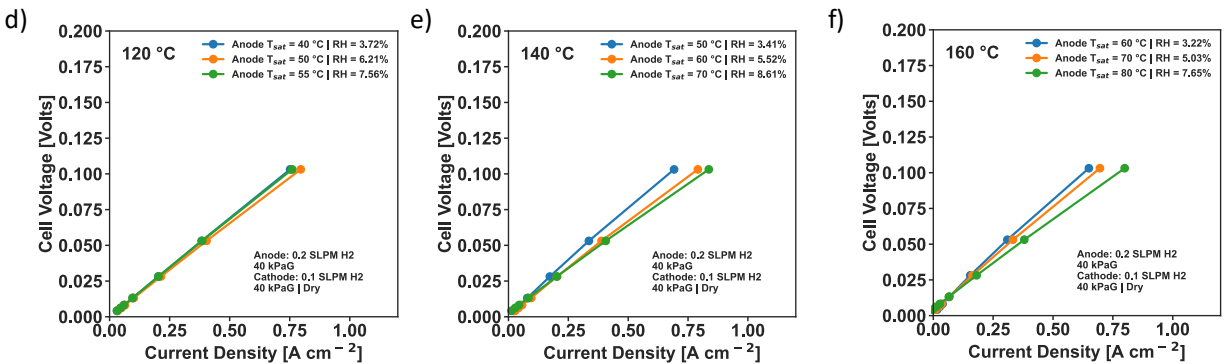
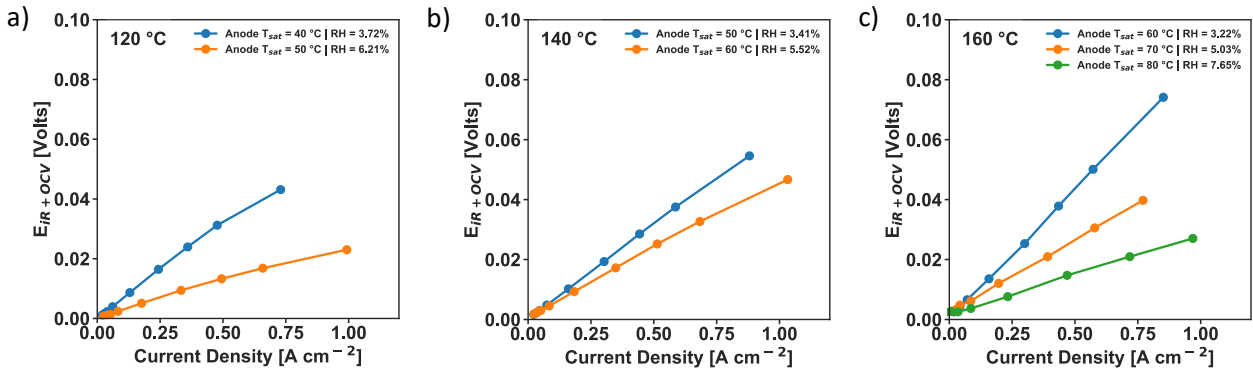


Figure 8.41 Polarization curves of ion-pair HT-PEM EHP with PtRu/C vs. Pt/C electrodes for 120, 140, 160 °C

Correcting for the ohmic losses further emphasizes the influence of humidity on the polarization associated with electrode processes (Figure 8.42). The most notable difference between the two MEAs is the lack of dependence on RH for the 120 °C case in the Pt/C anode, whereas the PtRu/C anode continues to demonstrate a high degree of dependence on humidification. Generally, it is evident that higher temperatures lead to a greater sensitivity to changes in relative humidity.

**PtRu/C Anode | Pt/C Cathode**



**Pt/C Anode | PtRu/C Cathode**

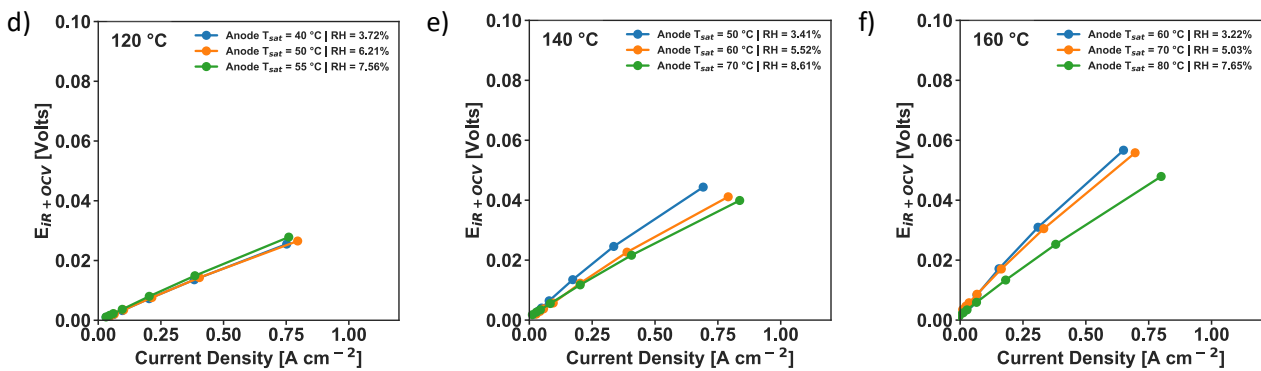


Figure 8.42 OCV and ohmic loss corrected polarization curves of ion-pair HT-PEM EHP with PtRu/C vs. Pt/C electrodes for 120, 140, 160 °C

Cyclic voltammograms of the two MEAs for all temperature cases are presented in below in Figure 8.43. The anodic cyclic voltammetry of the PtRu/C had signal noise present due to water condensation in the gas lines during the  $N_2$  gas cut that occurs contemporaneously with the cyclic voltammogram measurement. A strong dependence on temperature is prominent for the oxidation feature between  $\sim 0.3$  and  $0.65$  V that was previously associated with phosphonic acid formation, which is hypothesized to be favored at high temperatures from HT RDE experiments[235]. Pt/C electrodes show a more obvious trend with this regard, and also display an enhancement of the  $H_{upd}$  region with increasing temperature. PtRu/C  $H_{upd}$  region is not notably greater despite its better performance with respect to electrode impedance in the anode.

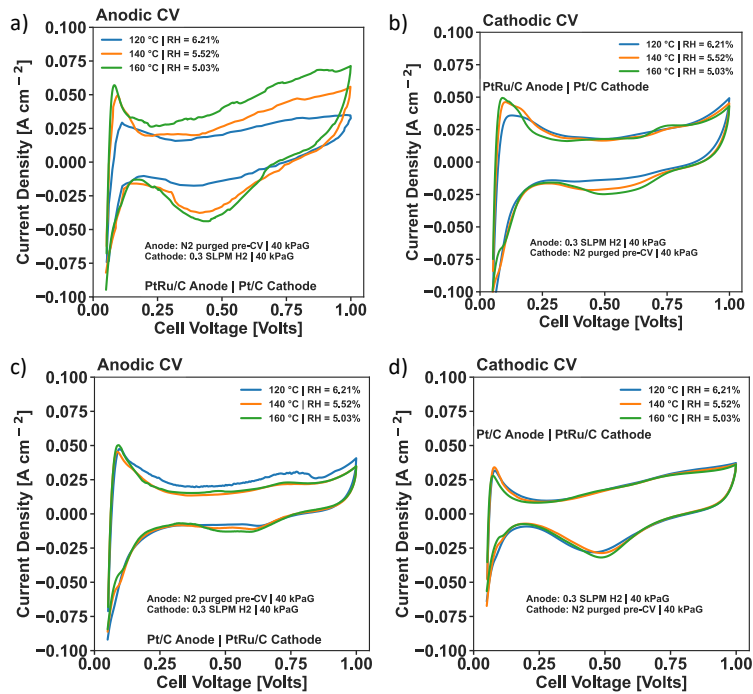
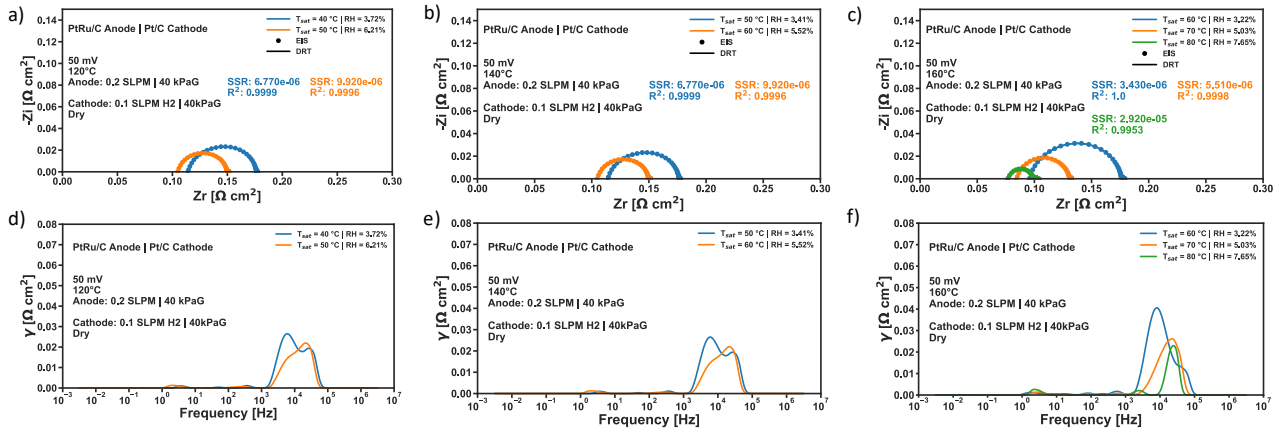


Figure 8.43 Cyclic voltammetry taken at 50 mV/sec of PtRu/C and Pt/C electrodes in MEA for 120, 140, and 160 °C

Electrochemical impedance spectroscopy and distribution of relaxation times analysis are applied at 50 mV for the range of temperature and humidification considered (Figure 8.44). DRT functions were well fitted with sum of squares residuals (SSR) on the order of 10<sup>-6</sup>. A shift in impedance to lower magnitude and higher frequency domains can be observed with increasing relative humidity, indicating improvements in electrode kinetics. One outlier case occurs at the T = 160 °C at relative humidity of 7.65% for the PtRu/C anode MEA where measured electrode impedance is very small making DRT fitting difficult and potentially unreliable - see Figure 8.44f.

**PtRu/C Anode | Pt/C Cathode**



**Pt/C Anode | PtRu/C Cathode**

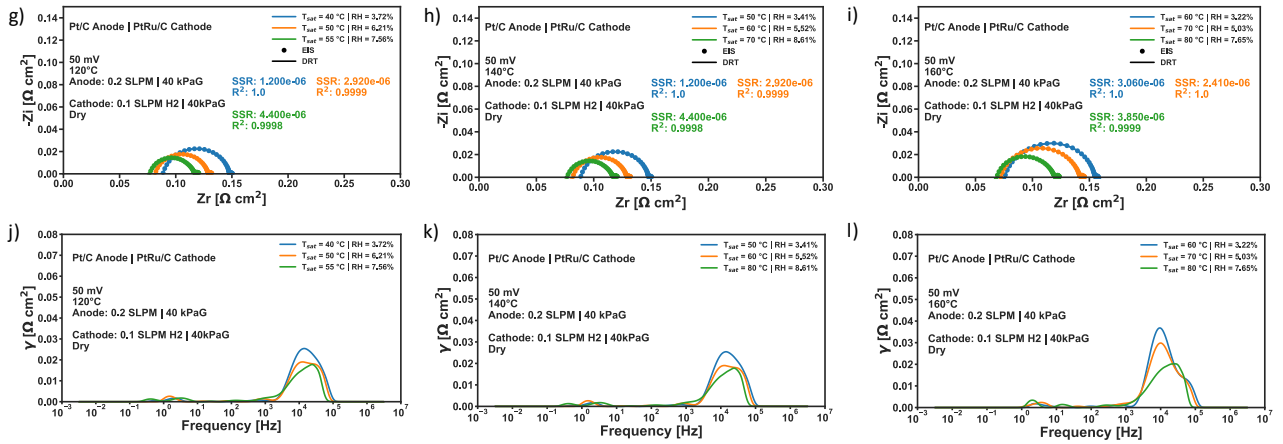


Figure 8.44 DRT at 50 mV for PtRu/C vs. Pt/C electrodes in ion-pair HT-PEM EHP for varying temperature and relative humidity.



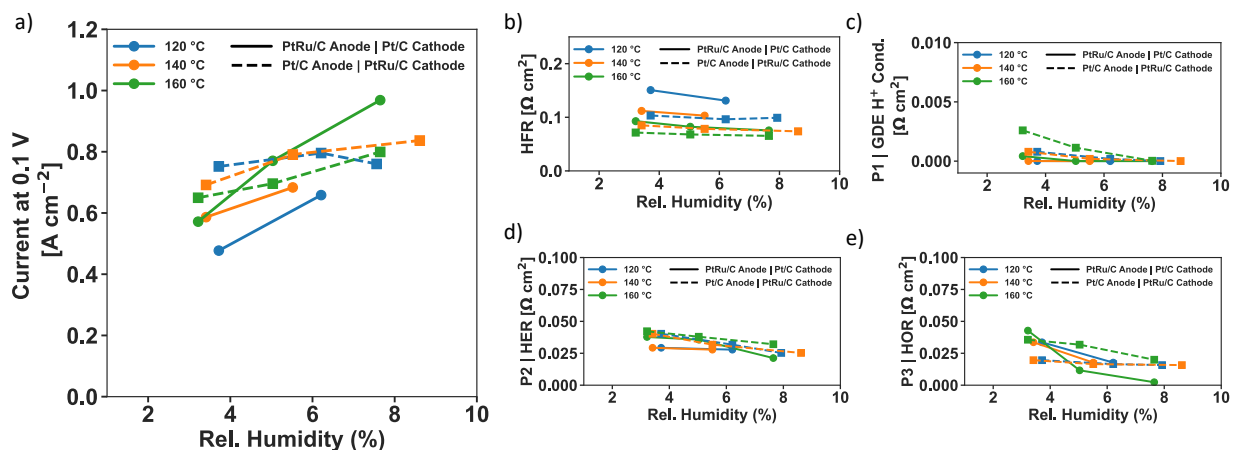


Figure 8.45 Net impedance contribution at 50 mV calculated from DRT for PtRu/C vs. Pt/C electrode ion-pair HT-PEM EHP.

The performance of the two ion-pair HT-PEM EHPs is further summarized with EIS and DRT impedance breakdown in Figure 8.45. There was a higher degree of HFR sensitivity to temperature than to relative humidity, however impedance associated with GDE  $\text{H}^+$  and HOR, as well as HER to a lesser extent, is more sensitive to the humidification. This lines up with the observed trends in the previous section with respect to  $R_{CT}$  growth in ion-pair HT-PEM EHP with ionomer. It is evident that the electrodes are a major limiting factor in performance and the primary issues that need to be addressed to improve stability and widen operating range of ion-pair based HT-PEM EHP.

#### 8.4.5 Natural Gas Separation with Ion-Pair HT-PEM EHP

$\text{H}_2$  blended with natural gas at low concentrations (< 20% vol  $\text{H}_2$ ) is an application of direct interest to HT-PEM EHP due to its capability of separating dilute mixtures of  $\text{H}_2$  to high purity as demonstrated in Chapter 5 with PBI-PA based HT-PEM EHP where the diluent was methane gas. While there are several examples of methane/hydrogen gas separation in the literature using EHP type cells[272][148][103][173][102], there are very limited examples of real natural gas as the diluent[273] and none in the low concentration range of interest in the near future for  $\text{H}_2$  co-transportation in natural gas infrastructure. To examine the stability and efficacy of the ion-pair HT-EHP in natural gas separation, a 10%  $\text{H}_2$  blend in real pipeline natural gas fed through a desulfurization process is processed by the HT-PEM EHP.

Pipeline natural gas is a blend of gaseous hydrocarbons, primarily consisting of methane, along with inert gases such as CO<sub>2</sub> and N<sub>2</sub>, and trace amounts of sulfur compounds (~1 ppm) and siloxanes. Natural gas from the 40 psig distribution line is mixed at the anode feed-in to the HT-PEM test stand with H<sub>2</sub> gas post de-sulfurization by adsorbent beds. The composition of the natural gas feed without blending and with cell feed conditions (10% H<sub>2</sub> and humidification followed by gas drying) was analyzed via gas chromatography with TCD and FID-methanizer to characterize the bulk constituents.

In the dry natural gas feed post de-sulfurization three peaks are prominent in the FID+Methanizer detector associated with CH<sub>4</sub>, CO<sub>2</sub>, and C<sub>2</sub>H<sub>6</sub> (Figure 8.45). TCD detector similarly detects the same peaks, but the sensitivity is poor, with 0.5 % vol reference gas signal indicating detection at sub 1% levels insufficient at the TCD detector. The TCD can measure H<sub>2</sub> signals from the 10% H<sub>2</sub> blend and pure H<sub>2</sub> that are not measurable with the FID detector due to the usage of a hydrogen flame in FID. There is no indication of CO in a measurable amount in any case, indicating that any secondary formation of CO from the presence of water vapor and CO<sub>2</sub> through reverse water-gas shift is minimal.

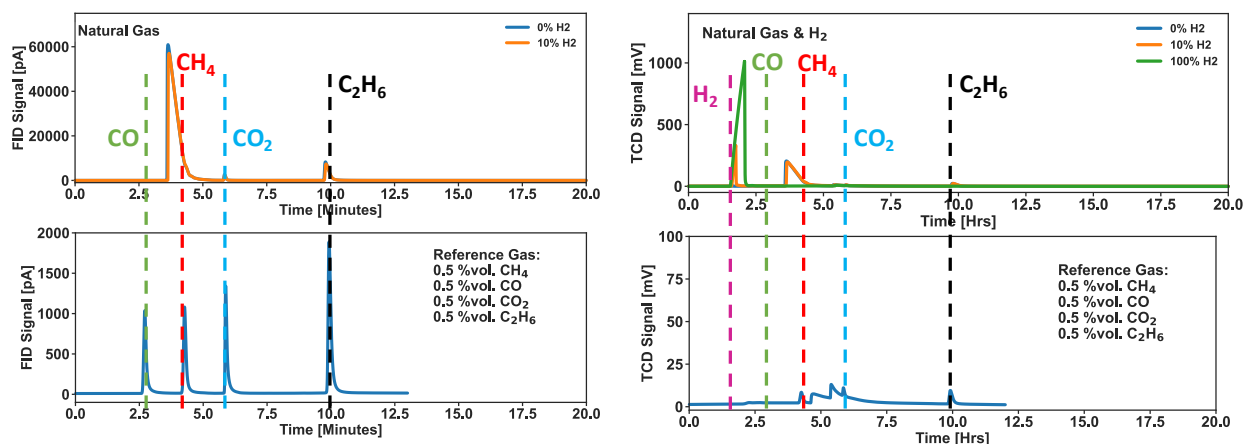


Figure 8.46 Gas chromatography of natural gas, H<sub>2</sub>, and humidified ( $T_{sat} = 60\text{ }^{\circ}\text{C}$ ) then dried ( $\sim T_{sat} = 20\text{ }^{\circ}\text{C}$ ) 10% H<sub>2</sub> in natural gas anodic feed to HT-PEM EHP for nat. gas separation testing.

*Table 8-5 Composition of de-sulfurized natural gas from 40 psig distribution line and composition of natural gas blended with 10% volumetric H<sub>2</sub> and fed through anode of HT-PEM EHP at humidification of T<sub>sat</sub> = 60 °C followed by drying at 20 °C.*

Natural Gas & H <sub>2</sub> Blend Composition [% Volumetric]						
H <sub>2</sub>	CH <sub>4</sub>	CO <sub>2</sub>	CO	C <sub>2</sub> H <sub>6</sub>	Other	H <sub>2</sub> O (v)
0	96.12	0.971	<25 ppm	2.526	0.383	-
10.02	84.02	0.892	<25 ppm	2.444	2.624	~2.34*

\*calculated from a saturation temperature of T = 20 °C following water drop-out and coalescing filter

The composition of the pipeline natural gas at the SoCalGas distribution line is relatively high in methane content exceeding 95% by volume. Natural gas does contain some trace gaseous species, likely consisting of propane and other higher hydrocarbons as well as N<sub>2</sub> and potentially some O<sub>2</sub>. Interestingly while ethane was detected, no other hydrocarbon signatures beyond ethane and methane were detected by the GC + FID.

Ion-pair HT-PEM EHPs benefit in performance with increasing humidity content in the anode hydrogen feed. Up to this point in this study continuous improvement and stable operation has been demonstrated up to vapor pressure of P<sub>v</sub> = 47 kPa corresponding to a T<sub>sat</sub> of 80 °C and a relative humidity of 7.6% at 160 °C cell temperature. In the scenario of gas separation for low volume content hydrogen feeds, high vapor pressure feeds can lead to appreciable dilution of the already low hydrogen content. (Figure 8.47) shows the ratio of dry hydrogen partial pressure in a diluent gas entering the separation system before humidification to the actual hydrogen partial pressure following humidification before entering the HT-PEM EHP for the range of vapor pressure studied for 160 °C operation.

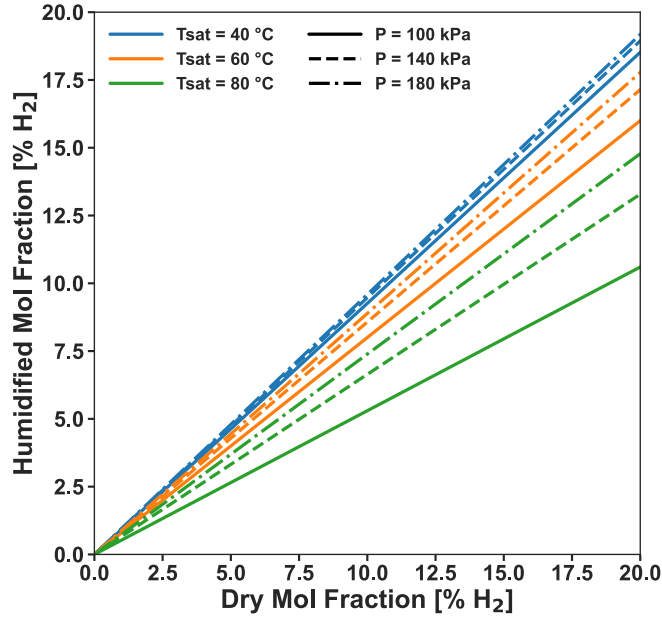


Figure 8.47 Dilution of hydrogen content in blended gas feed with increasing pressure and relative humidity.

At a  $T_{\text{sat}}$  of 40 °C the partial vapor pressure of water is only 7.4 kPa and the dilution effect is very small, with a 10% dry hydrogen feed having a concentration of 9.4 to 9.6 % post humidification, depending on the total operation pressure. The effect becomes far more pronounced at  $T_{\text{sat}} = 80$  °C, where a vapor pressure of 47 kPa means non-negligible dilution of other gases present. In this scenario, a 10% dry hydrogen feed can be diluted to as low as 7.4 to 5.3 % post humidification depending on the feed-in pressure.

In terms of separation performance at the cell, this dilution effect can potentially impact diffusion limited mass transport due to the lower effective concentration gradient from channel to reaction sites in the electrode leading to lower diffusive transport rate. More apparent is the potential impact on the thermodynamics of the process. By the Nernst equation, the open-circuit voltage (OCV) will shift according to the ratio of partial pressures at the anode and cathode of the HT-PEM EHP,

$$OCV = \frac{RT}{2F} \ln \left( \frac{P_{H_2,c}}{P_{H_2,an}} \right) \quad (\text{Eq. 8-16})$$

Where the partial pressure of H<sub>2</sub> at the anode depends on the mol fraction of the H<sub>2</sub> feed, the degree of vapor pressure due to humidification, and the total pressure of the anode feed. The cathode pressure depends on the degree of pressurization at the cathode as well as the concentration of H<sub>2</sub> which could be impacted by the degree of water vapor present due to water present in the membrane phase. The model of the PBI based HT-PEM EHP suggested that the vapor content is appreciable in the PBI based HT-PEM EHP on the cathode side (Chapter 6), but no measurements of cathode relative humidity were available at the time of that study to confirm this fact. Here relative humidity will be monitored on the cathode outlet during HT-PEM EHP operation.

In terms of the potential impact of OCV, there are two extremes where the cathode relative humidity is equivalent to the anode and where the cathode is completely dry (Figure 8.48). In the case of totally dry cathode, a higher OCV is expected due to the larger concentration gradient from anode to cathode relative to a fully humidified cathode scenario. In the case of a humidified cathode, at equivalent anode and cathode pressures, the OCV does not shift with increasing humidification. When the cathode is pressurized above anode operating pressures, the increase in open-circuit voltage is less due to the lower effective hydrogen partial pressure at the cathode. This does not account for the possibility that elevated cathode pressures could dry cathode further due to pressure driven hydraulic water transport as observed in LT-PEM EHP[86]. Due to the relatively low increase in overpotential when pressurizing the cathode in the humid cathode case, ~ 10 mV at 5% dry H<sub>2</sub> feed for T<sub>sat</sub> 60 °C for one example, the potential benefits of a compressed hydrogen gas product and potentially higher purity product are typically worth operating the HT-PEM EHP at higher pressure ratios.

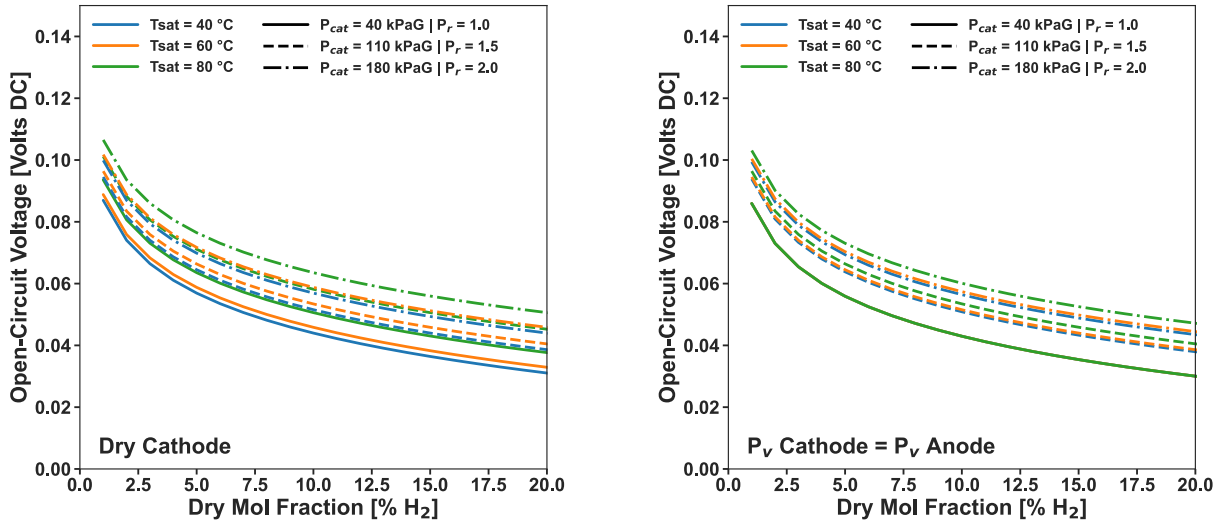


Figure 8.48 Open-circuit voltage variation due to varying partial pressures of hydrogen in EHP at 160 °C and 40 kPaG anode pressure with respect to varying cathodic pressure and humidification.

Lastly, there is the practical consideration of higher anodic humidification leading to higher degree of cathode humidification, meaning that the H<sub>2</sub> product on the cathode outlet is diluted by the presence of water vapor. Since the goal of H<sub>2</sub> separation and compression systems is a high purity product, a lower anode gas feed humidification is desirable from a product purity standpoint and from a simplicity standpoint as higher humidification requires greater degree of system thermal control to maintain water in vapor phase.

Measurements in 100% H<sub>2</sub> EHP operation suggested that T<sub>sat</sub> = 60 °C provided reasonable performance and stability at 160 °C operating temperature. This humidification point was deemed most reasonable for the operation of ion-pair HT-PEM EHP in H<sub>2</sub> gas separation characterization testing to balance trade-offs in the form of higher ohmic impedances and lower mass transport limitations as well as higher product purity compared to operating at higher anodic relative humidities.

MEA1 (Table 8-3) from the previous section is operated on the 10% H<sub>2</sub> + natural gas blend at total anodic flow rate of 1.0 SLPM and a pressure ratio of 1.5 with anode pressure 140 kPa and cathodic pressure 210 kPa. Despite a maximum theoretical current density of 2.85 A cm<sup>-2</sup> corresponding to 100% faradaic efficiency mass transport limitations begin to appear around the 0.5 A cm<sup>-2</sup> mark which is 17.5 % of the theoretical limiting current or in other words a hydrogen

recovery factor (HRF) of 17.5% (Figure 8.49). An OCV shift of 50 mV is in-line with the slightly drier cathode condition due to 0.1 SLPM of dry H<sub>2</sub> sweep gas applied during polarization curve to maintain pressure at the lower current density conditions.

Stability of the HT-PEM EHP is assessed at potentiostatic hold of 0.15 V as this point occurs before significant mass transport limitations occur which cause EHP separation processes to dramatically drop off in separation efficiency. Hourly EIS measurements at the 0.15 V condition are recorded as well to track the changing impedance response for better understanding of limiting factors in cell stability.

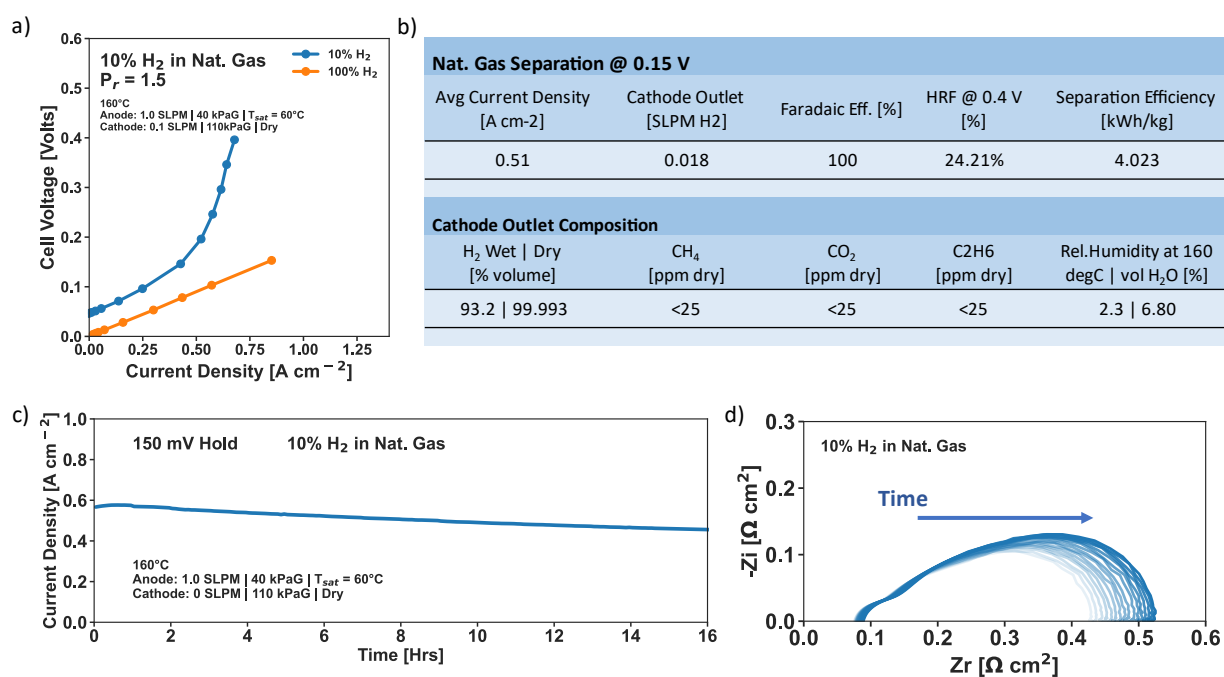


Figure 8.49 10% H<sub>2</sub>/Natural Gas blend separation in ion-pair HT-PEM EHP at 1.0 SLPM anode flow rate and pressure ratio of 1.5 a) Polarization curve b-d) 16 hour 0.15 V potentiostatic stability and separation test

Cathode outlet flow rate was monitored during separation process with an average flow rate of 0.018 SLPM H<sub>2</sub> – for an average current density of 0.51 A cm<sup>-2</sup> the expected 100% faradaic efficiency outflow is 0.01785 SLPM H<sub>2</sub> so the faradaic efficiency is determined to be roughly 100%.

Cathode outlet humidity was monitored continuously and found to be appreciable with a relative humidity of 2.3% at 160 °C corresponding to a vapor pressure of 14.26 kPa and a volumetric

concentration of 6.80 %. Preceding the GC measurement cooling and gravimetric drop-out of water followed by coalescing filter removes a large portion of the humidity content in the cathode outlet. In-line GC measurements indicate a very high purity  $H_2$  product on a dry basis, with only methane gas showing above the detection limits of 25 ppm for the FID-methanizer detector.

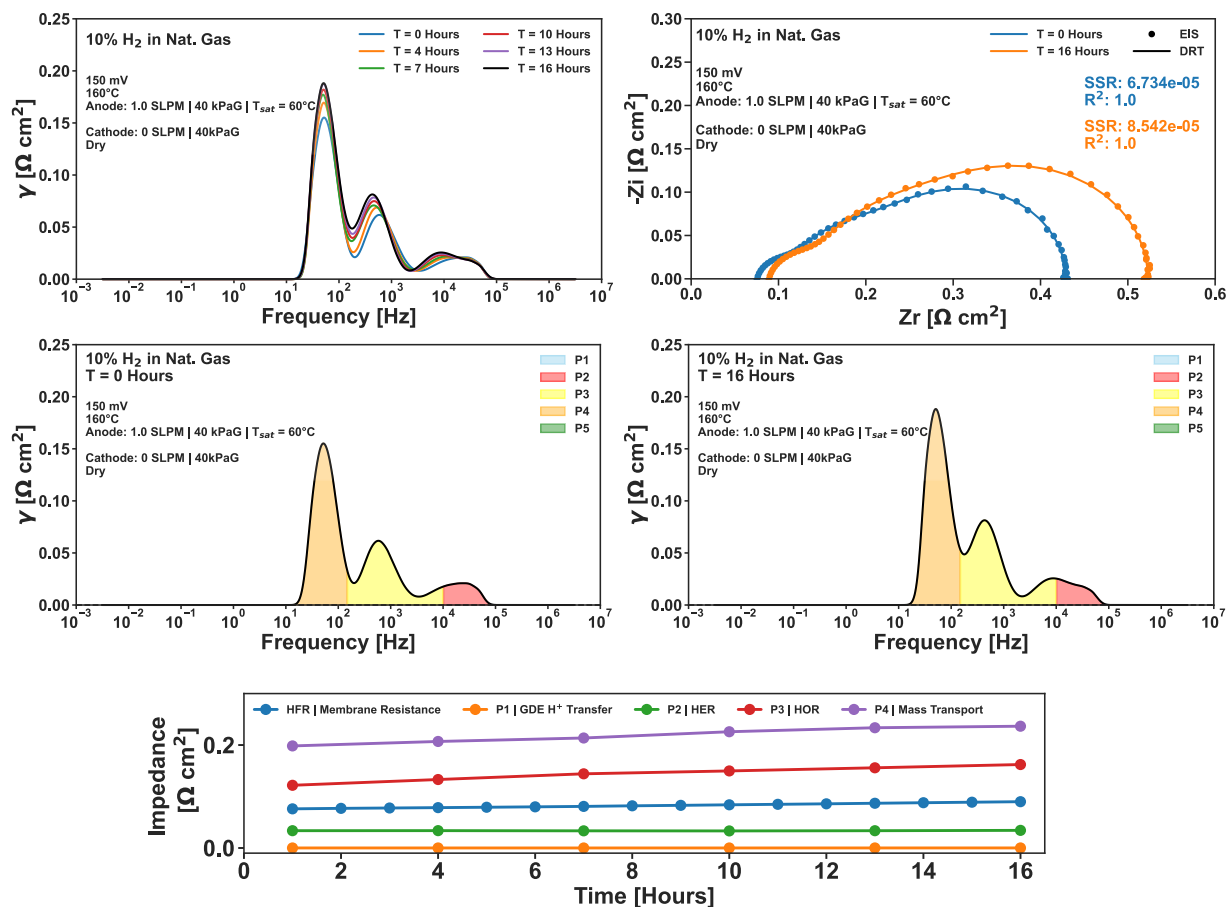


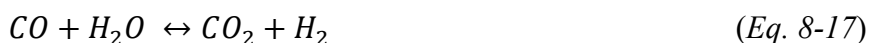
Figure 8.50 DRT and EIS data from 16-hour stability of 10%  $H_2$ /Natural Gas separation testing.

Impedance data from the 16-hour natural gas separation testing at 0.15 V is further processed into a distribution of relaxation times function. The higher frequency impedance domains associated with proton conduction and cathodic HER processes are largely unaffected, while a significant growth in impedance occurs in regions associated with anodic HOR processes as well as mass transport limiting phenomenon.

Another strong driver of impedance growth is the contribution from high frequency resistance (HFR) associated with protonic conduction in the membrane and electronic conduction. One



possible explainer for these effects is the high anodic flow rates leading to enhanced local evaporation rates and thus uneven cooling rates across the MEA. Another could be contributions due to impurities in the natural gas feed. The desulfurization beds minimize the presence of sulfur compounds, but trace amounts of sulfur compounds could still have deleterious impact at the anode. Furthermore, the potential secondary chemical formation of CO through reverse water-gas shift ((Eq. 8-17) inside the cell due to the elevated temperature, high concentration of H<sub>2</sub> and CO<sub>2</sub> relative to CO and H<sub>2</sub>O, and presence of platinum catalyst could further impede electrode kinetics[256] with the secondary formation of CO from H<sub>2</sub> and CO<sub>2</sub> mixtures observed on Pt surfaces in LT-PEM EHP[274].



Longer term stability of the ion-pair HT-PEM EHP was examined following the 16-hour stability test at 0.3 V potentiostatic hold for 100 hours. 0.3 V was selected to ensure that limiting current was reached for the longer-term hold so that cathodic pressure was maintained through sufficient HER reaction rate. In the first 48 hours, current decay was relatively high at an average loss rate of -10.4 mA/cm<sup>2</sup>/hr. Near the end of the 100-hour period, the current decay seemed to be settling, with the decay rate in the final 24 hours only at -2.8 mA/cm<sup>2</sup>/hr and the HFR increase seeming to have leveled off.

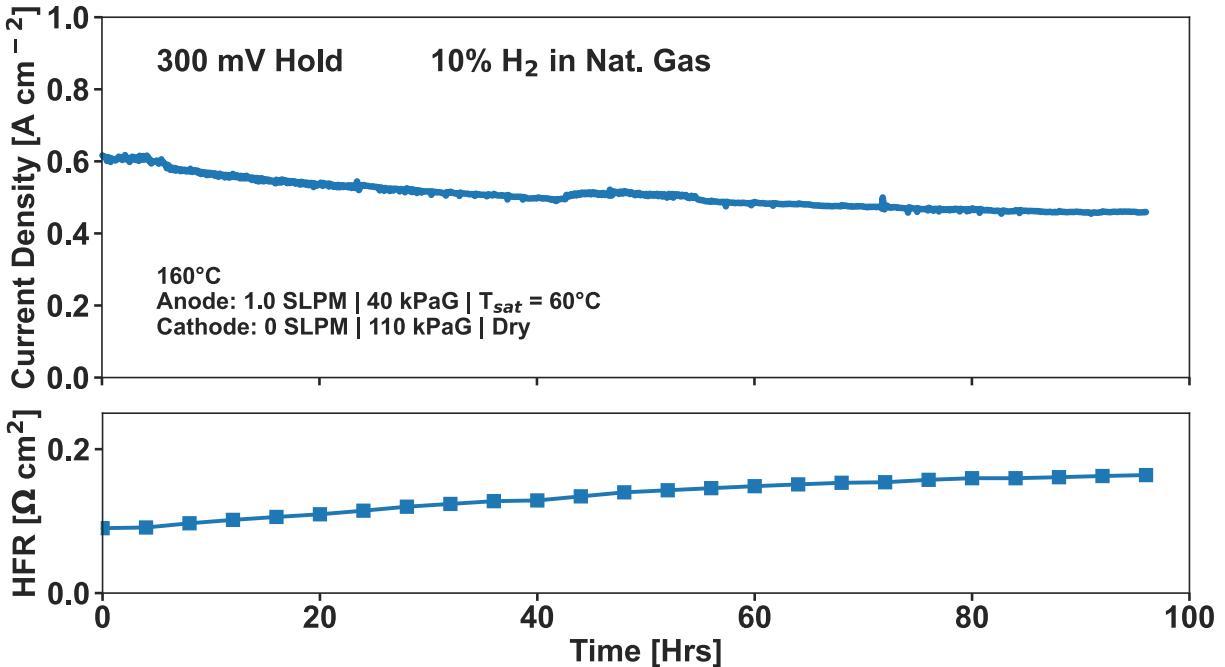


Figure 8.51 300 mV 100 hour stability test of 10% H<sub>2</sub>/ Natural Gas blend separation with HFR change.

While stability testing indicates that the ion-pair HT-PEM EHP was not completely stable within the time periods considered, the 100 hours test shows promise of eventual stabilization on longer timescales. Electrode impedance and in particular mass transport losses dominate, and the maximum hydrogen recovery factor is far lower than what was feasible in conventional PBI-PA HT-PEM EHP (Chapter 5).

## 8.5 Conclusions

For the first time ion-pair HT-PEM cells based on phosphoric acid doped QAPOH membranes have been studied in MEA in EHP with both ionomeric and non-ionomeric electrode systems. In fuel cell configurations, the ion-pair HT-PEMs exhibit reasonable stability and performance in dry gas feed conditions at temperatures up to 180 °C without phosphonated ionomer[111] and with ionomeric binder[155][157], however in EHP configuration the absence of any water generation leads to unique reaction environment that requires more careful consideration in terms of cell humidification. The presence of Nafion®/PWN ionomeric binder served to stabilize electrode impedance given sufficient humidification. In the absence of ionomeric binder, the formation of an electrochemically reversible species inhibited electrode kinetics, the effect of

which was favored in drier operating conditions. Given the window of potential at which this electrochemical recovery occurred ( $>0.7$  V vs . RHE), it is likely that the formation of phosphonic acid in the phosphoric acid aqueous phase was the main contributor to this impedance growth. This is reinforced by the observation that  $R_{CT}$  impedance growth can occur at higher humidities. Previously phosphoric acid anhydrides that form in low water content aqueous phosphoric acid systems had been hypothesized to contribute to electrode impedance growth, however at the poisoning effect was observed at humidities corresponding to phosphoric acid systems in which the formation of these anhydrides would not be favored. Furthermore, the presence of the ionomeric Nafion®/PWN serves to inhibit the formation of phosphonic acid anhydrides and furthermore could be inhibiting the further formation of phosphonic acid in the aqueous phase due to presence of stabilized phosphonic acid in the PWN binder.

Electrodes based on PtRu/C electrocatalyst had a beneficial effect on performance of the ion-pair HT-PEM EHP when employed in the anode with Pt/C based electrodes on the cathode. The reverse case had a negligible effect on electrode performance. Pt-Ru binary electrocatalyst systems are known to suppress negative interactions with aromatic hydrocarbons present in the ionomer (phenyl groups). In this case the PtRu/C based anode exhibited a high sensitivity to humidification indicating structural differences contributing to the difference in electrode impedance versus the Pt/C based anode.

Pipeline natural gas blended with low volumetric concentration (10% volume)  $H_2$  gas were separated in an EHP cell for the first time with cell lifetime in excess of 100 hours. Fuel cell grade  $H_2$  gas was separated out at a purity of 99.993% by operating at cathodic to anodic pressure ration of 1.5 demonstrating co-compression and separation of  $H_2$  gas. Mass transport in the ion-pair HT-PEM EHPs was a strong limiting factor in performance with onset of limiting current occurring at around 24% hydrogen recovery factor as opposed to hydrogen recovery factors of 80% attained in the PBI-PA HT-PEM EHP (Chapter 5).

## **Chapter 9 Characterization of highly sulfonated ionomers in Ion-Pair based HT-PEM EHP electrodes for H<sub>2</sub> gas separation from low H<sub>2</sub> content H<sub>2</sub>/Natural Gas Blends**

### **9.1 Introduction**

The introduction of ionomeric binders as a thin film in the electrode have played a critical role in increasing the performance and reducing the necessary amount of catalyst in LT-PEMFC[275] and in recent years a similar push has been observed in alkaline exchange membrane fuel cells (AEMFC)with appreciable impacts on performance and stability[269][276]. In HT-PEMFCs based on PA-PBI membranes, the implementation of PA-PBI as an ionomeric binder phase as well as the membrane as is commonly employed in Nafion® based LT-PEMFC cells, led to PA flooding due to the hydrophilic PBI ionomer[277][278]. Hydrophobic non-ionomeric binder such as PTFE or PVDF binder is considered state of the art, and is utilized to prevent PA flooding in some hydrophobic domains allowing gas diffusion pathways to other domains filled with phosphoric acid electrolyte wetted catalyst.

Phosphonic acid (H<sub>3</sub>PO<sub>3</sub>) has high intrinsic proton conductivity slightly lower than phosphoric acid (H<sub>3</sub>PO<sub>4</sub>) but unlike phosphoric acid is capable of chemically grafting to polymer structures through stable P-C bonds[279]. This opens up the possibility of a chemically stabilized proton conducting polymer without aqueous electrolyte that can flood and poison electrode environment of the HT-PEM. As a candidate for proton conducting high temperature membranes these phosphanated polymers struggle due to the low anhydrous conductivity of phosphonic acid[280][281] and further complicated by their poor mechanical[282] and chemical stability[153] when cast in polymer form.

The mechanical properties and degree of proton conductivity are less critical when considering phosphanated polymers as an ionomeric binder due to the thin film formation of the ionomer in the electrode. A limited number of phosphanated ionomers have been implemented in HT-PEMFCs with varying success. Polyvinylphosonic acid (PVPA) as an ionomer has been investigated in HT-PEM EHP[283] and HT-PEMFC[155] however the propensity to form low conductivity anhydrides limited their performance. In 2010 Atanasov et al. synthesized highly

phosphanated polypentafluorostyrene dubbed ‘PWN2010’ that demonstrated high proton conductivities at temperatures exceeding 100 °C at vapor pressure of  $10^5$  ( $T_{\text{sat}} = 100$  °C), orders of magnitude higher than PVPA and higher than Nafion® in the same conditions[154].

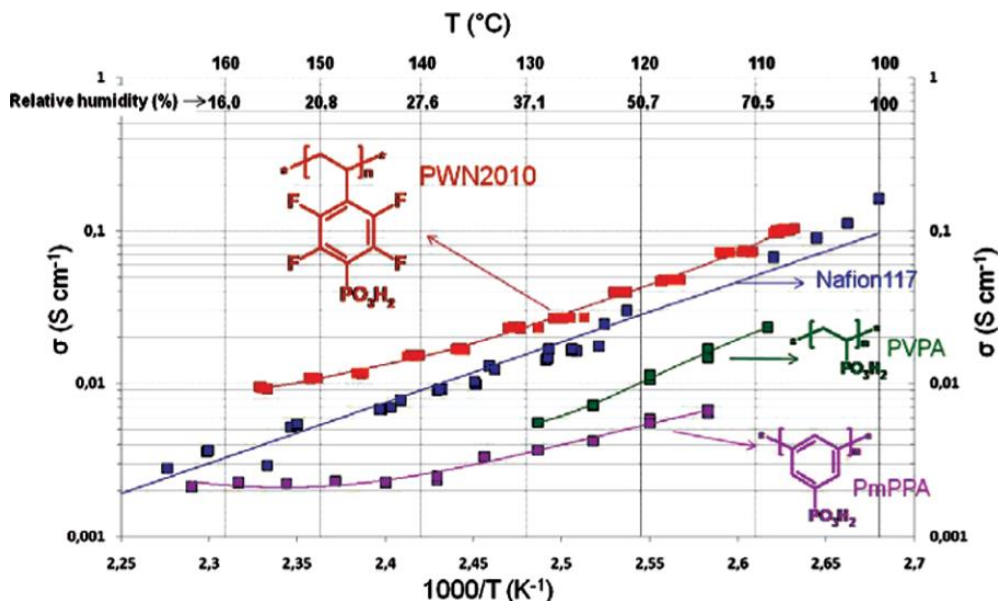


Figure 9.1  $H^+$  conductivity of PWN2010 compared to Nafion®, PVPA, and PmPRA in  $P_v = 10^5$  Pa at 100 to 160 °C. Reproduced from [154].

PWN as an ionomeric binder enabled enhanced stability and long-term performance in PA-PBI based HT-PEMFC through enhanced mass transport and improved ORR kinetics as compared to PTFE based ionomeric binders, although the degree of its efficacy was sensitive to the degree of polymer phosphonation[133]. When paired with QAPOH-PA ion-pair HT-PEMFC a PWN binder with 70% degree phosphonation ‘PWN70’ exhibited superior performance to PVPA and to PA-doped quaternary ammonium tethered polystyrene (QASOH-PA) ion-pair ionomeric binder[155] [111]. The enhanced performance was attributed to the lowered propensity for PWN to form anhydrides due to the fluorophenyl ring, and the higher hydrophobicity and acid retention over the PA-doped QASOH-PA which contains 10x the amount of acid sites as the PWN70 and thus still suffers from flooding and phosphate poisoning.

To extend the low temperature performance of ion-pair HT-PEMFC following the promising results of QAPOH-PA membranes paired with PWN70 ionomeric binder electrodes, Nafion® was added as a blended ionomer with the PWN70. The result was an overall enhanced electrode

for HT-PEMFC across a wide range of temperatures with maximum power density of the HT-PEMFC exceeding  $1 \text{ W cm}^{-2}$  at  $200 \text{ }^\circ\text{C}$  and  $0.78 \text{ W cm}^{-2}$  at  $160 \text{ }^\circ\text{C}$ . The improvement in performance at temperatures above which Nafion® is typically effective was attributed to a protonation of phosphonic acid by the perfluorosulfonic acid (PFSA) site on the Nafion® increasing the acidity of the sites[157]. NMR analysis indicates the formation of these protonation bonds and the reduction of phosphonic acid anhydrides in the PWN in the presence of PFSA[157][283].

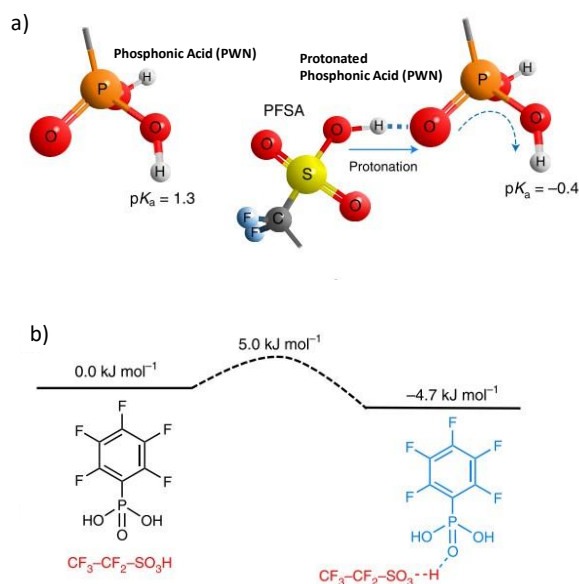


Figure 9.2 a) Protonation of phosphonic acid sites on PWN binder and enhanced acidity of the resulting ‘protonated’ ionomer b) DFT calculations on propensity of protonation between phosphonic acid and sulfonic acid site of the PFSA. Reproduced from [157].

The promising results of the ‘protonated’ phosphonic acid electrodes in ion-pair HT-PEMFC indicate potential to further optimize electrodes for HT-PEM EHP in gas separation. To date, the performance of ion-pair HT-PEM EHP is not well understood as compared to the ion-pair HT-PEMFC which in and of itself is in the very early stages of research and development. Little research has been done studying the ionomeric binder that performs best in HT-PEM EHP environments where the degree of humidification is entirely dependent on the gas feed humidification and the impacts of mass transport in gas separation become more critical.

In their study of the protonated phosphonic acid electrodes, Lim et al found that varying the degree of phosphonation in the PWN when blending with Nafion® had an optimal degree of phosphonation due to trade-offs in proton conductivity - which was maximized with maximum degree of phosphonation - and mass transfer limitations at high degree of phosphonation. Furthermore, the amount of Nafion® content for a given degree of phosphonation lead to an optimal weight fraction of 40-60% Nafion and 40-60% PWN with 66% degree phosphonation. At 1:1 weight ratio of Nafion®/PWN this corresponded to a ratio of sulfonic acid and phosphonic acid sites (P/S ratio) of 2.0[157]. In another study of PFSA ionomers blended with phosphanated ionomers, an optimal P/S ratio of 1.56 to 2.0 was determined for Aquivion® and PWN binder (62% degree phosphonation)[283]. It was postulated that the higher ion exchange capacity of Aquivion (~1.36 meq/g) as compared to Nafion® 211 (0.9 meq/g) resulted in the observed lower optimal P/S ratio and higher proton conductivity.

Sulfonated polypentafluorostyrene (SPPsf) is a highly conductive ionomer capable of attaining complete sulfonation. At 100% degree sulfonation, SPPsf demonstrated proton conductivity of 35 mS cm<sup>-1</sup> at 160 °C and 10<sup>5</sup> Pa vapor pressure far higher than the phosphanated counterpart PWN, and order of magnitude higher than Nafion® in the same conditions. Furthermore, the degree of sulfonation of the SPPsf binder is tunable during synthesis. The high proton conductivity and the chemically similar polymer backbone make SPPsf a potential candidate for the PFSA component of protonated phosphonic acid electrodes in HT-PEM.

## **9.2 Experimental Materials**

### **9.2.1 Membrane**

Orion CMX membranes are prepared in like manner to the method outlined in 8.2.1 .In brief, membranes were acquired in Br<sup>-</sup> form and prepared for HT-PEM application through a series of ion exchange processes to convert to a biphosphate ion-pair form.

### **9.2.2 Catalyst Inks & Gas Diffusion Electrodes**

Phosphanated polypentafluorostyrene with 62% degree phosphonation (PWN) as well as sulfonated polypentafluorostyrene with 55% degree sulfonation (SPPsf-55) and 80% degree sulfonation (SPPsf-80) were provided by the Atanasov group of Institute of Chemical Process Engineering at Universität Stuttgart. Nafion® D5211 was purchased from Fuel Cell Store. The

chemical structure of the ionomers along with the ion exchange capacity in mmol/g is shown in Figure 9.3.

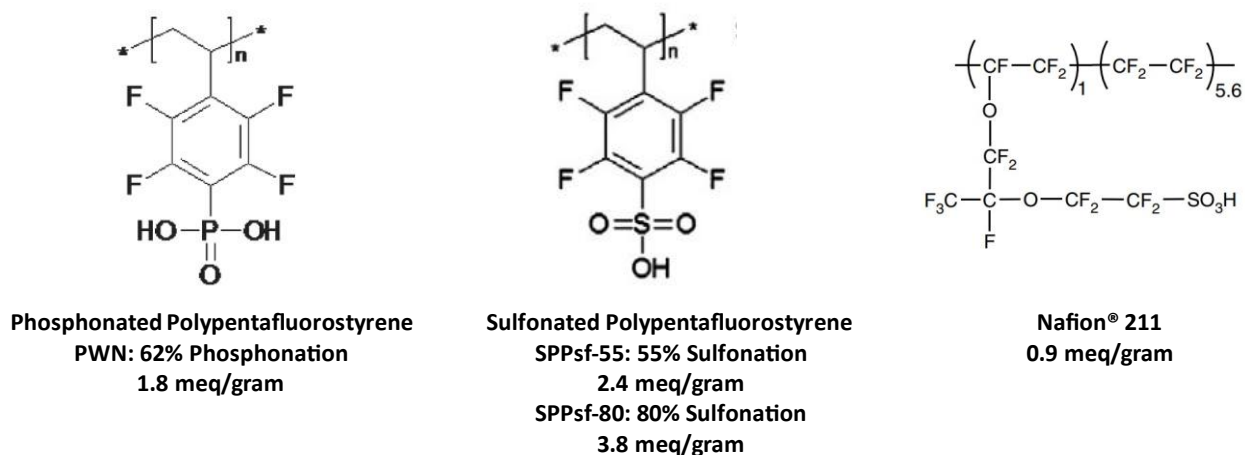


*Figure 9.3 From left to right: Chemical structure and ion exchange capacity of PWN, SPPsf-55/SPPsf-80, and Nafion® 211 ionomeric binders.*

PWN ionomer and Nafion® ionomer were dispersed in NMP solution at 5% wt concentration. For electrodes containing PWN and Nafion® binder a 5% wt PWN+Nafion® 1:1 wt ratio dispersion in NMP was prepared. SPPsf ionomers showed cross-linking behaviors in NMP and water-IPA dispersions at weight concentrations down to 1% wt and were thus left in powder form before catalyst ink preparation.

Catalyst inks were prepared by dispersion of Pt/C catalysts and ionomer into NMP solvent and water-IPA solvent. NMP based inks led to better reproducibility in electrodes and were used moving forward in the MEA characterization. Analysis of dispersion media hypothesized that anhydrous solvents such as NMP led to improved mechanical stability of the catalyst layers of PWN/Nafion® binder electrode systems[159]. Table 9-1 outlines the ink compositions and targeted parameters including I/C and P/S ratios. I/C ratio was kept constant to simplify the number of parameters varied.



Table 9-1 Catalyst ink composition and GDE loading targets.

Electrode & Catalyst Ink Compositions							
Ionomer	Pt loading mg Pt cm <sup>-2</sup>	wt Ratio		NMP mL	Pt/C mg	I/C Ratio	P/S Ratio
		PWN:PFSA Ionomer	Ionomer mg				
PWN	1.0	-	15.9	5	100	0.3	-
Nafion®/PWN (P/S = 2.0)	1.0	1:1	15.9	5	100	0.3	2
SPPsf-55/PWN (P/S = 0.75)	1.0	1:1	15.9	5	100	0.3	0.75
SPPsf-80/PWN (P/S = 0.47)	1.0	1:1	15.9	5	100	0.3	0.47
SPPsf-55/PWN (P/S = 2.0)	1.0	3:1	15.9	5	100	0.3	2

The resulting inks were ball milled for at least 24 hours followed by 30 minutes of bath sonication before spray-coating on to gas diffusion layers. CeTech WS1011 carbon cloth gas diffusion layers (380  $\mu\text{m}$  thickness) with microporous layers were coated by air spray-gun with targeted loading of 1.0 mg Pt cm<sup>-2</sup>. Final platinum loading of the GDEs were verified by gravimetric and X-ray fluorescence measurements.

### 9.2.3 MEA Assembly

5 cm<sup>2</sup> active area membrane electrode assemblies for ion-pair HT-PEM EHP with QAPOH-PA membranes were assembled as described in section 8.2.2 . Gas diffusion electrodes with varying ionomeric binder types and concentrations per Table 9-1 are employed in symmetric electrode fashion with the same GDE applied at anode and cathode. Celtec® sol-gel PA doped PBI membrane based electrode assemblies were assembled with 1 mg pt cm<sup>-2</sup> Tecnologia De Nora gas diffusion electrodes employed in Chapter 5 for PBI-PA and in 8.4.1 for ion-pair HT-PEM EHP.

## 9.3 Experimental Methods

### 9.3.1 Ion-pair HT-PEM EHP Start-up & Conditioning

Ion-pair HT-PEM EHPs are plumbed to the HT-PEM test stand and heated initially up to 40 °C with dry N<sub>2</sub> gas flow on anode and cathode. At 40 °C cyclic voltammetry is performed on the

cathode side to gather low temperature  $H_{\text{upd}}$  characteristics where faradaic HER currents are less likely to obfuscate than at high temperatures[242]. Linear sweep voltammetry is performed with dry  $H_2$  on the anode and  $N_2$  at the cathode to assess initial shunt resistance and  $H_2$  gas cross-over.

Following initial characterization, the HT-PEM EHP at 40 °C, the cell is heated to 160 °C under inert gas flow ( $N_2$  dry both sides). Upon reaching 160 °C, the gas is switched to humidified 0.2 SLPM  $H_2$  at  $T_{\text{sat}} = 80$  °C ( $P_v = 47$  kPa) and 0.1 SLPM  $H_2$  dry sweep gas on the cathode side for conditioning and pressurized to 80kPaG back pressure. The EHP is held at 0.1 V potentiostatic condition for at least 12 hours to allow sufficient time for equilibration. Prior to any characterization at a different humidification the ion-pair HT-PEM re-equilibrated for at least 12 hours at new condition prior to any characterization.

### 9.3.2 Sol-Gel PBI HT-PEM EHP Start-up & Conditioning

PBI-PA based HT-PEM EHP assembled with Celtec-P membranes are heated initially up to 40 °C in inert dry  $N_2$  gas. Following cathodic cyclic voltammetry and linear sweep voltammetry at 40 °C, the PBI-PA HT-PEM EHP is heated to 160 °C under inert dry gas condition (dry  $N_2$ ) at both anode and cathode. At 160 °C the gas flow is switched to humidified  $H_2$  gas at  $T_{\text{sat}} = 30$  °C on the anode side and dry  $H_2$  sweep gas at 0.2 and 0.1 SLPM  $H_2$  respectively.

## 9.4 Results & Discussion

### 9.4.1 Comparison of ionomeric binders in 100% $H_2$ pump

HT-PEM EHPs with symmetric GDEs at ionomer blends of 1:1 wt ratios were investigated at ‘optimal’ HT-PEM EHP condition according to ion-pair membrane performance and Nafion®/PWN ionomeric binder configuration. The 1:1 wt ratio blend of Nafion®/PWN ionomer is the pre-dominant approach for the protonated phosphonic acid electrode HT-PEMFC in the literature [157][158][159]. Maintaining the 1:1 wt ratio with the higher IEC of the PFSA containing SPPsf ionomer provides a wide array of P/S ratio for initial investigation into the best option for HT-PEM EHP in gas separation.

Cyclic voltammetry at beginning of life at 40 °C indicates suppressed  $H_{\text{upd}}$  region for increasing ratios of sulfonic acid. Due to the need for water to provide  $H^+$  conduction between the PFSA sites in the electrode, it is not entirely surprising that in dry condition high sulfonic acid content electrodes could show minimal catalytic activity.

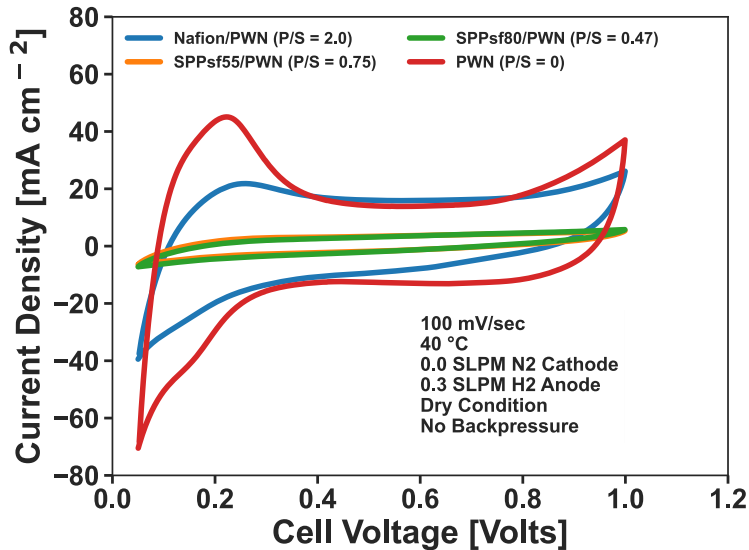


Figure 9.4 Initial characterization cyclic voltammetry at 40 °C of 1:1 wt ratio PWN/PFSA ionomer blends and PWN only ionomer in ion-pair HT-PEM EHP.

Figure 9.5 displays the performance of the HT-PEM EHP at 160 °C with an anode humidification of  $T_{\text{sat}} = 80$  °C which was previously determined to provide optimal performance and stability for the HT-PEM EHP (8.4.2). The addition of sulfonic acid containing ionomers do contribute to an improvement in cell performance likely as a consequence of enhanced proton conductivity[157][283]. The highly sulfonated SPPsF-80 (80% degree sulfonation) exhibited higher HFR relative to the other sulfonic acid blend cases indicating potentially an excessive amount of hydrogen-bonded sulfonic/phosphonic acid pairs inhibiting proton mobility by hydrogen bonding of the phosphonic acid rather than protonation that occurs at excessive sulfonic acid concentrations. The blend containing Nafion® exhibited the highest electrode impedance, followed by the non-sulfonic acid containing electrode, counter to the magnitude of the apparent  $H_{\text{upd}}$  region at 40 °C in Figure 9.4 indicating the low temperature  $H_{\text{upd}}$  region is a poor indication of HOR/HER activity in typical operating conditions for the HT-PEM EHP.

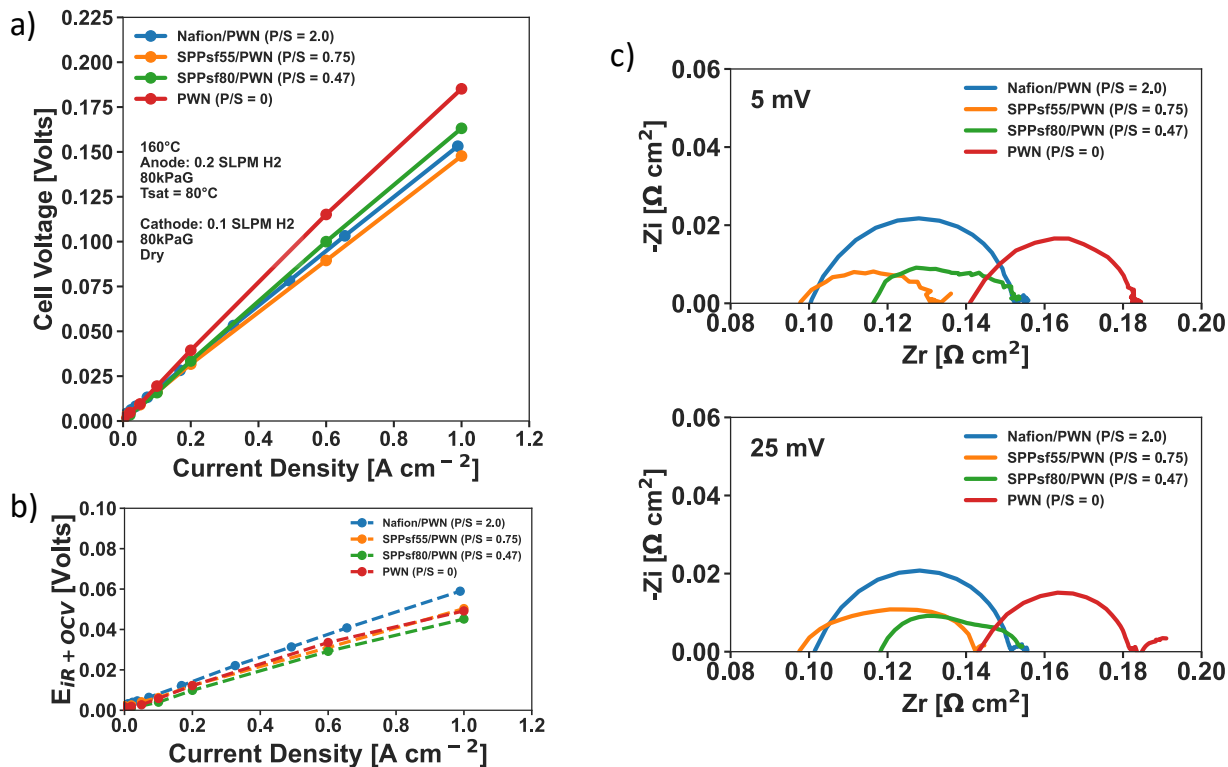


Figure 9.5 a) 100% H<sub>2</sub> polarization curves at 160 °C, T<sub>sat</sub> 80 °C for 1:1 wt ratio PWN/PFSA ionomer ion-pair HT-PEM EHP b) iR-corrected polarization curve c) 5 and 25mV EIS spectra.

The ionomeric binder blend of SPPsf55/PWN in 1:1 wt ratios and resulting P/S ratio of 0.75 demonstrated the lowest potentials for EHP operation and was thus selected for further study in HT-PEM EHP for natural gas separation. As the 1:1 wt ratio blend of Nafion®/PWN ionomeric binder had been demonstrated in fuel cell literature to exhibit the best performance in ion-pair HT-PEMFC systems, it was also included as comparison case.

Figure 9.6 displays the anode relative humidity dependence of performance on the HT-PEM EHP with both ionomeric binder systems. In wetter anode feed conditions, the differences in performance are relatively negligible. In the drier anode condition of 40 °C the SPPsf55 containing electrodes show slightly better performance. In all cases, the electrode impedance R<sub>CT</sub> was lowest at 60 °C, potentially due to the higher reactant concentration at lower vapor pressures in the anode, although the difference in magnitude is very small and the R<sub>CT</sub> can also be said to be leveling off beyond T<sub>sat</sub> = 60 °C (Figure 9.6d).

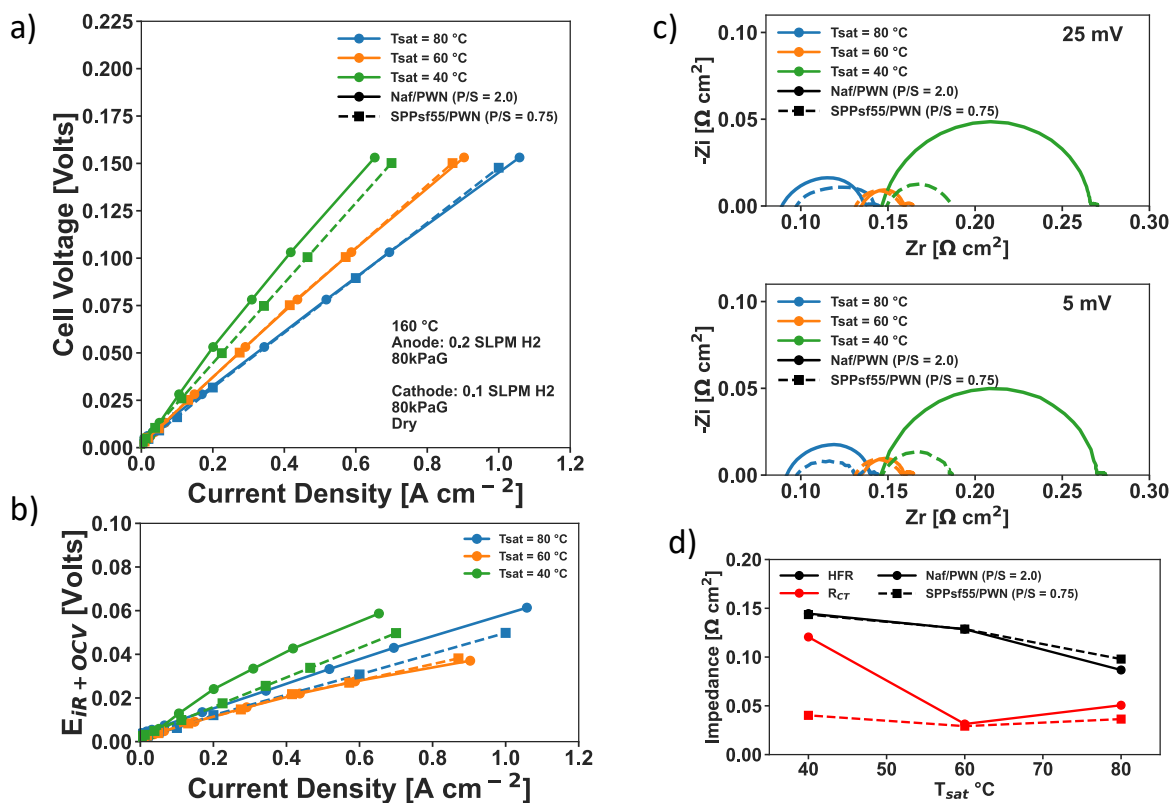


Figure 9.6 a) 100%  $H_2$  polarization curve at 160 °C with varying anodic humidity for ion-pair HT-PEM EHP with Nafion®/PWN ionomeric binder blend vs. SPPsf55/PWN ionomeric binder blend at 1:1 wt ratios b)  $iR$  and OCV corrected polarization curve c) 5 and 25 mV EIS spectra d) ECM fitted HFR and  $R_{CT}$  values from EIS spectra at 25 mV

HFR continues to decrease with increasing humidity content due to the enhanced proton conductivity of the ion-pair membrane with increasing water content (Figure 9.6d).  $iR$ -corrected polarization response indicates that electrode impedance is more sensitive to the degree of humidification for Nafion® containing electrodes. The  $iR$ -corrected polarization response also indicates that the higher membrane conductivity offsets increase in electrode impedance at the high RH condition for both electrodes, and this effect is stronger for the Nafion® containing electrode.

The disparity between the two sulfonic acid ionomers could be related to the higher proton conductivity of SPPsf in elevated temperatures compared to Nafion® at fixed humidity conditions, although measurements of proton conductivity below 16% RH at 160 °C are not available[284]. This could also be a consequence of different gas transport characteristics with

respect to the solubility and diffusivity of hydrogen through SPPsf55 relative to Nafion® or different characteristics of the sulfonic acid group interactions with platinum surface and phosphonic acid groups. The availability of sulfonic acid groups is higher for the SPPsf-55 containing electrode so this could also simply be a consequence of greater number of triple-phase boundary reaction sites. This would be further supported by the RH dependence, as growing proton conduction phase interconnectivity with increasing electrode water content could offset the lower number of interconnected sulfonic acid sites, although the higher impedance at high water content suggests that there is a trade-off at least for the Nafion® containing system that is not due to a high number of sulfonic acid sites.

The sensitivity of the performance of the HT-PEM EHP with SPPsf55 to the number of sulfonic acid sites was probed by adjusting the weight ratio of SPPsf55 to PWN in the electrodes to fix the P/S ratio. Increasing degrees of sulfonic acid to phosphonic acid ratios have been shown to have diminishing returns with respect to performance improvement - although this had previously been studied by varying the number of phosphonic acid sites on PWN ionomer and blended with Nafion® 211 ionomer (~0.9 meq/g)[157]. To provide a comparison with 1:1 wt Nafion, a P/S ratio of 2.0 with SPPsf55 was also examined by varying the weight ratios of SPPsf55 to PWN (Figure 9.7).

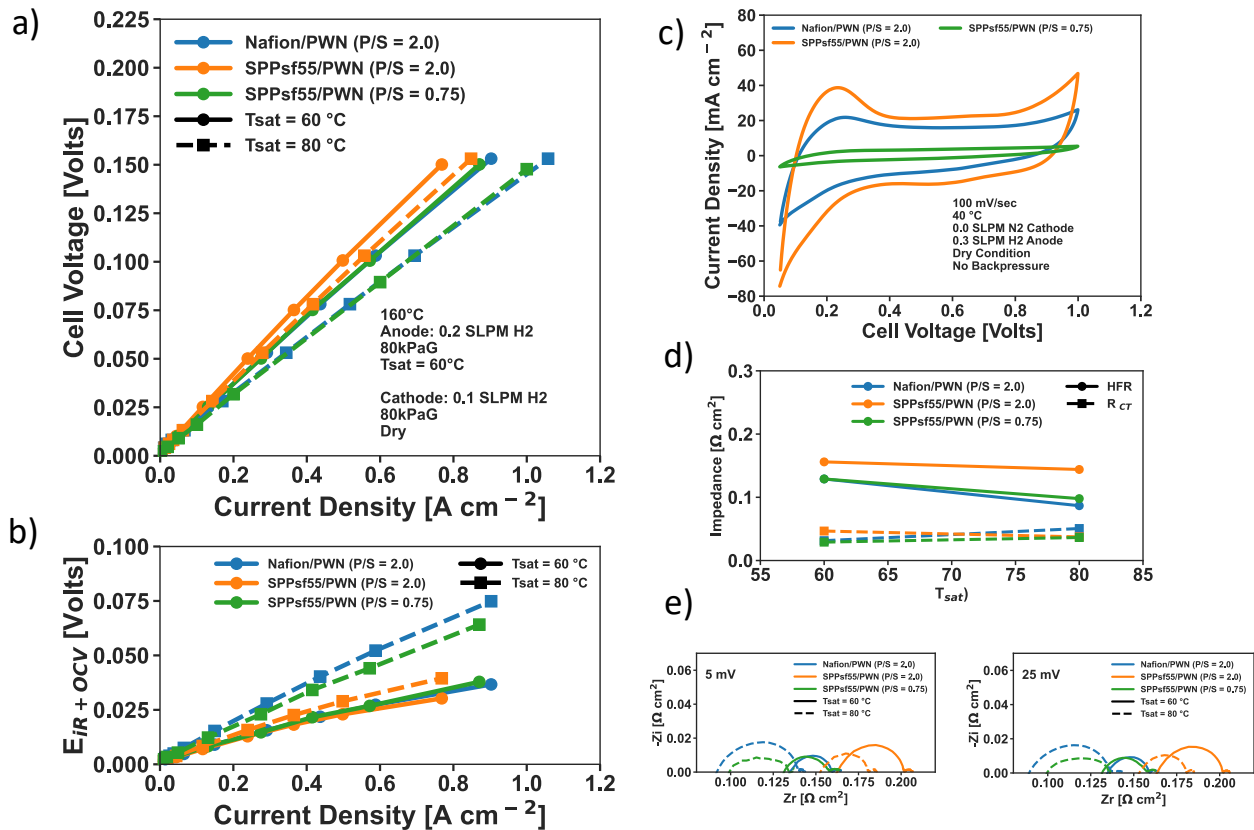


Figure 9.7 Humidity dependence of ion-pair HT-PEM EHP with Nafion®/PWN ionomer vs. SPPsf-55/PWN ionomer at P/S ratio 0.75 and 2.0 a) polarization curve b)  $iR + OCV$  corr. polarization curve c) initial cyclic voltammetry at 40 °C d) ECM fitted HFR and  $R_{CT}$  e) EIS at 5 and 25 mV

At a P/S ratio of 2.0, the SPPsf55 ionomer shows consistently increased HFR relative to the P/S = 0.75 case and relative to the Nafion® case also at a P/S ratio of 2.0, and showed less sensitivity to humidity change. The difference in water uptake characteristics could partially explain the difference in performance with Nafion® at the same P/S ratio. Conversely, the charge transfer resistance showed negligible difference between the different ionomeric blends. Cyclic voltammetry at 40 °C in dry condition on start-up showed some  $H_{upd}$  activity for the lower sulfonic acid ratio SPPsf55 at P/S = 2.0, matching the trend observed initially with higher sulfonic acid contents leading to diminished  $H_{upd}$  for the PWN/sulfonic acid ionomer blends in the low temperature and dry condition (Figure 9.4).

#### 9.4.2 Gas Separation & Compression with Ion-pair HT-PEM EHP

Of primary interest to the investigation of the EHP is its ability to contemporaneously compress and separate  $H_2$  gas from dilute  $H_2$  gas systems. To assess the capability of the ion-pair HT-PEM

EHP to accomplish these processes, electrodes using the SPPsf-55/PWN ionomeric binder blends are considered for the high P/S ratio (2.0) and low P/S ratio (0.75) case in the separation of H<sub>2</sub> blended with methane and natural gas at concentrations from 2 – 10% by volume in-line with short term expectations of potential H<sub>2</sub> concentrations in existing natural gas infrastructure. Additionally, electrodes containing Nafion®/PWN blends ionomer (P/S = 2.0) with ion-pair PEM as well as current state of the art sol-gel PBI PEM (Celtec ®) paired with De Nora Electrodes optimized for PBI based HT-PEM are studied as baseline comparisons. In total, four MEA configurations are considered for varying blends of H<sub>2</sub>/CH<sub>4</sub> and H<sub>2</sub>/Natural Gas (Table 9-2).

*Table 9-2 HT-PEM EHP MEAs for gas separation performance comparisons*

<b>MEAs considered for varying ionomeric composition in Ion-Pair HT-PEM EHP for gas separation</b>					
<b>MEA</b>	<b>Membrane</b>	<b>Ionomer Ratio [wt PWN:PFSA]</b>	<b>I/C Ratio</b>	<b>Pt Loading An   Cat [mg Pt cm-2]</b>	<b>GDL</b>
Nafion®/PWN (P/S = 2.0)	QAPOH-PA	1:1	0.65	1.08   1.10	CeTech
SPPsf-55/PWN (P/S = 0.75)	QAPOH-PA	1:1	0.65	0.98   0.95	CeTech
SPPsf-55/PWN (P/S = 2.0)	QAPOH-PA	3:1	0.65	1.02   0.99	CeTech
Celtec Sol-gel PBI	PBI Sol-gel	-	-	1.0   1.0	De Nora

The polarization response for all four cases of MEA considered when increasing from a cathode to anode pressure ratio  $P_r$  from  $P_r = 1.0$  to  $P_r = 1.5$  in pure H<sub>2</sub> feed condition was examined for anodic pressure of 40 kPaG vs cathodic pressures of 40 kPaG and 110 kPaG as this pressure ratio demonstrated fuel cell quality H<sub>2</sub> gas separation with minimal faradaic inefficiency loss in separation of H<sub>2</sub> from natural gas. When pressurizing the cathode, overpotential of the PBI based MEA increases for across all polarization regimes roughly according to Nernst potential predictions, increasing slightly at higher current densities which could be partially explained by higher local partial pressures of H<sub>2</sub> at the cathode at the higher current densities. In the case of



the ion-pair MEAs, there is a lower overpotential difference between the  $P_r = 1$  and  $P_r = 1.5$  pressure cases at increasing current densities, far below the predicted Nernstian voltage behavior, suggesting some changes in kinetics contributing to the potential difference.

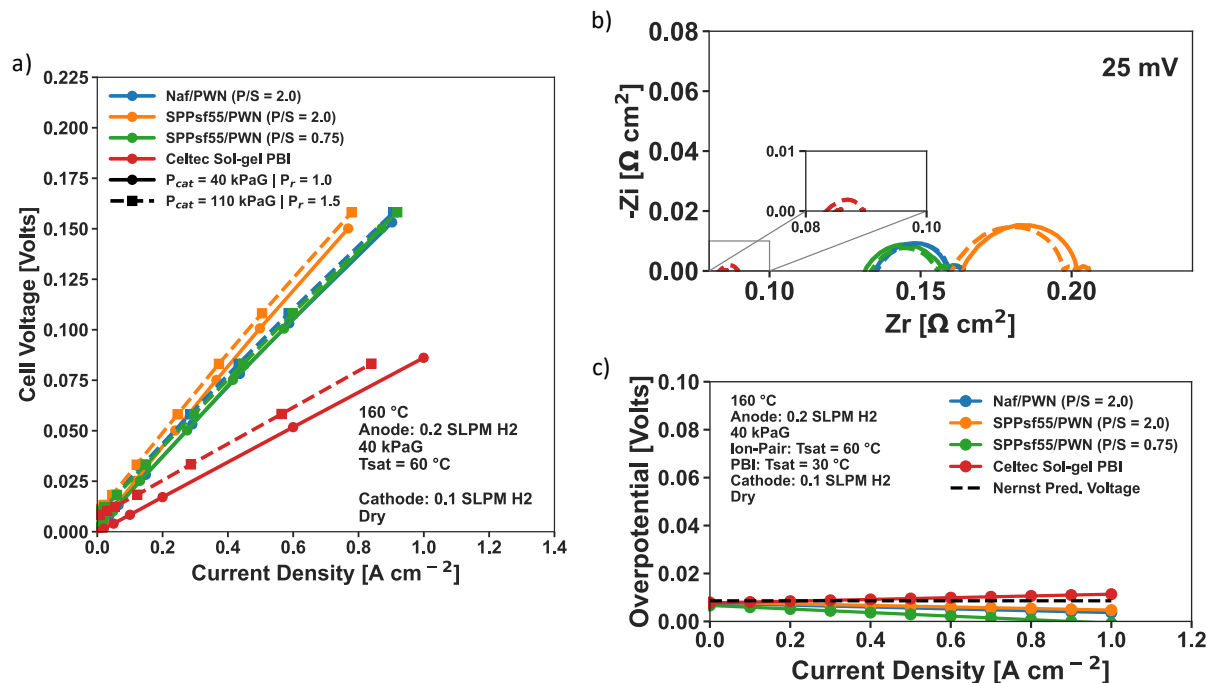


Figure 9.8 Polarization dependence of HT-PEM EHP with stepping of compression ratio from  $P_r = 1.0$  to  $P_r = 1.5$  a) polarization curve b) EIS spectra at 25 mV c) overpotential increase versus current density at  $P_r = 1.5$  versus  $P_r = 1.0$

The higher humidity involved in the ion-pair tests along with the increased sensitivity in performance due to local humidity contents could explain these differences. It could be the case that the elevated pressure at the cathode lowers the velocity of the cathode gas flow due to the hydrogen sweep gas and the produced hydrogen which reduces the effective evaporation rate of liquid water from the MEA phase into the gas phase ultimately leading to higher local water content in the cathode and lowering the cathode electrode impedance. The correlation with increasing current density could possibly be related to non-negligible electro-osmotic drag of water from anode to cathode, which has not been characterized for the QAPOH-PA ion-pair membranes and is found to be effectively zero in PA doped PBI membranes [285].

DRT analysis of the two cases provides some further elucidation of the contributing factors to the potential differences between the MEAs for increasing pressures. Frequency domains and an outline of the DRT approach is discussed in 8.3.3. Due to the overall low impedance for all

cases in pure H<sub>2</sub>, the relative contributions of different time domains to impedance were small and differences are minor. P2 and P3 peaks correlated with HER at the cathode and HOR at the anode respectively are difficult to deconvolute due to the fast kinetics of the underlying reactions in a pure hydrogen environment. Due to this difficulty in differentiation, P2+P3 are combined for analysis under pure H<sub>2</sub> conditions. Some high frequency impedance associated with H<sup>+</sup> conduction in the GDE is observed as well.

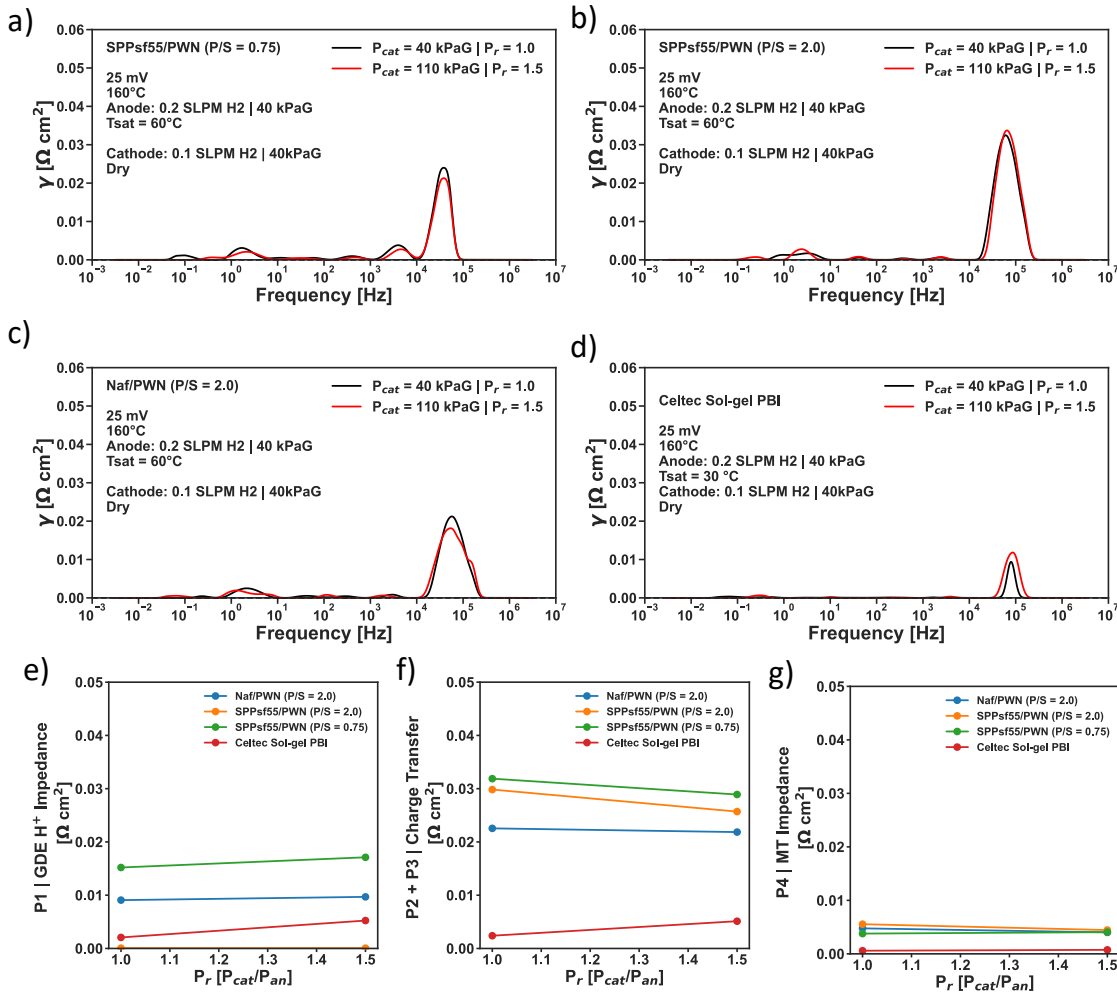


Figure 9.9 a-d) DRT analysis of 100% H<sub>2</sub> EHP operation at  $P_r = 1.0$  and  $P_r = 1.5$  for the four different HT-PEM EHP MEAs e-g) Net impedance change due to pressure ratio calculated from DRT analysis

The Celtec PBI sees a slight uptick in P1 and P2+P3 impedances but due to the very low impedance response measured in EIS, it is difficult to interpret much due to potential overfitting of the small response. For the ion-pair based HT-PEM there is a slight drop in the high frequency domain corresponding largely to peaks P2+P3 which is correlated with HER at the cathode and

HOR at the anode charge transfer impedances as well as some increase in the highest frequency range P1 correlated with protonic ion-pair HT-PEM the P2+P3 domain displayed lower impedance suggesting kinetic improvements at elevated cathodic pressure and consistently did not demonstrate appreciable change in the higher frequency P1 domain correlated to GDE protonic impedance.

Mixtures of low concentration H<sub>2</sub> blended with methane are introduced to the HT-PEM EHPs with concentrations of 10, 5, and 2% on a volumetric basis blended in balance with methane gas. The HT-PEM EHPs are operated at a net flow of 1.0 SLPM at the anode, humidified to T<sub>sat</sub> = 60 °C for the ion-pair HT-PEM EHP and T<sub>sat</sub> = 30 °C for sol-gel PBI-PA HT-PEM EHP, and a 0.1 SLPM H<sub>2</sub> sweep gas of dry H<sub>2</sub> is set on the cathode for polarization curves to maintain elevated cathodic pressure at low current density measurements. A compression ratio of 1.5 is used for gas separation testing with the anode feed-in pressure at 40 kPaG and cathodic pressure of 110 kPaG.

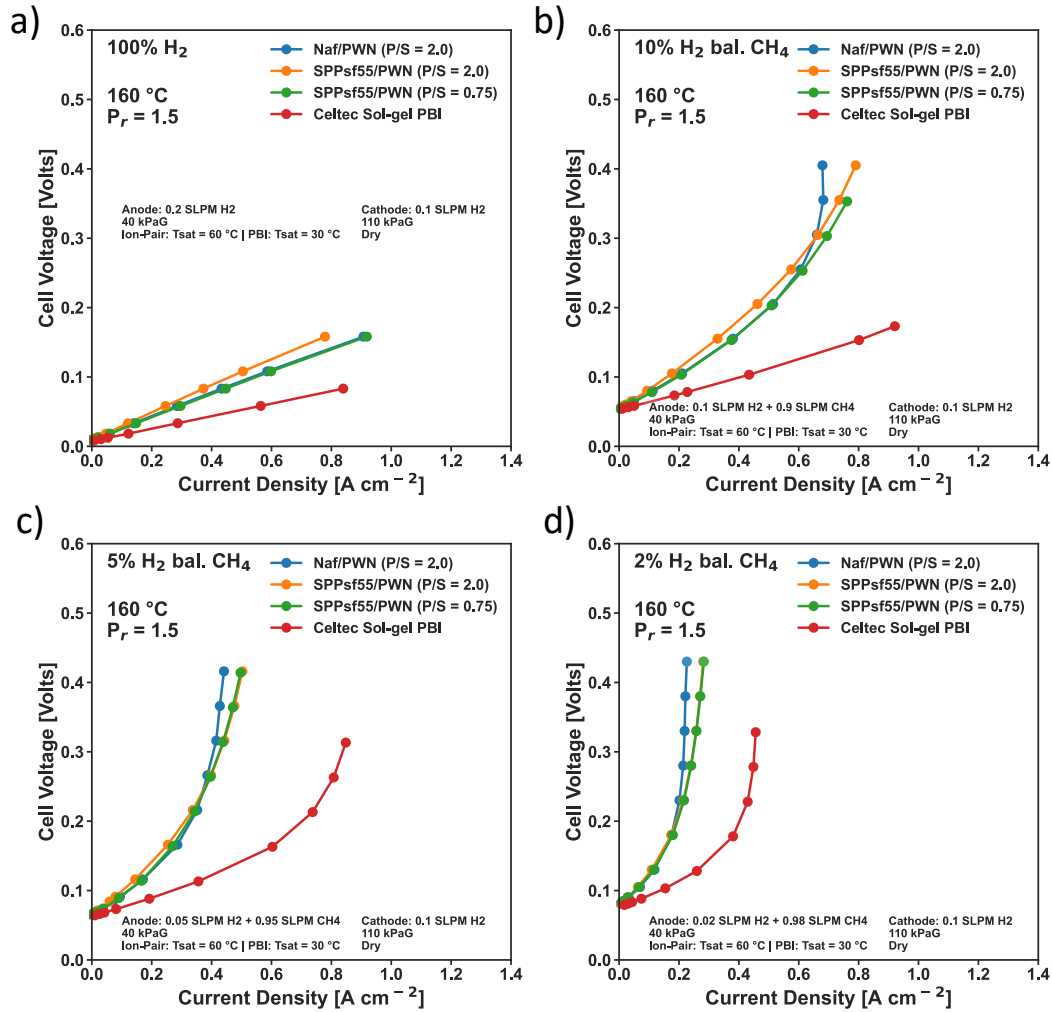


Figure 9.10 Polarization curves of HT-PEM EHP with blends of H<sub>2</sub> and CH<sub>4</sub> gas for 10/5/2% volumetric concentrations of H<sub>2</sub> gas in the blend.

The polarization response of the HT-PEM EHPs with decreasing concentrations of H<sub>2</sub> balanced in CH<sub>4</sub> is shown in Figure 9.10 and highlight a key limiting factor in the ion-pair HT-PEM EHP performance. In pure H<sub>2</sub> operation, the overall lower impedance of the PBI-PA HT-PEM EHP based on sol-gel PBI-PA membranes makes for a clear performance improvement in the ohmic limited regime that EHPs typically operate in. When diluting the H<sub>2</sub> anodic gas feed, mass limited polarization behavior was observed in all cases for the ion-pair HT-PEM EHP utilizing protonated phosphonic acid electrodes. The PA-PBI based HT-PEM EHP did not observe a similar trend only reaching mass limited polarization when approaching the theoretical faradaic limit of hydrogen oxidation reaction at the anode.

Table 9-3 Hydrogen recovery factor of HT-PEM EHPs based on theoretical limiting current for H<sub>2</sub>/CH<sub>4</sub> gas separation

Limiting current in low concentration H <sub>2</sub> H <sub>2</sub> +CH <sub>4</sub> blend EHP operation						
MEA	10% H <sub>2</sub>		5% H <sub>2</sub>		2% H <sub>2</sub>	
	Theo. Limit = 2.85 A cm <sup>-2</sup>		Theo. Limit = 1.42 A cm <sup>-2</sup>		Theo. Limit = 0.57 A cm <sup>-2</sup>	
	% HRF @ 0.4 V	% HRF @ 0.2 V	% HRF @ 0.4 V	% HRF @ 0.2 V	% HRF @ 0.4 V	% HRF @ 0.2 V
Nafion®/PWN (P/S = 2.0)	23.51	17.89	28.87	24.65	40.35	35.09
SPPsf-55/PWN (P/S = 0.75)	28.42	17.54	35.14	23.94	49.12	38.60
SPPsf-55/PWN (P/S = 2.0)	27.72	16.14	35.21	23.94	49.12	36.84
Celtec Sol-gel PBI	N/A	N/A	63.38	52.11	80.00	75.44

Table 9-3 calculates the hydrogen recovery factor (HRF) based on the measured current response and the corresponding maximum theoretical current per Faraday's law of electrolysis assuming 100% faradaic efficiency (Eq. 9-1). HRF at 0.4 V corresponds to the mass transport limited regime of polarization for the HT-PEM EHPs apart from the 10% H<sub>2</sub> case in the PBI HT-PEM

$$HRF = \frac{j}{j_{Lim}} \quad (Eq. 9-1)$$

$$j_{Lim} = \frac{2Fn_{H_2,an,in}}{A} \quad (Eq. 9-2)$$

EHP case. HRF at 0.2 V more accurately reflects a reasonable operating potential for gas separation, at least in the PBI case where this is not yet in the mass transport limited regime. At best, the ion-pair HT-PEM EHPs achieve just under 50% HRF in the 2% H<sub>2</sub> case where polarization is well into mass transport limited regime. There was a considerable and consistent improvement in protonated phosphonic acid electrodes containing SPPsf over Nafion® as the PFSA in terms of limiting current independent of P/S ratio. Generally, HT-PEM based on PBI-PA with no ionomeric binder see limiting currents on the order of 60-80% of the theoretical limit while the ion-pair based HT-EHP with ionomeric binders saw limiting currents in the range of 25-50% for the same operating conditions.

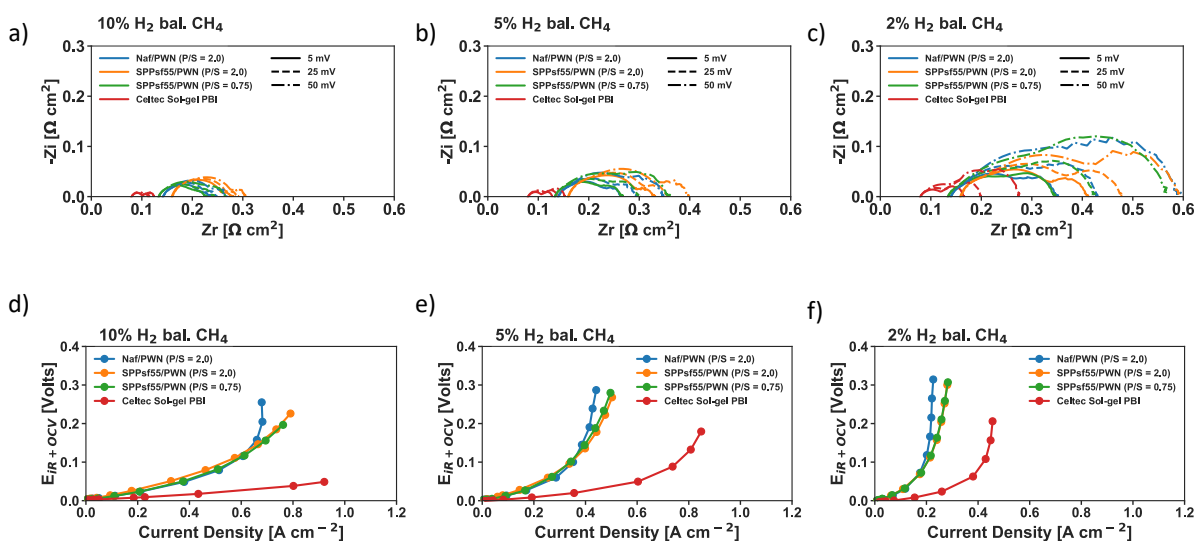


Figure 9.11 a-c) EIS spectra at 5, 25, and 50 mV from OCV and d-f)  $iR$ -corrected polarization curves of HT-PEM EHP in  $CH_4$

Electrochemical impedance spectroscopy indicate that a large contributor to the difference in performance between the PBI-PA system and the ion-pair system lies in the electrode impedance as suggested by the mass transport limiting effects observed previously. EIS data is shown above in Figure 9.11a-c for 5, 25, and 50 mV above open-circuit voltage (OCV). Correcting for  $iR$  from measured HFR values and for OCV due to the varying fugacity of  $H_2$  gas at the anode and cathode,  $iR$ -corrected polarization further reflects this disparity in electrode impedance. Outside of the mass transport limiting region, the overpotential of the HT-PEM based on PBI-PA is small and when correcting for HFR the overpotential is largely non-existent for the PBI-PA system. Conversely,  $iR$ -correction for the ion-pair HT-PEM indicated significant electrode losses at low current densities well before reaching current limited polarization.

DRT analysis was applied for the 25 and 50 mV overpotential from OCV potentiostatic case (Figure 9.12) for the varying degrees of  $H_2$  in  $CH_4$ . From the DRT function a clear trend in lower frequency impedance growth with decreasing  $H_2$  concentration is observed, strongest in the 50 mV case. This aligns with previously set domain frequencies that attribute these domains to HOR (150 to 10000 Hz) and mass transport (0.1 to 150 Hz) phenomena (see - Figure 8.32). This effect is further pronounced at 50 mV where mass transport limits have greater influence.

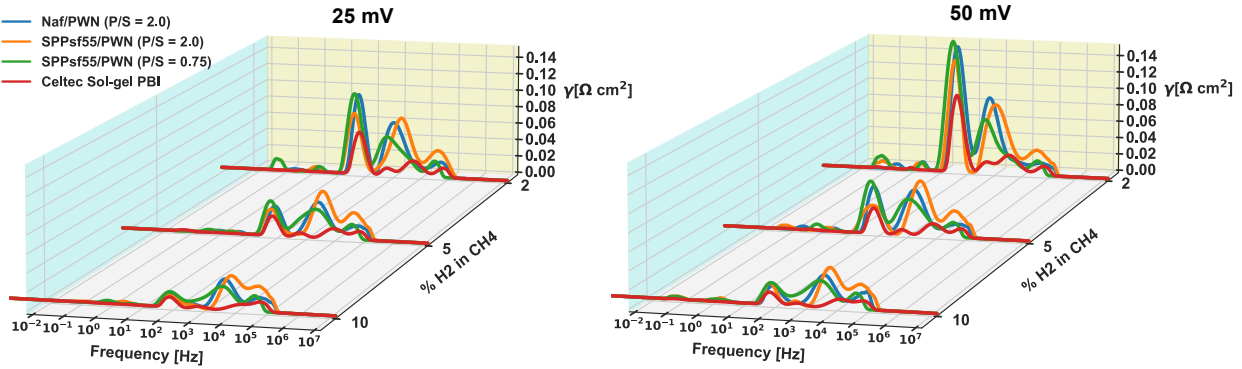


Figure 9.12 DRT analysis from EIS analysis of 10/5/2 % vol.  $H_2$  blended with  $CH_4$  in HT-PEM EHPs at 25 and 50 mV applied voltage over OCV.

Net impedance calculated from the DRT and EIS analysis is shown in Figure 9.13. PBI-PA HT-PEM EHP showed the lowest impedance across all cases with the most significant differentiation point prominent in the trend of HOR impedance. Mass transport impedance, while lower for the PBI-PA case, is relatively comparable at 10%  $H_2$  and follows a similar trend to the ion-pair HT-PEM EHPs. HFR for all cases is slightly higher than the 0.2 SLPM pure  $H_2$  cases, increasing by approximately ~10% for all EHPs likely due to the high stoichiometric anodic flow either through increased evaporation and/or thermal gradients across the MEA.

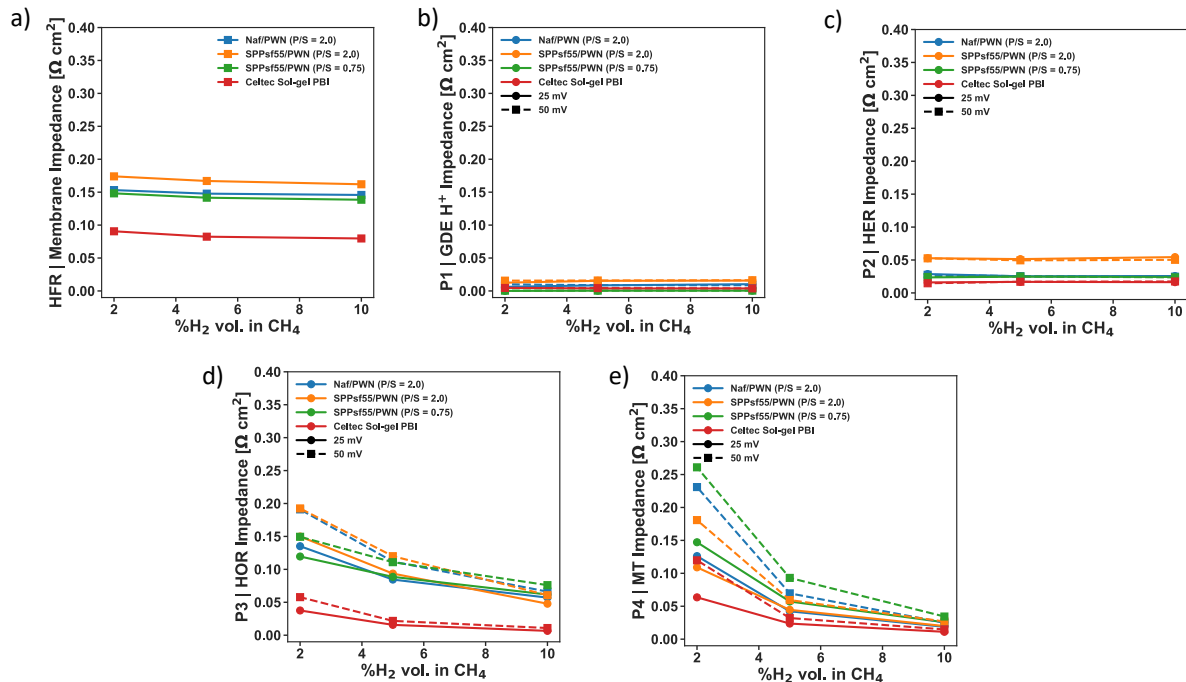


Figure 9.13 Impedance contributions calculated from DRT analysis at 25 and 50 mV overpotential from OCV for HT-PEM EHP with H<sub>2</sub>/CH<sub>4</sub> gas blend anodic feed.

The highest impedance associated with electrode kinetics (HOR + HER) were generally associated with SPPsf55/PWN at P/S ratio of 2.0, whereas the Nafion®/PWN and SPPsf55/PWN (P/S = 0.75) had relatively comparable charge transfer impedances for HOR and HER. The estimated concentration of phosphonic acid groups from the ionomeric binder in the electrode (mol H<sub>3</sub>PO<sub>3</sub>/cm<sup>3</sup>) is largest for the SPPsf/PWN (P/S = 2.0) case, while the latter two ion-pair HT-PEM EHPs have the same concentration. Thus, it is reasonable that a higher degree of phosphonic acid poisoning of Pt surfaces may have occurred in the SPPsf/PWN (P/S = 2.0) case. None of the observed trends in impedance across the ion-pair HT-PEM EHPs aligns with volumetric concentration of sulfonic acid groups.

The higher limiting currents when employing SPPsf55 as PFSA ionomer does not translate to lower mass transport related impedances at the 25 and 50 mV overpotentials, which aligns with the polarization behavior showing similar overpotentials even after iR-correction.

Following methane+H<sub>2</sub> gas blend testing, ion-pair HT-PEM EHP utilizing SPPsf55/PWN blend with a P/S ratio of 0.75 was tested on pipeline natural gas + H<sub>2</sub> blends of 10, 5, and 2 % volume



H<sub>2</sub>. For comparison the ion-pair HT-PEM EHP based on the Nafion®/PWN ionomeric binder blend was also assessed in natural gas as well as the sol-gel PBI-PA HT-PEM EHP. The sol-gel PBI-PA HT-PEM EHP was not able to survive extended testing in methane followed by natural gas separation testing and suffered membrane failure within the first 24 hours of CH<sub>4</sub> and natural gas separation blends. Figure 9.14 shows the equilibration 0.3 V potentiostatic hold at 5% H<sub>2</sub> performed before polarization curve and GC measurements for methane and then equilibrated again for natural gas. Due to failure of the sol-gel PBI during equilibration in natural gas, following completion of methane blend testing, no steady state polarization data could be achieved for sol-gel PBI-PA HT-PEM EHP in natural gas and only the two ion-pair HT-PEM EHP cases are considered for natural gas + H<sub>2</sub> blend separation.

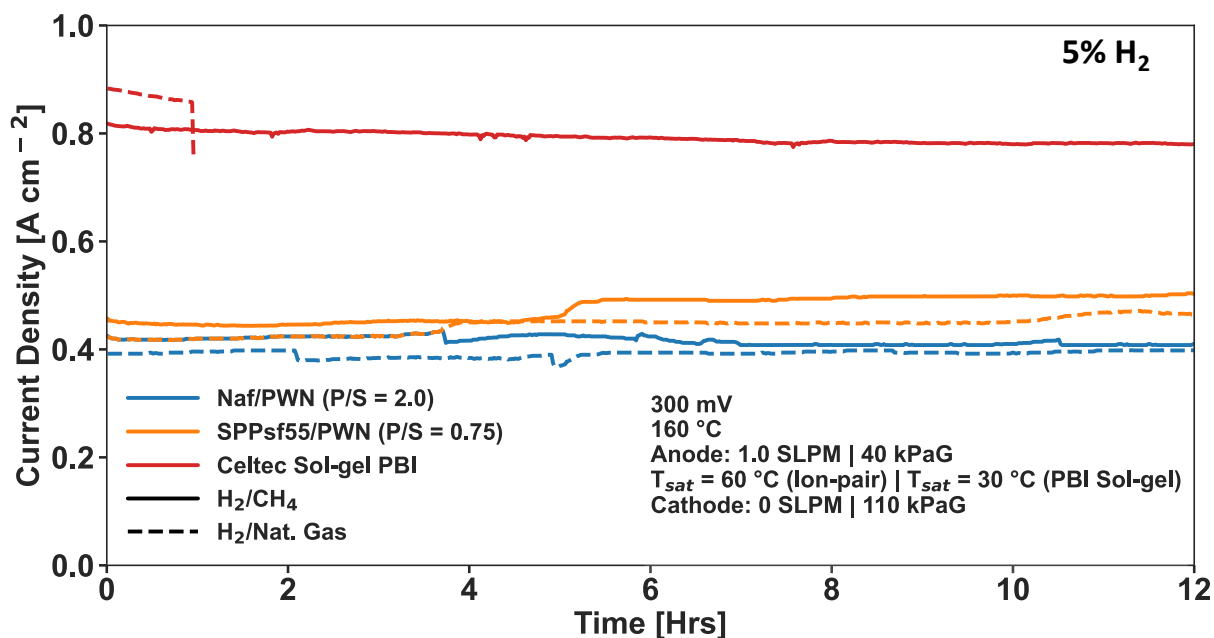


Figure 9.14 12-hour equilibration at 0.3 V for CH<sub>4</sub> and natural gas H<sub>2</sub> gas blends containing 5 % vol H<sub>2</sub>. Failure of Sol-gel PBI in H<sub>2</sub>/Nat. Gas.

Polarization was only slightly impacted in natural gas blends as compared to the methane gas blends with H<sub>2</sub>, but clearly shows a slightly worse performance in the de-sulfurized natural gas feed compared to the high purity methane (Figure 9.15). EIS and iR-corrected polarization further show that while HFR is slightly higher for the natural gas case at lower H<sub>2</sub> concentrations, the overpotentials remain higher in the iR-corrected polarization curves for natural gas feed (Figure 9.16).

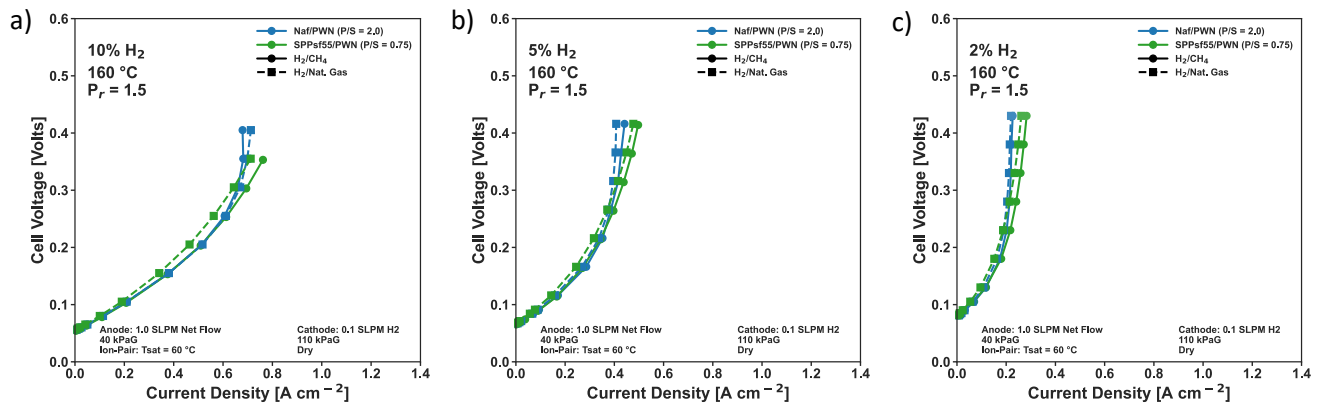


Figure 9.15 Polarization curves of HT-PEM EHP with blends of  $H_2$  in natural gas and pure methane gas for 10/5/2% volumetric concentrations of  $H_2$  gas in the blend.

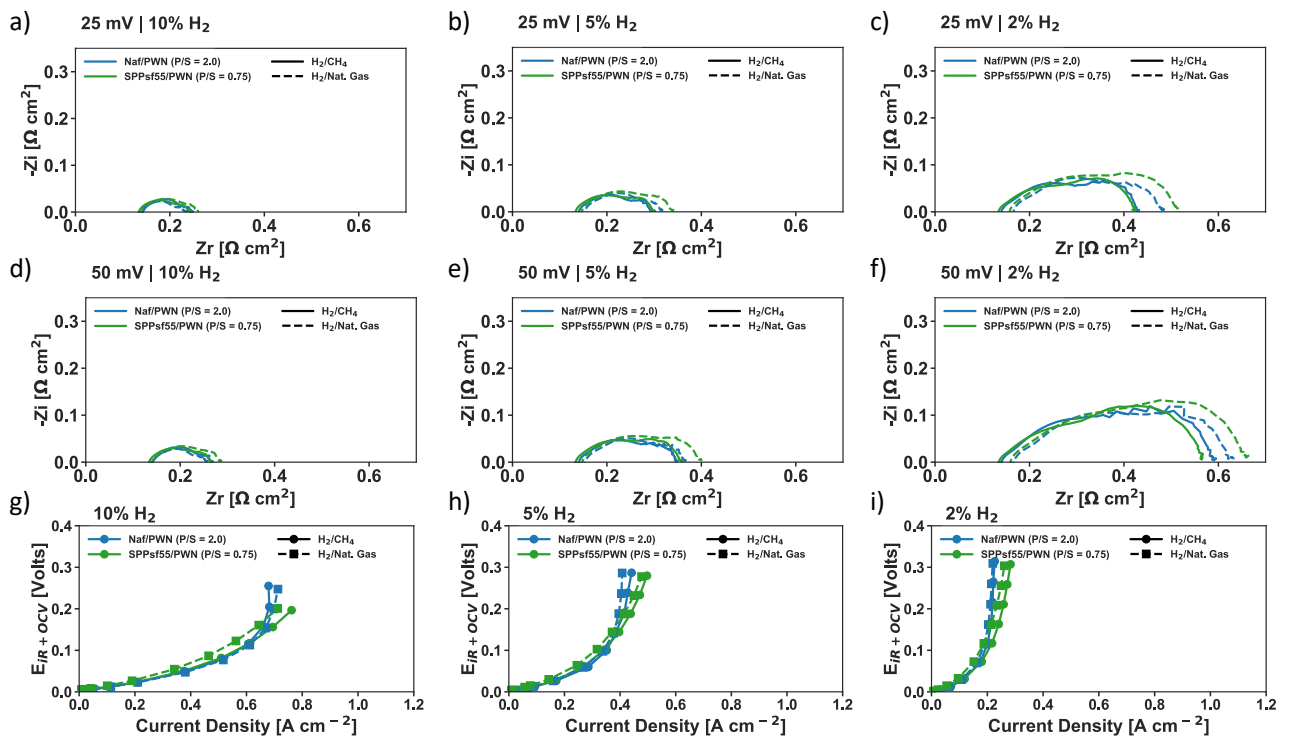


Figure 9.16 a-c) EIS taken at 25 mV overpotential and d-f) EIS at 50 mV overpotential for both methane and natural gas  $H_2$  blends g-i)  $iR$ -corrected polarization curves of HT-PEM EHP in natural gas and pure methane gas  $H_2$  blends.

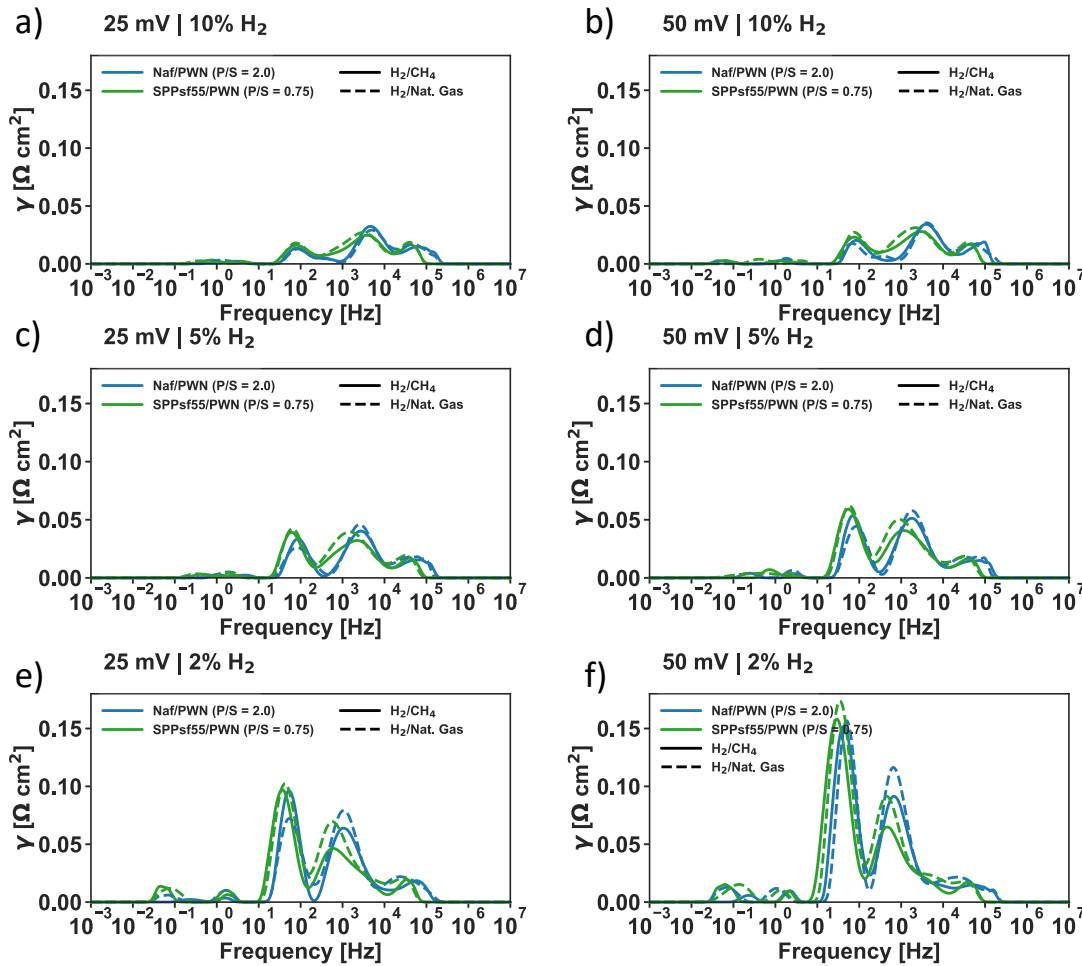


Figure 9.17 DRT functions for methane and natural gas blends in 10/5/2 % vol. hydrogen at 25 and 50 mV overpotentials.

DRT functions show very little difference in impedance response for 10% H<sub>2</sub> between methane and natural gas blends, but the differences grow more pronounced at the lower concentrations and higher overpotential. Impedance analysis of the DRT functions indicate that there is a consistent increase in HOR related impedance in the natural gas feed over the methane gas feed, and while the overall magnitude is small, a similar effect at the HER impedance (Figure 9.18). The impact of this showing up on both HOR and to a lesser extent HER, has been correlated with the presence of CO<sub>2</sub> and second-hand platinum poisoning due to RWGS formation of CO species[256]. In this case, the concentration of CO<sub>2</sub> is very small at ~1% by volume in the dry natural gas feed, further diluted by the addition of water vapor and H<sub>2</sub> gas. Another possible source is trace amounts of sulfur compounds such as ethyl mercaptan that were not entirely scrubbed by the desulfurization beds upstream of the test stand natural gas feed.

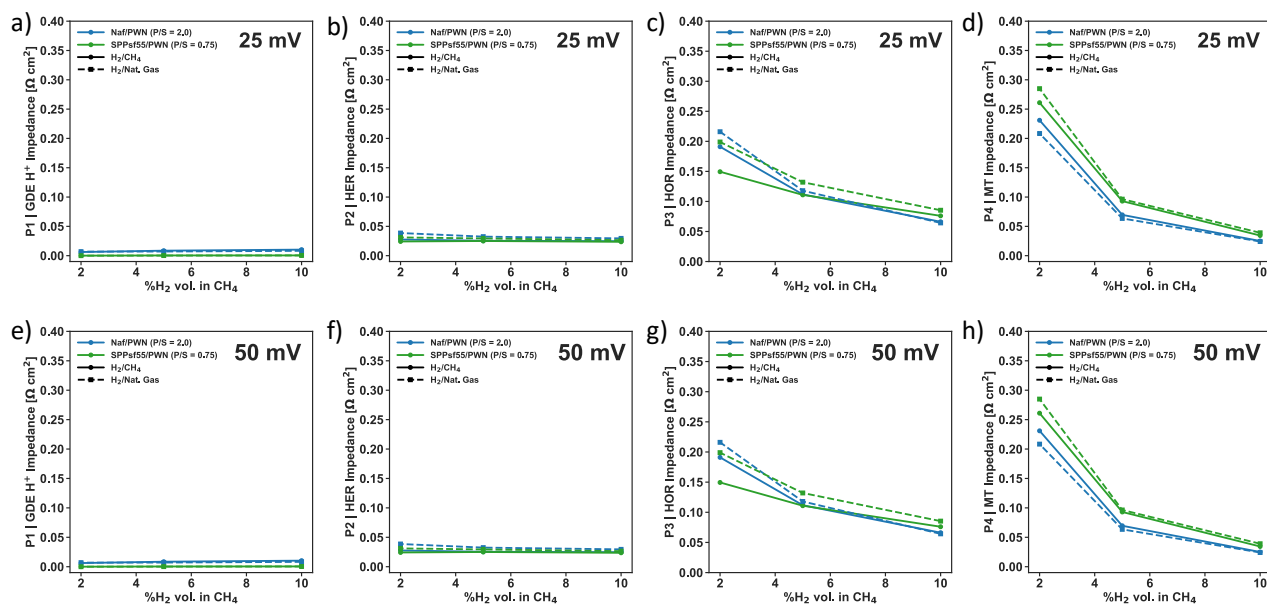
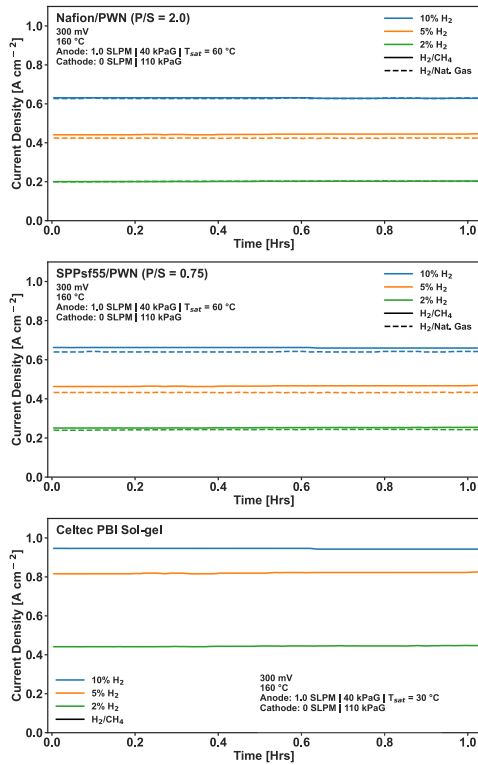


Figure 9.18 Impedance analysis from DRT functions for methane and natural gas blends in 10/5/2 % vol. hydrogen at 25 and 50 mV overpotentials.

The separation characteristics for methane and natural gas at 10, 5, and 2% concentrations are displayed below (Figure 9.19) for a 1-hour 0.3 V potentiostatic hold at a H<sub>2</sub> compression ratio of  $P_r = 1.5$ . Cathode gas purity was sampled at the end of the 1 hour potentiostatic hold. Due to membrane failures, no sol-gel PA-PBI MEA data for natural gas separation is available, only for methane/H<sub>2</sub> blends. The ion-pair HT-PEM EHP exhibited greater hydrogen gas purity despite lower hydrogen flux due relative to sol-gel PBI. For the 5 and 10% H<sub>2</sub> case, hydrogen gas meets fuel cell quality standards for total H<sub>2</sub> purity and methane content on a dry basis, and all other impurities are below the detection limits of the FID-methanizer of 25 ppm CO<sub>2</sub> and CO. For 2 % H<sub>2</sub> feeds in natural gas and methane, the methane concentration exceeded 100 ppm, albeit slightly, suggesting slightly higher cathodic compression could achieve sufficient purity. On a wet basis, the hydrogen at the cathode outlet was diluted significantly by water vapor suggesting a high degree of water transport across the ion-pair HT-PEM.



Gas Separation GC Measurements: Nafion/PWN (P/S = 2.0)								
H <sub>2</sub> /CH <sub>4</sub> [% vol H <sub>2</sub> ]	J <sub>avg</sub> @ 0.3 V [A cm <sup>-2</sup> ]	HRF [%]	%H <sub>2</sub> Wet	%H <sub>2</sub> Dry	ppm CH <sub>4</sub> dry	ppm CO <sub>2</sub> dry	ppm C <sub>2</sub> H <sub>6</sub> dry	% vol H <sub>2</sub> O(v)
10%	0.621	21.789	93.2	100.00	<25	<25	<25	6.80
5%	0.427	30.070	92.61	99.990	103.83	<25	<25	7.38
2%	0.21	36.842	92.16	99.984	161.47	<25	<25	7.82
H <sub>2</sub> /Nat. Gas								
10%	0.623	21.860	93.2	100.00	<25	<25	<25	6.80
5%	0.408	28.732	92.62	99.997	32.88	<25	<25	7.38
2%	0.208	36.491	91.72	99.988	122.08	<25	<25	8.27

Gas Separation GC Measurements: SPPsf55/PWN (P/S = 0.75)								
H <sub>2</sub> /CH <sub>4</sub> [% vol H <sub>2</sub> ]	J <sub>avg</sub> @ 0.3 V [A cm <sup>-2</sup> ]	HRF [%]	%H <sub>2</sub> Wet	%H <sub>2</sub> Dry	ppm CH <sub>4</sub> dry	ppm CO <sub>2</sub> dry	ppm C <sub>2</sub> H <sub>6</sub> dry	% vol H <sub>2</sub> O(v)
10%	0.656	23.018	93.36	100.00	<25	<25	<25	6.64
5%	0.47	33.099	92.61	99.991	98.38	<25	<25	7.38
2%	0.243	42.632	92.17	99.985	146.51	<25	<25	7.38
H <sub>2</sub> /Nat. Gas								
10%	0.629	22.070	93.20	100	<25	<25	<25	6.80
5%	0.415	29.225	92.33	99.995	45.52	<25	<25	7.67
2%	0.228	40.000	92.02	99.990	106.57	<25	<25	7.97

Gas Separation GC Measurements: Celtec SolGel PBI								
H <sub>2</sub> /CH <sub>4</sub> [% vol H <sub>2</sub> ]	J <sub>avg</sub> @ 0.3 V [A cm <sup>-2</sup> ]	HRF [%]	%H <sub>2</sub> Wet	%H <sub>2</sub> Dry	ppm CH <sub>4</sub> dry	ppm CO <sub>2</sub> dry	ppm C <sub>2</sub> H <sub>6</sub> dry	% vol H <sub>2</sub> O(v)
10%*	0.951	33.368	98.17	99.972	276.38	<25	<25	1.8**
5%	0.824	58.028	98.17	99.971	285.17	<25	<25	1.8**
2%	0.435	76.316	98.16	99.966	341.13	<25	<25	1.8**

\* 10% held at 0.175 V due to current limits of potentiostat      \*\* Maximum possible humidity based on anode feed - RH was not measured for these tests

Figure 9.19 Methane and natural gas H<sub>2</sub> blend HT-PEM EHP separations for 10, 5 and 2 %, cathode effluent composition at 0.3 V 1-hour holds.

Electrical power consumption cost of hydrogen pumping vs mass flux and hydrogen recovery factor are displayed in Figure 9.20 for natural gas/H<sub>2</sub> blends for the ion-pair HT-PEM MEAs. Hydrogen recovery factors were very low, on the order of ~20-40% at best before reaching limiting current density in the HT-PEM EHP. To keep the specific energy cost of separation below 10% of the lower heating value of the separated hydrogen gas at 3.3 kWh/kg H<sub>2</sub> only a hydrogen recovery factor of 8, 11, 14% for 2, 5, 10% H<sub>2</sub> by volume in natural gas is achievable.

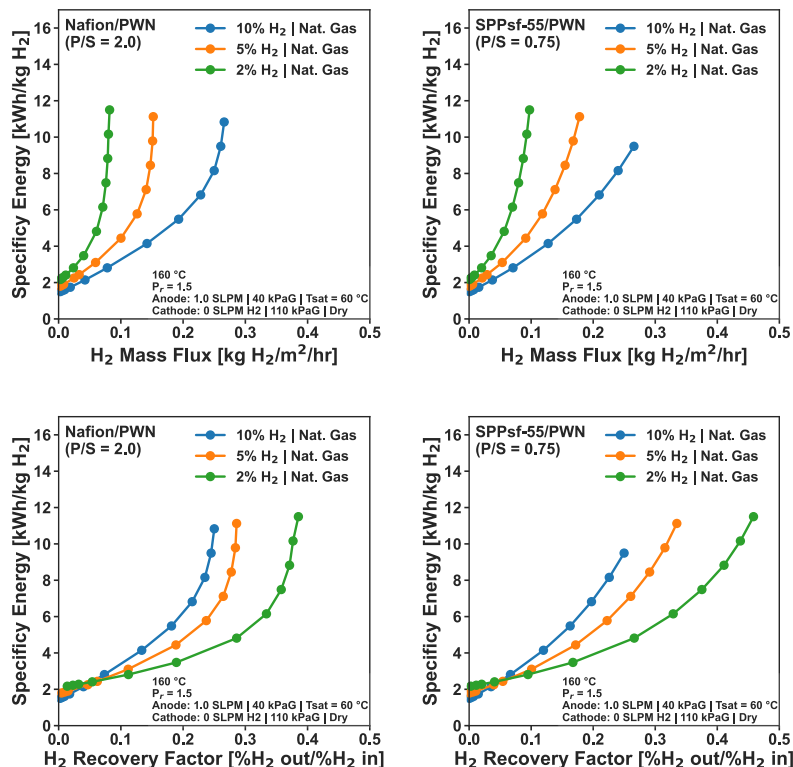


Figure 9.20 Specific energy of separated  $H_2$  gas versus outlet mass flux per active cell area (top) and hydrogen recovery factor (bottom).

## 9.5 Conclusions

Sulfonated polypentafluorostyrene (SPPsf) was blended with phosphanated polypentafluorostyrene (PWN) and incorporated into gas diffusion electrodes for ion-pair HT-PEM EHP. SPPsf with 55% degree of sulfonation (SPPsf-55) performed comparably to Nafion® when blended with PWN ionomer in the electrode, and both performed better than PWN alone and SPPsf with 80% (SPPsf-80) degree sulfonation reinforcing findings that ratio of sulfonic acid groups to phosphonic acid groups (P/S ratio) is optimal at a value of around 0.75 to 2 for ion-pair HT-PEM. Varying the P/S ratio for SPPsf-55/PWN to 2 and comparing Nafion®/PWN at a P/S ratio of 2 did not show appreciable difference in performance compared to SPPsf-55/PWN at a P/S ratio of 0.75. In mass transport limited operation SPPsf-55/PWN based electrodes showed slightly higher limiting current densities regardless of P/S ratio over Nafion®/PWN based electrodes suggesting a higher gas permeability of SPPsf based ionomers.

Impedance analysis with electrochemical impedance spectroscopy (EIS) and distribution of relaxation times (DRT) showed that the charge transfer related impedances of the ionomeric

GDEs in ion-pair HT-PEM EHP are 2-3x higher on average than the phosphoric acid based GDE with sol-gel PA-PBI while mass transport related impedance was 1.5-2x higher. In methane/H<sub>2</sub> separations, the limiting current densities of ion-pair HT-PEM EHP were around 20-36% of the theoretical value for Nafion®/PWN ionomeric binder blends and 24-42% for SPPSf/PWN ionomeric binder blends, far lower than PA-PBI which was around 58-76%. Further studies of the GDE micro- and nano- structure for ionomeric GDEs employed with the ion-pair HT-PEM EHP are needed to better understand where the mass transport related issues originate from. In part, they could be explained by the higher vapor pressure present in ion-pair HT-PEM leading to dilution of the reactant gas, but this does not wholly explain the discrepancy to PBI-PA. Furthermore, charge transfer losses are the more significant difference according to impedance analysis suggesting adverse interactions between the phosphonic and/or sulfonic acid based ionomers and the electrocatalyst inhibiting electrode kinetics.

De-sulfurized Pipeline natural gas and hydrogen gas blends down to 2% by vol H<sub>2</sub> were tested in the ion-pair HT-PEM EHP and fuel cell quality hydrogen gas on a dry basis was produced in single-stage separation with co-compression at a compression ratio of  $P_r = 1.5$  for H<sub>2</sub> concentrations of 5 and 10% by volume in natural gas. The total flux of hydrogen and thus the hydrogen recovery factor was relatively low for the ion-pair HT-PEM EHP due to low limiting currents that were not observed in PBI-PA HT-PEM EHP. Thus, ion pair HT-PEM EHP are able to exhibit very high H<sub>2</sub> selectivity over natural gas components and achieve the single-stage separation of fuel cell quality H<sub>2</sub> in concentrations down to 2% in real pipeline natural gas while compressing the product hydrogen. No other separation technology has been demonstrated with this capability, and with further materials development and MEA development focusing on the improvement of the reaction kinetics and mass transport in the electrodes, HT-PEM EHP based on ion-pair could be a promising technology for efficient recovery of high purity product from any low %H<sub>2</sub> content gas blend, particularly when challenging impurities are present.

## Chapter 10 Summary & Conclusions

### 10.1 Summary

This dissertation set out with the goal to investigate the feasibility of separating high purity hydrogen gas that could be used in valuable, difficult to decarbonize end-uses, from natural gas/H<sub>2</sub> blends at concentrations of very limited concentrations of hydrogen as predicted by the current policy and regulatory landscape. These concentrations, typically around 5-10% by volume H<sub>2</sub>, sometimes as low as 1-2% by volume H<sub>2</sub>, and reaching as high as 25% by volume H<sub>2</sub>, are too low for conventional separation technologies that are common throughout chemical processing industries. Electrochemical based gas separation with electrochemical hydrogen pump (EHP) was a promising candidate for this process due to the inherent advantages of electrochemical processes (surface area scaling, relatively low temperatures, charge based transport mechanisms) and its inherent suitability specifically to hydrogen gas separation. Current state-of-the-art surrounding LT-PEM EHP, however, is not as well suited to natural gas due to the presence of sulfur and other challenging impurities for that technology. This dissertation was thus organized around the study of high-temperature EHP for natural gas hydrogen blend separations.

Chapter 5-7 encompasses studies concerning the application of the relatively mature phosphoric acid doped polybenzimidazole (PA-PBI) as a proton conductor for HT-PEM EHP in the separation of low % H<sub>2</sub> gaseous blends. Chapter 5 studied these cells at the 5 cm<sup>2</sup> MEA level with respect to different construction parameters and operating conditions. Chapter 6 attempted to study the morphological changes of HT-PEM EHP with X-ray CT in operando. Chapter 7 presented the detailed physical model of an HT-PEM EHP for H<sub>2</sub> gas separation, informed by and validated on experimental data gathered in Chapter 5 and 6.

In Chapters 8 and 9, a new class of HT-PEM type electrochemical cells denoted as ion-pair HT-PEM with protonated phosphonic acid electrodes was considered for EHP in H<sub>2</sub> gas separation based on their promising characteristics in HT-PEM fuel cell testing. Chapter 8 focused on the stability of the ion-pair HT-PEM and the role that the ionomeric binders play in its performance in the EHP operating environment. The long-term stability of natural gas/H<sub>2</sub> separations in ion-pair HT-PEM EHP was demonstrated and the sources of degradation were further informed by



impedance spectroscopy analysis. Chapter 9 investigated alternative ionomeric binders in MEA for the ion-pair HT-PEM and studied the impacts of natural gas vs methane on gas separation performance for ion-pair HT-PEM.

## 10.2 Conclusions

In **Chapters 5 through 7**, the HT-PEM EHP based on PBI-PA was studied extensively for the separation of hydrogen gas at fuel cell quality from low concentrations in methane. Methane was used as an analogue to natural gas for initial assessment of HT-PEM EHP performance. From this study the following major findings and accomplishments were,

- For conventional PA-PBI with lower ADL, humidification is required to sufficient degree to prevent the formation of phosphoric acid anhydrides that drive up electrode impedance.
- The amount of phosphoric acid in the electrodes of HT-PEM EHP greatly impacts the performance and can be tuned by addition of phosphoric acid to the electrode surface. Too much phosphoric acid leads to electrode flooding, while too little leads to poor kinetics and high ohmic losses.
- HT-PEM EHP based on PA-PBI can achieve comparable polarization response to state-of-the-art LT-PEM EHP for 20% H<sub>2</sub> bal. in methane and at 100% H<sub>2</sub>.
- HT-PEM EHP operation at 2% H<sub>2</sub> bal. in methane was demonstrated at specific energy of separations of 2 to 6 kWh/kg H<sub>2</sub> for hydrogen recovery factors of 50%, showing better performance than literature model scenarios in terms of separation efficiency.
- Fuel cell quality hydrogen according to current ISO and SAE standards was obtained by co-compression of separated hydrogen gas in PA-PBI based HT-PEM EHP for gas feeds of 10 and 20% H<sub>2</sub> hydrogen.
- A HT-PEM EHP was imaged by X-ray CT at synchrotron facility in operando at 160 °C at dry and humidified conditions. No appreciable change in morphology was observed, particularly with respect to membrane swelling.
- A 2-D physical model of HT-PEM EHP was validated on experimental data for low % H<sub>2</sub> in methane gas feeds.

- The 2-D physical model was able to capture the impact of varying electrode acid content on HT-PEM EHP polarization losses. The difference in acid phase composition and distribution compared to HT-PEMFC supported the notion that HT-PEM EHP benefits from a lack of water generation in long-term stability.
- Power-loss based voltage breakdown analysis was employed to identify sources of polarization loss in the HT-PEM EHP. Increasingly low H<sub>2</sub> content and high compression ratios led to high thermodynamic limitations on the separation efficiency.
- Gas cross-over and membrane water transport were integrated into the 2-D HT-PEM EHP model. The implementation of gas cross-over exhibited limitations at high pressure differentials. Both exhibited the benefits on gas purity by operating at high pressure ratios.
- The HT-PEM EHP model highlighted a key advantage of EHP operation; increasing compression ratios do not lead to appreciably higher potential when already operating at current densities as much of the polarization loss at high current comes from ohmic and kinetic losses which are not sensitive to increasing cathodic pressures and, in some cases, benefits from higher cathodic pressures.

**Chapters 8 and 9** focused on the development of HT-PEM EHP based on quaternary ammonium membranes with benzyltrimethyl ammonium cations doped with phosphoric acid (QAPOH-PA) denoted as ion-pair type HT-PEM. These ion-pair HT-PEM are paired with ionomeric binder blends of phosphanated polypentafluorostyrene (PWN) and sulfonic acid containing ionomers such as Nafion® in electrodes, denoted ‘protonated phosphonic acid electrodes’, in HT-PEM fuel cell literature. These material sets showed promising capabilities in fuel cell condition but the overall literature on their implantation is limited to-date and their utilization in HT-PEM EHP is novel in and of itself.

In **Chapter 8** the focus was on the general stability and suitability of the ion-pair HT-PEM for EHP operation and subsequently for H<sub>2</sub>/natural gas blend operation. The following major findings were,

- The presence of an ionomer binder was crucial to ion-pair HT-PEM EHP performance. Unlike PA-PBI based EHP without ionomer the ion-pair HT-PEM EHP without ionomer showed high prohibitively high electrode impedance growth.
- Ion-pair HT-PEM EHP without ionomeric binder exhibited recoverable electrode impedance when cycling anodic potentials above 0.7 vs. RHE coinciding with the potential window for the electrochemical oxidation of phosphonic acid. At low anodic potentials phosphonic acid formation is known to occur at elevated temperatures, suggesting that the formation of phosphonic acid plays a role in the high electrode impedance observed in the non-ionomeric ion-pair HT-PEM EHP.
- Ion-pair HT-PEM EHP performed best at high degrees of gas humidification, far higher than what would be physically feasible for PA-PBI. At lower humidification, such as what would be employed in PA-PBI, the HT-PEM EHP with PA-PBI shows lower overall impedance particularly at the electrodes.
- Ionomeric gas diffusion electrodes based on 50% PtRu/C had lower charge transfer losses than 47% wt Pt/C electrodes with the effect more strongly pronounced for PtRu/C at the anode. This was most likely due to the thinner electrode as the former is 25% wt carbon while the latter is 53% wt carbon.
- The HFR, and thus membrane resistance, of the ion-pair HT-PEM EHP was highly dependent on temperature for a range of 120 to 160 °C, and not strongly reliant on relative humidity for a range of 3 to 8%.
- Impedance analysis with distribution of relaxation times indicated that HOR and HER charge transfer related impedances were positively influenced by increasing relative humidity to a degree before leveling off, suggesting a growth of interconnectivity in the proton conducting domains that reaches saturation. Temperature did not play a strong role in HOR/HER.
- The stability of the ion-pair HT-PEM EHP in 10% H<sub>2</sub> blended with de-sulfurized pipeline natural gas was demonstrated for over 100 hours of operation. Cathode exhaust showed 99.993% H<sub>2</sub> concentration on a dry basis, 93.2% on wet basis indicating significant water transport across the membrane phase.
- Stability testing with impedance analysis through distribution of relaxation times showed that impedance growth in anodic processes were the dominated sources of EHP

polarization loss over time in natural gas/H<sub>2</sub> separation environment, with a small growth in HFR observed for the first 80 hours.

In **Chapter 9**, the influence of different sulfonic acid-based ionomers in ion-pair HT-PEM was considered. The best performing ionomeric binder blends for ion pair HT-PEM EHP were examined for H<sub>2</sub>/CH<sub>4</sub> gas blend separations and compared against PA-PBI HT-PEM EHP. Impedance analysis was used to identify limiting factors in ion-pair HT-PEM EHP performance compared to PA-PBI. Natural gas/H<sub>2</sub> blends were studied in like manner and compared against methane/H<sub>2</sub> gas blends to assess the impact of natural gas on HT-PEM EHP.

- Sulfonated polypentafluorostyrene (SPPsf) ionomer at 55% sulfonation (SPPsf-55) exhibited similar performance when blended with PWN ionomer at 1:1 wt ratios to Nafion®/PWN ionomer blends at 1:1 wt ratios. Both outperform solely PWN ionomer GDEs and 80% sulfonation SPPsf-80 blended with PWN.
- Controlling for the ratio of phosphonic acid to sulfonic acid (P/S ratio) groups leads to slightly worse performance of SPPsf-55/PWN blends at P/S = 2 compared to Nafion®/PWN blends at P/S = 2.
- Ion-pair HT-PEM EHP with Nafion®/PWN and SPPsf/PWN binders showed HOR and HER related impedances 2-3x higher than sol-gel PA-PBI for H<sub>2</sub>/CH<sub>4</sub> gas separations, and mass transport related impedances that were 1.5 to 2x higher.
- Natural gas hydrogen blends exhibited slightly higher polarization correlated with increased anode charge transfer impedance compared to methane hydrogen gas blends in ion-pair HT-PEM EHP.
- Ion-pair HT-PEM EHP were able to extract fuel cell quality hydrogen gas from 10 and 5% H<sub>2</sub> gas blends in methane and natural gas with respect to total hydrogen content and methane purity requirements on a dry gas basis. All other gaseous impurities were below minimum detection limits (<25 ppm CO<sub>2</sub>/CO/C<sub>2</sub>H<sub>6</sub>).
- Ion-pair HT-PEM EHP suffered greatly from very low limiting current densities in 10, 5, and 2% H<sub>2</sub> blends, only reaching ~40% of theoretical current limits at best compared to PA-PBI that can reach upwards of 80% of the theoretical limit.

### 10.3 Future Work

The work provides an encouraging start to further develop the technology of HT-PEM EHP, ignited by the potential need for a technological niche that is otherwise prohibitively difficult to accomplish through other means. Each finding of this study brings up more questions, of which the most pertinent are listed below for recommendations on further work in this area,

- While PA-PBI based HT-PEM EHP exhibit promising performance already for H<sub>2</sub> gas separation, the actual economics surrounding their implementation is not known as literature generally on the economics of HT-PEM technology is not very prevalent. A techno-economic analysis of HT-PEM EHP would provide useful for informing whether this approach has longevity compared to less efficient but more technologically mature separation technologies.
- High platinum loadings are required currently for effective operation in HT-PEM, however this dissertation has observed that optimization of the electrode acid content can significantly impact electrode kinetics. Further study on the reduction of platinum catalyst loading combined with optimization of the electrode acid content could lead to improvements in both areas.
- Ion-pair HT-PEM exhibit relatively high electrode impedances and the underlying reasons are not well understood, a number of research efforts could be undertaken to better understand,
  - Gas diffusion layer study to take advantage of differences with respect to LT-PEM or PA-PBI based HT-PEM technology for which most GDLs are designed ie; no liquid water removal, minimal acid content, less need for efficient heat removal.
  - Rheological and morphological study of electrodes to better understand distribution of binary ionomer system in electrodes and improve electrode micro and nano-structure.
  - Raman spectroscopy to investigate the presence of different phosphoric acid species present with respect to temperature and humidity and determine whether

phosphoric acid and/or phosphonic acid anhydrides occur even in the presence of protonated phosphonic acid.

- The water tolerance of the ion-pair based HT-PEM could make it a viable candidate for high temperature vapor electrolysis (HT PEMEZ), but the chemical stability in high anodic potential environment needs to be assessed. A combination of MEA studies, fenton chemical stability testing, and mechanical testing under high humidity could determine this suitability.
- Power-loss based voltage breakdown analysis from simulation studies and voltage breakdown analysis from impedance analysis via distribution of relaxation times could be used in tandem to better understand cell processes and validate the two approaches.
- Ion-pair HT-PEM EHP exhibited reasonable performance down to 120 °C. Lower temperature operation is favorable from a thermodynamic standpoint for gas separation and compression. A study of the efficacy of the EHP at lower temperatures in natural gas should be conducted.
- Maximum viable compression ratios and trade-offs between membrane thickness and performance are key performance parameters for gas separation in EHP. The ion-pair studied here is relatively thin at 50  $\mu\text{m}$  post doping. A study of thicker membranes and parametric sweep of higher compression ratios and higher inlet pressures at the anode could provide better operating characteristics for the HT-PEM EHP.

## References

- [1] Core Writing Team, H. Lee, and J. Romero, “Climate Change 2023: Synthesis Report. Contribution of Working Groups I, II and III to the Sixth Assessment Report of the Intergovernmental Panel on Climate Change,” 2023. doi: 10.59327/IPCC/AR6-9789291691647.
- [2] International Energy Agency, “Net Zero by 2050: A Roadmap for the Global Energy Sector,” p. 70, 2021.
- [3] IEA, “International Energy Agency (IEA) World Energy Outlook 2022,” 2022. [Online]. Available: <https://www.iea.org/reports/world-energy-outlook-2022>
- [4] IRENA (International Renewable Energy Agency), *Renewable Power Generation Costs in 2018*. 2019.
- [5] M. Z. Jacobson *et al.*, “100% Clean and Renewable Wind, Water, and Sunlight All-Sector Energy Roadmaps for 139 Countries of the World,” *Joule*, vol. 1, no. 1, pp. 108–121, 2017, doi: 10.1016/j.joule.2017.07.005.
- [6] M. Z. Jacobson *et al.*, “100% clean and renewable wind, water, and sunlight (WWS) all-sector energy roadmaps for the 50 United States,” *Energy Environ. Sci.*, vol. 8, no. 7, pp. 2093–2117, 2015, doi: 10.1039/c5ee01283j.
- [7] R. Jones, B. Haley, G. Kwok, J. Hargreaves, and J. Williams, “Electrification and the future of electricity markets: Transitioning to a low-carbon energy system,” *IEEE Power Energy Mag.*, vol. 16, no. 4, pp. 79–89, 2018, doi: 10.1109/MPE.2018.2823479.
- [8] A. García-Olivares, J. Solé, and O. Osychenko, “Transportation in a 100% renewable energy system,” *Energy Convers. Manag.*, vol. 158, no. January, pp. 266–285, 2018, doi: 10.1016/j.enconman.2017.12.053.
- [9] B. Tarroja *et al.*, “Translating climate change and heating system electrification impacts on building energy use to future greenhouse gas emissions and electric grid capacity requirements in California,” *Appl. Energy*, vol. 225, no. January, pp. 522–534, 2018, doi: 10.1016/j.apenergy.2018.05.003.
- [10] S. Powell, G. V. Cezar, L. Min, I. M. L. Azevedo, and R. Rajagopal, “Charging infrastructure access and operation to reduce the grid impacts of deep electric vehicle adoption,” *Nat. Energy*, vol. 7, no. 10, pp. 932–945, 2022, doi: 10.1038/s41560-022-01105-7.
- [11] R. Borup, T. Krause, and J. Brouwer, “Hydrogen is Essential for Industry and Transportation Decarbonization,” *Electrochem. Soc. Interface*, vol. 30, no. 4, pp. 79–83, 2021, doi: 10.1149/2.F18214IF.
- [12] H. Olcay, R. Malina, A. A. Upadhye, J. I. Hileman, G. W. Huber, and S. R. H. Barrett, “Techno-economic and environmental evaluation of producing chemicals and drop-in aviation biofuels via aqueous phase processing,” *Energy Environ. Sci.*, vol. 11, no. 8, pp. 2085–2101, 2018, doi: 10.1039/c7ee03557h.
- [13] S. Horvath, M. Fasihi, and C. Breyer, “Techno-economic analysis of a decarbonized shipping sector: Technology suggestions for a fleet in 2030 and 2040,” *Energy Convers. Manag.*, vol. 164, no. x, pp. 230–241, 2018, doi: 10.1016/j.enconman.2018.02.098.
- [14] H. Wiertzema, M. Åhman, and S. Harvey, “Bottom-up methodology for assessing electrification options for deep decarbonisation of industrial processes,” *Eceee Ind. Summer Study Proc.*, vol. 2018-June, pp. 389–397, 2018.
- [15] D. Schüwer and C. Schneider, “Electrification of industrial process heat: Long-term

- applications, potentials and impacts,” *Eceee Ind. Summer Study Proc.*, vol. 2018-June, pp. 411–422, 2018.
- [16] California ISO (CAISO), “Managing Oversupply,” 2024.  
<https://www.caiso.com/informed/Pages/ManagingOversupply.aspx>
- [17] California ISO (CAISO), “2022 Total System Electric Generation,” 2022.  
<https://www.energy.ca.gov/data-reports/energy-almanac/california-electricity-data/2022-total-system-electric-generation>
- [18] F. Cebulla, J. Haas, J. Eichman, W. Nowak, and P. Mancarella, “How much electrical energy storage do we need? A synthesis for the U.S., Europe, and Germany,” *J. Clean. Prod.*, vol. 181, pp. 449–459, 2018, doi: 10.1016/j.jclepro.2018.01.144.
- [19] California Energy Commission, “California Energy Commission California Energy Storage System Survey,” 2023.  
[https://tableau.cnra.ca.gov/t/CNRA\\_CEC\\_PUBLIC/views/EnergyStorageDashboard/CaliforniaEnergyStorageSystemSurvey?embed=y&isGuestRedirectFromVizportal=y&display\\_count=n&showAppBanner=false&origin=viz\\_share\\_link&showVizHome=n](https://tableau.cnra.ca.gov/t/CNRA_CEC_PUBLIC/views/EnergyStorageDashboard/CaliforniaEnergyStorageSystemSurvey?embed=y&isGuestRedirectFromVizportal=y&display_count=n&showAppBanner=false&origin=viz_share_link&showVizHome=n)
- [20] Y. Yang, S. Bremner, C. Menictas, and M. Kay, “Battery energy storage system size determination in renewable energy systems: A review,” *Renew. Sustain. Energy Rev.*, vol. 91, no. January, pp. 109–125, 2018, doi: 10.1016/j.rser.2018.03.047.
- [21] M. R. Shaner, S. J. Davis, N. S. Lewis, and K. Caldeira, “Geophysical constraints on the reliability of solar and wind power in the United States,” *Energy Environ. Sci.*, vol. 11, no. 4, pp. 914–925, 2018, doi: 10.1039/c7ee03029k.
- [22] J. A. Dowling *et al.*, “Role of Long-Duration Energy Storage in Variable Renewable Electricity Systems,” *Joule*, vol. 4, no. 9, pp. 1907–1928, 2020, doi: 10.1016/j.joule.2020.07.007.
- [23] A. Mazza, E. Bompard, and G. Chicco, “Applications of power to gas technologies in emerging electrical systems,” *Renew. Sustain. Energy Rev.*, vol. 92, no. January 2017, pp. 794–806, 2018, doi: 10.1016/j.rser.2018.04.072.
- [24] A. Lewandowska-Bernat and U. Desideri, “Opportunities of power-to-gas technology in different energy systems architectures,” *Appl. Energy*, vol. 228, no. January 2017, pp. 57–67, 2018, doi: 10.1016/j.apenergy.2018.06.001.
- [25] IRENA, “Hydrogen from renewable power: Technology outlook for the energy transition,” 2018. [Online]. Available: [www.irena.org](http://www.irena.org)
- [26] A. Saeedmanesh, M. A. Mac Kinnon, and J. Brouwer, “Hydrogen is essential for sustainability,” *Curr. Opin. Electrochem.*, vol. 12, pp. 166–181, 2018, doi: 10.1016/j.coelec.2018.11.009.
- [27] IRENA, “Global Energy Transformation: A Roadmap to 2050,” 2019. [Online]. Available: <https://www.irena.org/publications/2019/Apr/Global-energy-transformation-A-roadmap-to-2050-2019Edition>
- [28] Hydrogen Council and McKinsey & Company, “Hydrogen for Net-Zero: A critical cost-competitive energy vector,” 2021. [Online]. Available: <https://hydrogencouncil.com/en/hydrogen-for-net-zero/>
- [29] CSIRO, “HyResource International Policy.”  
<https://research.csiro.au/hyresource/policy/international/>
- [30] M. Wappler, D. Unguder, X. Lu, H. Ohlmeyer, H. Teschke, and W. Lueke, “Building the green hydrogen market – Current state and outlook on green hydrogen demand and electrolyzer manufacturing,” *Int. J. Hydrogen Energy*, vol. 47, no. 79, pp. 33551–33570,



- 2022, doi: 10.1016/j.ijhydene.2022.07.253.
- [31] M. J. Chae, J. H. Kim, B. Moon, S. Park, and Y. S. Lee, “The present condition and outlook for hydrogen-natural gas blending technology,” *Korean J. Chem. Eng.*, vol. 39, no. 2, pp. 251–262, 2022, doi: 10.1007/s11814-021-0960-8.
- [32] J. P. Maton, L. Zhao, and J. Brouwer, “Dynamic modeling of compressed gas energy storage to complement renewable wind power intermittency,” *Int. J. Hydrogen Energy*, vol. 38, no. 19, pp. 7867–7880, 2013, doi: 10.1016/j.ijhydene.2013.04.030.
- [33] A. Le Duigou, A. G. Bader, J. C. Lanoix, and L. Nadau, “Relevance and costs of large scale underground hydrogen storage in France,” *Int. J. Hydrogen Energy*, vol. 42, no. 36, pp. 22987–23003, 2017, doi: 10.1016/j.ijhydene.2017.06.239.
- [34] M. Reuß, T. Grube, M. Robinius, P. Preuster, P. Wasserscheid, and D. Stolten, “Seasonal storage and alternative carriers: A flexible hydrogen supply chain model,” *Appl. Energy*, vol. 200, pp. 290–302, 2017, doi: 10.1016/j.apenergy.2017.05.050.
- [35] M. E. Demir and I. Dincer, “Cost assessment and evaluation of various hydrogen delivery scenarios,” *Int. J. Hydrogen Energy*, vol. 43, no. 22, pp. 10420–10430, 2018, doi: 10.1016/j.ijhydene.2017.08.002.
- [36] S. Clegg and P. Mancarella, “Storing renewables in the gas network: Modelling of power-to-gas seasonal storage flexibility in low-carbon power systems,” *IET Gener. Transm. Distrib.*, vol. 10, no. 3, pp. 566–575, 2016, doi: 10.1049/iet-gtd.2015.0439.
- [37] J. Ogden, A. M. Jaffe, D. Scheitrum, Z. McDonald, and M. Miller, “Natural gas as a bridge to hydrogen transportation fuel: Insights from the literature,” *Energy Policy*, vol. 115, no. February 2017, pp. 317–329, 2018, doi: 10.1016/j.enpol.2017.12.049.
- [38] M. W. Melaina, O. Antonia, and M. Penev, “Blending Hydrogen into Natural Gas Pipeline Networks: A Review of Key Issues,” 2013. [Online]. Available: <http://www.osti.gov/bridge>
- [39] K. Topolski *et al.*, “Hydrogen Blending into Natural Gas Pipeline Infrastructure: Review of the State of Technology,” *Natl. Renew. Energy Lab.*, no. October, 2022, [Online]. Available: <https://www.nrel.gov/docs/fy23osti/81704.pdf>
- [40] M. Ruth *et al.*, “The Technical and Economic Potential of the H2@Scale Hydrogen Concept within the United States,” 2020.
- [41] C.J. Suchovsky, Lief Ericksen, Ted A. Williams, and Dragica Jeremic Nikolic, “Appliance and Equipment Performance with Hydrogen-Enriched Natural Gases,” no. May, 2021, [Online]. Available: <https://www.csagroup.org/wp-content/uploads/CSA-Group-Research-Appliance-and-Equipment-Performance-with-Hydrogen-Enriched-Natural-Gases.pdf>
- [42] Y. Zhao, V. McDonell, and S. Samuelsen, “Influence of hydrogen addition to pipeline natural gas on the combustion performance of a cooktop burner,” *Int. J. Hydrogen Energy*, vol. 44, no. 23, pp. 12239–12253, 2019, doi: 10.1016/j.ijhydene.2019.03.100.
- [43] Y. Zhao, V. McDonell, and S. Samuelsen, “Assessment of the combustion performance of a room furnace operating on pipeline natural gas mixed with simulated biogas or hydrogen,” *Int. J. Hydrogen Energy*, vol. 45, no. 19, pp. 11368–11379, 2020, doi: 10.1016/j.ijhydene.2020.02.071.
- [44] Y. Zhao, W. Shao, Y. Liu, X. Tang, Y. Xiao, and V. McDonell, “Numerical and Experimental Study of Geometry Effects on Fuel/Air Mixing and Combustion Characteristics of a DLN Burner.” Aug. 04, 2020. doi: 10.1115/POWER2020-16371.
- [45] S. Kuczynski, M. Łaciak, A. Olijnyk, A. Szurlej, and T. Włodek, “Thermodynamic and technical issues of hydrogen and methane-hydrogen mixtures pipeline transmission,”

- Energies*, vol. 12, no. 3, 2019, doi: 10.3390/en12030569.
- [46] Z. Hafsi, S. Elaoud, M. Akrouf, and E. Hadj-Taïeb, “Numerical Approach for Steady State Analysis of Hydrogen–Natural Gas Mixtures Flows in Looped Network,” *Arab. J. Sci. Eng.*, vol. 42, no. 5, pp. 1941–1950, 2017, doi: 10.1007/s13369-016-2393-y.
- [47] B. Meng *et al.*, “Hydrogen effects on X80 pipeline steel in high-pressure natural gas/hydrogen mixtures,” *Int. J. Hydrogen Energy*, vol. 42, no. 11, pp. 7404–7412, 2017, doi: 10.1016/j.ijhydene.2016.05.145.
- [48] J. A. Ronevich and C. San Marchi, “Materials Compatibility Concerns for Hydrogen Blended Into Natural Gas.” Jul. 13, 2021. doi: 10.1115/PVP2021-62045.
- [49] J. A. Ronevich, R. Shrestha, and C. San Marchi, “Misconceptions of Hydrogen Degradation of Pipeline Steels in Existing Natural Gas Infrastructure,” in *4th International Conference on Metals and Hydrogen*, Sandia National Laboratories, 2022.
- [50] E. Salzano, F. Cammarota, A. Di Benedetto, and V. Di Sarli, “Explosion behavior of hydrogen-methane/air mixtures,” *J. Loss Prev. Process Ind.*, vol. 25, no. 3, pp. 443–447, 2012, doi: 10.1016/j.jlp.2011.11.010.
- [51] S. D. Emami, M. Rajabi, C. R. C. Hassan, M. D. A. Hamid, R. M. Kasmani, and M. Mazangi, “Experimental study on premixed hydrogen/air and hydrogenemethane/air mixtures explosion in 90 degree bend pipeline,” *Int. J. Hydrogen Energy*, vol. 38, no. 32, pp. 14115–14120, 2013, doi: 10.1016/j.ijhydene.2013.08.056.
- [52] D. Mahajan, K. Tan, T. Venkatesh, P. Kileti, and C. R. Clayton, “Hydrogen Blending in Gas Pipeline Networks—A Review,” *Energies*, vol. 15, no. 10, 2022, doi: 10.3390/en15103582.
- [53] IEA, “Global Hydrogen Review 2022,” 2022. doi: 10.1787/a15b8442-en.
- [54] S. Faramawy, T. Zaki, and A. A. E. Sakr, “Natural gas origin, composition, and processing: A review,” *J. Nat. Gas Sci. Eng.*, vol. 34, pp. 34–54, 2016, doi: 10.1016/j.jngse.2016.06.030.
- [55] Energy Information Administration, “Natural Gas Processing : The Crucial Link Between Natural Gas Production and Its Transportation to Market Figure 1 . Generalized Natural Gas Processing Schematic,” no. January, p. 11, 2006.
- [56] U.S. Department of Energy, “Hydrogen Fuel Quality Specifications for Polymer Electrolyte Fuel Cells in Road Vehicles,” *Safety, Codes Stand. Progr.*, pp. 1–72, 2016.
- [57] V. Subramani, P. Sharma, L. Zhang, and K. Liu, “Catalytic Steam Reforming Technology for the Production of Hydrogen and Syngas,” in *Hydrogen and Syngas Production and Purification Technologies*, 2009, pp. 14–126. doi: <https://doi.org/10.1002/9780470561256.ch2>.
- [58] D. M. Ruthven, *Principles of adsorption and adsorption processes*. John Wiley & Sons, 1984.
- [59] A. M. Ribeiro, C. A. Grande, F. V. S. Lopes, J. M. Loureiro, and A. E. Rodrigues, “A parametric study of layered bed PSA for hydrogen purification,” *Chem. Eng. Sci.*, vol. 63, no. 21, pp. 5258–5273, Nov. 2008, doi: 10.1016/j.ces.2008.07.017.
- [60] C. A. Grande, “Advances in Pressure Swing Adsorption for Gas Separation,” *ISRN Chem. Eng.*, vol. 2012, pp. 1–13, Dec. 2012, doi: 10.5402/2012/982934.
- [61] G. Hu *et al.*, “A Review of Technical Advances, Barriers, and Solutions in the Power to Hydrogen (P2H) Roadmap,” *Engineering*, vol. 6, no. 12, pp. 1364–1380, 2020, doi: 10.1016/j.eng.2020.04.016.
- [62] L. Vermaak, H. W. J. P. Neomagus, and D. G. Bessarabov, “Recent advances in

- membrane-based electrochemical hydrogen separation: A review,” *Membranes (Basel)*, vol. 11, no. 2, pp. 1–32, 2021, doi: 10.3390/membranes11020127.
- [63] S. Adhikari and S. Fernando, “Hydrogen Membrane Separation Techniques,” *Ind. Eng. Chem. Res.*, vol. 45, no. 3, pp. 875–881, Feb. 2006, doi: 10.1021/ie0506441.
- [64] F. Liu and N. Zhang, “Strategy of purifier selection and integration in hydrogen networks,” *Chem. Eng. Res. Des.*, vol. 82, no. 10, pp. 1315–1330, 2004, doi: 10.1205/cerd.82.10.1315.46739.
- [65] A. B. Hinchliffe and K. E. Porter, “A Comparison of Membrane Separation and Distillation,” *Chem. Eng. Res. Des.*, vol. 78, no. 2, pp. 255–268, 2000, doi: <https://doi.org/10.1205/026387600527121>.
- [66] W. Liemberger, M. Groß, M. Miltner, and M. Harasek, “Experimental analysis of membrane and pressure swing adsorption (PSA) for the hydrogen separation from natural gas,” *J. Clean. Prod.*, vol. 167, pp. 896–907, 2017, doi: <https://doi.org/10.1016/j.jclepro.2017.08.012>.
- [67] S. P. Cardoso, I. S. Azenha, Z. Lin, I. Portugal, A. E. Rodrigues, and C. M. Silva, “Inorganic Membranes for Hydrogen Separation,” *Sep. Purif. Rev.*, vol. 47, no. 3, pp. 229–266, Jul. 2018, doi: 10.1080/15422119.2017.1383917.
- [68] B. Zornoza, C. Casado, and A. Navajas, “Chapter 11 - Advances in Hydrogen Separation and Purification with Membrane Technology,” L. M. Gandía, G. Arzamendi, and P. M. B. T.-R. H. T. Diéguez, Eds., Amsterdam: Elsevier, 2013, pp. 245–268. doi: <https://doi.org/10.1016/B978-0-444-56352-1.00011-8>.
- [69] G. Q. Lu *et al.*, “Inorganic membranes for hydrogen production and purification: A critical review and perspective,” *J. Colloid Interface Sci.*, vol. 314, no. 2, pp. 589–603, 2007, doi: <https://doi.org/10.1016/j.jcis.2007.05.067>.
- [70] H. T. Lu, W. Li, E. S. Miandoab, S. Kanehashi, and G. Hu, “The opportunity of membrane technology for hydrogen purification in the power to hydrogen (P2H) roadmap: a review,” *Front. Chem. Sci. Eng.*, vol. 15, no. 3, pp. 464–482, 2021, doi: 10.1007/s11705-020-1983-0.
- [71] M. A. Llosa Tanco, J. A. Medrano, V. Cechetto, F. Gallucci, and D. A. Pacheco Tanaka, “Hydrogen permeation studies of composite supported alumina-carbon molecular sieves membranes: Separation of diluted hydrogen from mixtures with methane,” *Int. J. Hydrogen Energy*, vol. 46, no. 37, pp. 19758–19767, May 2021, doi: 10.1016/j.ijhydene.2020.05.088.
- [72] M. Nordio, J. Melendez, M. van Sint Annaland, D. A. Pacheco Tanaka, M. Llosa Tanco, and F. Gallucci, “Comparison between carbon molecular sieve and Pd-Ag membranes in H<sub>2</sub>-CH<sub>4</sub> separation at high pressure,” *Int. J. Hydrogen Energy*, vol. 45, no. 53, pp. 28876–28892, Oct. 2020, doi: 10.1016/j.ijhydene.2020.07.191.
- [73] N. A. Al-Mufachi, N. V. Rees, and R. Steinberger-Wilkens, “Hydrogen selective membranes: A review of palladium-based dense metal membranes,” *Renew. Sustain. Energy Rev.*, vol. 47, pp. 540–551, 2015.
- [74] S. T. Oyama, M. Yamada, T. Sugawara, A. Takagaki, and R. Kikuchi, “Review on Mechanisms of Gas Permeation through Inorganic Membranes,” *J. Japan Pet. Inst.*, vol. 54, no. 5, pp. 298–309, 2011, doi: 10.1627/jpi.54.298.
- [75] G. J. Grashoff, C. E. Pilkington, and C. W. Corti, “The Purification of Hydrogen A REVIEW OF THE TECHNOLOGY EMPHASISING THE CURRENT STATUS OF PALLADIUM MEMBRANE DIFFUSION,” 1983. [Online]. Available:

- <https://api.semanticscholar.org/CorpusID:55723133>
- [76] N. W. Ockwig and T. M. Nenoff, “Membranes for Hydrogen Separation,” *Chem. Rev.*, vol. 107, no. 10, pp. 4078–4110, Oct. 2007, doi: 10.1021/cr0501792.
- [77] M. Vadrucci, F. Borgognoni, A. Moriani, A. Santucci, and S. Tosti, “Hydrogen permeation through Pd–Ag membranes: Surface effects and Sieverts’ law,” *Int. J. Hydrogen Energy*, vol. 38, no. 10, pp. 4144–4152, 2013, doi: <https://doi.org/10.1016/j.ijhydene.2013.01.091>.
- [78] M. Nordio, S. A. Wassie, M. Van Sint Annaland, D. A. Pacheco Tanaka, J. L. Viviente Sole, and F. Gallucci, “Techno-economic evaluation on a hybrid technology for low hydrogen concentration separation and purification from natural gas grid,” *Int. J. Hydrogen Energy*, vol. 46, no. 45, pp. 23417–23435, Jul. 2021, doi: 10.1016/j.ijhydene.2020.05.009.
- [79] W. Liemberger, D. Halmschlager, M. Miltner, and M. Harasek, “Efficient extraction of hydrogen transported as co-stream in the natural gas grid – The importance of process design,” *Appl. Energy*, vol. 233–234, no. November 2017, pp. 747–763, 2019, doi: 10.1016/j.apenergy.2018.10.047.
- [80] F. Gallucci, “Flexible Hybrid separation system for H<sub>2</sub> recovery from NG Grids HyGrid,” in *HyGrid Final Presentation*, European Union Horizon 2020, 2021.
- [81] W. T. Grubb and L. W. Niedrach, “Batteries with Solid Ion-Exchange Membrane Electrolytes II. Low-Temperature Hydrogen-Oxygen Fuel Cells,” *J. Electrochem. Soc.*, vol. 107, pp. 131–135, 1960, [Online]. Available: <https://api.semanticscholar.org/CorpusID:93154330>
- [82] H. Maget, “Process for gas purification,” 3,489,670, 1970
- [83] B. M. Stühmeier, M. R. Pietsch, J. N. Schwämmlein, and H. A. Gasteiger, “Pressure and Temperature Dependence of the Hydrogen Oxidation and Evolution Reaction Kinetics on Pt Electrocatalysts via PEMFC-based Hydrogen-Pump Measurements,” *J. Electrochem. Soc.*, vol. 168, no. 6, p. 064516, 2021, doi: 10.1149/1945-7111/ac099c.
- [84] P. W. Parfomak, “Energy Storage for Power Grids and Electric Transportation: A Technology Assessment,” 2012. [Online]. Available: <https://api.semanticscholar.org/CorpusID:107494268>
- [85] A. Witkowski, A. Rusin, M. Majkut, and K. Stolecka, “Comprehensive analysis of hydrogen compression and pipeline transportation from thermodynamics and safety aspects,” *Energy*, vol. 141, pp. 2508–2518, 2017, [Online]. Available: <https://api.semanticscholar.org/CorpusID:114943662>
- [86] D. Marcius, A. Kovač, and M. Firak, “Electrochemical hydrogen compressor: Recent progress and challenges,” *Int. J. Hydrogen Energy*, vol. 47, no. 57, pp. 24179–24193, 2022, doi: 10.1016/j.ijhydene.2022.04.134.
- [87] J. Zou *et al.*, “Electrochemical Compression Technologies for High-Pressure Hydrogen: Current Status, Challenges and Perspective,” *Electrochem. Energy Rev.*, vol. 3, no. 4, pp. 690–729, 2020, doi: 10.1007/s41918-020-00077-0.
- [88] J. Zou *et al.*, “Insights into electrochemical hydrogen compressor operating parameters and membrane electrode assembly degradation mechanisms,” *J. Power Sources*, vol. 484, no. September 2020, p. 229249, 2021, doi: 10.1016/j.jpowsour.2020.229249.
- [89] S. Ahmad, T. Nawaz, A. Ali, M. F. Orhan, A. Samreen, and A. M. Kannan, “An overview of proton exchange membranes for fuel cells: Materials and manufacturing,” *Int. J. Hydrogen Energy*, vol. 47, no. 44, pp. 19086–19131, 2022, doi:

- 10.1016/j.ijhydene.2022.04.099.
- [90] M.-T. Nguyen, S. A. Grigoriev, A. A. Kalinnikov, A. A. Filippov, P. Millet, and V. N. Fateev, "Characterisation of an electrochemical hydrogen pump using electrochemical impedance spectroscopy," *J. Appl. Electrochem.*, vol. 41, no. 9, pp. 1033–1042, 2011, doi: 10.1007/s10800-011-0341-9.
- [91] K. Nishida, T. Hosotani, M. Asa, S. Tsushima, and S. Hirai, "Separation Analysis of Electro-Osmosis and Diffusion of Water in Electrolyte Membrane of PEMFC under Low-Humidity Operation," *ECS Trans.*, vol. 58, no. 1, p. 621, 2013, doi: 10.1149/05801.0621ecst.
- [92] G. Sdanghi, J. Dillet, S. Didierjean, V. Fierro, and G. Maranzana, "Experimental evidence of local heterogeneities in a PEM Electrochemical Hydrogen Compressor," *Eur. Fuel Cells Forum 2019*, no. July 2020, 2019.
- [93] K. G. Gallagher, B. S. Pivovarov, and T. F. Fuller, "Electro-osmosis and Water Uptake in Polymer Electrolytes in Equilibrium with Water Vapor at Low Temperatures," *J. Electrochem. Soc.*, vol. 156, no. 3, p. B330, 2009, doi: 10.1149/1.3046150.
- [94] G. Sdanghi, J. Dillet, S. Didierjean, V. Fierro, and G. Maranzana, "Feasibility of Hydrogen Compression in an Electrochemical System: Focus on Water Transport Mechanisms," *Fuel Cells*, vol. 20, no. 3, pp. 370–380, 2020, doi: 10.1002/face.201900068.
- [95] P. J. Bouwman, "Advances in Electrochemical Hydrogen Compression and Purification," *ECS Trans.*, vol. 75, no. 14, pp. 503–510, Sep. 2016, doi: 10.1149/07514.0503ecst.
- [96] Giner ELX Inc, "Electrochemical Compression," *2019 DOE Hydrogen Fuel Cell Progr. Annu. Merit Rev.*, pp. 1–6, 2019.
- [97] Toray Industries Inc., "Research on Electrochemical Hydrogen Compressor. P13002, 20170000000203," 2017.
- [98] H. P. J. Bouman, "High Pressure Hydrogen ALL Electrochemical Decentralized Refueling Station," *PHAEDRUS Proj.*, vol. 31, no. 0, pp. 1–58, 2015, [Online]. Available: [http://www.sartre-project.eu/en/publications/Documents/SARTRE\\_Final-Report.pdf](http://www.sartre-project.eu/en/publications/Documents/SARTRE_Final-Report.pdf)
- [99] K. Onda, K. Ichihara, M. Nagahama, Y. Minamoto, and T. Araki, "Separation and compression characteristics of hydrogen by use of proton exchange membrane," *J. Power Sources*, vol. 164, pp. 1–8, 2007, [Online]. Available: <https://api.semanticscholar.org/CorpusID:96743817>
- [100] B. Ibeh, C. Gardner, and M. TERNAN, "Separation of hydrogen from a hydrogen/methane mixture using a PEM fuel cell," *Int. J. Hydrogen Energy*, vol. 32, no. 7, pp. 908–914, 2007, doi: 10.1016/j.ijhydene.2006.11.017.
- [101] M. Nordio *et al.*, "Experimental and modelling study of an electrochemical hydrogen compressor," *Chem. Eng. J.*, vol. 369, pp. 432–442, Aug. 2019, doi: 10.1016/j.cej.2019.03.106.
- [102] S. Mrusek, M. Blasius, F. Morgenroth, S. Thiele, and P. Wasserscheid, "Hydrogen extraction from methane-hydrogen mixtures from the natural gas grid by means of electrochemical hydrogen separation and compression," *Int. J. Hydrogen Energy*, vol. 50, no. 11, pp. 526–538, 2024, doi: 10.1016/j.ijhydene.2023.08.195.
- [103] B. Ibeh, C. Gardner, and M. TERNAN, "Separation of hydrogen from a hydrogen/methane mixture using a PEM fuel cell," *Int. J. Hydrogen Energy*, vol. 32, no. 7, pp. 908–914, May 2007, doi: 10.1016/j.ijhydene.2006.11.017.
- [104] M. Nordio, M. Egvaras Barain, L. Raymakers, M. Van Sint Annaland, M. Mulder, and F.

- Gallucci, "Effect of CO<sub>2</sub> on the performance of an electrochemical hydrogen compressor," *Chem. Eng. J.*, vol. 392, no. August 2019, 2020, doi: 10.1016/j.cej.2019.123647.
- [105] J. O. Jensen, H. A. Hjuler, D. Aili, and Q. Li, "Introduction BT - High Temperature Polymer Electrolyte Membrane Fuel Cells: Approaches, Status, and Perspectives," Q. Li, D. Aili, H. A. Hjuler, and J. O. Jensen, Eds., Cham: Springer International Publishing, 2016, pp. 1–4. doi: 10.1007/978-3-319-17082-4\_1.
- [106] M. Farooque, A. Kush, and S. Abens, "Novel electrochemical hydrogen separation device using phosphoric acid membrane cell," *Sep. Sci. Technol.*, vol. 25, no. 13–15, pp. 1361–1373, 1990, doi: 10.1080/01496399008050397.
- [107] J. S. Wainright, J. -T. Wang, D. Weng, R. F. Savinell, and M. Litt, "Acid-Doped Polybenzimidazoles: A New Polymer Electrolyte," *J. Electrochem. Soc.*, vol. 142, no. 7, pp. L121–L123, 1995, doi: 10.1149/1.2044337.
- [108] E. W. Neuse, "Aromatic polybenzimidazoles. Syntheses, properties, and applications," 1982. [Online]. Available: <https://api.semanticscholar.org/CorpusID:136774185>
- [109] T.-S. Chung, "A Critical Review of Polybenzimidazoles," *J. Macromol. Sci. Part C*, vol. 37, no. 2, pp. 277–301, May 1997, doi: 10.1080/15321799708018367.
- [110] J. H. Bitter and A. Asadi Tashvigh, "Recent Advances in Polybenzimidazole Membranes for Hydrogen Purification," *Ind. Eng. Chem. Res.*, 2022, doi: 10.1021/acs.iecr.2c00645.
- [111] K. S. Lee, J. S. Spendelow, Y. K. Choe, C. Fujimoto, and Y. S. Kim, "An operationally flexible fuel cell based on quaternary ammonium-biphosphate ion pairs," *Nat. Energy*, vol. 1, no. 9, pp. 1–7, 2016, doi: 10.1038/nenergy.2016.120.
- [112] Y.-L. Ma, J. S. Wainright, M. H. Litt, and R. F. Savinell, "Conductivity of PBI Membranes for High-Temperature Polymer Electrolyte Fuel Cells," *J. Electrochem. Soc.*, vol. 151, no. 1, p. A8, 2004, doi: 10.1149/1.1630037.
- [113] K. Fishel, G. Qian, and B. C. Benicewicz, "PBI Membranes Via the PPA Process BT - High Temperature Polymer Electrolyte Membrane Fuel Cells: Approaches, Status, and Perspectives," Q. Li, D. Aili, H. A. Hjuler, and J. O. Jensen, Eds., Cham: Springer International Publishing, 2016, pp. 217–238. doi: 10.1007/978-3-319-17082-4\_10.
- [114] F. Mack, S. Heissler, R. Laukenmann, and R. Zeis, "Phosphoric acid distribution and its impact on the performance of polybenzimidazole membranes," *J. Power Sources*, vol. 270, pp. 627–633, 2014, doi: 10.1016/j.jpowsour.2014.06.171.
- [115] Q. Li, R. He, R. W. Berg, H. A. Hjuler, and N. J. Bjerrum, "Water uptake and acid doping of polybenzimidazoles as electrolyte membranes for fuel cells," *Solid State Ionics*, vol. 168, no. 1–2, pp. 177–185, 2004, doi: 10.1016/j.ssi.2004.02.013.
- [116] L. Xiao *et al.*, "High-temperature polybenzimidazole fuel cell membranes via a sol-gel process," *Chem. Mater.*, vol. 17, no. 21, pp. 5328–5333, 2005, doi: 10.1021/cm050831+.
- [117] K. A. Perry, K. L. More, E. A. Payzant, R. A. Meisner, B. G. Sumpter, and B. C. Benicewicz, "A comparative study of phosphoric acid-doped m-PBI membranes," *J. Polym. Sci. Part B Polym. Phys.*, vol. 52, no. 1, pp. 26–35, 2014, doi: 10.1002/polb.23403.
- [118] J. A. Mader, L. Xiao, T. J. Schmidt, and B. C. Benicewicz, "Polybenzimidazole/Acid Complexes as High-Temperature Membranes," *Adv. Polym. Sci.*, vol. 216, pp. 63–124, 2008, [Online]. Available: <https://api.semanticscholar.org/CorpusID:51745079>
- [119] S. Yu, H. Zhang, L. Xiao, E. W. Choe, and B. C. Benicewicz, "Synthesis of Poly (2, 2'-(1, 4-phenylene) 5, 5'-bibenzimidazole) (para-PBI) and Phosphoric Acid Doped Membrane for Fuel Cells," *Fuel Cells*, vol. 9, no. 4, pp. 318–324, 2009, doi:

- 10.1002/fuce.200900062.
- [120] J. A. Asensio and P. Gómez-Romero, “Recent Developments on Proton Conducting Poly(2,5-benzimidazole) (ABPBI) Membranes for High Temperature Polymer Electrolyte Membrane Fuel Cells,” *Fuel Cells*, vol. 5, no. 3, pp. 336–343, Aug. 2005, doi: <https://doi.org/10.1002/fuce.200400081>.
- [121] A. L. Gullidge, B. Gu, and B. C. Benicewicz, “A new sequence isomer of AB-polybenzimidazole for high-temperature PEM fuel cells,” *J. Polym. Sci. Part A Polym. Chem.*, vol. 50, no. 2, pp. 306–313, Jan. 2012, doi: <https://doi.org/10.1002/pola.25034>.
- [122] T. J. Schmidt and J. Baurmeister, “Durability and Reliability in High-Temperature Reformed Hydrogen PEFCs,” *ECS Meet. Abstr.*, vol. MA2006-02, no. 8, pp. 604–604, 2006, doi: [10.1149/ma2006-02/8/604](https://doi.org/10.1149/ma2006-02/8/604).
- [123] T. J. Schmidt, “Durability and Degradation Mechanisms in High-Temperature Polymer Electrolyte Fuel Cells,” in *208th ECS Meeting, Abstract #1166*, p. 2006.
- [124] D. Aili, L. N. Cleemann, Q. Li, J. O. Jensen, E. Christensen, and N. J. Bjerrum, “Thermal curing of PBI membranes for high temperature PEM fuel cells,” *J. Mater. Chem.*, vol. 22, no. 12, pp. 5444–5453, 2012, doi: [10.1039/C2JM14774B](https://doi.org/10.1039/C2JM14774B).
- [125] X. Chen, G. Qian, M. A. Molle, B. C. Benicewicz, and H. J. Ploehn, “High temperature creep behavior of phosphoric acid-polybenzimidazole gel membranes,” *J. Polym. Sci. Part B Polym. Phys.*, vol. 53, no. 21, pp. 1527–1538, 2015, doi: [10.1002/polb.23791](https://doi.org/10.1002/polb.23791).
- [126] A. T. Pingitore, F. Huang, G. Qian, and B. C. Benicewicz, “Durable High Polymer Content m/p-Polybenzimidazole Membranes for Extended Lifetime Electrochemical Devices,” *ACS Appl. Energy Mater.*, vol. 2, no. 3, pp. 1720–1726, 2019, doi: [10.1021/acsaem.8b01820](https://doi.org/10.1021/acsaem.8b01820).
- [127] F. Huang, A. T. Pingitore, and B. C. Benicewicz, “High Polymer Content m/p-Polybenzimidazole Copolymer Membranes for Electrochemical Hydrogen Separation under Differential Pressures,” *J. Electrochem. Soc.*, vol. 167, no. 167, p. 063504, 2020, doi: [10.1149/1945-7111/ab81a0](https://doi.org/10.1149/1945-7111/ab81a0).
- [128] C. Siegel, S. Lang, E. Fontes, and P. Beckhaus, “Approaches for the Modeling of PBI/H3PO4 Based HT-PEM Fuel Cells - High Temperature Polymer Electrolyte Membrane Fuel Cells: Approaches, Status, and Perspectives,” Q. Li, D. Aili, H. A. Hjuler, and J. O. Jensen, Eds., Cham: Springer International Publishing, 2016, pp. 387–424. doi: [10.1007/978-3-319-17082-4\\_18](https://doi.org/10.1007/978-3-319-17082-4_18).
- [129] K. C. Neyerlin, W. Gu, J. Jorne, and H. A. Gasteiger, “Study of the Exchange Current Density for the Hydrogen Oxidation and Evolution Reactions,” *J. Electrochem. Soc.*, vol. 154, no. 7, p. B631, 2007, doi: [10.1149/1.2733987](https://doi.org/10.1149/1.2733987).
- [130] T. Engl, L. Gubler, and T. J. Schmidt, “Catalysts and Catalyst-Layers in HT-PEMFCs - High Temperature Polymer Electrolyte Membrane Fuel Cells: Approaches, Status, and Perspectives,” Q. Li, D. Aili, H. A. Hjuler, and J. O. Jensen, Eds., Cham: Springer International Publishing, 2016, pp. 297–313. doi: [10.1007/978-3-319-17082-4\\_14](https://doi.org/10.1007/978-3-319-17082-4_14).
- [131] F. Seland, T. Berning, B. Børresen, and R. Tunold, “Improving the performance of high-temperature PEM fuel cells based on PBI electrolyte,” *J. Power Sources*, vol. 160, no. 1, pp. 27–36, 2006, doi: [10.1016/j.jpowsour.2006.01.047](https://doi.org/10.1016/j.jpowsour.2006.01.047).
- [132] J. O. Park, K. Kwon, M. D. Cho, S.-G. Hong, T. Y. Kim, and D. Y. Yoo, “Role of Binders in High Temperature PEMFC Electrode,” *J. Electrochem. Soc.*, vol. 158, no. 6, pp. B675–B681, 2011, doi: [10.1149/1.3573773](https://doi.org/10.1149/1.3573773).
- [133] F. Arslan *et al.*, “The influence of intrinsically proton conductive electrode binder

- materials on HT-PEMFC performance,” *J. Power Sources*, vol. 553, no. May 2022, 2023, doi: 10.1016/j.jpowsour.2022.232297.
- [134] T. J. Kazdal, S. Lang, F. Kühn, and M. J. Hampe, “Modelling of the vapour-liquid equilibrium of water and the in situ concentration of H<sub>3</sub>PO<sub>4</sub> in a high temperature proton exchange membrane fuel cell,” *J. Power Sources*, vol. 249, pp. 446–456, 2014, doi: 10.1016/j.jpowsour.2013.10.098.
- [135] S. Matar, A. Higier, and H. Liu, “The effects of excess phosphoric acid in a Polybenzimidazole-based high temperature proton exchange membrane fuel cell,” *J. Power Sources*, vol. 195, no. 1, pp. 181–184, 2010, doi: <https://doi.org/10.1016/j.jpowsour.2009.06.084>.
- [136] F.C Nart and T. Iwasita, “ON THE ADSORPTION OF H<sub>2</sub>, PO<sub>4</sub>, ANDH<sub>2</sub>, PO<sub>4</sub>, ON PLATINUM : AN IN SITU FT-ir STUDY,” *Electrochim. Acta*, vol. 37, no. 3, p. 385, 1992.
- [137] R. Jinnouchi *et al.*, “The role of oxygen-permeable ionomer for polymer electrolyte fuel cells,” *Nat. Commun.*, vol. 12, no. 1, p. 4956, 2021, doi: 10.1038/s41467-021-25301-3.
- [138] T. Lazaridis, B. M. Stühmeier, H. A. Gasteiger, and H. A. El-Sayed, “Capabilities and limitations of rotating disk electrodes versus membrane electrode assemblies in the investigation of electrocatalysts,” *Nat. Catal.*, vol. 5, no. 5, pp. 363–373, 2022, doi: 10.1038/s41929-022-00776-5.
- [139] C. Wannek, I. Konradi, J. Mergel, and W. Lehnert, “Redistribution of phosphoric acid in membrane electrode assemblies for high-temperature polymer electrolyte fuel cells,” *Int. J. Hydrogen Energy*, vol. 34, no. 23, pp. 9479–9485, 2009, doi: 10.1016/j.ijhydene.2009.09.076.
- [140] N. Bevilacqua *et al.*, “Impact of catalyst layer morphology on the operation of high temperature PEM fuel cells,” *J. Power Sources Adv.*, vol. 7, no. July 2020, 2021, doi: 10.1016/j.powera.2020.100042.
- [141] S. Martin, Q. Li, and J. O. Jensen, “Lowering the platinum loading of high temperature polymer electrolyte membrane fuel cells with acid doped polybenzimidazole membranes,” *J. Power Sources*, vol. 293, pp. 51–56, 2015, doi: 10.1016/j.jpowsour.2015.05.031.
- [142] A. Kongkanand and M. F. Mathias, “The Priority and Challenge of High-Power Performance of Low-Platinum Proton-Exchange Membrane Fuel Cells,” *J. Phys. Chem. Lett.*, vol. 7, no. 7, pp. 1127–1137, Apr. 2016, doi: 10.1021/acs.jpcllett.6b00216.
- [143] S. J. Kim *et al.*, “Characterizations of polybenzimidazole based electrochemical hydrogen pumps with various Pt loadings for H<sub>2</sub>/CO<sub>2</sub> gas separation,” *Int. J. Hydrogen Energy*, no. 38, 2013, doi: <http://dx.doi.org/10.1016/j.ijhydene.2013.08.142>.
- [144] M. Thomassen, E. Sheridan, and J. Kvello, “Electrochemical hydrogen separation and compression using polybenzimidazole (PBI) fuel cell technology,” *J. Nat. Gas Sci. Eng.*, vol. 2, 2010, doi: 10.1016/j.jngse.2010.10.002.
- [145] J. Jiang, T. R. Aulich, M. E. Collings, and C. W. Sohn, “High-Pressure Electrochemical Hydrogen Purification Process Using a High-Temperature Polybenzimidazole (PBI) Membrane,” *ECS Trans.*, no. 28, 2010, doi: 10.1149/1.3501098.
- [146] K. A. Perry, G. A. Eisman, and B. C. Benicewicz, “Electrochemical hydrogen pumping using a high-temperature polybenzimidazole (PBI) membrane,” *J. Power Sources*, vol. 177, no. 2, pp. 478–484, 2008, doi: 10.1016/j.jpowsour.2007.11.059.
- [147] D. S. Maxwell *et al.*, “High Purity Hydrogen Separation with HT-PBI Based Electrochemical Pump Operation at 120 ° C High Purity Hydrogen Separation with HT-



- PBI Based Electrochemical Pump Operation at 120 ° C,” *J. Electrochem. Soc.*, vol. 170, 2023, doi: 10.1149/1945-7111/acc6f7.
- [148] L. Vermaak, H. W. J. P. Neomagus, and D. G. Bessarabov, “Hydrogen separation and purification from various gas mixtures by means of electrochemical membrane technology in the temperature range 100–160°C,” *Membranes (Basel)*, vol. 11, no. 4, 2021, doi: 10.3390/membranes11040282.
- [149] A. J. Kidnay, W. R. Parrish, and D. G. McCartney, *Fundamentals of natural gas processing*. CRC press, 2019.
- [150] C. S. Gittleman, H. Jia, E. S. De Castro, C. R. I. Chisholm, and Y. S. Kim, “Proton conductors for heavy-duty vehicle fuel cells,” *Joule*, vol. 5, no. 7, pp. 1660–1677, 2021, doi: 10.1016/j.joule.2021.05.016.
- [151] ZeroAvia, “ZeroAvia High Temperature Fuel Cell Testing Shows Large Aircraft and Rotorcraft Potential for Hydrogen-Electric Propulsion.” <https://zeroavia.com/htpem-fuel-cell-testing/> (accessed Jan. 02, 2024).
- [152] A. S. Lee, Y. Choe, I. Matanovic, and Y. S. Kim, “The energetics of phosphoric acid interactions reveals a new acid loss mechanism,” *J. Mater. Chem.*, no. 16, 2019, doi: 10.1039/C9TA01756A.
- [153] V. Atanasov, A. Oleynikov, J. Xia, S. Lyonard, and J. Kerres, “Phosphonic acid functionalized poly(pentafluorostyrene) as polyelectrolyte membrane for fuel cell application,” *J. Power Sources*, vol. 343, pp. 364–372, 2017.
- [154] V. Atanasov and J. Kerres, “Highly phosphonated polypentafluorostyrene,” *Macromolecules*, vol. 44, no. 16, pp. 6416–6423, 2011, doi: 10.1021/ma2011574.
- [155] V. Atanasov *et al.*, “Synergistically integrated phosphonated poly(pentafluorostyrene) for fuel cells,” *Nat. Mater.*, vol. 20, no. 3, pp. 370–377, 2021, doi: 10.1038/s41563-020-00841-z.
- [156] A. S. Lee, “Adapting high temperature polymer electrolyte membrane fuel cells for transportation applications,” *Springer Nature Research Communities*, 2022. <https://communities.springernature.com/posts/adapting-high-temperature-polymer-electrolyte-membrane-fuel-cells-for-transportation-applications>
- [157] K. H. Lim *et al.*, “Protonated phosphonic acid electrodes for high power heavy-duty vehicle fuel cells,” *Nat. Energy*, vol. 7, no. 3, pp. 248–259, 2022, doi: 10.1038/s41560-021-00971-x.
- [158] K. H. Lim *et al.*, “High Temperature Polymer Electrolyte Membrane Fuel Cells with High Phosphoric Acid Retention,” *ACS Energy Lett.*, vol. 8, no. 1, pp. 529–536, 2023, doi: 10.1021/acscenergylett.2c02367.
- [159] J. Jung *et al.*, “Dispersing Agents Impact Performance of Protonated Phosphonic Acid High-Temperature Polymer Electrolyte Membrane Fuel Cells,” *ACS Energy Lett.*, pp. 1642–1647, 2022, doi: 10.1021/acscenergylett.2c00359.
- [160] Q. Li, R. He, J. O. Jensen, and N. J. Bjerrum, “PBI-based polymer membranes for high temperature fuel cells - Preparation, characterization and fuel cell demonstration,” *Fuel Cells*, vol. 4, no. 3, pp. 147–159, 2004, doi: 10.1002/fuce.200400020.
- [161] X. Cheng *et al.*, “Hydrogen crossover in high-temperature PEM fuel cells,” *J. Power Sources*, vol. 167, no. 1, pp. 25–31, 2007, doi: 10.1016/j.jpowsour.2007.02.027.
- [162] S. J. Buelte, D. Lewis, and G. Eisman, “Effect of Phosphoric Concentration on Hydrogen Pump Performance and Platinum Catalyst Activity,” in *220th ECS Meeting, The Electrochemical Society Effect*, 2011.

- [163] M. K. Daletou, J. K. Kallitsis, G. Voyiatzis, and S. G. Neophytides, “The interaction of water vapors with H<sub>3</sub>PO<sub>4</sub> imbibed electrolyte based on PBI/polysulfone copolymer blends,” *J. Memb. Sci.*, vol. 326, no. 1, pp. 76–83, 2009, doi: 10.1016/j.memsci.2008.09.040.
- [164] M. Thomassen, E. Sheridan, and J. Kvello, “Electrochemical hydrogen separation and compression using polybenzimidazole (PBI) fuel cell technology,” *J. Nat. Gas Sci. Eng.*, vol. 2, no. 5, pp. 229–234, 2010, doi: 10.1016/j.jngse.2010.10.002.
- [165] A. G. Association, “Natural Gas Pipeline Systems: Delivering Resiliency,” *Am. Gas Assoc.*, pp. 1–8, 2014.
- [166] M. Schalenbach, M. Carmo, D. L. Fritz, J. Mergel, and D. Stolten, “Pressurized PEM water electrolysis: Efficiency and gas crossover,” *Int. J. Hydrogen Energy*, vol. 38, no. 35, pp. 14921–14933, 2013, doi: 10.1016/j.ijhydene.2013.09.013.
- [167] R. He, Q. Li, A. Bach, J. O. Jensen, and N. J. Bjerrum, “Physicochemical properties of phosphoric acid doped polybenzimidazole membranes for fuel cells,” *J. Memb. Sci.*, vol. 277, no. 1–2, pp. 38–45, Jun. 2006, doi: 10.1016/j.memsci.2005.10.005.
- [168] M. Schalenbach, T. Hoefner, P. Paciok, M. Carmo, W. Lueke, and D. Stolten, “Gas Permeation through Nafion. Part 1: Measurements,” *J. Phys. Chem. C*, vol. 119, no. 45, pp. 25145–25155, Nov. 2015, doi: 10.1021/acs.jpcc.5b04155.
- [169] M. Nordio *et al.*, “Experimental and modelling study of an electrochemical hydrogen compressor,” *Chem. Eng. J.*, vol. 369, no. January, pp. 432–442, 2019, doi: 10.1016/j.cej.2019.03.106.
- [170] C. K. Mittelsteadt and H. Liu, “Conductivity, permeability, and ohmic shorting of ionomeric membranes,” in *Handbook of Fuel Cells - Advances in Electrocatalysis, Materials, Diagnostics and Durability. Part 5: Conductive membranes for low-temperature fuel cells*, John Wiley & Sons, 2009.
- [171] P. Bouwman, “Electrochemical Hydrogen Compression (EHC) solutions for hydrogen infrastructure,” *Fuel Cells Bull.*, vol. 2014, no. 5, pp. 12–16, 2014, doi: 10.1016/S1464-2859(14)70149-X.
- [172] S. A. Grigoriev, I. G. Shtatniy, P. Millet, V. I. Poremsky, and V. N. Fateev, “Description and characterization of an electrochemical hydrogen compressor/concentrator based on solid polymer electrolyte technology,” *Int. J. Hydrogen Energy*, vol. 36, no. 6, pp. 4148–4155, 2011, doi: 10.1016/j.ijhydene.2010.07.012.
- [173] K. Onda, K. Ichihara, M. Nagahama, Y. Minamoto, and T. Araki, “Separation and compression characteristics of hydrogen by use of proton exchange membrane,” *J. Power Sources*, vol. 164, no. 1, pp. 1–8, 2007, doi: 10.1016/j.jpowsour.2006.10.018.
- [174] K. Onda, T. Araki, K. Ichihara, and M. Nagahama, “Treatment of low concentration hydrogen by electrochemical pump or proton exchange membrane fuel cell,” *J. Power Sources*, vol. 188, no. 1, pp. 1–7, 2009, doi: 10.1016/j.jpowsour.2008.11.135.
- [175] A. Cheng *et al.*, “A partial element stage cut electrochemical hydrogen pump model for hydrogen separation and compression,” *Sep. Purif. Technol.*, vol. 307, no. November 2022, p. 122790, 2023, doi: 10.1016/j.seppur.2022.122790.
- [176] M. Mukaddam, E. Litwiller, and I. Pinnau, “Gas Sorption, Diffusion, and Permeation in Nafion,” *Macromolecules*, vol. 49, no. 1, pp. 280–286, 2016, doi: 10.1021/acs.macromol.5b02578.
- [177] M. Omidvar *et al.*, “Unexpectedly Strong Size-Sieving Ability in Carbonized Polybenzimidazole for Membrane H<sub>2</sub>/CO<sub>2</sub> Separation,” *ACS Appl. Mater. Interfaces*, vol.

- 11, no. 50, pp. 47365–47372, 2019, doi: 10.1021/acsami.9b16966.
- [178] W. Maier *et al.*, “In-situ synchrotron X-ray radiography on high temperature polymer electrolyte fuel cells,” *Electrochem. commun.*, vol. 12, no. 10, pp. 1436–1438, 2010, doi: 10.1016/j.elecom.2010.08.002.
- [179] R. Kuhn *et al.*, “Measuring device for synchrotron X-ray imaging and first results of high temperature polymer electrolyte membrane fuel cells,” *J. Power Sources*, vol. 196, no. 12, pp. 5231–5239, 2011, doi: 10.1016/j.jpowsour.2010.11.025.
- [180] A. Tobias *et al.*, “Synchrotron X-ray radiosopic in situ study of high-temperature polymer electrolyte fuel cells - Effect of operation conditions on structure of membrane,” *J. Power Sources*, vol. 246, pp. 290–298, 2014, doi: 10.1016/j.jpowsour.2013.07.094.
- [181] S. H. Eberhardt, F. Marone, M. Stampanoni, F. N. Büchi, and T. J. Schmidt, “Operando X-ray Tomographic Microscopy Imaging of HT-PEFC: A Comparative Study of Phosphoric Acid Electrolyte Migration,” *J. Electrochem. Soc.*, vol. 163, no. 8, pp. F842–F847, 2016, doi: 10.1149/2.0801608jes.
- [182] S. H. Eberhardt, F. Marone, M. Stampanoni, F. N. Büchi, and T. J. Schmidt, “Quantifying phosphoric acid in high-temperature polymer electrolyte fuel cell components by X-ray tomographic microscopy,” *J. Synchrotron Radiat.*, vol. 21, no. 6, pp. 1319–1326, 2014, doi: 10.1107/S1600577514016348.
- [183] S. H. Eberhardt, M. Toulec, F. Marone, M. Stampanoni, F. N. Büchi, and T. J. Schmidt, “Dynamic Operation of HT-PEFC: In-Operando Imaging of Phosphoric Acid Profiles and (Re)distribution,” *J. Electrochem. Soc.*, vol. 162, no. 3, pp. F310–F316, 2015, doi: 10.1149/2.0751503jes.
- [184] S. H. Eberhardt, F. Marone, M. Stampanoni, F. N. Büchi, and T. J. Schmidt, “Imaging Phosphoric Acid Migration in High Temperature Polymer Electrolyte Fuel Cells by X-Ray Tomographic Microscopy,” *ECS Meet. Abstr.*, vol. MA2015-02, no. 37, pp. 1420–1420, 2015, doi: 10.1149/ma2015-02/37/1420.
- [185] J. J. Bailey *et al.*, “Lab-based X-ray micro-computed tomography coupled with machine-learning segmentation to investigate phosphoric acid leaching in high-temperature polymer electrolyte fuel cells,” *J. Power Sources*, vol. 509, no. June, p. 230347, 2021, doi: 10.1016/j.jpowsour.2021.230347.
- [186] P. Satjaritanun *et al.*, “Observation of Preferential Pathways for Oxygen Removal through Porous Transport Layers of Polymer Electrolyte Water Electrolyzers,” *iScience*, vol. 23, no. 12, p. 101783, 2020, doi: 10.1016/j.isci.2020.101783.
- [187] D. Kulkarni, S. J. Normile, L. G. Connolly, and I. V. Zenyuk, “Development of low temperature fuel cell holders for operando x-ray micro and nano computed tomography to visualize water distribution,” *JPhys Energy*, vol. 2, no. 4, 2020, doi: 10.1088/2515-7655/abb783.
- [188] D. Cheddie and N. Munroe, “Parametric model of an intermediate temperature PEMFC,” *J. Power Sources*, vol. 156, no. 2, pp. 414–423, 2006, doi: <https://doi.org/10.1016/j.jpowsour.2005.06.010>.
- [189] D. Cheddie and N. Munroe, “Three dimensional modeling of high temperature PEM fuel cells,” *J. Power Sources*, vol. 160, pp. 215–223, Sep. 2006, doi: 10.1016/j.jpowsour.2006.01.035.
- [190] D. Cheddie and N. Munroe, “Mathematical model of a PEMFC using a PBI membrane,” *Energy Convers. Manag.*, vol. 47, no. 11, pp. 1490–1504, 2006, doi: <https://doi.org/10.1016/j.enconman.2005.08.002>.

- [191] D. F. Cheddie and N. D. H. Munroe, "A two-phase model of an intermediate temperature PEM fuel cell," *Int. J. Hydrogen Energy*, vol. 32, no. 7, pp. 832–841, 2007, doi: <https://doi.org/10.1016/j.ijhydene.2006.10.061>.
- [192] D. F. Cheddie and N. D. H. Munroe, "Semi-analytical proton exchange membrane fuel cell modeling," *J. Power Sources*, vol. 183, no. 1, pp. 164–173, 2008, doi: <https://doi.org/10.1016/j.jpowsour.2008.04.067>.
- [193] C. P. Wang, H. Sen Chu, Y. Y. Yan, and K. L. Hsueh, "Transient evolution of carbon monoxide poisoning effect of PBI membrane fuel cells," *J. Power Sources*, vol. 170, no. 2, pp. 235–241, 2007, doi: [10.1016/j.jpowsour.2007.03.070](https://doi.org/10.1016/j.jpowsour.2007.03.070).
- [194] A. Bergmann, D. Gerteisen, and T. Kurz, "Modelling of CO Poisoning and its Dynamics in HTPEM Fuel Cells," *Fuel Cells*, vol. 10, no. 2, pp. 278–287, Apr. 2010, doi: <https://doi.org/10.1002/fuce.200900128>.
- [195] M. Mamlouk, T. Sousa, and K. Scott, "A High Temperature Polymer Electrolyte Membrane Fuel Cell Model for Reformate Gas," *SAGE-Hindawi Access to Res. Int. J. Electrochem.*, vol. 18, Jan. 2011, doi: [10.4061/2011/520473](https://doi.org/10.4061/2011/520473).
- [196] L. Lüke, H. Janssen, M. Kvesić, W. Lehnert, and D. Stolten, "Performance Analysis of HT-PEFC Stacks," *Int. J. Hydrogen Energy*, vol. 37, pp. 9171–9181, 2012, [Online]. Available: <https://api.semanticscholar.org/CorpusID:96318107>
- [197] P. Chippar, K. Oh, D. Kim, T.-W. Hong, W. Kim, and H. Ju, "Coupled mechanical stress and multi-dimensional CFD analysis for high temperature proton exchange membrane fuel cells (HT-PEMFCs)," *Int. J. Hydrogen Energy*, vol. 38, no. 18, pp. 7715–7724, 2013, doi: <https://doi.org/10.1016/j.ijhydene.2012.07.122>.
- [198] K. Oh, P. Chippar, and H. Ju, "Numerical study of thermal stresses in high-temperature proton exchange membrane fuel cell (HT-PEMFC)," *Int. J. Hydrogen Energy*, vol. 39, no. 6, pp. 2785–2794, 2014, doi: <https://doi.org/10.1016/j.ijhydene.2013.01.201>.
- [199] K. Jiao and X. Li, "A Three-Dimensional Non-isothermal Model of High Temperature Proton Exchange Membrane Fuel Cells with Phosphoric Acid Doped Polybenzimidazole Membranes," *Fuel Cells*, vol. 10, no. 3, pp. 351–362, Jun. 2010, doi: <https://doi.org/10.1002/fuce.200900059>.
- [200] K. Jiao, I. Alaefour, and X. Li, "Three-dimensional non-isothermal modeling of carbon monoxide poisoning in high temperature proton exchange membrane fuel cells with phosphoric acid doped polybenzimidazole membranes," *Fuel*, vol. 90, pp. 568–582, 2011, [Online]. Available: <https://api.semanticscholar.org/CorpusID:96961746>
- [201] P. Chippar and H. Ju, "Numerical modeling and investigation of gas crossover effects in high temperature proton exchange membrane (PEM) fuel cells," *Int. J. Hydrogen Energy*, vol. 38, no. 18, pp. 7704–7714, 2013, doi: <https://doi.org/10.1016/j.ijhydene.2012.07.123>.
- [202] D. Bezmalinovic, S. Strahl, V. Roda, and A. Husar, "Water transport study in a high temperature proton exchange membrane fuel cell stack," *Int. J. Hydrogen Energy*, vol. 39, 2014.
- [203] P. Chippar, K. Kang, Y.-D. Lim, W.-G. Kim, and H. Ju, "Effects of inlet relative humidity (RH) on the performance of a high temperature- proton exchange membrane fuel cell (HT-PEMFC)," *Int. J. Hydrogen Energy*, vol. 39, pp. 2767–2775, 2014.
- [204] C. R. Wilke, "A viscosity equation for gas mixtures," *J. Chem. Phys.*, vol. 18, no. 4, pp. 517–519, 1950, doi: [10.1063/1.1747673](https://doi.org/10.1063/1.1747673).
- [205] M. M. Tomadakis and T. J. Robertson, "Viscous permeability of random fiber structures: Comparison of electrical and diffusional estimates with experimental and analytical

- results,” *J. Compos. Mater.*, vol. 39, no. 2, pp. 163–188, 2005, doi: 10.1177/0021998305046438.
- [206] J. Dvorkin, “KOZENY-CARMAN EQUATION REVISITED,” Stanford University, 2009.
- [207] J. T. Gostick, M. W. Fowler, M. D. Pritzker, M. A. Ioannidis, and L. M. Behra, “In-plane and through-plane gas permeability of carbon fiber electrode backing layers,” *J. Power Sources*, vol. 162, no. 1, pp. 228–238, 2006, doi: 10.1016/j.jpowsour.2006.06.096.
- [208] R. J. Balliet and J. Newman, “Cold Start of a Polymer-Electrolyte Fuel Cell I. Development of a Two-Dimensional Model,” *J. Electrochem. Soc.*, vol. 158, no. 8, p. B927, 2011, doi: 10.1149/1.3592430.
- [209] R. J. Balliet, “Modeling Cold Start in a Polymer-Electrolyte Fuel Cell,” University of California, Berkeley, 2010.
- [210] B. Bird, W. Stewart, and E. Lightfoot, *Transport Phenomena*, 2nd ed. Wiley & Sons, 2002.
- [211] P. D. Neufeld, A. R. Janzen, and R. A. Aziz, “Empirical equations to calculate 16 of the transport collision integrals  $\Omega(1,8)^*$  for the lennard-jones (12-6) potential,” *J. Chem. Phys.*, vol. 57, no. 3, pp. 1100–1102, 1972, doi: 10.1063/1.1678363.
- [212] H. H. Chang and D.-T. Chin, “On the conductivity of phosphoric acid electrolyte,” *J. Appl. Electrochem.*, vol. 19, pp. 95–99, 1989.
- [213] D. I. MacDonald and J. Boyack, “Density, Electrical Conductivity, and Vapor Pressure of Concentrated Phosphoric Acid,” *J. Chem. Eng.*, pp. 380–384, 1969.
- [214] R. F. Jameson, “The Composition of the ‘Strong’ Phosphoric Acids,” *J. Chem. Soc.*, 1959.
- [215] E. H. Brown and C. D. Whitt, “Vapor Pressure of Phosphoric Acid,” *Ind. Eng. Chem.*, vol. 44, no. 3, 1952, doi: doi:10.1021/ie50507a050.
- [216] S. A. Grigoriev, A. A. Kalinnikov, N. V. Kuleshov, and P. Millet, “Numerical optimization of bipolar plates and gas diffusion electrodes for PBI-based PEM fuel cells,” *Int. J. Hydrogen Energy*, vol. 38, no. 20, pp. 8557–8567, 2013, doi: 10.1016/j.ijhydene.2012.12.021.
- [217] S. Lang, T. J. Kazdal, F. Kühn, and M. J. Hampe, “Diffusion coefficients and VLE data of aqueous phosphoric acid,” *J. Chem. Thermodyn.*, vol. 68, pp. 75–81, 2014, doi: 10.1016/j.jct.2013.08.028.
- [218] C. R. Wilke and P. Chang, “Correlation of diffusion coefficients in dilute solutions,” *AIChE J.*, vol. 1, no. 2, pp. 264–270, 1955, doi: 10.1002/aic.690010222.
- [219] O. W. Edwards and E. O. Huffman, “Viscosity of aqueous solutions of phosphoric acid at 25° C,” *J. Chem. Eng. Data*, vol. 3, no. 1, pp. 145–146, 1958, doi: 10.1021/i460003a028.
- [220] F. Ruiz-Beviá, J. Fernández-Sempere, and N. Boluda-Botella, “Variation of phosphoric acid diffusion coefficient with concentration,” *AIChE J.*, vol. 41, no. 1, pp. 185–189, 1995, doi: 10.1002/aic.690410118.
- [221] A. H. Persad and C. A. Ward, “Expressions for the Evaporation and Condensation Coefficients in the Hertz-Knudsen Relation,” *Chem. Rev.*, vol. 116, no. 14, pp. 7727–7767, 2016, doi: 10.1021/acs.chemrev.5b00511.
- [222] J. Durst, C. Simon, F. Hasché, and H. A. Gasteiger, “Hydrogen Oxidation and Evolution Reaction Kinetics on Carbon Supported Pt, Ir, Rh, and Pd Electrocatalysts in Acidic Media,” *J. Electrochem. Soc.*, vol. 162, no. 1, pp. F190–F203, 2015, doi: 10.1149/2.0981501jes.
- [223] J. Newman and K. E. Thomas-Alyea, *Electrochemical Systems*. New York: John Wiley &

- Sons, 2004.
- [224] M. W. J. Chase, “NIST-JANAF Thermochemical Tables,” *J. Phys. Chem. Ref. Data*, vol. 4th editio, 1998.
- [225] F. P. Incropera, D. P. Dewitt, T. L. Bergman, and A. S. Lavine, *Fundamentals of Heat and Mass Transfer*, 6th ed. John Wiley & Sons, 2016.
- [226] B. B. Luff and Z. T. Wakefield, “Thermal Conductivity of Phosphoric Acid,” *J. Chem. Eng. Data*, vol. 14, no. 2, pp. 254–256, 1969, doi: 10.1021/je60041a036.
- [227] A. Z. Weber and J. Newman, “Coupled Thermal and Water Management in Polymer Electrolyte Fuel Cells,” *J. Electrochem. Soc.*, vol. 153, no. 12, p. A2205, 2006, doi: 10.1149/1.2352039.
- [228] J. C. Fornaciari *et al.*, “The Role of Water in Vapor-fed Proton-Exchange-Membrane Electrolysis,” *J. Electrochem. Soc.*, vol. 167, no. 10, p. 104508, 2020, doi: 10.1149/1945-7111/ab9b09.
- [229] M. R. Gerhardt *et al.*, “Method—Practices and Pitfalls in Voltage Breakdown Analysis of Electrochemical Energy-Conversion Systems,” *J. Electrochem. Soc.*, vol. 168, no. 7, p. 074503, 2021, doi: 10.1149/1945-7111/abf061.
- [230] K. S. Lee, J. S. Spendelow, Y. K. Choe, C. Fujimoto, and Y. S. Kim, “An operationally flexible fuel cell based on quaternary ammonium-biphosphate ion pairs. Supplemental Information,” *Nat. Energy*, vol. 1, no. 9, pp. 1–13, 2016, doi: 10.1038/nenergy.2016.120.
- [231] G. Jerkiewicz, “Electrochemical Hydrogen Adsorption and Absorption. Part 1: Under-potential Deposition of Hydrogen,” *Electrocatalysis*, vol. 1, no. 4, pp. 179–199, 2010, doi: 10.1007/s12678-010-0022-1.
- [232] S. Trasatti and O. A. Petrii, “International Union of Pure and Applied Chemistry Physical Chemistry Division Commission on Electrochemistry: Real Surface Area Measurements in Electrochemistry,” *Pure Appl. Chem.*, vol. 63, no. 5, pp. 711–734, 1991, doi: 10.1351/pac199163050711.
- [233] K. J. J. Mayrhofer, D. Strmcnik, B. B. Blizanac, V. Stamenkovic, M. Arenz, and N. M. Markovic, “Measurement of oxygen reduction activities via the rotating disc electrode method: From Pt model surfaces to carbon-supported high surface area catalysts,” *Electrochim. Acta*, vol. 53, no. 7, pp. 3181–3188, 2008, doi: 10.1016/j.electacta.2007.11.057.
- [234] Q. He, X. Yang, W. Chen, S. Mukerjee, B. Koel, and S. Chen, “Influence of phosphate anion adsorption on the kinetics of oxygen electroreduction on low index Pt(hkl) single crystals,” *Phys. Chem. Chem. Phys.*, vol. 12, no. 39, pp. 12544–12555, Oct. 2010, doi: 10.1039/c0cp00433b.
- [235] H. Lin *et al.*, “High-Temperature Rotating Disk Electrode Study of Platinum Bimetallic Catalysts in Phosphoric Acid,” *ACS Catal.*, vol. 13, no. 8, pp. 5635–5642, 2023, doi: 10.1021/acscatal.3c00432.
- [236] N. M. Marković, T. J. Schmidt, B. N. Grgur, H. A. Gasteiger, R. J. Behm, and P. N. Ross, “Effect of Temperature on Surface Processes at the Pt(111) - Liquid Interface: Hydrogen Adsorption, Oxide Formation, and CO Oxidation,” *J. Phys. Chem. B*, vol. 103, no. 40, pp. 8568–8577, 1999, doi: 10.1021/jp991826u.
- [237] C. Korte, F. Conti, J. Wackerl, and W. Lehnert, “8. Phosphoric Acid and its Interactions with Polybenzimidazole-Type Polymers,” in *High Temperature Polymer Electrolyte Membrane Fuel Cells: Approaches, Status, and Perspectives*, Springer International Publishing Switzerland, 2016.

- [238] W. Haynes, *CRC Handbook of Chemistry and Physics.*, 93rd editi. Boca Raton: Taylor & Francis Ltd, 2013.
- [239] A. Huhtu and P. Gartaganis, “The composition of the strong phosphoric acids,” *Can J Chem*, vol. 34, pp. 785–797, 1956.
- [240] C. Higgins and W. Baldwin, “Dehydration of orthophosphoric acid,” *Anal Chem*, vol. 27, pp. 1780–1783, 1955.
- [241] A. Orfanidi, M. K. Daletou, L. Sygellou, and S. G. Neophytides, “The role of phosphoric acid in the anodic electrocatalytic layer in high temperature PEM fuel cells,” *J. Appl. Electrochem.*, vol. 43, no. 11, pp. 1101–1116, 2013, doi: 10.1007/s10800-013-0626-2.
- [242] T. Engl, K. E. Waltar, L. Gubler, and T. J. Schmidt, “Second Cycle Is Dead: Advanced Electrode Diagnostics for High-Temperature Polymer Electrolyte Fuel Cells,” *J. Electrochem. Soc.*, vol. 161, no. 4, pp. F500–F505, 2014, doi: 10.1149/2.072404jes.
- [243] S. J. Buelte, “Effects of Phosphoric Acid Concentration on Platinum Catalyst and Phosphoric Acid Hydrogen Pump Performance,” Rensselaer Polytechnic Institute, 2011. doi: 10.1149/1.3635725.
- [244] H. Sumi *et al.*, “AC impedance characteristics for anode-supported microtubular solid oxide fuel cells,” *Electrochim. Acta*, vol. 67, pp. 159–165, 2012, doi: 10.1016/j.electacta.2012.02.021.
- [245] M. E. Orazem, P. Shukla, and M. A. Membrino, “Extension of the measurement model approach for deconvolution of underlying distributions for impedance measurements,” *Electrochim. Acta*, vol. 47, no. 13–14, pp. 2027–2034, 2002, doi: 10.1016/S0013-4686(02)00065-8.
- [246] H. Schichlein, A. C. Müller, M. Voigts, A. Krügel, and E. Ivers-Tiffée, “Deconvolution of electrochemical impedance spectra for the identification of electrode reaction mechanisms in solid oxide fuel cells,” *J. Appl. Electrochem.*, vol. 32, no. 8, pp. 875–882, 2002, doi: 10.1023/A:1020599525160.
- [247] E. Ivers-Tiffée and A. Weber, “Evaluation of electrochemical impedance spectra by the distribution of relaxation times,” *J. Ceram. Soc. Japan*, vol. 125, no. 4, pp. 193–201, 2017, doi: 10.2109/jcersj2.125.P4-1.
- [248] F. Ciucci, “Modeling electrochemical impedance spectroscopy,” *Curr. Opin. Electrochem.*, vol. 13, pp. 132–139, 2019, doi: 10.1016/j.coelec.2018.12.003.
- [249] A. Bertei, E. Ruiz-Trejo, F. Tariq, V. Yufit, A. Atkinson, and N. P. Brandon, “Validation of a physically-based solid oxide fuel cell anode model combining 3D tomography and impedance spectroscopy,” *Int. J. Hydrogen Energy*, vol. 41, no. 47, pp. 22381–22393, 2016, doi: 10.1016/j.ijhydene.2016.09.100.
- [250] B. A. Boukamp and A. Rolle, “Use of a distribution function of relaxation times (DFRT) in impedance analysis of SOFC electrodes,” *Solid State Ionics*, vol. 314, no. September 2017, pp. 103–111, 2018, doi: 10.1016/j.ssi.2017.11.021.
- [251] J. P. Schmidt, P. Berg, M. Schönleber, A. Weber, and E. Ivers-Tiffée, “The distribution of relaxation times as basis for generalized time-domain models for Li-ion batteries,” *J. Power Sources*, vol. 221, pp. 70–77, 2013, doi: 10.1016/j.jpowsour.2012.07.100.
- [252] J. P. Schmidt, T. Chrobak, M. Ender, J. Illig, D. Klotz, and E. Ivers-Tiffée, “Studies on LiFePO<sub>4</sub> as cathode material using impedance spectroscopy,” *J. Power Sources*, vol. 196, no. 12, pp. 5342–5348, 2011, doi: 10.1016/j.jpowsour.2010.09.121.
- [253] N. Bevilacqua, M. A. Schmid, and R. Zeis, “Understanding the role of the anode on the polarization losses in high-temperature polymer electrolyte membrane fuel cells using the

- distribution of relaxation times analysis,” *J. Power Sources*, vol. 471, p. 228469, 2020, doi: 10.1016/j.jpowsour.2020.228469.
- [254] K. Yezerska *et al.*, “Analysis of the regeneration behavior of high temperature polymer electrolyte membrane fuel cells after hydrogen starvation,” *J. Power Sources*, vol. 449, no. December 2019, p. 227562, 2020, doi: 10.1016/j.jpowsour.2019.227562.
- [255] A. Weiß, S. Schindler, S. Galbiati, M. A. Danzer, and R. Zeis, “Distribution of Relaxation Times Analysis of High-Temperature PEM Fuel Cell Impedance Spectra,” *Electrochim. Acta*, vol. 230, pp. 391–398, 2017, doi: 10.1016/j.electacta.2017.02.011.
- [256] M. Braig and R. Zeis, “Distribution of relaxation times analysis of electrochemical hydrogen pump impedance spectra,” *J. Power Sources*, vol. 576, no. May, p. 233203, 2023, doi: 10.1016/j.jpowsour.2023.233203.
- [257] S. Wang, J. Zhang, O. Gharbi, V. Vivier, M. Gao, and M. E. Orazem, “Electrochemical impedance spectroscopy,” *Nat. Rev. Methods Prim.*, vol. 1, no. 1, 2021, doi: 10.1038/s43586-021-00039-w.
- [258] W. H. Doh *et al.*, “Scanning photoelectron microscopy study of the Pt/ phosphoric-acid-imbibed membrane interface under polarization,” *ChemElectroChem*, vol. 1, no. 1, pp. 180–186, 2014, doi: 10.1002/celec.201300134.
- [259] N. Sugishima, J. T. Hinatsu, and F. R. Foulkes, “Phosphorous Acid Impurities in Phosphoric Acid Fuel Cell Electrolytes: I. Voltammetric Study of Impurity Formation,” *J. Electrochem. Soc.*, vol. 141, no. 12, pp. 3325–3331, 1994, doi: 10.1149/1.2059334.
- [260] N. Sugishima, J. T. Hinatsu, and F. R. Foulkes, “Phosphorous Acid Impurities in Phosphoric Acid Fuel Cell Electrolytes: II. Effects on the Oxygen Reduction Reaction at Platinum Electrodes,” *J. Electrochem. Soc.*, vol. 141, no. 12, pp. 3332–3335, 1994, doi: 10.1149/1.2059335.
- [261] F. Ciucci and C. Chen, “Analysis of electrochemical impedance spectroscopy data using the distribution of relaxation times: A Bayesian and hierarchical Bayesian approach,” *Electrochim. Acta*, vol. 167, pp. 439–454, 2015, doi: 10.1016/j.electacta.2015.03.123.
- [262] T. H. Wan, M. Saccoccio, C. Chen, and F. Ciucci, “Influence of the Discretization Methods on the Distribution of Relaxation Times Deconvolution: Implementing Radial Basis Functions with DRTtools,” *Electrochim. Acta*, vol. 184, pp. 483–499, 2015, doi: 10.1016/j.electacta.2015.09.097.
- [263] M. B. Effat and F. Ciucci, “Bayesian and Hierarchical Bayesian Based Regularization for Deconvolving the Distribution of Relaxation Times from Electrochemical Impedance Spectroscopy Data,” *Electrochim. Acta*, vol. 247, pp. 1117–1129, 2017, doi: 10.1016/j.electacta.2017.07.050.
- [264] S. Dierickx, A. Weber, and E. Ivers-Tiffée, “How the distribution of relaxation times enhances complex equivalent circuit models for fuel cells,” *Electrochim. Acta*, vol. 355, p. 136764, 2020, doi: 10.1016/j.electacta.2020.136764.
- [265] M. Heinzmann, A. Weber, and E. Ivers-Tiffée, “Advanced impedance study of polymer electrolyte membrane single cells by means of distribution of relaxation times,” *J. Power Sources*, vol. 402, no. September, pp. 24–33, 2018, doi: 10.1016/j.jpowsour.2018.09.004.
- [266] Z. Guo, L. Hu, H. H. Yu, X. Cao, and H. Gu, “Controlled hydrogenation of aromatic compounds by platinum nanowire catalysts,” *RSC Adv.*, vol. 2, no. 8, pp. 3477–3480, 2012, doi: 10.1039/c2ra01097f.
- [267] V. E. Kazarinov, A. N. Frumkin, E. A. Ponomarenko, and V. N. Andreev, “Adsorption of benzene, phenol and naphthalene on platinum,” *Ehlektrkhimiya*, vol. 11, pp. 860–866,



- 1975.
- [268] D. Li, H. T. Chung, S. Maurya, I. Matanovic, and Y. S. Kim, "Impact of ionomer adsorption on alkaline hydrogen oxidation activity and fuel cell performance," *Curr. Opin. Electrochem.*, vol. 12, pp. 189–195, 2018, doi: 10.1016/j.coelec.2018.11.012.
- [269] S. Maurya *et al.*, "Rational design of polyaromatic ionomers for alkaline membrane fuel cells with >1 W cm<sup>-2</sup> power density," *Energy Environ. Sci.*, vol. 11, no. 11, pp. 3283–3291, 2018, doi: 10.1039/c8ee02192a.
- [270] D. Li, H. T. Chung, S. Maurya, I. Matanovic, and Y. S. Kim, "Impact of ionomer adsorption on alkaline hydrogen oxidation activity and fuel cell performance," *Curr. Opin. Electrochem.*, vol. 12, pp. 189–195, 2018, doi: 10.1016/j.coelec.2018.11.012.
- [271] I. Matanovic, H. T. Chung, and Y. S. Kim, "Benzene adsorption: A significant inhibitor for the hydrogen oxidation reaction in alkaline conditions," *J. Phys. Chem. Lett.*, vol. 8, no. 19, pp. 4918–4924, 2017, doi: 10.1021/acs.jpcclett.7b02228.
- [272] M. Nordio *et al.*, "Experimental and modelling study of an electrochemical hydrogen compressor," *Chem. Eng. J.*, vol. 369, no. November 2018, pp. 432–442, 2019, doi: 10.1016/j.cej.2019.03.106.
- [273] C. Jackson, G. Smith, and A. R. Kucernak, "Deblending and purification of hydrogen from natural gas mixtures using the electrochemical hydrogen pump," *Int. J. Hydrogen Energy*, vol. 52, pp. 816–826, 2024, doi: 10.1016/j.ijhydene.2023.05.065.
- [274] S. J. Kim *et al.*, "Highly active and CO<sub>2</sub> tolerant Ir nanocatalysts for H<sub>2</sub>/CO<sub>2</sub> separation in electrochemical hydrogen pumps," *Appl. Catal. B Environ.*, vol. 158–159, pp. 348–354, 2014, doi: 10.1016/j.apcatb.2014.04.016.
- [275] M. S. Wilson and S. Gottesfeld, "Thin-film catalyst layers for polymer electrolyte fuel cell electrodes," *J. Appl. Electrochem.*, vol. 22, no. 1, pp. 1–7, 1992, doi: 10.1007/BF01093004.
- [276] G. Huang *et al.*, "Composite Poly(norbornene) Anion Conducting Membranes for Achieving Durability, Water Management and High Power (3.4 W/cm<sup>2</sup>) in Hydrogen/Oxygen Alkaline Fuel Cells," *J. Electrochem. Soc.*, vol. 166, no. 10, pp. F637–F644, 2019, doi: 10.1149/2.1301910jes.
- [277] J. O. Park, K. Kwon, M. D. Cho, S.-G. Hong, T. Y. Kim, and D. Y. Yoo, "Role of Binders in High Temperature PEMFC Electrode," *J. Electrochem. Soc.*, vol. 158, no. 6, pp. B675–B681, 2011, doi: 10.1149/1.3573773.
- [278] H. Su, S. Pasupathi, B. Bladergroen, V. Linkov, and B. G. Pollet, "Optimization of gas diffusion electrode for polybenzimidazole-based high temperature proton exchange membrane fuel cell: Evaluation of polymer binders in catalyst layer," *Int. J. Hydrogen Energy*, vol. 38, no. 26, pp. 11370–11378, 2013, doi: 10.1016/j.ijhydene.2013.06.107.
- [279] M. Schuster, K. D. Kreuer, H. Steininger, and J. Maier, "Proton conductivity and diffusion study of molten phosphonic acid H<sub>3</sub>PO<sub>3</sub>," *Solid State Ionics*, vol. 179, no. 15–16, pp. 523–528, 2008, doi: 10.1016/j.ssi.2008.03.030.
- [280] L. Vilčiauskas, C. C. De Araujo, and K. D. Kreuer, "Proton conductivity and diffusion in molten phosphinic acid (H<sub>3</sub>PO<sub>2</sub>): The last member of the phosphorus oxoacid proton conductor family," *Solid State Ionics*, vol. 212, pp. 6–9, 2012, doi: 10.1016/j.ssi.2012.02.019.
- [281] T. Rager, M. Schuster, H. Steininger, and K. D. Kreuer, "Poly(1,3-phenylene-5-phosphonic acid), a fully aromatic poly electrolyte with high ion exchange capacity," *Adv. Mater.*, vol. 19, no. 20, pp. 3317–3321, 2007, doi: 10.1002/adma.200602788.

- [282] M. Schuster, T. Rager, A. Noda, K. D. Kreuer, and J. Maier, "About the choice of the protogenic group in PEM separator materials for intermediate temperature, low humidity operation: A critical comparison of sulfonic acid, phosphonic acid and imidazole functionalized model compounds," *Fuel Cells*, vol. 5, no. 3, pp. 355–365, 2005, doi: 10.1002/fuce.200400059.
- [283] K. Arunagiri, A. Jark-wah Wong, L. Briceno-Mena, J. A. Romagnoli, M. J. Janik, and C. G. Arges, "Deconvoluting charge-transfer, mass transfer, and ohmic resistances in phosphonic acid- sulfonic acid ionomer binders used in electrochemical hydrogen pumps," *Energy Environ. Sci.*, vol. 16, pp. 1–40, 2023.
- [284] V. Atanasov, M. Bürger, S. Lyonnard, L. Porcar, and J. Kerres, "Sulfonated poly(pentafluorostyrene): Synthesis & characterization," *Solid State Ionics*, vol. 252, pp. 75–83, 2013, doi: 10.1016/j.ssi.2013.06.010.
- [285] B. S. Pivovar, W. H. Smyrl, and E. L. Cussler, "Electro-osmosis in Nafion 117, Polystyrene Sulfonic Acid, and Polybenzimidazole," *J. Electrochem. Soc.*, vol. 152, no. 1, p. A53, 2005, doi: 10.1149/1.1827599.